Using external stimuli to design responsive supramolecular systems with predictable properties

Simona Bianco

Submitted in fulfilment of the requirements for the Degree of Doctor of Philosophy

School of Chemistry

College of Science and Engineering

University of Glasgow

February 2025

Declaration of Authorship

I declare that, except where explicit reference is made to the contributions of others, that this dissertation is the result of my own work and has not been submitted for any other degree at the University of Glasgow or any other institution.

Simona Bianco

Abstract

Supramolecular gels formed by the self-assembly of peptide-based LMWG are a class of soft materials that have attracted significant interest for a vast range of applications. Due to the non-covalent nature of the interactions underpinning the gel networks, these materials can exhibit stimuli-responsive behaviour to external triggers. By introducing this aspect in their design, a wide variety of new materials can be accessed with pre-determined properties with a high level of temporal and spatial control. In this Thesis, we describe how to harness external stimuli to induce predictable and reversible changes in supramolecular systems, achieving materials with desirable properties for different potential applications.

First, we show a dipeptide-based LMWG system undergoing pre-programmable gel-to-sol-to-gel transitions obtained by means of a pH cycle. We investigate the effect of mechanical stimuli applied during rheological measurements on the properties of these evolving materials, highlighting how varying parameters of strain and frequency can be used to obtain a wide range of gels with different properties starting from the same material. Building on these results, we then design a new system undergoing gel-to-sol-to-gel transitions capable of aligning under unidirectional shear in the solution phase. Using a novel combined technique of rheology, polarised light imaging and SAXS, we show the potential of this system to prepare gels with aligned domains using mechanical stimuli. We further highlight the versatility of this approach by inducing alignment using a magnetic field.

We then describe the use of a non-invasive light trigger to design a multicomponent system based on a LMWG and a photoacid molecule capable of switching pH under irradiation. We show how this approach yields a light-responsive system that reproducibly changes viscosity under irradiation. Using a variety of combined *in situ* techniques (rheology, NMR and SAXS), we elucidate the way these changes occur on a variety of length scales. We finally show how this stimuli-responsive system can be used to stop flow at specific locations using light and discuss potential applications.

Finally, we focus on the design of peptide-based gels for applications in drug storage and release by taking advantage of their unique response to mechanical stimulus. By using rheology, SAXS and release tests we show how gel mechanical properties, network morphology and choice of trigger can affect the ability of these systems to store and successfully release a cargo molecule. Based on this, we then establish a novel method to release biologics using a simple mechanical stimulus. Lastly, we test the stability of these systems under various real-world conditions for future applications in drug delivery.

Acknowledgements

Firstly, I would like to say a huge thank you to my supervisor Prof. Dave Adams for all his support and encouragement over these last four years and my placement in Utrecht. I feel really fortunate to have had the possibility to do a PhD in your lab, I could not have asked for a better supervisor. Thank you for the guidance, insight, mentorship and reminding me that "va tutto bene" when I was likely stressing out over something minor. I am truly grateful for all the amazing opportunities and trust you have given to me during these years, they have helped me become the scientist I am today. I hope I was able to give something back by teaching you some more Italian, grazie mille!

I would like to thank the University of Glasgow for being such a supportive place throughout my undergraduate degree and my PhD. I have never regretted moving away from home at 18, and the people in Glasgow have made all the difference. I would like to extend my thanks to the technical staff (Alec Mungall, Chris Kelly and Claire Wilson) and lecturers at the University for all their help during my time here. I would like to particularly thank my second supervisor, Dr. Drew Thomson, for his insight and invaluable support during my PhD. I would also like to thank Prof. Emily Draper for her advice and help, both in and out of the lab. It was a pleasure to have young women researchers like you to look up to.

Majority of this Thesis has been submitted as publications, which would not have been as successful without the help of collaborators and colleagues. As such, acknowledgements have been provided at the start of each Chapter where appropriate. Dr. Qingwen Guan, Prof. Dave Adams and Dr. Bart Dietrich (University of Glasgow) are thanked for synthesising the molecules used in Chapters 2 – 5. Thank you to Prof. Roland Kadar and Dr. Marko Bek (Chalmers University) for processing, analysing and visualising the Rheo-PLI-SAXS data in Chapter 3. Dr. Ravi R. Sonani and Prof. Edward Egelman (University of Virginia) are acknowledged for collecting the Cryo-EM data in Chapter 3. I would like to thank Fin Hallam Stewart (University of Glasgow) for collecting part of the rheological data in Chapter 3. Dr. Laura Wimberger and Prof. Jonathon Beves (UNSW) are thanked for providing the photoacid molecule used in Chapter 4. Thank you to Dr. Yaen Ben-Tal and Dr. George Williams (University of Southampton) for collecting the ^{1}H NMR measurements in Chapter 4. I would like to thank Dr. Matthew Wallace for collecting the STD-NMR data shown in Chapter 5. Finally, I would like to thank all the people who have helped me collecting the SAXS data presented in Chapters 2 – 5: Emma Bowley (University of Glasgow), Fin Hallam Stewart (University of Glasgow), Dr. Libby Marshall (University of Glasgow), Dr. Max Hill

(University of Glasgow), Dr. Chloe Wallace (University of Glasgow), Dr. Valentina Gauci (University of Glasgow), Connor MacDonald (University of Glasgow) and Dr. Alex Loch (University of Glasgow). Thank you to Dr. Rebecca Ginesi (University of Glasgow) for the support and help in setting up all the custom rheological methods presented in this work.

A massive thank you to the members of the Adams group past (Santanu, Lisa, Dan, Courtenay, Valentina, Maria Laura, Max, Chloe and Qingwen) and present (Dipankar, Libby, Emma, Rui, Fin, Tejaswini, Olivia, Helen and Hunter) for making this experience so enjoyable and helping me out throughout these years (especially at beamtimes). This work would not have been the same without the help of my so-called “academic family”. To my academic grandpa (sorry!), Santanu, I would not have been so successful in my work without your support during the first year of my PhD. I have learnt so much from you, you are a machine! Thank you for your patience, academic advice and encouragement, especially when helping me in trying to repeat our time sweeps again and again at 6 pm. To my academic mom, Libby, I don’t know if I would have been able to push through these years without you. You were such an inspiration from the start and always ready to provide support, advice and often a shoulder to cry on. Our screaming sessions in the office are unmatched (the boys office can’t compare), and I am glad we got to make silly memes to keep ourselves sane, thank you Wurt. You are so amazing at all you do and I can’t wait to see your career bloom! To my academic sister, Emma, I can’t believe I was there to show you how to make your first gels and I am so happy to have seen you grow into such a brilliant scientist. Thank you for all the support and help you have given me. Thank you for being my rock when we were both running on two hours on sleep and a dream at different synchrotrons around the world. To my academic son, Fin, thank you for being such a great student to supervise, I was so glad to see you join the lab as a fellow PhD student later on! I am, maybe, sorry I gave you the worm(-like micelles) in the brain and have made you become a SAXS and Inkscape nerd. Thank you for all the hilarious chats, less than great puns, cartoon advice and also joining me for crazy runs around synchrotrons (worth it for Wiener Melanges). I can now proudly say you have officially earned the promotion from SAXS boy to SAXS person. To Rui, who currently doesn’t have a position in this weird family tree, thank you for being such a ray of sunshine in our office and making me cry laugh all the time. Thank you for always offering to make Chinese food whenever I mention it and for providing me with cat pics in times of need.

A big thank you to the members of the Draper group past (Jakki, Becky, Rebecca) and present (Bart, Nick, Connor, Ziyao, Ben, Lineta and Ellen) for being such great lab mates.

To Nick, I can't believe we started together as wee undergrads and we are now finishing our PhDs! I am so proud of you and all the amazing work you have done these years. Thank you for always bringing such a fun energy in the lab, I will miss our 5 pm chats near the fumehoods. To Connor, thank you for being a great SANS partner in crime, ISIS will miss our co-ordinated grand jetes and Naruto runs. To Lineta, thank you for being such a great supporter throughout these years and always offering lovely chats in the rheometer room. To Ellen, I am sad I have not got to spend much time with you in the lab! Thank you for always being up to try new things and bringing us along, hope to see you soon flying off from a trapeze.

I would also like to thank all the visiting students who have made my experience in the lab so fun. To Paolino, I will never forget how you just invited yourself to my place during your first week to make lasagna, I knew it was going to be a great friendship from then. I am glad we get to see each other often in Puglia. To la mia amio Jessica, you have supported me and listened to me in probably one of the hardest times during my PhD and I will forever be grateful for that, you were one of the few reasons I still pushed myself to keep going. Thank you for all the silly Scottish trips, dinners, possibly co-ordinated breakdowns and for letting me babysit your "giels" (especially my son JM95). You are truly talented at what you do, I am looking forward to whatever you will do next. To Lucìetta, mis amore, I am so glad we got to spend so much time together in the lab, you are so fun to be around and always up for adventures (and chorizo). Thank you for all the support and celebrating my wins, small or big, and I hope I was able to do the same for you. To Sofia, I am so thankful for having spent the last few months of my PhD together, you are so much more amazing than you think. Thank you for being my aerialist partner in crime and always being up to do silly stuff in the air, our synchro egg will forever be my favourite.

All the work presented in this thesis heavily relies on the use of scattering techniques. I would like to thank all the beamline scientists who have helped me setting up my experiments, provided helpful discussions and were happy to discuss new and weirder set-ups. Thanks to Dr. Andy Smith (Diamond), Dr. Ann Terry and Dr. Tomás Plivelic (MAXIV), Dr. Thomas Bizien (SOLEIL), Dr. James Doutch (ISIS Neutron and Muon Source), Dr. Ralf Schweins and Dr. Sylvain Prévost (ILL). I would also like to thank Prof. Annela Seddon for her invaluable help with small angle scattering and all her support, insightful chats and help during my PhD.

Thank you to all the people in Glasgow who have been there for me during this time. To Paula, my fellow screaming gibbon, thank you for being a constant source of support throughout this time. We have started this journey together and I am so proud of us for everything we have achieved, you are brilliant at what you do. Thank you for always being there to listen to all my rants about gels and offering help in the form of your "songs", I have to admit that the little simo song is a banger. We have been through a lot these years and I am glad we have been there for each other through it all. To Giulia, my "wife", thank you for being by my side since our undergrad, I truly cherish our memories together in the haunted mice flat and our long chats while brushing our teeth. I can't believe we were able to finish Pasión de Gavilanes before our PhDs, honestly one of our biggest achievements. Thank you for all your help during these years, I am grateful for all the fun adventures we have embarked on together, especially finally having our deserved (*expensive) afternoon tea. To the scorregge pals, Riccardo and Francesco, thank you for all the laughs, coffee trips, vongole and our runs together. I am very happy you guys were there for my first half marathon, hoping to race more together soon. To Isacco, thank you for the morning chats and, unfortunately, also the very questionable jokes. You have always celebrated my wins, even when I did not feel like I needed to, and I could never thank you enough for that. To Emmanuelle, my French counterpart, I believe that everyone should have a friend like you in their life! Thank you for the lovely lunch breaks, karaoke sessions and, most importantly, your honesty, it has been central for my success.

Grazie a tutti i miei amici che si trovano un po' sparsi per l'Italia per tutto l'appoggio in questi anni. A Chiara, sono troppo contenta di essere riuscita a condividere con te la mia Glasgow questo mese e di poter aver scritto questi ringraziamenti con te. Grazie per essere sempre pronta ad ascoltarmi parlare per ore di chimica, gels e sincrotroni, nonostante tu non abbia la minima idea di cosa stia parlando. Grazie di tutte le videochiamate, serie iniziate e mai finite e aiuto con i miei processi creativi. A mama y papa, Luigia e Lorenzo, grazie per essere sempre pronti ad ospitarmi quando faccio i miei viaggi pazzi per Bologna. Il nostro viaggio a Manchester è uno dei miei ricordi preferiti di questo periodo, sono davvero grata per la vostra amicizia. A Marianna, il mio plus one preferito, non vedo l'ora di poter celebrare con te qui a Glasgow. Grazie per l'affetto e il supporto che mi hai sempre dato in questi anni, soprattutto durante le nostre lunghe chiacchierate in macchina a Cozze.

Questa tesi non sarebbe stata possibile senza l'amore, appoggio e affetto della mia famiglia, che è stata pronta ad accettare la mia decisione di andare via per tutti questi anni. A mia madre, Angela, è sempre un piacere parlare di chimica con te. Sono contenta di essere

riuscita a condividere una parte del mio lavoro e intersecarla alla tua, grazie per essere sempre presente nella mia vita. A mio padre, Giovanni, che mi fa sempre morire dalle risate. È stato un anno difficile per te, sei una persona fortissima. Grazie per aver appoggiato ogni mia decisione in questi anni, e sotto sotto so che ormai sei innamorato della Scozia. A mio fratello, Stefano, grazie per essere uno dei miei più grandi fan. Sono davvero felice che porteremo a termine questi grandi traguardi insieme. Alle mie nonne, Maria e Adriana, siete delle donne grandiose e una grande fonte di ispirazione per la mia carriera. Ai miei nonni, Pietro e Stefano, che purtroppo non sono più qui per poter celebrare con me. Grazie per tutto l'affetto che mi avete mostrato sin da piccola, spero di avervi reso orgogliosi!

List of Publications arising from this Degree

1. **S. Bianco**,* R. R. Sonani,* D. Ghosh, T. Maurya, T. Bizien, A. Pincham, A. J. Smith, K. Inoue, A. Seddon, M. Vassalli, E. H. Egelman and D. J. Adams, Modular salt-induced nanostructures formed by a functionalized dipeptide system, submitted.

2. Y. Wang, R. R. Sonani, L. Marshall, **S. Bianco**, K. Marshall, A. Pincham, L. C. Serpell, A. M. Seddon, E. H. Egelman, D. Thomson and D. J. Adams, Polydispersity effects in oligopeptide self-assembly, submitted.

3. Z. Deng, C. B. Tovani, **S. Bianco**, G. Comandini, A. Elghajiji, D. J. Adams, F. Scarpa, M. R. Whitehouse, A. M. Seddon, J. P. K. Armstrong, Coagulative Granular Hydrogels with an Enzyme Catalyzed Fibrin Network for Endogenous Tissue Regeneration, submitted.

4. R. R. Sonani, **S. Bianco**, M. Kreutzberger, D. J. Adams and E. H. Egelman, Cryo-EM for atomic characterization of supramolecular gels, *Faraday Discussions*, 2024, DOI: 10.1039/D4D00181H.

5. **S. Bianco**, F. Hallam Stewart, S. Panja, A. Zyar, E. Bowley, M. Bek, R. Kádár, A. Terry, R. Appio, T. S. Plivelic, M. Maguire, H. Poptani, M. Marcello, R. R. Sonani, E. H. Egelman and D. J. Adams, Forging out-of-equilibrium supramolecular gels, *Nature Synthesis*, 2024, **3**, 1481–1489.

6. **S. Bianco**,* M. Hasan,* A. Ahmad, S.-J. Richards, B. Dietrich, M. Wallace, Q. Tang, A. J. Smith, M. I. Gibson and D. J. Adams, Mechanical release of homogenous proteins from supramolecular gels, *Nature*, 2024, **631**, 544–548. (*Joint authors)

7. **S. Bianco**, L. Wimberger, Y. Ben‐Tal, G. T. Williams, A. J. Smith, J. E. Beves and D. J. Adams, Reversibly Tuning the Viscosity of Peptide‐Based Solutions Using Visible Light, *Chemistry – A European Journal*, 2024, **30**, e202400544.

8. R. R. Sonani, **S. Bianco**, B. Dietrich, J. Doutch, E. R. Draper, D. J. Adams and E. H. Egelman, Atomic structures of naphthalene dipeptide micelles unravel mechanisms of assembly and gelation, *Cell Rep Phys Sci*, 2024, **5**, 101812.

9. E. L. Bowley, **S. Bianco**, F. H. Stewart, C. M. Wallace, R. E. Ginesi, A. S. Loch, M. Rosenthal, A. J. Smith and D. J. Adams, Designing and Controlling Transient Supramolecular Gels, *ChemSystemsChem*, 2024, 202400073, 1–8.

10. R. Ghanbari, A. Terry, S. Wojno, M. Bek, K. Sekar, A. K. Sonker, K. Nygård, V. Ghai, **S. Bianco**, M. Liebi, A. Matic, G. Westman, T. Nypelö and R. Kádár, Propagation of Orientation Across Lengthscales in Sheared Self‐Assembling Hierarchical Suspensions via Rheo‐PLI‐SAXS, *Advanced Science*, 2024, 2410920, 1–13.

11. **S. Bianco** and D. J. Adams, in *Peptide Self‐Assembly and Engineering*, Wiley, 2024, pp. 81–107.

12. S. K. Chaubey, R. Kumar, P. L. Lalaguna, M. Kartau, **S. Bianco**, V. Tabouillot, A. R. Thomson, A. Sutherland, O. Lyutakov, N. Gadegaard, A. S. Karimullah and M. Kadodwala, Ultrasensitive Raman Detection of Biomolecular Conformation at the Attomole Scale using Chiral Nanophotonics, *Small*, 2024, 2404536.

13. P. Ravarino, S. Panja, **S. Bianco**, T. Koev, M. Wallace and D. J. Adams, Controlled Annealing in Adaptive Multicomponent Gels, *Angewandte Chemie International Edition*, 2023, **62**, e202215813.

14. L. J. Marshall, **S. Bianco**, R. E. Ginesi, J. Doutch, E. R. Draper and D. J. Adams, Investigating multigelator systems across multiple length scales, *Soft Matter*, 2023, **19**, 4972–4981.

15. **S. Bianco**, S. Panja and D. J. Adams, Using Rheology to Understand Transient and Dynamic Gels, *Gels*, 2022, **8**, 132.

16. S. Panja, **S. Bianco**, B. Dietrich and D. J. Adams, Macroscopic volume phase transitions in supramolecular gels directed by covalent crosslinking, *Mater Chem Front*, 2022, **6**, 2703–2708.

Table of Contents

List of Abbreviations

$\dot{\gamma}$ – Shear rate

°C – Degrees Celsius

1D – 1-dimensional

^{1}H – Proton

2D – 2-dimensional

^{2}H – Deuterium

3D – 3-dimensional

Å – Angstrom

AFM – Atomic Force Microscopy

C – Cylinder

C-terminus – Carboxyl-terminus

Ca^{2+} – Calcium ion

$CaCl_2$ – Calcium chloride

CCD – Charged-coupled device

CD – Circular dichroism

CMC **–** Critical micellar concentration

CRAB – Cavitation Rheometer Analyser Box

Cryo-EM – Cryogenic-electron microscopy

d – d-spacing

D_2O – Deuterated water

d6-DMSO – Deuterated dimethyl sulfoxide

Da – Dalton

DCl – Deuterium chloride

DMSO – Dimethyl sulfoxide

DNA – Deoxyribonucleic acid

EC – Elliptical cylinder

EDC – 1-Ethyl-3-(3-dimethylaminopropyl)carbodiimide

eq – Molar equivalent

F – Phenylalanine amino acid (see also Phe)

FCE – Flexible elliptical cylinder

FE-SEM – Field emission scanning electron microscopy

FITC-D – Fluorescein isothiocyanate dextran

Fmoc – Fluorenylmethyloxycarbonyl

G – Gauge

G′ – Storage modulus

G″ – Loss modulus

GdL – Glucono-δ-lactone

H_2O – Water

HCl – Hydrochloric acid

HPLC – High-performance liquid chromatography

HT – High tension

I – Isoleucine amino acid

IR – Infrared

K – Kelvin

K_2CO_3 – Potassium carbonate

KCl – Potassium chloride

keV – Kilo-Electronvolt

KOH – Potassium hydroxide

LED – Light-emitting diode

LMWG – Low molecular weight gelator

LVER/LVE – Linear viscoelastic region

M – Molar

mM – Millimolar

Mr – Relative molecular mass

MRI – Magnetic resonance imaging

mRNA – Messenger ribonucleic acid

NaOH – Sodium hydroxide

Nap – Naphthyloxyl

NDI – Naphthalene diimide

nm – Nanometre

NMR – Nuclear magnetic resonance

N-terminus – Amine-terminus

PA – Peptide amphiphile

Pa – Pascal

PBI – Perylene bisimide

PEG – Polyethylene glycol

PL – Power law

PLI – Polarised light imaging

ppm – Parts per million

PVC – Polyvinyl chloride

PXRD – Powder X-ray Diffraction

q – Scattering vector

rpm – Rotations per minute

RQC – Residual quadrupolar coupling

SANS – Small angle neutron scattering

SAXS – Small angle X-ray scattering

SEM – Scanning electron microscopy

SIPLI – Shear-induced polarised light imaging

SLD – Scattering length density

STD NMR – Saturation transfer difference nuclear magnetic resonance

T – Tesla

tanδ – Damping factor

TEM – Transmission electron microscopy

T_{gel} – Gelation temperature

TRIS – Tris(hydroxymethyl)aminomethane

UEA – University of East Anglia

UofG – University of Glasgow

UV – Ultraviolet

UV-Vis – Ultraviolet-visible

V – Valine amino acid

Chapter 1. Introduction

This Chapter is adapted from the following publication:

"Stimuli-responsive Structural Transformations of Peptide Supramolecular Gels"

S. Bianco and D.J. Adams, in Peptide Self-Assembly and Engineering, Wiley, 2024, pp. 81–107.

Simona Bianco researched, created the figures and wrote the manuscript. Prof. Dave J. Adams (University of Glasgow) supervised the project and contributed to the final draft of the chapter. All authors have read and agreed to the published version of the chapter.

1. Introduction

1.1 Hydrogels

Gels constitute a type of soft material made of three-dimensional networks that entrap a liquid, such as water or organic solvents.[1] When gels are formed from water they are referred to as hydrogels,[2] while in the case of organic solvents they are termed organogels.[3] These materials can retain large amounts of liquid, while still maintaining their three-dimensional structure.[4] Because of this, gels exhibit viscoelastic behaviour: elasticity is given by their solid network, whilst the solution trapped in the pores gives rise to the viscous behaviour.[5] Gels have been of particular interest for a broad range of applications, such as tissue engineering,[6] medicine,[7] drug delivery,[8] cell culture[9,10] and environmental remediation.[11]

A variety of molecules can be used to synthesise gels, among which are naturally occurring and synthetic polymers.[12] Based on the forces holding the networks together, gels can be classified as 'chemical' gels or 'physical' gels.[13] In chemical gels, the polymer chains are linked together through covalent cross-linking (Figure 1.1a). Conversely, physical gels, or supramolecular gels, are held by non-covalent forces, such as hydrogen bonding, π-π stacking and hydrophobic interactions between the monomers making up the chains (Figure 1.1b).[14] Thus, compared to permanently cross-linked chemical gels, physical gels show lower mechanical stability and tend to break at lower strains. However, the presence of these non-covalent interactions means that the networks in physical gels can be reversed by application of external energy.[15] Supramolecular gels formed by the self-assembly of small molecules, namely low molecular weight gelators (LMWGs), have gained significant attention in recent years.[16]

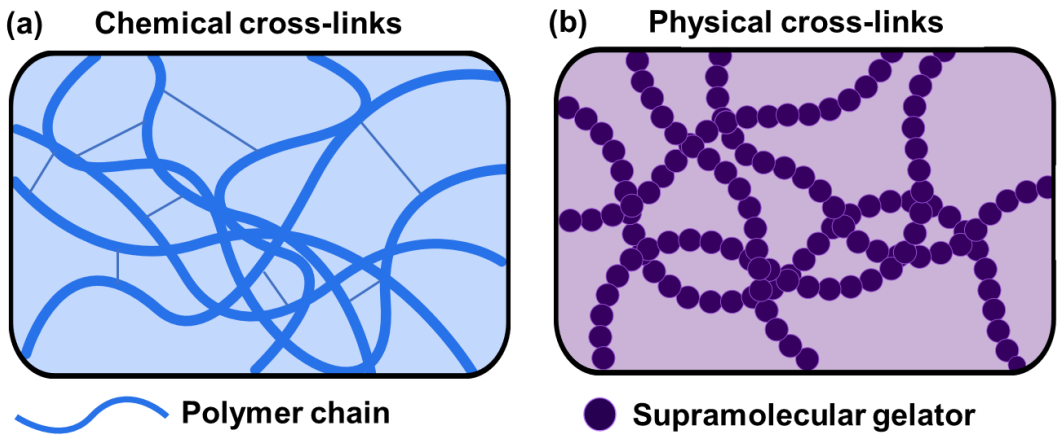

Figure 1.1. Schematic drawing representing the underlying networks for (a) chemical gels formed by covalent cross-links and (b) physical gels formed by non-covalent interactions.

1.2 Low molecular weight gelators

Low molecular weight gels are formed through the self-assembly of small organic molecules (low molecular weight gelators) into long fibrillar structures by non-covalent forces.[17] To form a supramolecular gel, the gelator molecules are first dissolved or suspended in solution (Figure 1.2, left). Upon addition of a gelation trigger, self-assembly into long fibres in the nanometre scale *via* non-covalent interactions is promoted (Figure 1.2, centre). In turn, the fibres will entangle to form a three-dimensional network at the micrometre scale, which entraps the solvent or water, resulting in a self-supporting material which is stable upon inversion (Figure 1.2, right).[16,17] The main driving forces leading self-assembly are typically strong hydrogen bonding, π-π stacking, donor-acceptor interactions, metal coordination, hydrophobic interactions as well as van der Waals interactions.[18]

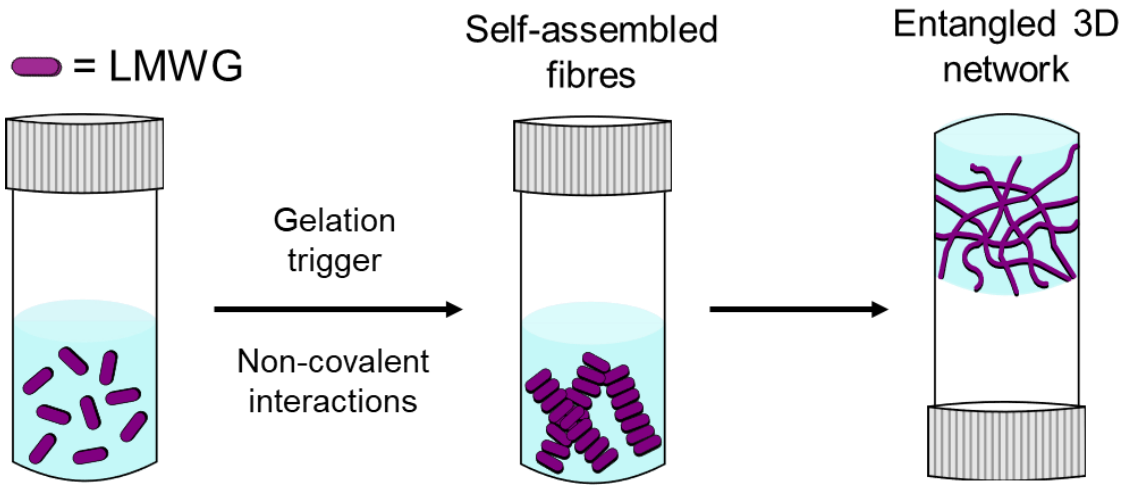

Figure 1.2. Cartoon representing the gelation mechanism for supramolecular gels. When a gelation trigger is applied, the gelator molecules undergo self-assembly, forming fibrillar structures (centre). The fibres will entangle and grow, forming a three-dimensional network that traps the solvent. A self-supporting gel is formed as a result (right).

A variety of triggers can be used to form supramolecular gels, such as temperature,[19] pH changes,[20] solvent changes,[21] addition of salts[22] and enzymatic reactions.[23] Although different, all these methods rely on changing the environment around the gelator, reducing its solubility and, thus, inducing self-assembly. It is worth noting that the choice of gelation trigger affects the self-assembly process, meaning that different gelation conditions lead to different final mechanical properties of the gels.[24–26]

Due to the non-covalent nature of the interactions within supramolecular gels, the main advantage of such materials is that gel formation is reversible and highly sensitive to a

variety of external stimuli, making them "smart".[27] For instance, hydrogen-bonding motifs can be influenced by pH, often leading to a collapse of the gel upon addition of acid or base. Furthermore, reversible changes in aggregation, volume or phase can be obtained through changes in heat, light, electrical fields or mechanical stress.[28–30] As a result, these materials have been particularly interesting for applications in sensing, drug-release, actuation or self-healing. Among the various gelators that can lead to stimuli-responsive gels, gelators based on amino acids or peptides have attracted significant interest.[31]

1.3 Designing peptide-based supramolecular gelators

Peptide molecules provide an ideal candidate for the design of stimuli-responsive supramolecular gels, due to their ability to adopt different secondary structures such as α-helix, coiled-coils, β-sheets. These can then further self-assemble hierarchically to form higher order aggregates, making them particularly suited for supramolecular gel design.[31] Furthermore, the different amino acids that form peptide sequences provide a wide range of physical properties.[32] For instance, incorporation of various non-covalent interactions can be possible, like hydrogen bonding from polar amino acids, hydrophobic interactions from non-polar amino acids, π-stacking from aromatic amino acids, electrostatic interactions from charged side-chains or even covalent bond formation through disulfide bonds (Figure 1.3).[33] Hence, rational design of molecules containing these functions can allow control over molecular organization in response to applied stimuli, fine-tuning the material properties based on its design.

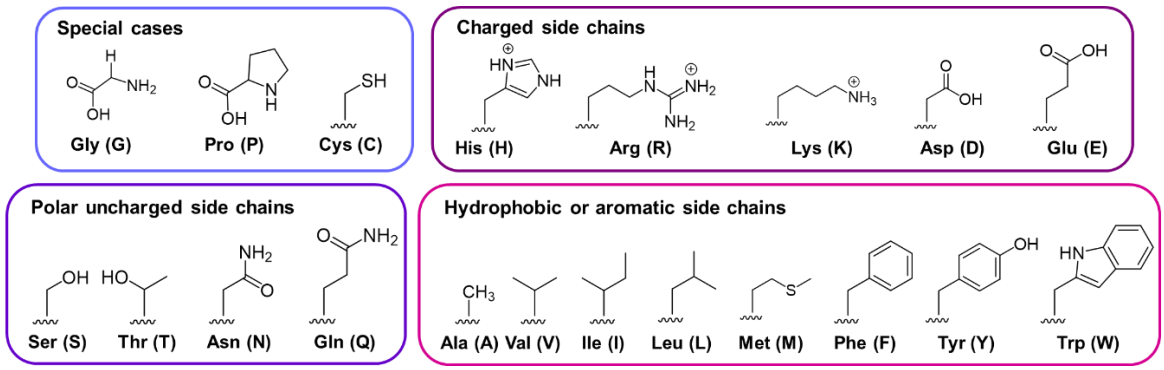

Figure 1.3. Representation of the side chains of the essential amino acids.

During self-assembly, peptides can also adopt different nanostructure shapes, such as micellar aggregates, fibrillar structures (fibres, nanotubes) and vesicles (Figure 1.4).[34] Micellar structures typically form spontaneously above a critical micelle concentration (CMC) and can be spherical, worm-like or disk-shaped.[35]

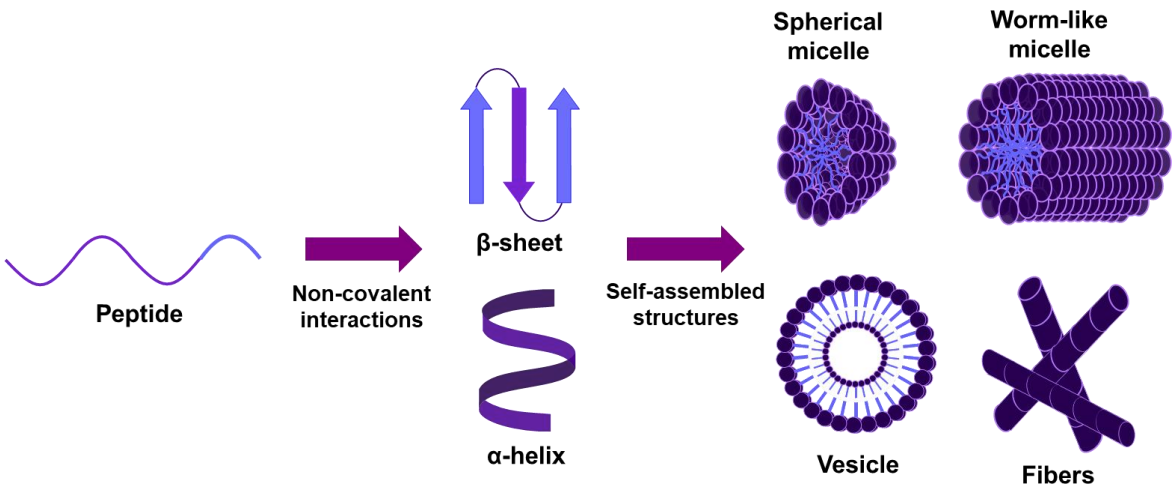

Figure 1.4. Different self-assembled structures that can be adopted by peptides through inter or intra molecular non-covalent interactions.

Based on these considerations and peptide science, several small peptide gelators have been designed to contain sequences predisposed to form specific supramolecular structures. Short peptide sequences are advantageous due to ease of synthesis, cost and scalability as well as the fact that they are easier to modify.[36] Common hydrogelators are peptide amphiphiles (PA), where the peptide chains are typically functionalized with aliphatic chains or aromatic chains at the *N*-terminus (Figure 1.5).[37] In such systems, self-assembly relies on the balance between hydrophilic and hydrophobic regions to ensure a balance between solubility and hydrophobicity.

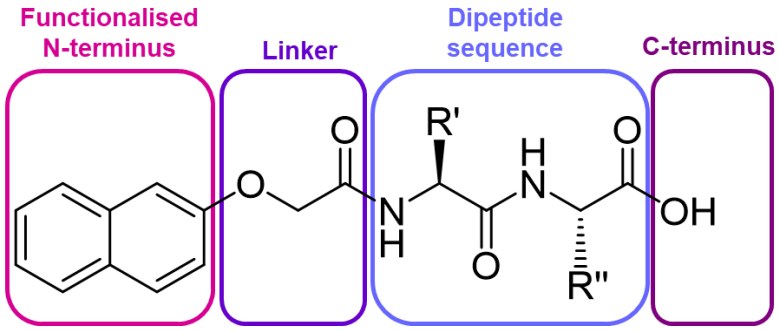

Figure 1.5. Representative structure of a peptide amphiphile with an aromatic group at the *N*-terminus. As a common example, a naphthalene dipeptide is shown.

The structure of a peptide amphiphile can typically be identified in four main regions: a hydrophobic region at the *N*-terminus, a linker, the peptide sequence, and the *C*-terminus, which can be either left unprotected or functionalized to impart bioactivity.[38] Firstly, the *N*-terminus is functionalized with a hydrophobic group, which typically drives self-assembly and gelation. For this purpose, long alkyl chains can be used. It is relevant to note that the

chains must be of sufficient length, as shorter chains might not be hydrophobic enough to induce self-assembly and subsequent gelation.[38,39] Another useful approach is to functionalize the *N*-terminus with aromatic groups. These allow an ulterior level of directionality, as self-assembly will further be directed by aromatic π-π stacking interactions. For self-assembling peptide-based hydrogels, the fluorenylmethoxycarbonyl (Fmoc) moiety is specifically common due to its role as a protecting group in peptide synthesis. The Fmoc group has been found to facilitate gelation for a variety of peptide-based systems.[40–42] Other synthetic aromatic groups have also been used to design peptide-based molecules capable of self-assembly such as naphthalene,[43] anthracene,[44] pyrene[45] or azobenzene.[46] Groups such as naphthalene can also be functionalized with different groups at various positions on the ring, affecting self-assembly and final gel properties.[47]

The choice of linker between the peptide chain and the aromatic group has also been found to affect the self-assembly of such peptide-based gelators. For instance, Fleming *et al.* investigated the effect of the methoxycarbonyl linker for fluorenyl moieties on hydrogelation.[48] The methoxy linker of the Fmoc moiety was found to allow more extensive aromatic stacking interactions compared to fluorenyl analogues with shorter linkers. This behaviour was ascribed to the fact that the shorter linkers restricted available molecular orientations in the molecule. Similarly, it was observed that the naphthoxy group allowed to form gels, while other naphthalene amphiphiles with different linkers failed to promote gelation.[43] Molecular dynamic calculations indicated that an increase in curvature of the molecules was responsible for the observed behaviour, suggesting that more linear geometries were necessary to allow optimal hydrogen bonding and π - π stacking. The methoxy group acts as an H-bond acceptor, which could further direct intermolecular interactions among the gelators.

As previously mentioned, the peptide sequence can have a significant effect on self-assembly, due to the wide range of possible molecular interactions that can be accessed. Therefore, they are an important aspect for the design of supramolecular gelators.[36] However, predicting whether a given molecule will form a hydrogel based on the amino acid sequence is still challenging and many gelators are often found by trial-and-error.[49] In part, this can be due to the fact that most gel systems are formed in metastable states and, thus, the self-assembly of the structures formed also depends on gelation pathway and environmental conditions.[24]

Diphenylalanine is a popular choice due to Gazit's pioneering work,[50] suggesting that the presence of aromatic side chains can facilitate gelation through π-stacking interactions. Aromatic residues in the peptide sequence have also been observed to increase the stiffness of the network formed, as well as increase the rate of gelation.[51] Nevertheless, the order of the amino acid sequences in the peptide backbone plays a substantial role in the process of self-assembly and, therefore, gelation. For instance, the Stupp group showed that the order of amino acid sequence in a tetrapeptide amphiphile can significantly affect the type of 1D self-assembled structures by switching the position of two adjacent amino acids in the sequence.[52] Furthermore, simply switching the order of dipeptide sequences has been shown lead to drastic changes and can for example turn gelator molecules into non-gelators.[53,54]

1.4 Gelation triggers

1.4.1 pH trigger

When the LMWG presents a functional group that can be protonated or de-protonated, such as carboxylic acids or amines, pH modulation can be exploited to prepare gels. Typically, gelator molecules are first dissolved or suspended in aqueous phase by altering the pH of the solution.[55] For gelator molecules containing carboxylic acids, dissolution is obtained at high pH due to de-protonation. Then, self-assembly is triggered by lowering the pH of the solution below the apparent pK_a of the gelator: re-protonation of the free carboxylic acid reduces the solubility of the LMWG, yielding gels (Figure 1.6).[56] The pH of the solution can be lowered in a variety of ways, even by direct addition of acids such as hydrochloric acid (HCl). However, non-homogeneous formation of gels was observed *via* this method, ascribed to faster rates of gelation than HCl diffusion throughout the sample.[20] Instead, to form homogeneous and reproducible gels, Adams *et al.* made use of the slow hydrolysis of glucono-δ-lactone (GdL) to achieve control over the pH decrease.[20] GdL hydrolyses in water to give gluconic acid, releasing protons. As the rate of hydrolysis is slower than the rate of GdL mixing, homogeneous and reproducible gels can be obtained using this approach. In a similar manner, other small ester-containing molecules that slowly hydrolyse and furnish acid can be used to induce self-assembly, such as sultones,[57] formates and caprolactones.[58] The hydrolysis of anhydrides has also been used to produce gels by Draper *et al*., showing that the rate of gel formation affects both the final gel mechanical properties as well as their homogeneity.[59]

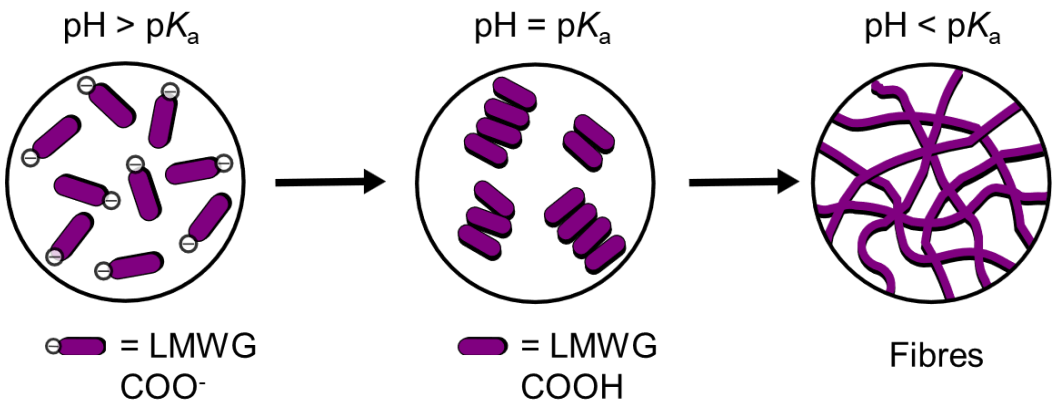

Figure 1.6. Cartoon showing the self-assembly and gelation process for a LMWG gel with a free carboxylic acid terminus. Self-assembly of the molecule begins when the pH is lowered to the pK_a value, with fibre formation occurring as the pH decreases further to form a gel.

In a similar way, for LMWGs that form gels at high pH, other than simple addition of a strong base, self-assembly has also been induced by diffusing ammonium hydroxide (NH_4OH) vapours.[60] Control over homogeneous gelation can be achieved by generating NH_3 *in situ* by exploiting the slow enzymatic reaction between urea and urease.[61] This will further be discussed in Section 1.5.3.1.

Another method to generate local changes in pH is to exploit photoacid molecules. When irradiated with light, these molecules produce protons and bring about a reduction in pH. In presence of a LMWG, photoacids can be used to re-protonate the gelator and form gels. These photoacid molecules have been used to form light-triggered supramolecular gels[62–67] and form gels on photo-patterned surfaces.[68] Not all LMWG can be triggered using this method, but nevertheless, addition of these photoacid molecules allows to induce further self-assembly changes.[62] For instance, a photoacid generator was used to locally increase the stiffness of gels formed using GdL.[67] We have shown that such photoacids can be further used to change the viscosity of solutions of LMWG,[69] which will be further investigated in Chapter 4.

1.4.2 Salt trigger

One approach to trigger gelation is to take advantage of the ability of specific groups on gelator molecules to chelate metal ions, resulting in cross-linking and self-assembly. For instance, LMWGs that possess carboxylic acid moieties can chelate divalent metal ions at the carboxylate terminus (Figure 1.7). Notably, this type of gelation can only occur if pre-

formed fibres are present in solution, as this method relies on forming salt bridges between the binding groups on worm-like micelles.[70] Indeed, for systems forming non-persistent spherical aggregates, salt-induced gelation was not observed.[71] The effect of salt correlates to the Hofmeister series and salt-induced self-assembly can further be altered by the valence of the metal ion, salt concentration and gelator concentration.[72,73]

Most commonly, calcium salts are used to trigger gels *via* chelation of the Ca^{2+} ions, which bind together the negatively charged COO^- group of the worm-like micelles.[74,75] It follows that this approach is very attractive to form gels at desired pH values above the pK_a. For instance, gels at physiological pH can be formed using this approach.[76] In particular, due to the presence of mono and divalent salts in buffer solutions, gels can also be obtained using buffers at desired pH values or cell culture media.[77–79]

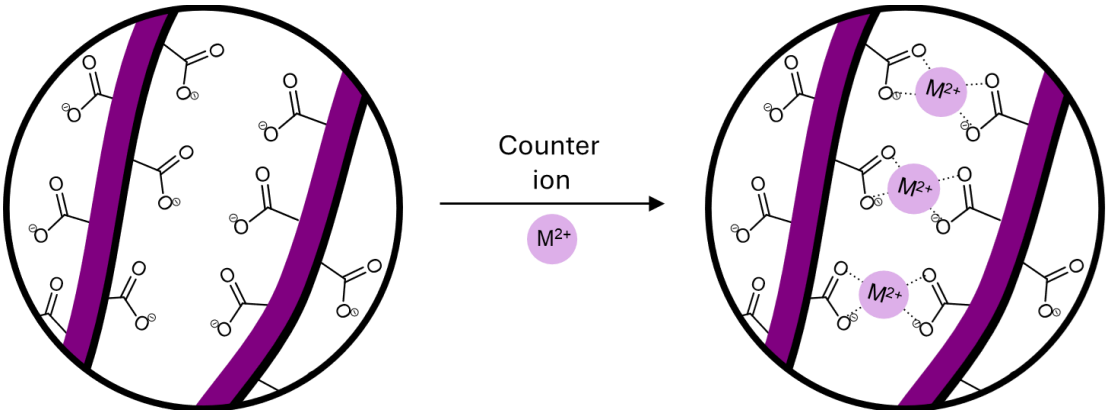

Figure 1.7. Cartoon showing the chelation of divalent metal ions (M^{2+}) to induce gelation of LMWG.

1.4.3 Solvent trigger

Solvent-switch gelation relies on the good solubility of LMWGs in water-miscible solvents, but poor solubility in water.[21] In order to prepare gels using this method, the gelator molecule is first dissolved in a water-miscible solvent, such as dimethyl sulfoxide (DMSO). Then, water is added to the sample in one aliquot, reducing the solubility of the gelator molecule.[80,81] As a result, self-assembly is induced rapidly. The mechanical properties and microstructure of the formed material can further be influenced by altering the ratio of the two solvents.[82] Furthermore, the final properties of the gel can even be affected by the choice of organic solvent.[83]

Due to the ease of preparation and fast gelation times, solvent-switch is widely used as a gelation trigger. In Chapters 2 and 3, we will describe how this fast gel formation can be exploited to design systems capable of evolving through different phases.

1.4.4 Temperature trigger

As gelation is triggered by solubility changes, temperature is often used to form gels. Temperature-triggered gelation relies on the solubility of the LMWG in the solvent at high temperatures. Once heated and dissolved, the LMWG solubility starts to decrease as the temperature lowers. This process drives self-assembly and subsequent gelation when the gelation temperature T_{gel} is reached.[84] Temperature-induced gelation is widely used for the preparation of organogels,[19,85] although it has also been used to prepare hydrogels.[86,87] Generally, the final properties of temperature-triggered gels are affected by rate of cooling, gelator concentration and solvent used.

1.5 Stimuli-responsive changes in supramolecular gels

Generally, the self-assembled structures making up supramolecular gels tend not to change their properties with time once they are formed. However, due to the non-covalent interactions making up the network of the gels, these materials can show tuneable and switchable behaviour when exposed to external stimuli. This highly stimuli-responsive behaviour means that the material properties can be modulated through external changes given by chemical, mechanical, optical or electrical stimuli. Therefore, there has been an increasing interest in designing supramolecular materials that transiently change properties or phase over time as a function of a variety of triggers, such as pH change, enzymes and redox reactions.[88–94]

Upon application of a stimulus, changes in aggregation and morphology of the system are typically brought about as a response. Often, supramolecular gels collapse or undergo a gel-sol transition because of a reduction or increase in the solubility of the gelator molecules. However, it is possible for the molecules to reassemble into a different aggregate simultaneously, leading to materials that show interconversions between multiple physical states. Such “smart” materials that show changes such as swelling, shrinking, colour, extent of cross-linking are particularly interesting for applications in sensing, actuators, and drug delivery. Examples of supramolecular gels showing stimuli-responsive changes are summarised in Table 1.1.

Table 1.1. Representative examples of peptide-based supramolecular gel systems that show stimuli-responsive structural changes with different triggers.

Stimulus	Example gelator	Response
Aging	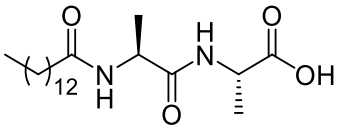	Turbidity change; increase in stiffness (Reference n. 105)
Light	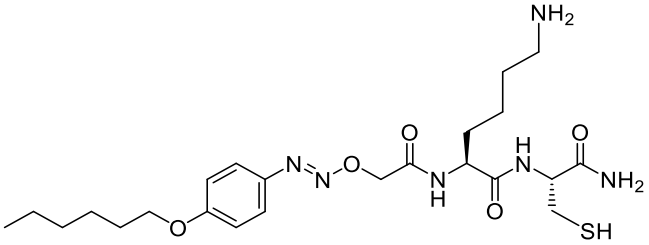	Volume decrease (Reference n. 117)
Chemical	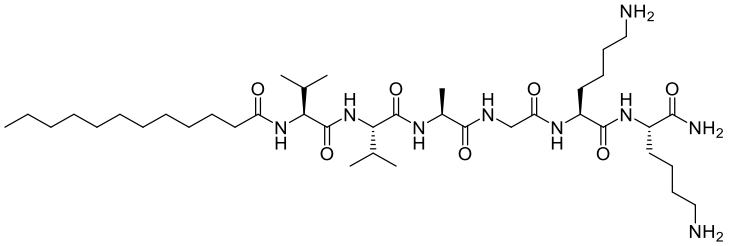	Colour change; increase in stiffness. (Reference n. 142)
Electrical	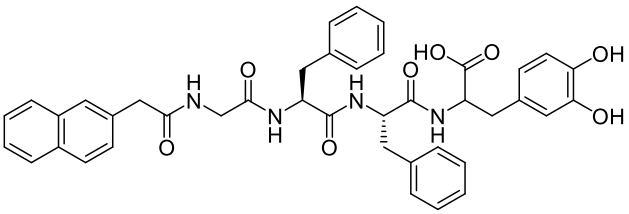	Volume decrease; increase in stiffness (Reference n. 165)
Mechanical	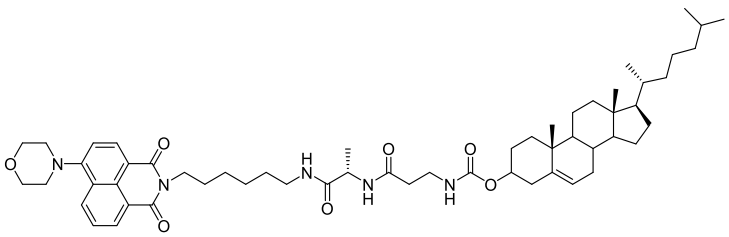	Morphological change; higher thermostability (Reference n. 172)

It is relevant to note that the term "structural changes" is quite ambiguous when referring to these systems. The self-assembly process underpinning gelation is a hierarchical process, going from intra-molecular interactions between free gelator molecules at the Angstrom (Å)

length scale to the formation of 1D-structures at the nanometre scale, which then form a three-dimensional network at the micrometre scale (Figure 1.8). It follows then that the term "structural change" can apply to several levels of changes. For instance, molecular changes can be brought about by a *trans* to *cis* transformation in a gelator molecule, while other changes might not affect the molecular scale, but generate visual and bulk changes for instance in volume or colour. Therefore, it is paramount to use appropriate techniques to characterize changes on each of these length scales.[95] On the molecular scale, infrared (IR) spectroscopy or nuclear magnetic resonance (NMR) can be used to probe the interactions between molecular building blocks.[96] At the next length scale, the nanoscale 1D-structures can be studied by microscopy, such as scanning electron microscopy (SEM) or atomic force microscopy (AFM).[97] For these techniques, the gels need to be dried, which may lead to artefacts.[98] Because of this, small-angle X-ray or neutron scattering (SAXS or SANS) can provide more accurate complementary information on the 1D-nanostructures in the wet gel state.[99] Finally, the macroscopic behaviour from the gel network can be probed by rheology, giving information on the mechanical properties of the bulk gel.[100] The way these techniques are used to investigate LMWGs will be discussed in Section 1.7.

Here, we will discuss stimuli-responsive structural changes that occur across all different length scales accessed from hierarchical self-assembly. In the context of this Thesis, we will mainly focus on systems where such changes occur as structural transitions in the gel and the sol state.

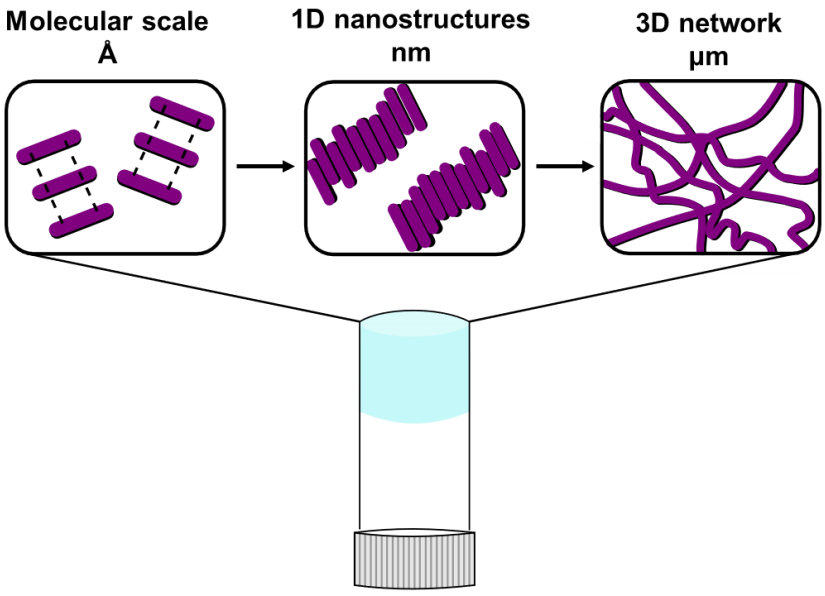

Figure 1.8. Cartoon representing the different length scales associated with self-assembly of small-molecule supramolecular gels.

1.5.1 Aging

Among the ways structural changes can occur within supramolecular gels, the process of aging plays a significant role. Although often overlooked, the effect of aging is crucial to determine the stability of these materials for their desired applications. Due to the dynamic nature of self-assembly, the assembled network may re-arrange over time or 'self-correct' to a more homogeneous network. In particular, this can occur when the self-assembly process occurs under kinetic control and not in a thermodynamic minimum.[101,102] As a result, the bulk properties of the gel can change over time, with changes in mechanical strength, visual appearance, and microstructure.

For instance, while studying a small library of small molecule hydrogelators, Shi *et al*. reported a phenylalanine-based compound that formed opaque gels at low pH.[103] The gel was found to turn into a clear hydrogel after aging for 10 days. It is hypothesized that the aging process aided the molecules to disperse and self-assemble over time. A similar unusual transition was also reported by the Adams group, where a 2-thiophene diphenylalanine LMWG was shown to go from a turbid gel to transparent over three days.[104] This change was accompanied by an increase in rheological properties compared to the turbid gel, suggesting a change in the bulk gel properties. SEM images before and after gel-to-gel transition show a morphological transition from large spherical structures to a fibrous network. The rearrangement of the fibres appeared to be triggered by an increased presence of carbonate, stressing the importance of conditions for specific applications.

Conversely, a time-dependent gradual transformation from transparent to turbid gel was observed for a peptide-based amphiphilic gelator molecule containing a long aliphatic chain at the *N*-terminus, **MAA**.[105] The gel was formed through a heat/cool process in a phosphate buffer solution. At a concentration of 4.5 mg/mL, the time-dependent transformation was observed across 2 days (Figure 1.9, left). However, the dynamic visual transition was found to be significantly dependent on gelator concentration, rate of cooling of the gelator solution and time. SAXS and electron microscope images show that this transition occurred due to a compaction of the packing pattern of the gelator assemblies over time (Figure 1.9a and 1.9b). The data indicate that with time, the fibres become more ordered and show prominent twisting, leading to a five-fold increase in the stiffness of the gel with time. Time-dependent fluorescence with pyrene also suggests that an increase in the hydrophobic environment around the gelator molecules occurs within the gel matrix.

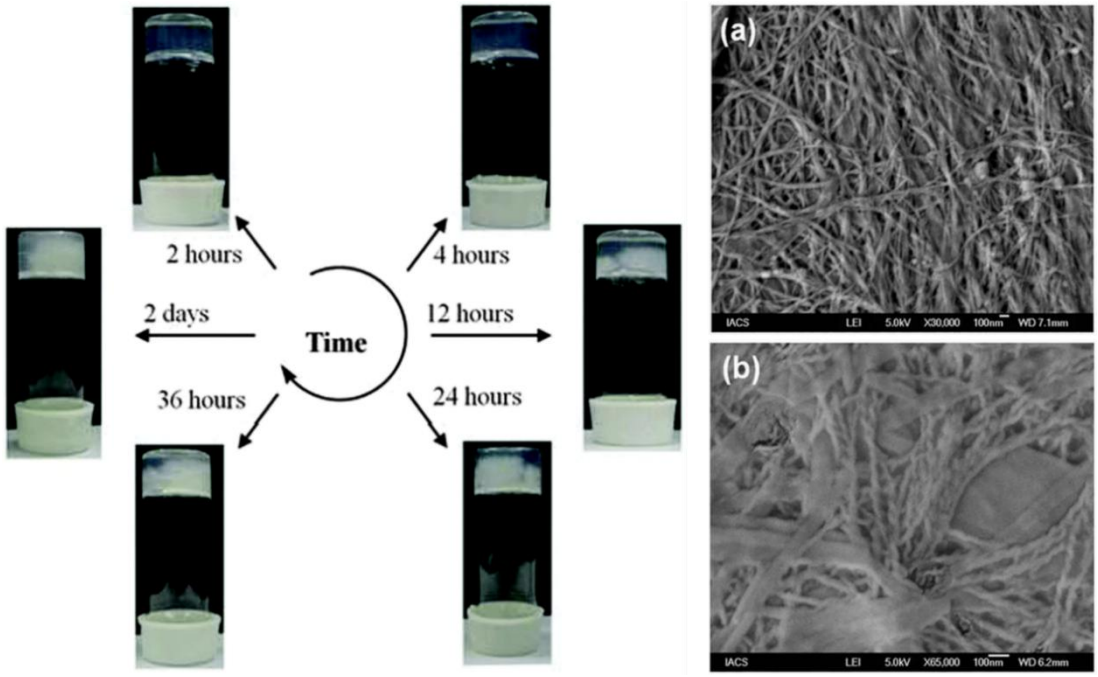

Figure 1.9. Left: transparent to opaque gel-to-gel transformation of dipeptide **MAA** at a concentration of 4.5 mg/mL over time; right: FE-SEM images showing twisted fibres for **MAA** dried gel freshly prepared (a) and after aging (b). Reproduced from Ref. 105 with permission from the Royal Society of Chemistry.

Other than changes in turbidity, the hydrophobicity of gelator molecules can also lead to contraction of the gel over time, a phenomenon called 'syneresis'. Shrinking or swelling of materials can be important for many applications, such as purification of polluted water or controlled drug release. Shrinking in supramolecular hydrogels has been reported due to external stimuli, while "self-shrinking" hydrogels are seldom observed. Duraisamy *et al.* recently reported a self-shrinking hydrogel under physiological pH.[106] The LMWG consists of a fluorenylmethoxycarbonyl functionalized β-L-phenylalanine (Fmoc-β-Phe) formed *via* a temperature switch. Here, the gel showed a reduction in size in 30 minutes, with expulsion of the buffer. The morphological change in this system was proposed to be a minor rearrangement or adjustment from J-like aggregates to H-like aggregates with time. The shrinking was exploited to test the gel application for toxic dye removal in presence of both anionic dyes and cationic dyes. The Fmoc-β-Phe gel was shown to be able to trap cationic dyes efficiently, as >85% were trapped within the hydrogel.

Similarly, a triphenylalanine-based hydrogel capable of self-shrinking over time was reported for removal of organic dyes and lead (Pb^{2+}) ions from wastewater.[107] Here, shrinking occurred as a result of the rather high hydrophobic nature of the nanofibres obtained by self-assembly of the gelator. Over seven days, the hydrophobic character of the

gel increased, leading to fibre contraction and expulsion of water molecules. Interestingly, electron microscopy images showed that both the fresh and the shrunken gel contained intertwined nano-fibres, indicating that syneresis in this system did not have a significant effect on the morphology of the gel. However, a negative effect on the final mechanical strength of the gel was observed after shrinking.

1.5.2 Light triggered response

Light can be a particularly suitable candidate for the design of stimuli responsive materials as it can reversibly change the state of the hydrogel in a non-invasive manner. Furthermore, light allows to target specific areas in a spatially controlled manner, allowing formation of patterned gel surfaces.[30] Light-triggered dynamic changes in gels can be stimulated without the need to introduce any external chemical, making the system free from waste generation or contaminants. Such photoresponsive gel systems can be particularly useful for biomedical applications or optoelectronics.[108] Here, peptide-based supramolecular materials can be designed to incorporate photoresponsive moieties in their structure to form photoresponsive gelators or can interact non-covalently with photoresponsive molecules present in within the gel matrix.

These photoresponsive groups can undergo reactions upon irradiation, like bond cleavage, bond formation or molecular switching. These bring about changes to the environment surrounding the gelator molecules. As a result, this causes a modulation of the supramolecular interactions at the molecular level. For this purpose, photoisomerisable molecules that switch between *trans*- and *cis*- forms are typically used, such as azobenzene and stilbene.[18,30] Other photosensitive molecules that show light-induced ring-opening or photodimerisation such as spiropyrans,[109] coumarin[110] and anthracene[44] have also been reported. In most of these cases, light-induced changes typically result in gel-to-sol transitions or gelation from a solution state. In Chapter 4, we will discuss light-induced changes in self-assembly in solution state, resulting in stimuli-induced viscosity changes.

1.5.2.1 Photodimerisation

One powerful approach to induce structural changes using light is to make use of conjugated molecules that exhibit photodimerisation. Molecules such as coumarins, alkenes, anthracenes undergo photodimerisation to highly stressed cyclobutene rings upon irradiation.[111] This covalent cross-linking between neighbouring molecules can fix the orientation and conformation of different groups within the gel matrix. In general, due to the increase in molecule size, photodimerisation can lead to a reduction in solubility and a

disruption of the gel network. However, positive enhancement on the gel network can also occur due to a stabilization of the products through intermolecular forces.

For instance, a photo-responsive dipeptide-based LMWG showed an increase in rheological properties upon irradiation.[112] In this study, a coumarin moiety was attached to the *N*-terminus of a diphenylalanine peptide. Gelation of the LMWG was achieved through acidification using the hydrolysis of GdL as pH trigger and electrochemically using hydroquinone. Irradiation with a 365 nm LED caused photodimerisation of the coumarin group between the neighbouring fibres (Figure 1.10a), leading to an enhancement of the rheological properties of the gel.

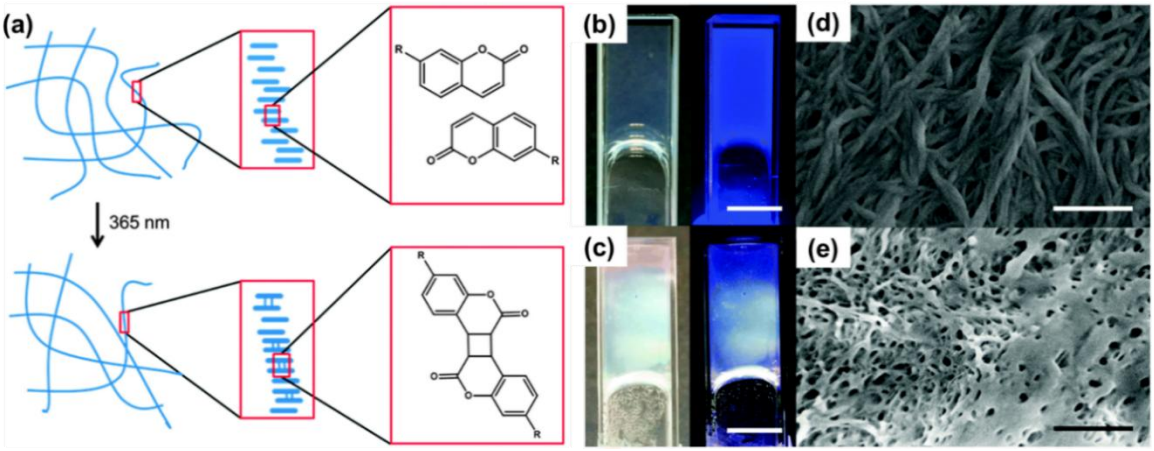

Figure 1.10. (a) Schematic showing the possible way in which dimerization can occur using UV-light between coumarin dimers. Gels obtained using GdL before (b) and after (c) irradiation with 365 nm light. SEM images of GdL gel before (d) and after (e) irradiation. Scale bar represents 500 nm. Adapted from Ref. 112 with permission from the Royal Society of Chemistry.

The change in rheological properties was hypothesized to be caused by stiffening within the fibres rather than fibre cross-linking, as the fibre diameter decreased from 42 nm to 39 nm. SEM images indicate that the network comprising the gel significantly changes after an hour of irradiation, showing less defined structures (Figure 1.10d and 1.10e).

Similarly, stiffening of the individual nanofibres of hydrogels was observed for a 7-diethylamino coumarin functionalized dilysine peptide.[113] Upon irradiation of the sample in just pure water with 365 nm light, an increase of the elastic storage modulus, G′, was observed from 20 Pa to ~150 Pa. The data suggested formation of intrafibre crosslinks due to association between the individual molecules, resulting in stiffening of the fibres.

Additionally, ruthenium-complex-catalysed photo-crosslinking has also been used to cross-link tyrosine-containing peptide supramolecular gels.[114] Here, photo-crosslinking seemed to stabilize the *β*-sheet structures of the self-assembled network by increasing entanglement of the peptide fibrils. This was further suggested by a decrease in pore size from ~ 100 nm to 10-50 nm.

1.5.2.2 Photoisomerisation

Photoisomerisation is a process by which molecules possessing a *trans* or *cis* bond can undergo *trans-cis* isomerisation upon irradiation or *vice versa*. Such changes in structures are likely to cause a large effect on the packing between self-assembled molecules. For this purpose, azobenzene-containing LMWGs are typically used, where the azobenzene group can be directly incorporated in the short peptide sequences. Typically, due to dramatic changes in planarity of the molecule, the π-π stacking interactions among the azobenzene molecules are dramatically affected, ultimately leading to disruption or formation of gels,[115,116] whereas structural changes that do not affect the gel phase are less likely to occur.

Recently, the Das group reported instead a gel that exhibits a gel-to-gel structural change due to light-triggered *trans-cis* isomerisation.[117] The peptide-based gel contains an azobenzene group and a cysteine residue. At basic pH, dimerisation of the cysteine residue assists the self-assembly of the gelator as well as π-π stacking between the azobenzene groups. Under irradiation with 365 nm light, shrinkage of the initial gel was observed. HPLC shows that the shrunken gel is still constituted by the disulfide-linked dimer. However, based on circular dichroism (CD) and powder x-ray diffraction (PXRD), the structural isomerisation caused a significant change in the self-assembly state of the gel. In both cases, β-sheet like arrangement can be observed, although the number of π-π interactions appeared to have increased in the shrunken gel. This change is further observed in the morphology of the gels, where the initial gel possessed thin fibres, ~1 μm long rod-like structures are observed for the shrunken gel. It follows that presumably the packing of the molecules requires less water for stabilization, leading to shrinkage of the gel.

Another way to maintain gel integrity upon irradiation is to introduce the photo-responsive group separately from the gelator molecule. For instance, a multicomponent system was designed by Xie *et al.*, comprising of an azobenzene pyridinium salt (AzoPy) and an L-glutamic acid amphiphile (OGac) (Figure 1.11a).[118] Initially, the two components form a gel by mixing in certain ratios by a heat/cool process. Shrinking of the gelator to a smaller gel (S-gel) occurs over time at room temperature at rest, expelling water (Figure 1.11b).

Interestingly, a new swollen gel could be formed again by irradiating the S-gel with UV light. This process was found to be very reversible, and the shrunken gel could be re-obtained by subjecting the gel to visible light (Figure 1.11b, top). The photoirradiated swollen gel was mainly composed of the *cis*-form azobenzene, indicating a *trans* to *cis* transformation from the S-gel upon irradiation. A change in morphology is further observed upon the change, as the swollen gel presented wider and twisted fibres compared to the long nanofibres in the initially formed gel (Figure 1.11b, bottom).

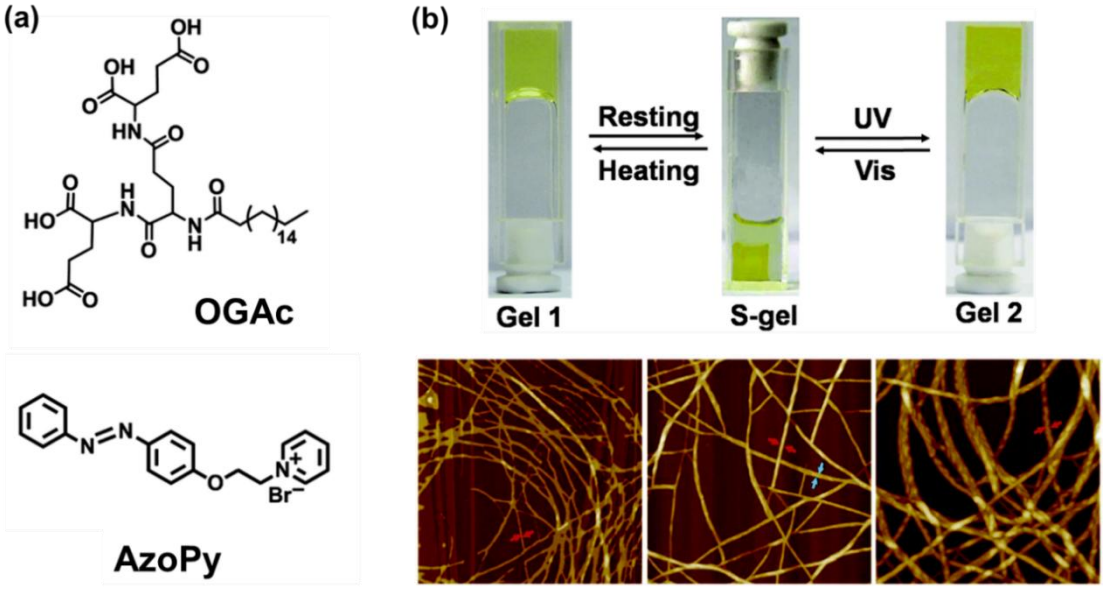

Figure 1.11. (a) Structures of AzoPy and the L-glutamic amphiphile (OGAc); (b) Shrinking and photo-induced re-swelling of the gel on resting and UV light irradiation (top) with representative 2 μm x 2 μm AFM images of the three gels (bottom). Adapted from Ref. 118 with permission from the Royal Society of Chemistry.

1.5.2.3 Photoreduction

Structural changes in peptide-based supramolecular gels can also be imparted where the light-response is due to a change in the electronic configuration of a component in the gel. Specific gelators that show these properties either incorporate photo-reducible metal ions or possess highly conjugated rings such as perylene bisimides (PBI) and naphthalene diimides (NDI). Upon irradiation, such molecules can form radical anions, altering the way the conjugated rings may stack, therefore affecting the electrostatic interactions in the systems.[119,120]

A rare response to irradiation as a result of photoreduction was reported by Draper *et al.* for an amino acid functionalized PBI gelator.[121] The molecule forms gels at low pH using a pH switch. Upon irradiation with 365 nm light, photoreduction lead to the formation of the

radical anion, accompanied by a visible change in the colour of the gel from red to dark purple. The change brought about an unusual enhancement of the rheological properties in both stiffness and mechanical strength. Small-angle neutron scattering (SANS) data suggests that the mechanical changes are due to a greater density of entanglement due to a reduced distance between cross-links.

1.5.3 Chemical responsive gels

Due to the possibility of appending functional groups to peptide-based precursors, control of the response of the material through chemical stimuli can further be obtained. By introducing functional groups that interact covalently or non-covalently with the environment through chemical reactions, the self-assembly process can be adapted in a predictable manner. As such, many different chemical reactions can be taken advantage of to rupture or make bonds, leading to gelation or dissolution. Furthermore, such stimuli may be reversible, and their response can be temporally programmable if multiple stimuli are included in the medium.

The first self-assembled system fuelled by a chemical reaction was reported in the seminal work by Boekhoven *et al.*[122] In their work, a self-assembling molecule containing anionic carboxylate groups was associated to a reaction cycle to induce the formation of a transient gel (Figure 1.12a). To induce the transient gel formation, the net charge on the molecule was changed by formation of a methyl ester through carboxylate alkylation. Under these conditions, self-assembly of the building blocks occurs, leading to hydrogel formation (Figure 1.12b centre). Since esters can hydrolyse spontaneously in aqueous solutions, the negative charge on the molecule is regenerated. By doing so, the system reverts to the initial inactive solution phase (Figure 1.12b, right). The main advantage of these transient self-assembled systems is that the lifetime and stiffness of the transient gel can be directly controlled by changing reaction conditions (e.g. the amount of chemical fuel added) and, thus, the kinetics.[122]

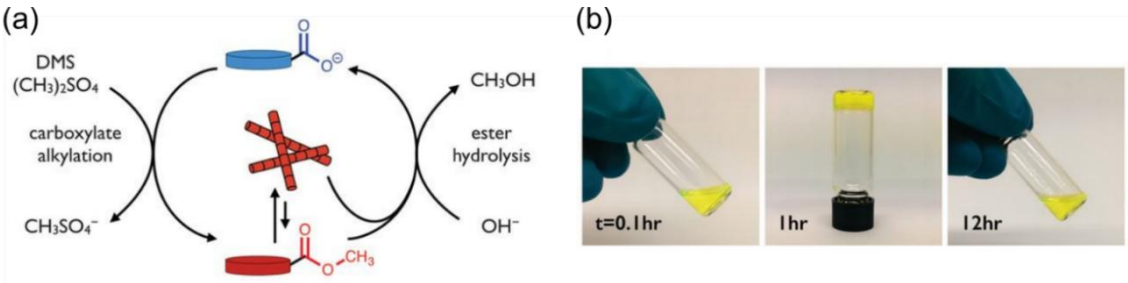

Figure 1.12. (a) Reaction cycle for transient self-assembled system. The carboxylate group reacts with dimethyl sulfate to form methyl esters, which self-assemble. Disassembly is then driven by hydrolysis of the methyl ester, regenerating the carboxylate precursor. (b) Photographs of the transient hydrogel over time after dimethyl sulfate is added. From J. Boekhoven, W. E. Hendriksen, G. J. M. Koper, R. Eelkema and J. H. van Esch, Transient assembly of active materials fueled by a chemical reaction, Science (1979), 2015, 349, 1075–1079. Reprinted with permission from AAAS.

Since then, several approaches have been introduced to drive self-assembled materials out-of-equilibrium. Most examples rely on the incorporation of a "chemical fuel" to drive either non-active precursor building blocks in solution or self-assemblies out of equilibrium, leading to metastable self-assembled or disassembled states respectively with a tuneable lifetime (Figure 1.13, right).[123]

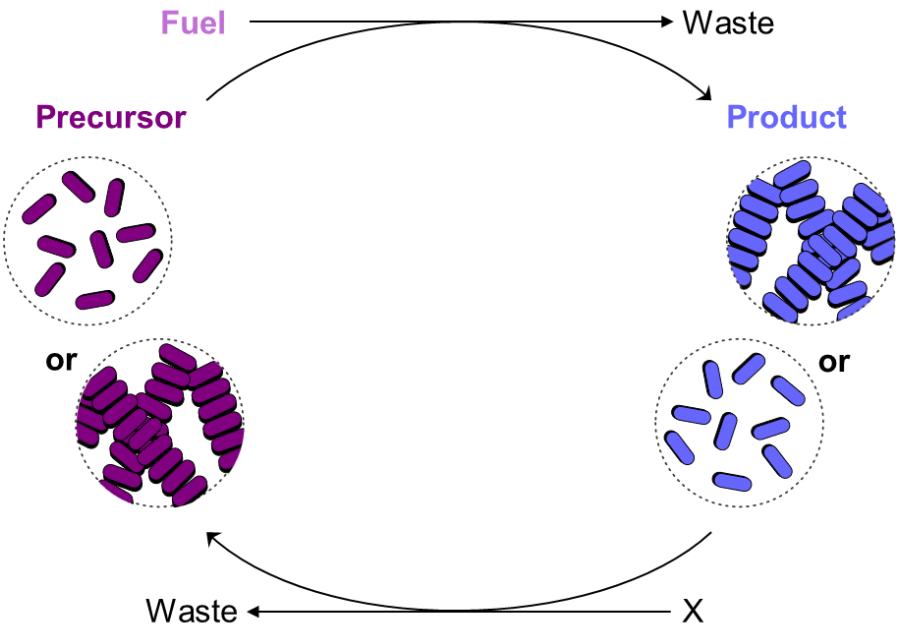

Figure 1.13. Schematic representation of a chemical reaction cycle for transient self-assembly or disassembly driven by fuel consumption.

The key to prepare such transient hydrogel reaction cycles is that the rate of activation (self-assembly or de-assembly) should be higher than the rate of deactivation (de-assembly or self-assembly) at the start.[124,125]

Towards this goal, a variety of chemical fuels and reactions have been exploited to generate dynamic self-assembled systems.

1.5.3.1 pH triggered changes

As discussed in Section 1.4.1, pH is one of the most common ways to induce gelation if the gelator molecule contains ionisable pendant groups, such as amine or carboxylic acids. It follows that assembly or disassembly can be tuned in peptide hydrogels at pH above or below the apparent pK_a of the gelator molecule, depending on the type of functional group. For instance, deprotonation of a carboxylic acid moiety would lead to an increase in electrostatic repulsion and result in gel-to-sol transitions when the pH increases above the apparent pK_a.[20,126] Conversely, if the pH of a gel based on an amine-functionalized gelator is lowered below the pK_a, formation of ammonium ions would also lead to transition to a solution state.[127] Taking advantage of the pH responsiveness of these molecules, several pH-triggered gel-to-sol-to-gel transitions have been reported in literature.[128–130] Adaptable pH responses can be either tuned by direct addition of acid or base, or transient pH changes can further be induced by introducing triggers to controllably change the pH, such as enzymatic reactions or slow hydrolysis reactions.[131–133]

One of the most used acid-to-base switches consists in the autocatalytic reaction between urea and urease to produce ammonia (Figure 1.14a).[134]

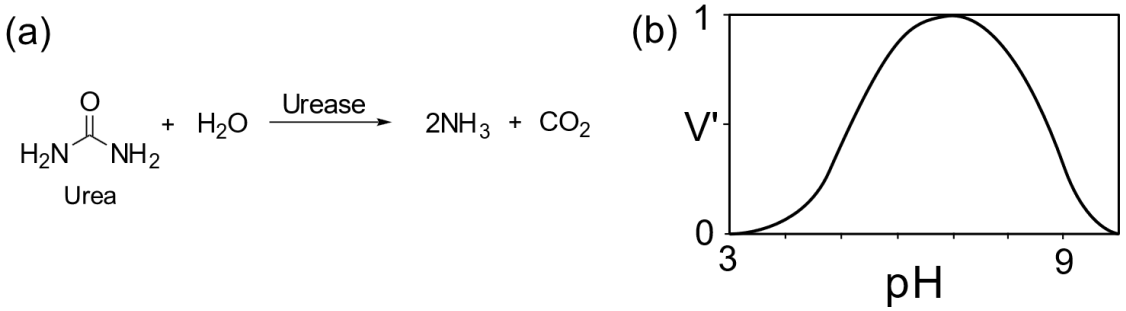

Figure 1.14. (a) Schematic representing the autocatalytic enzymatic reaction between urea and urease to produce ammonia and CO_2; (b) Dependence of the relative enzyme rate v' on pH. The enzyme activity shows a bell-shaped behaviour which peaks at pH ~ 7.

First introduced by Jee *et al.* to drive the controlled formation of an hydrogel,[135] this reaction provides a way to gradually increase the pH of the medium. Furthermore, the enzyme

activity exhibits a bell-curve behaviour, with a peak at pH 7 (Figure 1.14b).[134] Therefore, by pairing the urea-urease reaction to chemical reactions that either increase or decrease the pH, pH-responsive dynamic hydrogel systems can be prepared.[132,136]

For example, the Walther group reported systems by which an initial acidic trigger (citric acid/sodium citrate buffer) and the urea-urease counter-trigger were added to the system to induce self-regulating behaviour. An acidic promoter is injected in solution at the start, causing a rapid decrease in pH and gel formation. Then, deactivation occurs slowly driven by production of ammonia. It is relevant to note that the lifetime of the transient gels was controlled depending on the urease concentration or the buffer strength.[131,137] Mondal *et al.* reported a transient hydrogel of benzyloxycarbonyl-L-phenylalanine prepared in a similar manner, simply changing the initial acidic trigger to HCl.[138]

Building on their previous system, the Walther group synthesised a transient DNA hydrogel based on two competing pH-modulating enzymatic triggers. The urea-urease reaction was employed to slowly increase the pH, while the esterase-catalysed hydrolysis of ethyl acetate was used to gradually decrease the pH. In both reactions, the rate of pH change could be modulated by varying the concentration of the enzyme. Hence, by incorporating these reactions, the authors were able to obtain temporal control over self-assembly and disassembly in a fully programmable way.[133]

Structural changes in gel-to-gel-to-gel systems can be achieved by incorporating multicomponent systems bearing groups with opposite pH-responsiveness. Tena-Solsona *et al.* designed tetrapeptidic gelators containing ionizable groups with opposite charges (Figure 1.15a).[139] At neutral pH, a co-assembled gel was formed (Figure 1.15b), which could be turned into single component gel by either lowering or increasing the pH. This would be obtained through either protonation of the amine or deprotonation of the carboxylic acid functionality, leading to the dissolution of one of the two components. The change in morphology can be studied by TEM, where fibrillar structures can be observed in all cases. After the addition of acid or base, the sample morphology resembled the one obtained for the pure compound that remained within the network.

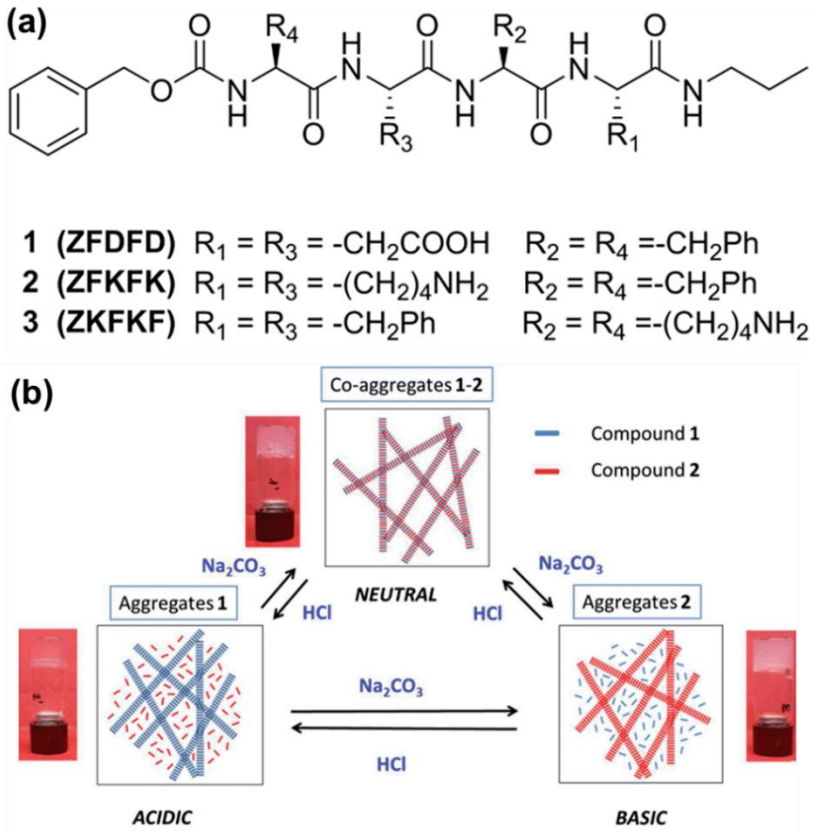

Figure 1.15. (a) Structures of the different pH-responsive gelators used in the study; (b) Schematic representing the pH-responsive behavior of the mixtures of gelator **1** and gelator **2**. Adapted from Ref. 139 with permission from the Royal Society of Chemistry.

A similar approach was used by Panja *et al.* to tune structural gel properties using oppositely charged functionalities.[140] Here, the two peptide-based amphiphiles are non-gelling and bear opposite functionalities: a carboxylic acid moiety and an amine. The pH-response of such system was also pathway dependent, based on the way deprotonation of the groups was obtained. Gelation occurs through a solvent switch at both pH 6.3 and 9.9 in DMSO/H_2O (20/80, v/v). Sequential addition of NaOH causes successive deprotonation of the terminal carboxylic acid at pH 6.3 and protonation of the ammonium ion at pH 9.9. Interestingly, a gel was obtained in both cases, where gel formation at lower pH was believed to be driven by electrostatic interactions between the NH_3^+ and COO^-. A transition between these two gel states could be achieved by addition of 0.006 M NaOH on top of the lower pH gel. This slow diffusion method resulted in a gradual increase of both G′ and G″, accompanied by a significant change in structures observed by SAXS and a decrease in volume by ~30%. Syneresis was ascribed to changes in the molecular packing, where the molecules were able to stack more effectively, causing an enhancement of the intermolecular interactions.

1.5.3.2 Dynamic chemical transformations

Changes in the molecular packing can be induced by affecting the non-covalent interactions in the systems. However, one issue for applications of such supramolecular materials is that they can often exhibit poor mechanical strength, as they break at low strain. One way to overcome this is to drive *in situ* cross-linking of the gelator molecules driven by chemical reactions. When a gel is formed, they can be exposed to a chemical stimulus that instigates covalent crosslinking, leading to changes in the material properties and improvement of the mechanical strength. Methods in which this can be obtained through light have been explored in Section 1.5.2, but they can further involve for instance disulfide, imine and amide formation.[141]

The Ikeda group recently reported a peptide-based supramolecular system that autonomously forms and shrinks to a second gel upon a single chemical input.[142] This was obtained through exploiting the hydrazone-oxime exchange in presence of hydroxylamine. The precursor gelator was designed to contain a diphenylalanine dipeptide and a carboxybenzyl group at the *N*-terminus. To induce chemical responsiveness, the molecule was functionalized at the *C*-terminus with a hydrazone bond and a negatively charged hydrophilic sulfonate group. The electrostatic repulsion between sulfonate groups allowed the sample to be dispersed in water. In presence of hydroxylamine, removal of the charged sulfonate groups produced hydrazide-containing molecules and converted to a transparent gel at pH 5.5. Over two hours, the gel spontaneously shrunk, accompanied by morphological transformations of the nanostructures. Upon gel shrinking, the long fibres of the first gel appeared to increase in radius and form bundles. Interestingly, the appearance of the shrunk nanofibre network depended on the speed and the extent of the hydrazone-oxime reaction, further highlighting the pathway dependence of such chemoresponsive gels.

Another approach to impart chemical stimulus-changes in supramolecular systems is to take advantage of chemical cross-linking or coupling agents, such as glutaraldehyde or 1-ethyl-3-(3-dimethylaminopropyl)carbodiimide (EDC).[143] Glutaraldehyde has been previously used to induce a dynamic imine covalent bond between amine and aldehyde groups by the Guler group.[144] The gelator was based on a peptide amphiphile molecule, Lauryl-VVAGKK-Am that forms gels at pH > 7. The cross-linking agent was added after gel formation and UV-Vis spectroscopy confirmed the presence of the imine bond. Stiffer gels were observed by rheology, but interestingly the cross-linking stimulus did not appear to cause changes in the morphology and fibre structure of the gel. This is ascribed to the presence of the increased cross-linking within the fibres rather than between.

Marshall *et al.* used a similar approach to induce predictable changes in the mechanical properties of a peptide-based gel after formation by varying the position of the lysine residues within the gelator.[145] The response of the gelator to the glutaraldehyde was dependent on the position of the lysine residue, resulting in enhanced cross-linking where less steric hinderance was present between the residues. As a result, different degrees of enhancement of the mechanical properties could be achieved with higher level of control. SANS data showed an increase in the radii upon cross-linking, suggesting that the increased stiffness of the gels could be related to formation of imine bonds between adjacent fibres.

The chemical stimulus approach can be further expanded by introducing multi-component systems with different responses to chemical triggers. In this way, selective responses to a variety of reagents can be envisioned, allowing further control over the switching between structures. Our group recently explored this, by introducing a multi-component system with gelators containing amino-acid residues bearing either a carboxylic acid or an amine group (Figure 1.16a).[146] Here, cross-linking can be brought about by either using EDC to link the two components or glutaraldehyde to selectively cross-link the molecules of the amine-functionalized gelator through formation of an imine bond. The gel forms through a solvent-switch method and different gels could be obtained at both pH values of 9.3 and 10.8 by addition of different equivalents of NaOH. Cross-linking was induced post-assembly, introducing either EDC or glutaraldehyde on top of the gels. The response of the system was found to be highly pH dependent. At pH 9.3, the mechanical properties of the gel did not appear to be affected by cross-linking. As the gel structure is maintained by electrostatic interactions at such pH, cross-linking is expected to destroy the salt bridge between the two gelators. Thus, the lack of changes in the mechanical properties of the gel strongly suggested that inter-fibre cross-linking allowed the system to retain its mechanical properties. However, dramatic changes in microstructure were observed, with more intertwined fibres observed for the cross-linked gels. Changes in the microstructure were further accompanied on the bulk level by a visual swelling of the gel (Figure 1.16c, left vial). At pH 10.8, the response to the two cross-linking agents instead brought different responses, where EDC caused an expansion in gel volume and glutaraldehyde caused a contraction (Figure 1.16c, right vial). Therefore, such chemical-responsive systems allow control of the final structures of the gel as well as the macroscopic volume.

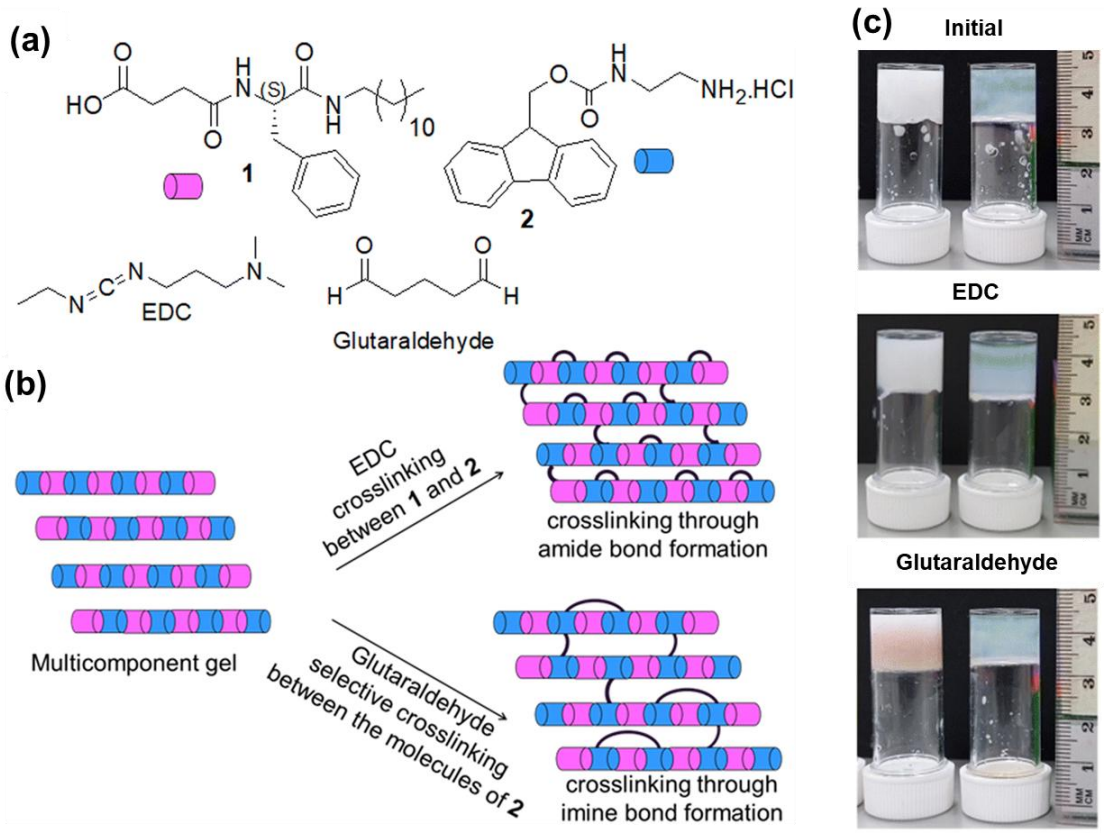

Figure 1.16. (a) Chemical structures of gelators used in the study and crosslinking agents EDC and glutaraldehyde; (b) schematic showing potential covalent cross-linking among the multicomponent gelators; (c) photographs highlighting the changes in gel volume after exposure to EDC and glutaraldehyde at pH 9.3 (left vial) and pH 10.8 (right vial). Adapted from Ref. 146 with permission from the Royal Society of Chemistry.

The approaches considered so far all rely on inducing structural changes post-assembly from a starting gel state. However, the fuel-driven approach has emerged recently to design supramolecular peptide-based systems with tuneable lifetimes by means of reversible chemical reaction cycles.[88,122,147–150]

As an example, the hydrolysis of carbodiimides has been widely used by several groups to induce formation of anhydrides from charged dicarboxylate-based precursors.[88,101,151–153] Due to the loss of charge on the molecule, dissipative self-assembly occurs, leading to the formation of a gel. Deactivation and return to solution state then takes place, driven by natural hydrolysis of anhydrides in aqueous environments.[152] The lifetime of the product is governed by the amount of fuel, which in turn also determines the properties of the supramolecular material.[88]

Ulijn and co-workers further introduced the use of enzymes to induce transient bond formation and dynamic self-assembly.[150,154] The enzyme α-chymotrypsin was used to

catalyse peptide bond formation between a tyrosine-based precursor and a second amino acid (the fuel). The reaction afforded a dipeptide product, which self-assembled to form a transient hydrogel. In this case, the same enzyme catalysed the hydrolysis of the dipeptide to the precursor, making the dipeptide metastable. Notably, the authors were able to tune the lifetime of the hydrogel by changing the enzyme concentration.[89]

Most of the work here is aimed at either inducing transient self-assembly through a sol-to-gel-to-sol cycle or to induce structural gel to gel changes by transitioning through a disassembled state.[129,155] Nevertheless, reversible network changes from an initial gel state to a new gel state using reaction networks rather than post-assembly modification can further be envisioned using this method. Examples of such systems have been recently published for polymer-based hydrogels,[156,157] although this remains largely unexplored for peptide-based materials.

One example of an amphiphile gelator containing an amino-acid residue undergoing a self-regulated gel-to-gel transition was reported by Panja *et al.*[158] To induce the chemically fuelled transition, EDC was used to promote reversible conversion to the anhydride form of the gelator, which would then slowly hydrolyse back to the original gelator. The anhydride form is further capable of forming a gel by co-assembly with the gelator molecule, resulting in a gel-to-gel transition. The kinetics of these unusual transitions could be controlled by the amount of fuel added, which also affected the underlying packing of the molecules at the end. As a result, a change in rheological properties and an improvement in mechanical strength was also observed. This behaviour is ascribed to the presence of kinetically trapped co-assemblies at different concentrations of EDC, suggesting that the rate of hydrolysis would then govern the observed properties of the materials.

1.5.3.3 Redox response

An interesting strategy to induce structural changes in gels is to use redox reactions. Generally, redox-responsive gelators are designed so that they bear redox-active units in their backbone, such as tetrathiafulvalenes,[159] ferrocenes or thiophenes, among others.[160] Redox-active metal ions can also be incorporated in supramolecular systems that change oxidation state upon electrical stimuli, causing a change in ion mobility and intermolecular interactions.[161] Redox changes can be achieved both chemically by addition of reagents and electrochemically, by exposing the gelators to externally applied electrical fields. In general, modification of the redox-active units of the gelator can lead to significant changes in solubility, triggering gel-to-sol transitions.[162] In some cases, changes in hydrophobicity of

the fibres can also lead to volume changes, making these materials interesting for applications as actuators. Responsive hydrogel actuators have been designed based on covalently cross-linked hydrophilic homopolymer or copolymer networks.[163,164] However, due to the reversible nature of the bonds in supramolecular gels, there is a potential to modulate such changes electrochemically in a reversible manner.

An example of this has been recently reported by Xue *et al.* using a tripeptide based hydrogelator coupled to 3,4-dihydroxyphenylalanine (Dopa) at the *C*-terminus (Figure 1.17a, left). [165] Dopa can be electrochemically oxidized to dopaquinone (Figure 1.17a, right), making this system redox-responsive. The Dopa-containing gelator formed gels *via* a solvent-switch method in DMSO and phosphate buffer saline. By applying a +5 V potential, oxidation of the gel was obtained, accompanied by a significant change both microscopically and macroscopically (Figures 1.17b and 1.17c).

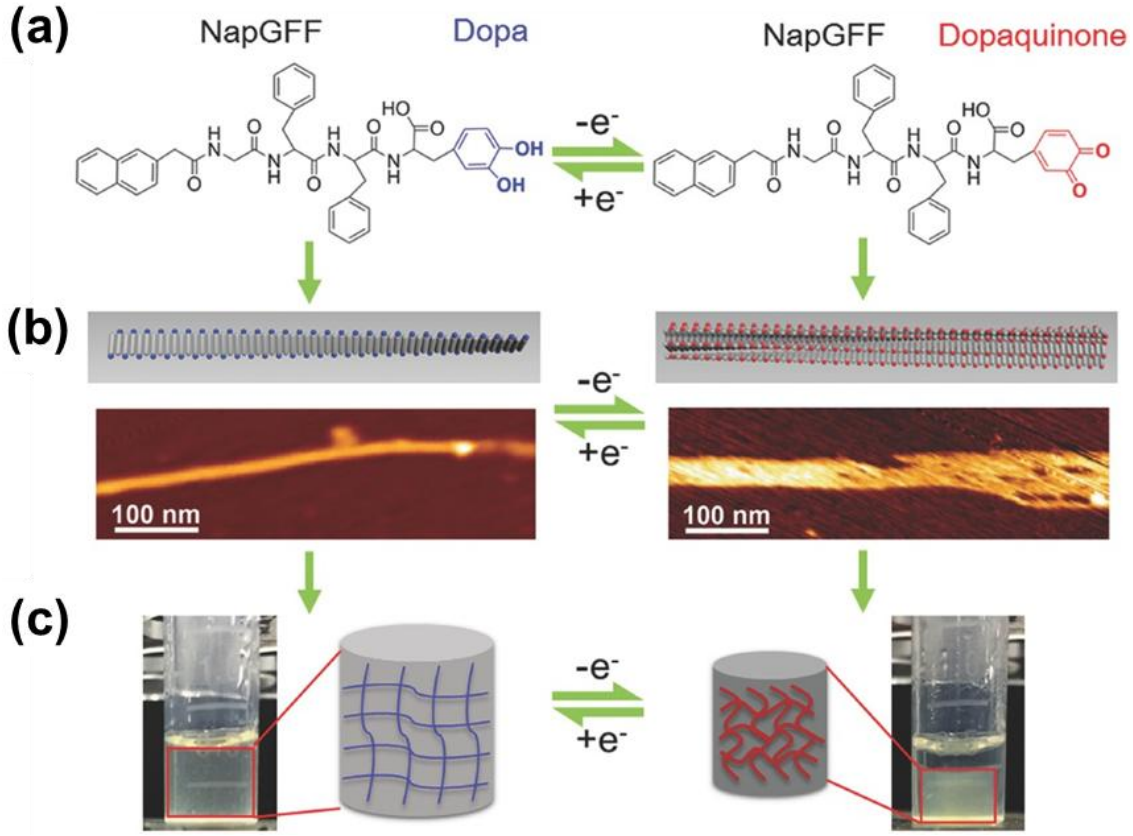

Figure 1.17. (a) Chemical structure of redox-responsive supramolecular tripeptide gelator containing a Dopa segment which can be oxidized to dopaquinone; changes in (b) morphology and (c) volume upon applied potential in the electro-responsive system. Source: Adapted from [165], Figure 1.17 Reproduced with permission of © 2016 WILEY-VCH Verlag GmbH & Co. KGaA, Weinheim.

By atomic force microscopy (AFM), an increase in height of the nanofibres formed by the gel was observed, indicating bundling of the fibres and increased interfibre cross-linking (Figure 1.17b, right). This further led to a dramatic decrease in the volume of the hydrogel by ~50% and increased stiffness. Based on these changes, a hydrogel actuator capable of unidirectional expansion and shrinkage by changing the redox states of the peptide was designed.

Other examples of redox-responsive systems rely on the use of redox chemical reaction networks to induce sol-to-gel-to-sol cycles. In such systems, transient gel formation is achieved by taking advantage of the reduction of disulfide bonds into free thiols and *vice versa*.[166,167]

1.5.4 Mechanical response

In some cases, self-assembly might be kinetically disfavoured and a stimulus might be necessary to overcome the high energy activation barrier and access different aggregation pathways. Mechanical stimuli such as ultrasound or sonication have recently emerged as an effective way of controlling supramolecular aggregation and disrupt noncovalent interactions to re-shape interactions[168] and aid gelation.[15,169] For instance, Wang *et al.* observed that ultrasound treatment of a cyclohexane solution containing Fmoc-protected octylglycine (Fmoc-OG) resulted in gelation, due to a switch from intramolecular to intermolecular H-bonds.[170] Sonication has also shown potential to form interlocked gel states *via* intermolecular interactions by breaking intramolecular bonds or π-stacking.[171]

Building on this behaviour, sonication was further shown to be effective in inducing direct gel-to-gel transitions for peptide-based compounds containing L-alanine residues.[172] In particular, the gelator was found to undergo this instantaneous transition upon sonication in both acetonitrile and toluene due to changes in aggregation. In acetonitrile, SEM images show that a transition from a core-shell structure surrounded by entangled fibres to just entangled nanofibres occurs upon sonication. It is believed that under sonication, the entangled fibres around the core were stretched and cut, while the micro-ball making up the core was incised into forming nanoballs. These further assembled into cross-linked fibres, resulting in the rapid gel to partial gel transformation. When the same process was performed in toluene, a transformation from 100 nm wide fibres to spindly fibres was observed, with a significant reduction in width to 20-50 nm. These final gels obtained through this method were also found to be more homogeneous and stable than gels obtained through sonication of high temperature solutions of the molecules. It is assumed that the U-shaped dimers

formed by the molecules aggregate in different initial conformations in the two solvents due to the solvophilic effect of toluene, leading to lamellar structures (Figure 1.18, centre). Sonication appears not to cleave the intermolecular hydrogen bonding between the molecules, but rather allows to make the π-stacking and hydrophobic interactions more homogeneous. This then results in a change in morphologies to ones more favourable for gelation. (Figure 1.18).

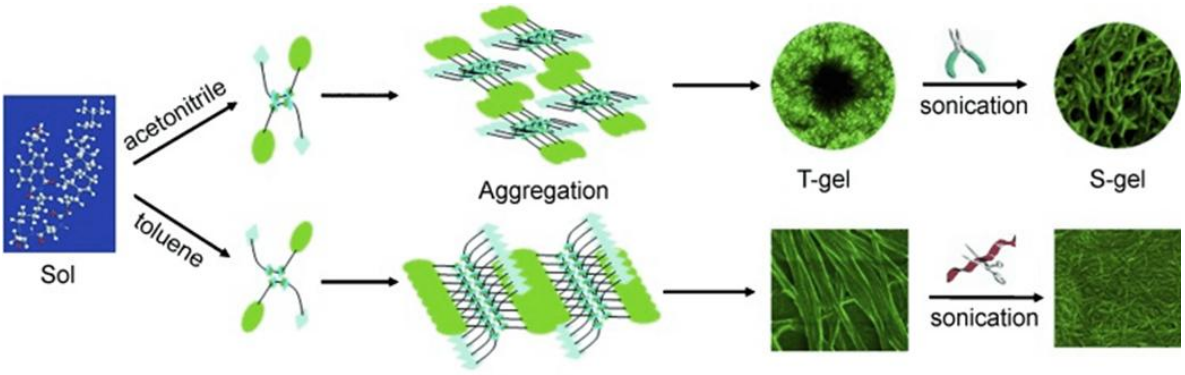

Figure 1.18. Schematic representation of the aggregation changes of the gelator in different solvents and upon sonication. The molecule adopts a different conformation in toluene, leading to lamellar structures in the first gel. Under sonication, both gels undergo a gel-to-gel transition to fibrous networks. Source: [172]. Reproduced with permission of © 2010 WILEY-VCH Verlag GmbH & Co. KGaA, Weinheim.

An ultrasound-induced transition between two gel states was also reported by the Yi group observed for a peptide-based organogel.[173] In the gelator structure, a lysine group was introduced into the linker, creating an umbrella molecule containing two cholesterol groups. In toluene, the molecule self-assembles into fully closed nano-rings structures upon heat-cool, forming a transparent gel. Upon treatment with ultrasound for two minutes, no gel collapse was observed. By AFM and SEM, it appeared that the initial nano-ring was destroyed while simultaneously smaller nano-rings were formed from the original shells. This phenomenon was assumed to occur on a quicker timescale than observation, allowing retainment of the gel state across the change in structure.

Mechanical triggers can also be used as directional stimuli to impart anisotropy in supramolecular systems. Long-range alignment is often found within biological systems and therefore designing materials comprising of aligned fibrils is particularly attractive for tissue engineering applications.[174] Supramolecular systems containing aligned fibres have been obtained by extrusion techniques[175–177] and by application of shear in a rheometer[178–180], taking advantage of the ability of long fibres to align under unidirectional shear.

In Chapters 2 and 3, we will discuss how mechanical stimuli can direct changes in evolving supramolecular systems and how gels containing anisotropic domains can be obtained using this approach.

1.5.5 Magnetic fields

Another interesting but less explored stimulus to direct anisotropy in peptide-based supramolecular gels is the use of strong magnetic fields. Magnetic fields are contact-free and effective stimuli to affect the orientation of supramolecular fibres, because of the diamagnetism of organic molecules. When an external magnetic field is applied, the movement of electrons will be changed such that a small internal magnetic field will be generated in the opposite direction.[181] Although this force is typically very weak, magnetic susceptibility can be increased by introducing magnetically responsive groups to favour magnetic orientation. Due to the free movement of electrons around the ring in aromatic moieties[182] and the partial double bond character of peptide bonds, peptides possess structural features that make them optimal molecules to align within a magnetic field.[183]

Magnetic fields have been used to generate morphological changes in self-assembly and induce transitions from an assembled to a disassembled state in systems comprising of α-helices and rod-coil amphiphiles.[184] Control over the organization of nanofibres formed by the self-assembly of peptide amphiphiles (PA) was also achieved using magnetic fields by the van Hest group, to yield highly anisotropic materials.[185,186] Wallace *et al.* exploited the high anisotropy of *N*-functionalised dipeptides assemblies to align fibres in a magnetic field during gelation. Here, the LMWG was found to self-assemble into wormlike micelles, which are amenable to alignment in a magnetic field. By adding a gelation trigger directly within the magnetic field, the magnetic induced alignment can be "locked in" to produce anisotropic gels. Gels prepared away from the field instead showed a more discontinuous appearance. Interestingly, the magnetic alignment here was shown to induce a change only on the nanometre level: the supramolecular packing was found to be unaffected by the magnetic field by analysis of the IR spectra of both gels.[187]

1.6 Applications of stimuli-responsive systems

By designing supramolecular materials such as hydrogels capable of changing upon application of stimuli, innovative "smart" materials can be envisioned.[188] Since the emergence of these dynamic materials, a few applications have been proposed.

Tena-Solsona *et al.* showed the possibility of producing self-erasing inks by taking advantage of carbodiimide hydrolysis. By converting fluorenylmethyloxycarbonyl-protected aspartic acid (Fmoc-D) to its anhydride, formation of spherulitic self-assemblies was induced. This resulted in an increase in turbidity of the solution, which would revert to clear over time due to the natural hydrolysis of anhydrides. By incorporating this solution in a polyacrylamide hydrogel, self-erasing inks with controllable lifetimes could be generated (Figure 1.19a).[88] Time-programmable self-erasing behaviour was further observed by Hu *et al.* for a dynamic polymeric gel of a triblock copolymer. In this case, the glucose/glucose oxidase (GOx) enzymatic reaction was used to provide controlled generation of acid, which triggered the dissociation of the physical crosslinks in the hydrogel. Programmable degradation to the sol state allowed to control the lifetime of the self-erasing inks.[189]

Furthermore, transient self-assembled gels with tuneable lifetimes have potential applications in regenerative medicine,[89] as well as for temporary drug delivery devices.[190] Heuser and co-workers showed that time-programmable hydrogels could be used as burst-release systems. By controlling the lifetime of a pH-responsive transient gel using the urea-urease reaction, pre-programmed release of a hydrophilic dye was demonstrated (Figure 1.19b).[137]

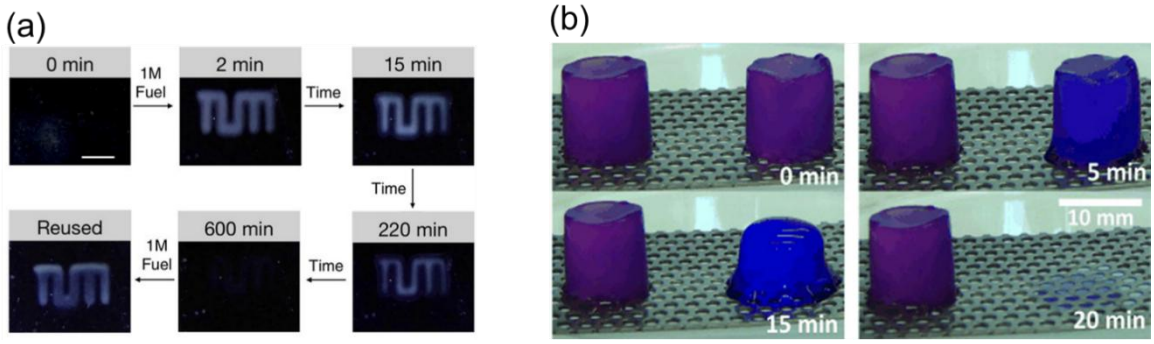

Figure 1.19. (a) Photographs of self-erasing inks formed by transient self-assembly of anhydrides from Fmoc-D *via* carbodiimide hydrolysis. (b) Photographs highlighting preprogrammed burst release of encapsulated dye from a transient hydrogel (right). A static hydrogel is shown on the left to compare the behaviour over time. Figure 1.19a is adapted with permission from M. Tena-Solsona, B. Rieß, R. K. Grötsch, F. C. Löhrer, C. Wanzke, B. Käsdorf, A. R. Bausch, P. Müller-Buschbaum, O. Lieleg and J. Boekhoven, Non-equilibrium dissipative supramolecular materials with a tunable lifetime, Nat Commun, 2017, **8**, 15895 (CC BY 4.0), Figure 1.19b is adapted from source: [137]. Reproduced with permission of © 2015 WILEY-VCH Verlag GmbH & Co. KGaA, Weinheim.

1.7 Characterisation of stimuli-responsive supramolecular systems

1.7.1 Rheology

1.7.1.1 Oscillatory Rheology

Rheology studies the way materials flow and deform under an applied force.[191] In oscillatory rheology, the mechanical properties of the hydrogel are assessed by measuring the response of the material once a deformation is applied. In strain-controlled rheometers, this is achieved by applying a shear strain, γ, to the sample as a sinusoidal oscillation such that:

$$\gamma(t) = \gamma_0(\sin \omega t), \qquad Equation\ 1.1$$

where ω is the applied angular frequency. The resulting shear stress, τ, is then measured as a phase shifted sine wave with:

$$\tau(t) = \tau_0(\sin \omega t + \delta), \qquad Equation\ 1.2$$

where δ indicates the phase difference between the two waves (Figure 1.20).[100,191]

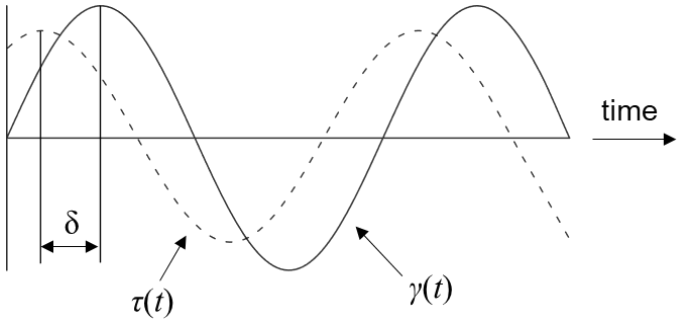

Figure 1.20. Schematic representation of the oscillatory rheology test, showing the pre-set shear strain γ sine curve and the resulting shear stress τ sine curve. For a viscoelastic material, the two curves are offset by a phase shift, δ.

In the case of a purely elastic material, the strain and stress waves are in phase, namely when $\delta = 0$. Conversely, for a purely viscous material, the two waves would be out of phase by $\delta = 90°$. It follows, then, that for viscoelastic materials such as hydrogels the phase shift would take place in the values between ($0 < \delta < 90°$).[192]

In oscillatory shear rheology, the shear storage modulus, G′, and the loss modulus, G″, are monitored as a function of several parameters, such as strain, frequency and time. The G′ value represents the deformation energy stored by the sample during shear, giving an indication of the stiffness of the material. G″ instead is a measure of the energy dissipated

by the sample during shear and, thus, lost. Hence, the G″ value describes the viscous or liquid-like behaviour of the material under study.[193] Therefore, if G′ > G″, the sample behaves more as an elastic solid, while it behaves more as a viscous liquid if G″ > G′.[194] The ratio between the viscous and elastic moduli, G″/G′ is defined as the damping factor, tan δ, and provides information on the viscoelastic nature of the material. In general, for a true gel, tan δ ≤ 0.1, i.e. the G′ occurs at an order of magnitude greater than G″.[195]

To fully characterise the mechanical properties of supramolecular gels, several tests can be performed using oscillatory rheology. For instance, the behaviour of both rheological moduli (G′ and G″) can be measured as a function of strain, while keeping the frequency constant. This allows to identify the linear viscoelastic region (LVER), defined as the region in which G′ and G″ are independent of strain (Figure 1.21a). Beyond this region, the material starts to break and flow, with a decrease in G′.[100] Conversely, by measuring the change in moduli with respect to frequency, information on the behaviour of the gel across short and long time scales can be obtained (Figure 1.21b).[196] Typically, true gels should exhibit frequency-independent behaviour if the strain is kept within the LVER.[191]

For all these measurements, a four-bladed vane geometry is used in this thesis (Figure 1.21c). The vane geometry penetrates fully into the gel material and therefore provides information on its bulk mechanical properties. In addition, this geometry is advantageous as it minimises sample loading-induced artefacts and wall-slip effects, compared to parallel plate geometries.[197,198]

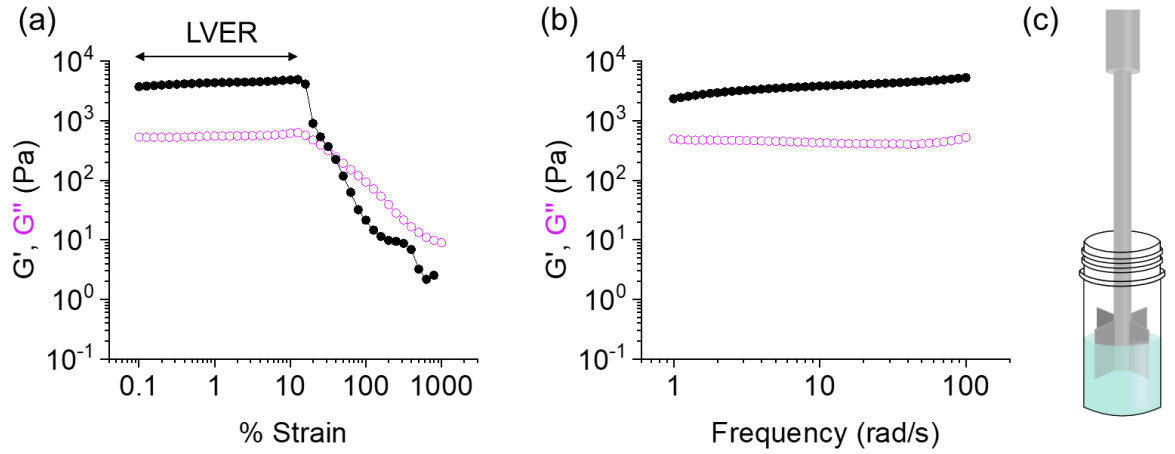

Figure 1.21. Example oscillatory shear rheology measurements of supramolecular hydrogels. (a) Strain sweep, indicating the linear viscoelastic region (LVER) of the gel. (b) Frequency sweep showing frequency-independent behaviour. (c) Schematic representation of a vane geometry in a gel prepared in a Sterilin vial.

Moreover, to gain insights in the gelation kinetics of self-assembled systems, the evolution of G′ and G″ can be measured over time *via* time sweep rheology. To perform these time-dependent experiments, G′ and G″ are recorded under constant values of angular frequency and applied strain.[191] These values are generally appropriately determined from the strain and frequency sweeps of the materials. In particular, the strain is typically kept low (< 1%) to ensure that the data falls within the LVER of the gel.[196,199]

It follows, then, that time-sweep rheology can be a particularly useful tool to elucidate the mechanisms of changing materials, making it ideal to gain insights on the evolving mechanical properties of stimuli-responsive hydrogel systems. Nevertheless, time-dependent measurements are seldom provided when rheological data of such systems is recorded. For example, frequency sweeps at specific points during the evolution process are provided[153,154], or plots in which only G′ is represented[147,166,167], although the formation of a true gel cannot be confirmed without considering G″ and tan δ.[195]

In Chapter 2, we will discuss the effects of performing time-sweep rheological measurements on evolving systems and how the mechanical properties of the final materials can be tuned further by the rheological measurement itself.

1.7.1.2 Rotational Rheology – Viscosity measurements

In Section 1.3, we discussed the ability of LMWG to self-assemble to form micellar aggregates, such as fibrils, worm-like micelles, nanotubes and spherical micelles. To provide additional information on the identity of the aggregates, rotational rheology is commonly used to measure the viscosity of the materials in solution.

When measuring viscosity, solutions are sandwiched between a bottom stationary plate and an upper plate which can rotate parallel to the bottom plate. To fully understand what is being measured in rotational rheology, the parameters of shear rate ($\dot{\gamma}$) and shear stress (τ) need to be introduced. The shear rate ($\dot{\gamma}$) defines the relative velocity at which layers of a fluid move past each other, and it is expressed as the ratio between velocity and the gap between the two plates. The shear stress (τ) quantifies the force acting on the material parallel to the surface, and it is expressed as the ratio between the shear parallel force and the shear area.[193]

In a typical viscosity measurement, a ramping shear rate is applied, while the geometry measures the shear stress required to move the material at that velocity. The viscosity (η) is then obtained as the following equation:

$$\eta = \frac{\tau}{\dot{\gamma}} \qquad Equation\ 1.3$$

Essentially, viscosity is a property of a fluid to resist to shear deformation.[200] Based on the relationship between stress and shear rate, fluids can be distinguished in Newtonian and non-Newtonian fluids. According to Newton, the shear stress must be directly proportional to the shear rate and, thus, Newtonian fluids exhibit constant viscosity independent of shear rate.[193,200]

Due to the presence of micellar aggregates in the solution phase, most supramolecular LMWG systems tend to behave as non-Newtonian liquids instead. As an example, dipeptide-based LMWG systems have been shown to self-assemble at high pH to form worm-like micelles.[201] Worm-like micelles are very flexible and long cylindrical micelles, which continuously "break" and reform under shear.[195] This results in unique viscoelastic properties, often exhibiting shear-thinning behaviour in the viscosity curve.[202] Shear-thinning is associated with the alignment of these micelles at high shear rates, resulting in a decrease in viscosity.[203] Conversely, non-associating spherical aggregates do not contribute to the overall viscosity, resulting in water-like viscosity.

1.7.1.3 Shear-induced polarized light imaging

In Chapter 3, we will explore materials that can be aligned under shear by using rheology. The extent of alignment can be visualized and quantified using a combined rheology and optics technique called shear-induced polarized light imaging (SIPLI).

In SIPLI, both the geometry and bottom plate are not only involved in the shearing but also take part in the optical system. Indeed, the bottom plate is made of glass, allowing to view the sample, while the geometry is directly involved in the optics. In a typical SIPLI set-up (Figure 1.22), white light is polarised through a polarisation filter and deflected towards the sample. The rotating geometry then reflects the light, which goes through an analyser filter before reaching a CCD camera. Notably, the analyser filter is positioned at 90° with respect to the plane of polarisation of the polarising filter.[204]

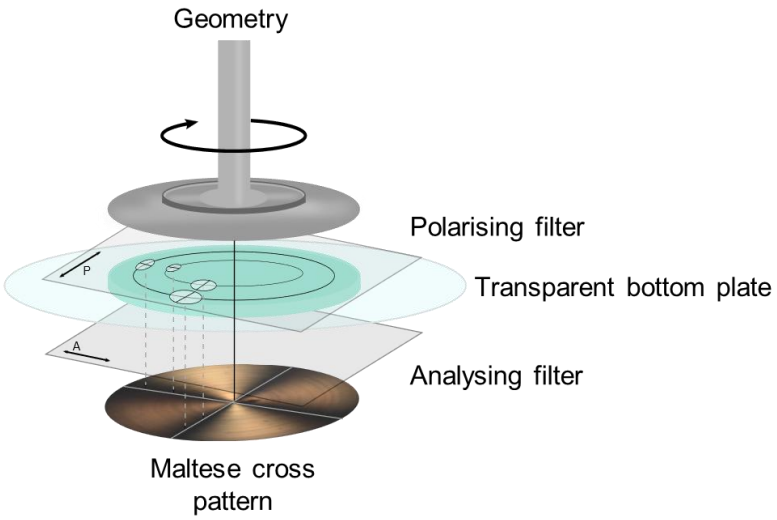

Figure 1.22. Schematic representation of a SIPLI set-up. Polarised light travels through the sample and gets reflected by the geometry through an analysing filter before reaching the camera to give an image. The analyser and the polarisers are set at 90° with respect to each other.

Orientation of molecules along flow direction will give rise to a phenomenon called flow birefringence. This is manifested by the existence of orientation dependent differences in their refractive index. Therefore, when polarised light travels through a shear-aligned sample, it will emerge with a different polarisation and it will pass through the analyser, generating an image. Under radial shear in SIPLI, shear-alignment can be observed by the presence of a Maltese cross pattern (Figure 1.22), with the four dark fringes representing the four positions at which either principal stress direction of the refractive index coincides with the plane of polarisation of the polariser.[205]

1.7.2 Small angle X-ray and Neutron Scattering

To probe the self-assembled structures on the nanoscale level, several approaches can be taken. It is often common to use microscopy techniques such as scanning electron microscopy (SEM) or transmission electron microscopy (TEM). Whilst useful, these techniques are prone to artefacts arising from sample drying during preparation,[16,98] which may change the observed structure morphologies.

Small angle scattering approaches such as small angle X-ray scattering (SAXS) and small angle neutron scattering (SANS) are instead powerful techniques to study the underlying self-assembled structures of LMWGs, as they are non-destructive and can be performed on the materials in their bulk hydrated state.[206,207] Small angle scattering relies on the

interactions between structures and incident X-ray or neutron beams. In SAXS, X-rays scatter off electrons, while in SANS neutrons scatter off the nuclei of atoms.[208]

In a routine scattering experiment, an X-ray or neutron beam is fired at the sample. Most of the beam will be transmitted through the sample and blocked by a beamstop. However, a small proportion of the beam will be elastically scattered and the angle at which the scattering occurs (θ) is inversely proportional to the size of the scattering objects in the sample. Therefore, larger objects scatter to smaller angles and *vice versa* (Figure 1.23).[209]

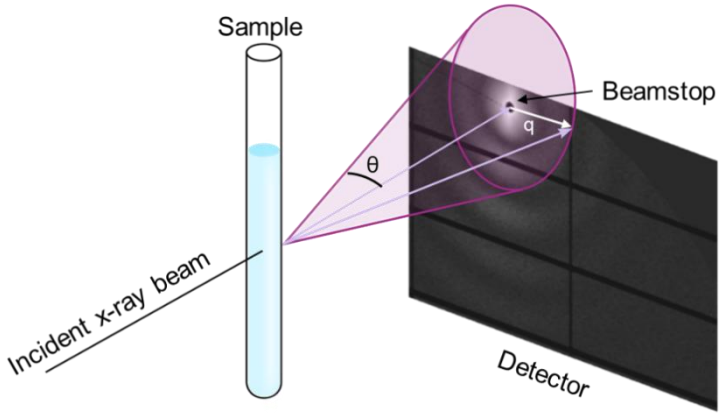

Figure 1.23. Schematic showing a typical small angle scattering experiment.

Scattering intensity is measured as a function of the scattering vector *q*, which is related to the scattering angle according to Equation 1.4:

$$q = \frac{4\pi}{\lambda}\sin\left(\frac{\theta}{2}\right) \qquad Equation\ 1.4$$

To achieve efficient scattering, there must be sufficient difference in the scattering length density (SLD) between the sample and the solvent. For X-ray scattering, contrast arises from differences in the electron density, whilst for neutron scattering contrast comes from differences in atomic nuclei.[210] Therefore, samples for SANS measurements are prepared in deuterated solvents to exploit the difference in SLD between hydrogen and deuterium and produce high-quality scattering data. [206]

The raw scattering pattern from a typical experiment is a two-dimensional scattering pattern (Figure 1.23), which is then reduced to a one-dimensional plot of scattering intensity versus *q*. This data provides information on the size, shape and length of the scattering object and can be fit to mathematical models.[206]

An attractive advantage of scattering experiments is the possibility to perform these experiments in combination with other techniques, such as rheology,[211] polarised light

imaging,[180,212,213] irradiation[69,214,215] or electrochemistry.[216] In this way, changes across a variety of length scales can be monitored *in situ*. Throughout this Thesis, we will explore a variety of custom experimental set-ups to perform *in situ* SAXS measurements on stimuli-responsive systems to characterise their underlying structures upon application of stimulus.

1.7.3 NMR

^{1}H NMR spectroscopy can be used as a tool to investigate the aggregation processes occurring at the molecular level in supramolecular self-assembling systems. As the molecules assemble to form larger aggregates, they become NMR invisible due to slow diffusion and very short transversal relaxation times.[217] Through this approach, the kinetics of gelation or aggregation can be tracked by following the disappearance of gelator peaks and the percentage assembly can be calculated.[218]

Techniques taking advantage of NMR spectroscopy are particularly useful to test materials that align as a response to magnetic stimuli. Indeed, degree of alignment can be measured and quantified using deuterium (^{2}H) NMR. When deuterium probes interact with anisotropically oriented structures, a splitting of the ^{2}H resonance is observed, called the residual quadrupolar coupling (RQC). This approach has been previously used in the Adams group to probe the magnetic alignment of worm-like micelles formed by the self-assembly of peptide-based materials.[187,219]

1.8 Aims of this Thesis

Supramolecular gels formed by the self-assembly of peptide-based LMWGs are interesting materials for a vast range of applications owing to their ease of synthesis and non-covalent self-assembly. By introducing a stimuli-responsive aspect in their design, the reversible self-assembly of these systems can be exploited to access a wide variety of new materials with pre-determined properties. Therefore, this thesis aims to exemplify how stimuli-responsiveness can be used as a method to design systems that exhibit predictable changes upon application of stimuli, resulting in materials with pre-programmed final properties.

In Chapter 2, dipeptide-based LMWG systems undergoing pre-programmable gel-to-sol-to-gel transitions using a pH cycle are investigated. We demonstrate how time sweep rheology is an essential method to measure these evolving materials. Building on this, the effect of mechanical stimuli on the resulting gel properties is further explored to prepare a variety of gels with different bulk properties starting from the same material.

In Chapter 3, we build on the results from Chapter 2 to design a new system undergoing pH-triggered gel-to-sol-to-gel transitions. We exemplify how this system can be used to prepare gels with aligned domains using shear as a stimulus. Rheology combined with polarised light imaging is used to optimise the alignment in the system and reproducibly obtain gels with aligned fibres. A novel combined technique comprising of rheology, polarised light imaging and SAXS is further employed to investigate the evolving system on a wide range of length scales. Finally, we show the versatility of this approach by inducing this alignment using a strong magnetic field.

In Chapter 4, we investigate a multicomponent system based on a dipeptide-based LMWG and a photoacid molecule capable of switching pH under irradiation. This design is exploited to form a light-responsive system that can reproducibly change viscosity under irradiation. A variety of combined techniques (rheology, NMR and SAXS) were employed to assess changes in the system *in situ* in the dark and upon irradiation. We finally investigate the capability of this stimuli-responsive system to stop flow at specific locations using light.

Finally, in Chapter 5, we investigate how to design peptide-based gels for applications in drug storage and release by taking advantage of their unique response to mechanical stimulus. Initially, the influence of gel mechanical properties, network morphology and choice of trigger on the ability of these systems to store and successfully release a cargo molecule is thoroughly studied. Then, this information is used to establish a novel method to release biologics using a simple mechanical stimulus. We finally test the stability of these systems under various real-world conditions for future applications in drug delivery.

1.9 References

1 M. de Loos, B. L. Feringa and J. H. van Esch, Design and Application of Self-Assembled Low Molecular Weight Hydrogels, *Eur. J. Org. Chem.*, 2005, **2005**, 3615–3631.

2 L. A. Estroff and A. D. Hamilton, Water gelation by small organic molecules, *Chem. Rev.*, 2004, **104**, 1201–1217.

3 P. Terech and R. G. Weiss, Low molecular mass gelators of organic liquids and the properties of their gels, *Chem. Rev.*, 1997, **97**, 3133–3159.

4 J. Kopeček, Hydrogel biomaterials: A smart future?, *Biomaterials*, 2007, **28**, 5185–5192.

5 A. Tirella, G. Mattei and A. Ahluwalia, Strain rate viscoelastic analysis of soft and highly hydrated biomaterials, *J. Biomed. Mater. Res. A*, 2014, **102**, 3352–3360.

6 C. D. Spicer, Hydrogel scaffolds for tissue engineering: The importance of polymer choice, *Polym. Chem.*, 2020, **11**, 184–219.

7 J. M. Saul and D. F. Williams, in *Handbook of Polymer Applications in Medicine and Medical Devices*, Elsevier, Oxford, 2011, pp. 279–302.

8 M. Hamidi, A. Azadi and P. Rafiei, Hydrogel nanoparticles in drug delivery, *Adv. Drug. Deliv. Rev.*, 2008, **60**, 1638–1649.

9 M. W. Tibbitt and K. S. Anseth, Hydrogels as extracellular matrix mimics for 3D cell culture, *Biotechnol. Bioeng.*, 2009, **103**, 655–663.

10 N. Zanna, S. Focaroli, A. Merlettini, L. Gentilucci, G. Teti, M. Falconi and C. Tomasini, Thixotropic Peptide-Based Physical Hydrogels Applied to Three-Dimensional Cell Culture, *ACS Omega*, 2017, **2**, 2374–2381.

11 B. O. Okesola and D. K. Smith, Applying low-molecular weight supramolecular gelators in an environmental setting-self-assembled gels as smart materials for pollutant removal, *Chem. Soc. Rev.*, 2016, **45**, 4226–4251.

12 E. M. Ahmed, Hydrogel: Preparation, characterization, and applications: A review, *J. Adv. Res.*, 2015, **6**, 105–121.

13 A. S. Hoffman, Hydrogels for biomedical applications, *Adv. Drug. Deliv. Rev.*, 2002, **54**, 3–12.

14 G. Fichman and E. Gazit, Self-assembly of short peptides to form hydrogels: Design of building blocks, physical properties and technological applications, *Acta Biomater*, 2014, **10**, 1671–1682.

15 C. D. Jones and J. W. Steed, Gels with sense: Supramolecular materials that respond to heat, light and sound, *Chem. Soc. Rev.*, 2016, **45**, 6546–6596.

16 E. R. Draper and D. J. Adams, Low-Molecular-Weight Gels: The State of the Art, *Chem*, 2017, **3**, 390–410.

17 P. R. A. Chivers and D. K. Smith, Shaping and structuring supramolecular gels, *Nat. Rev. Mater.*, 2019, **4**, 463–478.

18 J. Zhang, Y. Hu and Y. Li, *Gel chemistry interactions, structures and properties*, Springer Nature, Singapore, 2018.

19 J. Cui, A. Liu, Y. Guan, J. Zheng, Z. Shen and X. Wan, Tuning the helicity of self-assembled structure of a sugar-based organogelator by the proper choice of cooling rate, *Langmuir*, 2010, **26**, 3615–3622.

20 D. J. Adams, M. F. Butler, W. J. Frith, M. Kirkland, L. Mullen and P. Sanderson, A new method for maintaining homogeneity during liquid-hydrogel transitions using low molecular weight hydrogelators, *Soft Matter*, 2009, **5**, 1856–1862.

21 A. Mahler, M. Reches, M. Rechter, S. Cohen and E. Gazit, Rigid, self-assembled hydrogel composed of a modified aromatic dipeptide, *Adv. Mater.*, 2006, **18**, 1365–1370.

22 A. Z. Cardoso, L. L. E. Mears, B. N. Cattoz, P. C. Griffiths, R. Schweins and D. J. Adams, Linking micellar structures to hydrogelation for salt-triggered dipeptide gelators, *Soft Matter*, 2016, **12**, 3612–3621.

23 A. K. Das, R. Collins and R. V. Ulijn, Exploiting enzymatic (reversed) hydrolysis in directed self-assembly of peptide nanostructures, *Small*, 2008, **4**, 279–287.

24 J. Raeburn, A. Z. Cardoso and D. J. Adams, The importance of the self-assembly process to control mechanical properties of low molecular weight hydrogels, *Chem. Soc. Rev.*, 2013, **42**, 5143–5156.

25 C. Colquhoun, E. R. Draper, R. Schweins, M. Marcello, D. Vadukul, L. C. Serpell and D. J. Adams, Controlling the network type in self-assembled dipeptide hydrogels, *Soft Matter*, 2017, **13**, 1914–1919.

26 B. Ding, Y. Li, M. Qin, Y. Ding, Y. Cao and W. Wang, Two approaches for the engineering of homogeneous small-molecule hydrogels, *Soft Matter*, 2013, **9**, 4672–4680.

27 C. D. Jones and J. W. Steed, Gels with sense: Supramolecular materials that respond to heat, light and sound, *Chem. Soc. Rev.*, 2016, **45**, 6546–6596.

28 M. Vázquez-González and I. Willner, Stimuli-Responsive Biomolecule-Based Hydrogels and Their Applications, *Angew. Chem., Int. Ed.*, 2020, **59**, 15342–15377.

29 Z. Li, Y. Zhou, T. Li, J. Zhang and H. Tian, Stimuli-responsive hydrogels: Fabrication and biomedical applications, *View*, 2022, **3**, 20200112.

30 B. Pramanik and S. Ahmed, Peptide-Based Low Molecular Weight Photosensitive Supramolecular Gelators, *Gels*, 2022, **8**, 533.

31 A. Dasgupta, J. H. Mondal and D. Das, Peptide hydrogels, *RSC Adv.*, 2013, **3**, 9117–9149.

32 R. V. Ulijn and A. M. Smith, Designing peptide based nanomaterials, *Chem. Soc. Rev.*, 2008, **37**, 664–675.

33 R. J. Mart, R. D. Osborne, M. M. Stevens and R. V. Ulijn, Peptide-based stimuli-responsive biomaterials, *Soft Matter*, 2006, **2**, 822–835.

34 S. Xian and M. J. Webber, Temperature-responsive supramolecular hydrogels, *J. Mater. Chem. B*, 2020, **8**, 9197–9211.

35 R. S. Tu and M. Tirrell, Bottom-up design of biomimetic assemblies, *Adv. Drug. Deliv. Rev.*, 2004, **56**, 1537–1563.

36 S. Fleming and R. V. Ulijn, Design of nanostructures based on aromatic peptide amphiphiles, *Chem. Soc. Rev.*, 2014, **43**, 8150–8177.

37 S. Das and D. Das, Rational Design of Peptide-based Smart Hydrogels for Therapeutic Applications, *Front. Chem.*, 2021, **9**, 770102.

38 H. Cui, M. J. Webber and S. I. Stupp, Self-assembly of peptide amphiphiles: From molecules to nanostructures to biomaterials, *Biopolymers*, 2010, **94**, 1–18.

39 J. T. Meijer, M. Roeters, V. Viola, D. W. P. M. Löwik, G. Vriend and J. C. M. Van Hest, Stabilization of peptide fibrils by hydrophobic interaction, *Langmuir*, 2007, **23**, 2058–2063.

40 E. R. Draper, K. L. Morris, M. A. Little, J. Raeburn, C. Colquhoun, E. R. Cross, T. O. McDonald, L. C. Serpell and D. J. Adams, Hydrogels formed from Fmoc amino acids, *CrystEngComm*, 2015, **17**, 8047–8057.

41 V. Castelletto, G. Cheng, B. W. Greenland, I. W. Hamley and P. J. F. Harris, Tuning the self-assembly of the bioactive dipeptide l -carnosine by incorporation of a bulky aromatic substituent, *Langmuir*, 2011, **27**, 2980–2988.

42 V. Jayawarna, M. Ali, T. A. Jowitt, A. F. Miller, A. Saiani, J. E. Gough and R. V. Ulijn, Nanostructured hydrogels for three-dimensional cell culture through self-assembly of fluorenylmethoxycarbonyl-dipeptides, *Adv. Mater.*, 2006, **18**, 611–614.

43 Z. Yang, G. Liang, M. Ma, Y. Gao and B. Xu, Conjugates of naphthalene and dipeptides produce molecular hydrogelators with high efficiency of hydrogelation and superhelical nanofibers, *J. Mater. Chem.*, 2007, **17**, 850–854.

44 P. R. A. Chivers, R. S. Dookie, J. E. Gough and S. J. Webb, Photo-dissociation of self-assembled (anthracene-2-carbonyl)amino acid hydrogels, *Chem. Commun.*, 2020, **56**, 13792–13795.

45 V. Zhang, Z. Yang, F. Yuan, H. Gu, P. Gao and B. Xu, Molecular recognition remolds the self-assembly of hydrogelators and increases the elasticity of the hydrogel by 106-fold, *J. Am. Chem. Soc.*, 2004, **126**, 15028–15029.

46 W. Ji, Y. Tang, P. Makam, Y. Yao, R. Jiao, K. Cai, G. Wei and E. Gazit, Expanding the Structural Diversity and Functional Scope of Diphenylalanine-Based Peptide Architectures by Hierarchical Coassembly, *J. Am. Chem. Soc.*, 2021, **143**, 17633–17645.

47 L. Chen, T. O. McDonald and D. J. Adams, Salt-induced hydrogels from functionalised-dipeptides, *RSC Adv.*, 2013, **3**, 8714–8720.

48 S. Fleming, D. Sisir, P. W. J. M. Frederix, T. Tuttle and R. V. Ulijn, Aromatic peptide amphiphiles: Significance of the Fmoc moiety, *Chem. Commun.*, 2013, **49**, 10587–10589.

49 J. H. Van Esch, We can design molecular gelators, but do we understand them?, *Langmuir*, 2009, **25**, 8392–8394.

50 M. Reches and E. Gazit, Casting metal nanowires within discrete self-assembled peptide nanotubes, *Science (1979)*, 2003, **300**, 625–627.

51 R. Orbach, I. Mironi-Harpaz, L. Adler-Abramovich, E. Mossou, E. P. Mitchell, V. T. Forsyth, E. Gazit and D. Seliktar, The rheological and structural properties of Fmoc-peptide-based hydrogels: The effect of aromatic molecular architecture on self-assembly and physical characteristics, *Langmuir*, 2012, **28**, 2015–2022.

52 H. Cui, A. G. Cheetham, E. T. Pashuck and S. I. Stupp, Amino acid sequence in constitutionally isomeric tetrapeptide amphiphiles dictates architecture of one-dimensional nanostructures, *J. Am. Chem. Soc.*, 2014, **136**, 12461–12468.

53 R. Orbach, L. Adler-Abramovich, S. Zigerson, I. Mironi-Harpaz, D. Seliktar and E. Gazit, Self-assembled Fmoc-peptides as a platform for the formation of nanostructures and hydrogels, *Biomacromolecules*, 2009, **10**, 2646–2651.

54 D. J. Adams, K. Morris, L. Chen, L. C. Serpell, J. Bacsa and G. M. Day, The delicate balance between gelation and crystallisation: Structural and computational investigations, *Soft Matter*, 2010, **6**, 4144–4156.

55 X. Du, J. Zhou, J. Shi and B. Xu, Supramolecular Hydrogelators and Hydrogels: From Soft Matter to Molecular Biomaterials, *Chem. Rev.*, 2015, **115**, 13165–13307.

56 C. Tang, A. M. Smith, R. F. Collins, R. V. Ulijn and A. Saiani, Fmoc-Diphenylalanine Self-ASsembly Mechanism Induces Apparent pK a Shifts, *Langmuir*, 2009, **25**, 9447–9453.

57 G. Panzarasa, T. Sai, A. L. Torzynski, K. Smith-Mannschott and E. R. Dufresne, Supramolecular assembly by time-programmed acid autocatalysis, *Mol. Syst. Des. Eng.*, 2020, **5**, 445–448.

58 T. Heuser, A.-K. Steppert, C. Molano Lopez, B. Zhu and A. Walther, Generic Concept to Program the Time Domain of Self-Assemblies with a Self-Regulation Mechanism, *Nano Lett.*, 2015, **15**, 2213–2219.

59 E. R. Draper, L. L. E. Mears, A. M. Castilla, S. M. King, T. O. McDonald, R. Akhtar and D. J. Adams, Using the hydrolysis of anhydrides to control gel properties and homogeneity in pH-triggered gelation, *RSC Adv.*, 2015, **5**, 95369–95378.

60 A. Mata, L. Hsu, R. Capito, C. Aparicio, K. Henrikson and S. I. Stupp, Micropatterning of bioactive self-assembling gels, *Soft Matter*, 2009, **5**, 1228–1236.

61 S. Panja and D. J. Adams, Maintaining homogeneity during a sol-gel transition by an autocatalytic enzyme reaction, *Chem. Commun.*, 2019, **55**, 47–50.

62 J. Raeburn, T. O. Mc Donald and D. J. Adams, Dipeptide hydrogelation triggered via ultraviolet light, *Chem. Commun.*, 2012, **48**, 9355–9357.

63 C. Maity, W. E. Hendriksen, J. H. Van Esch and R. Eelkema, Spatial structuring of a supramolecular hydrogel by using a visible-light triggered catalyst, *Angew. Chem., Int. Ed.*, 2015, **54**, 998–1001.

64 M. Liu, C. N. Creemer, T. J. Reardon and J. R. Parquette, Light-driven dissipative self-assembly of a peptide hydrogel, *Chem. Commun.*, 2021, **57**, 13776–13779.

65 D. J. Cornwell and D. K. Smith, Photo-patterned multi-domain multi-component hybrid hydrogels, *Chem. Commun.*, 2020, **56**, 7029–7032.

66 V. Javvaji, A. G. Baradwaj, G. F. Payne and S. R. Raghavan, Light-Activated Ionic Gelation of Common Biopolymers, *Langmuir*, 2011, **27**, 12591–12596.

67 L. Thomson, R. Schweins, E. R. Draper and D. J. Adams, Creating Transient Gradients in Supramolecular Hydrogels, *Macromol. Rapid Commun.*, 2020, **41**, 2000093.

68 B. Yang, M. Lledos, R. Akhtar, G. Ciccone, L. Jiang, E. Russo, S. Rajput, C. Jin, M. G. F. Angelereou, T. Arnold, J. Rawle, M. Vassalli, M. Marlow, D. J. Adams and M. Zelzer, Surface-controlled spatially heterogeneous physical properties of a supramolecular gel with homogeneous chemical composition, *Chem. Sci.*, 2021, **12**, 14260–14269.

69 S. Bianco, L. Wimberger, Y. Ben-Tal, G. T. Williams, A. J. Smith, J. E. Beves and D. J. Adams, Reversibly Tuning the Viscosity of Peptide-Based Solutions Using Visible Light, *Chem. Eur. J.*, 2024, **30**, e202400544.

70 L. Chen, G. Pont, K. Morris, G. Lotze, A. Squires, L. C. Serpell and D. J. Adams, Salt-induced hydrogelation of functionalised-dipeptides at high pH, *Chem. Commun.*, 2011, **47**, 12071–12073.

71 L. Chen, T. O. McDonald and D. J. Adams, Salt-induced hydrogels from functionalised-dipeptides, *RSC Adv.*, 2013, **3**, 8714–8720.

72 S. Roy, N. Javid, P. W. J. M. Frederix, D. A. Lamprou, A. J. Urquhart, N. T. Hunt, P. J. Halling and R. V. Ulijn, Dramatic specific-ion effect in supramolecular hydrogels, *Chem. Eur. J.*, 2012, **18**, 11723–11731.

73 J. C. Stendahl, M. S. Rao, M. O. Guler and S. I. Stupp, Intermolecular Forces in the Self-Assembly of Peptide Amphiphile Nanofibers, *Adv. Funct. Mater.*, 2006, **16**, 499–508.

74 J. Shi, Y. Gao, Y. Zhang, Y. Pan and B. Xu, Calcium ions to cross-link supramolecular nanofibers to tune the elasticity of hydrogels over orders of magnitude, *Langmuir*, 2011, **27**, 14425–14431.

75 M. A. Greenfield, J. R. Hoffman, M. O. De La Cruz and S. I. Stupp, Tunable mechanics of peptide nanofiber gels, *Langmuir*, 2010, **26**, 3641–3647.

76 C. M. Wallace, M. M. Rovers, R. Bellan, M. G. T. A. Rutten, A. Seddon, M. J. Dalby, P. Y. W. Dankers and D. J. Adams, Investigating the self-assembly of 2NapFF and ureido-pyrimidinone multicomponent systems for cell culture, *J. Mater. Chem. B*, 2024, **12**, 9283–9288.

77 K. Rajagopal, M. S. Lamm, L. A. Haines-Butterick, D. J. Pochan and J. P. Schneider, Tuning the pH responsiveness of β-hairpin peptide folding, self-assembly, and hydrogel material formation, *Biomacromolecules*, 2009, **10**, 2619–2625.

78 L. Haines-Butterick, K. Rajagopal, M. Branco, D. Salick, R. Rughani, M. Pilarz, M. S. Lamm, D. J. Pochan and J. P. Schneider, Controlling hydrogelation kinetics by peptide design for three-dimensional encapsulation and injectable delivery of cells, *Proc. Natl. Acad. Sci. U.S.A.*, 2007, **104(19)**, 7791–7796.

79 B. Ozbas, J. Kretsinger, K. Rajagopal, J. P. Schneider and D. J. Pochan, Salt-triggered peptide folding and consequent self-assembly into hydrogels with tunable modulus, *Macromol.*, 2004, **37**, 7331–7337.

80 R. Orbach, L. Adler-Abramovich, S. Zigerson, I. Mironi-Harpaz, D. Seliktar and E. Gazit, Self-Assembled Fmoc-Peptides as a Platform for the Formation of Nanostructures and Hydrogels, *Biomacromolecules*, 2009, **10**, 2646–2651.

81 N. A. Dudukovic and C. F. Zukoski, Evidence for equilibrium gels of valence-limited particles, *Soft Matter*, 2014, **10**, 7849–7856.

82 L. Chen, J. Raeburn, S. Sutton, D. G. Spiller, J. Williams, J. S. Sharp, P. C. Griffiths, R. K. Heenan, S. M. King, A. Paul, S. Furzeland, D. Atkins and D. J. Adams, Tuneable mechanical properties in low molecular weight gels, *Soft Matter*, 2011, **7**, 9721–9727.

83 J. Raeburn, C. Mendoza-Cuenca, B. N. Cattoz, M. A. Little, A. E. Terry, A. Zamith Cardoso, P. C. Griffiths and D. J. Adams, The effect of solvent choice on the gelation and final hydrogel properties of Fmoc-diphenylalanine, *Soft Matter*, 2015, **11**, 927–935.

84 L. A. Estroff and A. D. Hamilton, Water gelation by small organic molecules, *Chem. Rev.*, 2004, **104**, 1201–1217.

85 T. Kar, S. K. Mandal and P. K. Das, Organogel-hydrogel transformation by simple removal or inclusion of N-Boc-protection, *Chem. Eur. J.*, 2011, **17**, 14952–14961.

86 A. Friggeri, B. L. Feringa and J. van Esch, Entrapment and release of quinoline derivatives using a hydrogel of a low molecular weight gelator, *J. Control. Release*, 2004, **97**, 241–248.

87 R. Vegners, I. Shestakova, I. Kalvinsh, R. M. Ezzell and P. A. Janmey, Use of a gel-forming dipeptide derivative as a carrier for antigen presentation, *J. Pept. Sci.*, 1995, **1**, 371–378.

88 M. Tena-Solsona, B. Rieß, R. K. Grötsch, F. C. Löhrer, C. Wanzke, B. Käsdorf, A. R. Bausch, P. Müller-Buschbaum, O. Lieleg and J. Boekhoven, Non-equilibrium dissipative supramolecular materials with a tunable lifetime, *Nat. Commun.*, 2017, **8**, 15895.

89 B. Rieß and J. Boekhoven, Applications of Dissipative Supramolecular Materials with a Tunable Lifetime, *ChemNanoMat*, 2018, **4**, 710–719.

90 S. Pal, A. Reja, S. Bal, B. Tikader and D. Das, Emergence of a Promiscuous Peroxidase Under Non-Equilibrium Conditions**, *Angew. Chem. Int. Ed.*, 2022, **61**, e202111857.

91 S. Dhiman, K. Jalani and S. J. George, Redox-Mediated, Transient Supramolecular Charge-Transfer Gel and Ink, *ACS Appl. Mater. Interfaces*, 2020, **12**, 5259–5264.

92 Y. Zhong, P. Li, J. Hao and X. Wang, Bioinspired Self-Healing of Kinetically Inert Hydrogels Mediated by Chemical Nutrient Supply, *ACS Appl. Mater. Interfaces*, 2020, **12**, 6471–6478.

93 F. della Sala, S. Neri, S. Maiti, J. L. Y. Chen and L. J. Prins, Transient self-assembly of molecular nanostructures driven by chemical fuels, *Curr. Opin. Biotechnol.*, 2017, **46**, 27–33.

94 M. Kretschmer, B. Winkeljann, B. A. K. Kriebisch, J. Boekhoven and O. Lieleg, Viscoelastic behavior of chemically fueled supramolecular hydrogels under load and influence of reaction side products, *Commun. Mater.*, 2021, **2**, 97.

95 V. J. Nebot and D. K. Smith, in *Funcional Molecular Gels*, Royal Society of Chemistry, Cambridge, 2013, pp. 30–66.

96 G. Yu, X. Yan, C. Han and F. Huang, Characterization of supramolecular gels, *Chem. Soc. Rev.*, 2013, **42**, 6697–6722.

97 B. R. Denzer, R. J. Kulchar, R. B. Huang and J. Patterson, Advanced Methods for the Characterization of Supramolecular Hydrogels, *Gels*, 2021, **7**, 158.

98 L. L. E. Mears, E. R. Draper, A. M. Castilla, H. Su, Zhuola, B. Dietrich, M. C. Nolan, G. N. Smith, J. Doutch, S. Rogers, R. Akhtar, H. Cui and D. J. Adams, Drying Affects the Fiber Network in Low Molecular Weight Hydrogels, *Biomacromolecules*, 2017, **18**, 3531–3540.

99 B. R. Pauw, Everything SAXS: small-angle scattering pattern collection and correction, *J. Phys. Condens. Matter*, 2014, **26**, 239501.

100 C. Yan and D. J. Pochan, Rheological properties of peptide-based hydrogels for biomedical and other applications, *Chem. Soc. Rev.*, 2010, **39**, 3528–3540.

101 R. K. Grötsch and J. Boekhoven, in *Self-assembling Biomaterials*, Elsevier, 2018, pp. 235–250.

102 F. Tantakitti, J. Boekhoven, X. Wang, R. V. Kazantsev, T. Yu, J. Li, E. Zhuang, R. Zandi, J. H. Ortony, C. J. Newcomb, L. C. Palmer, G. S. Shekhawat, M. O. De La Cruz, G. C. Schatz and S. I. Stupp, Energy landscapes and functions of supramolecular systems, *Nat. Mater.*, 2016, **15**, 469–476.

103 J. Shi, Y. Gao, Z. Yang and B. Xu, Exceptionally small supramolecular hydrogelators based on aromatic-aromatic interactions, *Beilstein J. Org. Chem.*, 2011, **7**, 167–172.

104 E. R. Draper, T. O. McDonald and D. J. Adams, A low molecular weight hydrogel with unusual gel aging, *Chem. Commun.*, 2015, **51**, 6595–6597.

105 A. Baral, S. Basak, K. Basu, A. Dehsorkhi, I. W. Hamley and A. Banerjee, Time-dependent gel to gel transformation of a peptide based supramolecular gelator, *Soft Matter*, 2015, **11**, 4944–4951.

106 D. K. Duraisamy, P. D. Sureshbhai, P. Saveri, A. P. Deshpande and G. Shanmugam, A “self-shrinking” supramolecular hydrogel with a 3D shape memory performance from an unnatural amino acid derivative, *Chem. Commun.*, 2022, **58**, 13377–13380.

107 S. Basak, N. Nandi, S. Paul, I. W. Hamley and A. Banerjee, A tripeptide-based self-shrinking hydrogel for waste-water treatment: Removal of toxic organic dyes and lead (Pb2+) ions, *Chem. Commun.*, 2017, **53**, 5910–5913.

108 F. Sheehan, D. Sementa, A. Jain, M. Kumar, M. Tayarani-Najjaran, D. Kroiss and R. V. Ulijn, Peptide-Based Supramolecular Systems Chemistry, *Chem. Rev.*, 2021, **121**, 13869–13914.

109 Z. Qiu, H. Yu, J. Li, Y. Wang and Y. Zhang, Spiropyran-linked dipeptide forms supramolecular hydrogel with dual responses to light and to ligand-receptor interaction, *Chem. Commun.*, 2009, **7345**, 3342–3344.

110 Q. Liu, H. Wang, G. Li, M. Liu, J. Ding, X. Huang, W. Gao and W. Huayue, A photocleavable low molecular weight hydrogel for light-triggered drug delivery, *Chin. Chem. Lett.*, 2019, **30**, 485–488.

111 V. Ramamurthy and J. Sivaguru, Supramolecular Photochemistry as a Potential Synthetic Tool: Photocycloaddition, *Chem. Rev.*, 2016, **116**, 9914–9993.

112 E. R. Draper, T. O. McDonald and D. J. Adams, Photodimerisation of a coumarin-dipeptide gelator, *Chem. Commun.*, 2015, **51**, 12827–12830.

113 S. H. Kim, Y. Sun, J. A. Kaplan, M. W. Grinstaff and J. R. Parquette, Photo-crosslinking of a self-assembled coumarin-dipeptide hydrogel, *New J. Chem.*, 2015, **39**, 3225–3228.

114 Y. Ding, Y. Li, M. Qin, Y. Cao and W. Wang, Photo-cross-linking approach to engineering small tyrosine-containing peptide hydrogels with enhanced mechanical stability, *Langmuir*, 2013, **29**, 13299–13306.

115 W. Li, I. S. Park, S. K. Kang and M. Lee, Smart hydrogels from laterally-grafted peptide assembly, *Chem. Commun.*, 2012, **48**, 8796–8798.

116 Y. Huang, Z. Qiu, Y. Xu, J. Shi, H. Lin and Y. Zhang, Supramolecular hydrogels based on short peptides linked with conformational switch, *Org. Biomol. Chem.*, 2011, **9**, 2149–2155.

117 B. K. Das, B. Pramanik, S. Chowdhuri, O. A. Scherman and D. Das, Light-triggered syneresis of a water insoluble peptide-hydrogel effectively removes small molecule waste contaminants, *Chem. Commun.*, 2020, **56**, 3393–3396.

118 F. Xie, L. Qin and M. Liu, A dual thermal and photo-switchable shrinking-swelling supramolecular peptide dendron gel, *Chem. Commun.*, 2016, **52**, 930–933.

119 S. Roy, D. Kumar Maiti, S. Panigrahi, D. Basak and A. Banerjee, A new hydrogel from an amino acid-based perylene bisimide and its semiconducting, photo-switching behaviour, *RSC Adv.*, 2012, **2**, 11053–11060.

120 A. Das and S. Ghosh, H-bonding directed programmed supramolecular assembly of naphthalene-dIImide (NDI) derivatives, *Chem. Commun.*, 2016, **52**, 6860–6872.

121 E. R. Draper, R. Schweins, R. Akhtar, P. Groves, V. Chechik, M. A. Zwijnenburg and D. J. Adams, Reversible Photoreduction as a Trigger for Photoresponsive Gels, *Chem. Mater.*, 2016, **28**, 6336–6341.

122 J. Boekhoven, W. E. Hendriksen, G. J. M. Koper, R. Eelkema and J. H. van Esch, Transient assembly of active materials fueled by a chemical reaction, *Science (1979)*, 2015, **349**, 1075–1079.

123 B. Rieß, R. K. Grötsch and J. Boekhoven, The Design of Dissipative Molecular Assemblies Driven by Chemical Reaction Cycles, *Chem*, 2020, **6**, 552–578.

124 K. Das, R. Chen, S. Chandrabhas, L. Gabrielli and L. J. Prins, in *Out-of-Equilibrium (Supra)molecular Systems and Materials*, Wiley, 2021, pp. 191–213.

125 S. De and R. Klajn, Dissipative Self-Assembly Driven by the Consumption of Chemical Fuels, *Adv. Mater.*, 2018, **30**, 1706750.

126 J. D. Hartgerink, E. Beniash and S. I. Stupp, Self-Assembly and Mineralization of Peptide-Amphiphile Nanofibers, *Science (1979)*, 2001, **294**, 1684–1688.

127 K. J. C. Van Bommel, C. Van Der Pol, I. Muizebelt, A. Friggeri, A. Heeres, A. Meetsma, B. L. Feringa and J. Van Esch, Responsive cyclohexane-based low-molecular-weight hydrogelators with modular architecture, *Angew. Chem. Int. Ed.*, 2004, **43**, 1663–1667.

128 S. Panja, A. M. Fuentes-Caparrós, E. R. Cross, L. Cavalcanti and D. J. Adams, Annealing Supramolecular Gels by a Reaction Relay, *Chem. Mater.*, 2020, **32**, 5264–5271.

129 N. Singh, G. J. M. Formon, S. De Piccoli and T. M. Hermans, Devising Synthetic Reaction Cycles for Dissipative Nonequilibrium Self-Assembly, *Adv. Mater.*, 2020, **32**, 1906834.

130 S. Panja and D. J. Adams, Gel to gel transitions by dynamic self-assembly, *Chem. Commun.*, 2019, **55**, 10154–10157.

131 T. Heuser, A. K. Steppert, C. Molano Lopez, B. Zhu and A. Walther, Generic Concept to Program the Time Domain of Self-Assemblies with a Self-Regulation Mechanism, *Nano Lett.*, 2015, **15**, 2213–2219.

132 S. Panja and D. J. Adams, Urea-Urease Reaction in Controlling Properties of Supramolecular Hydrogels: Pros and Cons, *Chem. Eur. J.*, 2021, **27**, 8928–8939.

133 L. Heinen, T. Heuser, A. Steinschulte and A. Walther, Antagonistic enzymes in a biocatalytic ph feedback system program autonomous DNA hydrogel life cycles, *Nano Lett.*, 2017, **17**, 4989–4995.

134 G. Hu, J. A. Pojman, S. K. Scott, M. M. Wrobel and A. F. Taylor, Base-Catalyzed Feedback in the Urea−Urease Reaction, *J. Phys. Chem. B*, 2010, **114**, 14059–14063.

135 E. Jee, T. Bánsági, A. F. Taylor and J. A. Pojman, Temporal Control of Gelation and Polymerization Fronts Driven by an Autocatalytic Enzyme Reaction, *Angew. Chem. Int. Ed.*, 2016, **128**, 2167–2171.

136 S. Panja, C. Patterson and D. J. Adams, Temporally-Programmed Transient Supramolecular Gels, *Macromol. Rapid. Commun.*, 2019, **40**, 1900251.

137 T. Heuser, E. Weyandt and A. Walther, Biocatalytic Feedback-Driven Temporal Programming of Self-Regulating Peptide Hydrogels, *Angew. Chem. Int. Ed.*, 2015, **54**, 13258–13262.

138 S. Mondal, D. Podder, S. K. Nandi, S. Roy Chowdhury and D. Haldar, Acid-responsive fibrillation and urease-assisted defibrillation of phenylalanine: A transient supramolecular hydrogel, *Soft Matter*, 2020, **16**, 10115–10121.

139 M. Tena-Solsona, S. Alonso-De Castro, J. F. Miravet and B. Escuder, Co-assembly of tetrapeptides into complex pH-responsive molecular hydrogel networks, *J. Mater. Chem. B*, 2014, **2**, 6192–6197.

140 S. Panja, A. Seddon and D. J. Adams, Controlling hydrogel properties by tuning non-covalent interactions in a charge complementary multicomponent system, *Chem. Sci.*, 2021, **12**, 11197–11203.

141 F. Picchioni and H. Muljana, Hydrogels based on dynamic covalent and non covalent bonds: A chemistry perspective, *Gels*, 2018, **4**, 21.

142 T. Sugiura, T. Kanada, D. Mori, H. Sakai, A. Shibata, Y. Kitamura, M. Ikeda, M. Ikeda, M. Ikeda and M. Ikeda, Chemical stimulus-responsive supramolecular hydrogel formation and shrinkage of a hydrazone-containing short peptide derivative, *Soft Matter*, 2020, **16**, 899–906.

143 F. Schnitter, A. M. Bergmann, B. Winkeljann, J. Rodon Fores, O. Lieleg and J. Boekhoven, Synthesis and characterization of chemically fueled supramolecular materials driven by carbodiimide-based fuels, *Nat. Protoc.*, 2021, **16**, 3901–3932.

144 M. A. Khalily, M. Goktas and M. O. Guler, Tuning viscoelastic properties of supramolecular peptide gels via dynamic covalent crosslinking, *Org. Biomol. Chem.*, 2015, **13**, 1983–1987.

145 L. J. Marshall, O. Matsarskaia, R. Schweins and D. J. Adams, Enhancement of the mechanical properties of lysine-containing peptide-based supramolecular hydrogels by chemical cross-linking, *Soft Matter*, 2021, **17**, 8459–8464.

146 S. Panja, S. Bianco, B. Dietrich and D. J. Adams, Macroscopic volume phase transitions in supramolecular gels directed by covalent crosslinking, *Mater. Chem. Front.*, 2022, **6**, 2703–2708.

147 N. Singh, B. Lainer, G. J. M. Formon, S. De Piccoli and T. M. Hermans, Re-programming Hydrogel Properties Using a Fuel-Driven Reaction Cycle, *J. Am. Chem. Soc.*, 2020, **142**, 4083–4087.

148 B. Zhang, I. M. Jayalath, J. Ke, J. L. Sparks, C. S. Hartley and D. Konkolewicz, Chemically fueled covalent crosslinking of polymer materials, *Chem. Commun.*, 2019, **55**, 2086–2089.

149 C. A. Angulo-Pachón and J. F. Miravet, Sucrose-fueled, energy dissipative, transient formation of molecular hydrogels mediated by yeast activity, *Chem. Commun.*, 2016, **52**, 5398–5401.

150 C. G. Pappas, I. R. Sasselli and R. V Ulijn, Biocatalytic Pathway Selection in Transient Tripeptide Nanostructures, *Angew. Chem. Int. Ed.*, 2015, **54**, 8119–8123.

151 S. Panja, K. Boháčová, B. Dietrich and D. J. Adams, Programming properties of transient hydrogels by an enzymatic reaction, *Nanoscale*, 2020, **12**, 12840–12848.

152 K. Dai, J. R. Fores, C. Wanzke, B. Winkeljann, A. M. Bergmann, O. Lieleg and J. Boekhoven, Regulating Chemically Fueled Peptide Assemblies by Molecular Design, *J. Am. Chem. Soc.*, 2020, **142**, 14142–14149.

153 S. Bal, K. Das, S. Ahmed and D. Das, Chemically Fueled Dissipative Self-Assembly that Exploits Cooperative Catalysis, *Angew. Chem. Int. Ed.*, 2019, **58**, 244–247.

154 S. Debnath, S. Roy and R. V. Ulijn, Peptide nanofibers with dynamic instability through nonequilibrium biocatalytic assembly, *J. Am. Chem. Soc.*, 2013, **135**, 16789–16792.

155 M. Tena-Solsona and J. Boekhoven, Dissipative Self-Assembly of Peptides, *Isr. J. Chem.*, 2019, **59**, 898–905.

156 H. Xu, S. Bai, G. Gu, Y. Gao, X. Sun, X. Guo, F. Xuan and Y. Wang, Bioinspired Self-Resettable Hydrogel Actuators Powered by a Chemical Fuel, *ACS Appl. Mater. Interfaces.*, 2022, **14**, 43825–43832.

157 M. Nakamoto, S. Kitano and M. Matsusaki, Biomacromolecule-Fueled Transient Volume Phase Transition of a Hydrogel, *Angew. Chem. Int. Ed.*, 2022, **61**, e202205125.

158 S. Panja, B. Dietrich and D. J. Adams, Chemically Fuelled Self-Regulating Gel-to-Gel Transition, *ChemSystemsChem*, 2020, **2**, e1900038.

159 S. K. M. Nalluri, N. Shivarova, A. L. Kanibolotsky, M. Zelzer, S. Gupta, P. W. J. M. Frederix, P. J. Skabara, H. Gleskova and R. V Ulijn, Conducting Nanofibers and Organogels Derived from the Self-Assembly of Tetrathiafulvalene-Appended Dipeptides, *Langmuir*, 2014, **30**, 12429–12437.

160 C.-W. Chu and C. A. Schalley, Recent Advances on Supramolecular Gels: From Stimuli-Responsive Gels to Co-Assembled and Self-Sorted Systems, *Org. Mater.*, 2021, **03**, 025–040.

161 X. Sui, X. Feng, M. A. Hempenius and G. J. Vancso, Redox active gels: Synthesis, structures and applications, *J. Mater. Chem. B*, 2013, **1**, 1658–1672.

162 B. Adhikari and H. B. Kraatz, Redox-triggered changes in the self-assembly of a ferrocene-peptide conjugate, *Chem. Commun.*, 2014, **50**, 5551–5553.

163 Y. Li, Y. Sun, Y. Xiao, G. Gao, S. Liu, J. Zhang and J. Fu, Electric Field Actuation of Tough Electroactive Hydrogels Cross-Linked by Functional Triblock Copolymer Micelles, *ACS Appl. Mater. Interfaces*, 2016, **8**, 26326–26331.

164 Y. Shin, M. Y. Choi, J. Choi, J. H. Na and S. Y. Kim, Design of an Electro-Stimulated Hydrogel Actuator System with Fast Flexible Folding Deformation under a Low Electric Field, *ACS Appl. Mater. Interfaces*, 2021, **13**, 15633–15646.

165 B. Xue, M. Qin, T. Wang, J. Wu, D. Luo, Q. Jiang, Y. Li, Y. Cao and W. Wang, Electrically Controllable Actuators Based on Supramolecular Peptide Hydrogels, *Adv. Funct. Mater.*, 2016, **26**, 9053–9062.

166 J. P. Wojciechowski, A. D. Martin and P. Thordarson, Kinetically Controlled Lifetimes in Redox-Responsive Transient Supramolecular Hydrogels, *J. Am. Chem. Soc.*, 2018, **140**, 2869–2874.

167 W. A. Ogden and Z. Guan, Redox Chemical-Fueled Dissipative Self-Assembly of Active Materials, *ChemSystemsChem*, 2020, **2**, e1900030.

168 C. G. Pappas, T. Mutasa, P. W. J. M. Frederix, S. Fleming, S. Bai, S. Debnath, S. M. Kelly, A. Gachagan and R. V. Ulijn, Transient supramolecular reconfiguration of peptide nanostructures using ultrasound, *Mater. Horiz.*, 2014, **2**, 198–202.

169 D. Bardelang, F. Camerel, J. C. Margeson, D. M. Leek, M. Schmutz, M. B. Zaman, K. Yu, D. V. Soldatov, R. Ziessel, C. I. Ratcliffe and J. A. Ripmeester, Unusual sculpting of dipeptide particles by ultrasound induces gelation, *J. Am. Chem. Soc.*, 2008, **130**, 3313–3315.

170 Y. Wang, C. Zhan, H. Fu, X. Li, X. Sheng, Y. Zhao, D. Xiao, Y. Ma, J. S. Ma and J. Yao, Switch from intra- to intermolecular H-bonds by ultrasound: Induced gelation and distinct nanoscale morphologies, *Langmuir*, 2008, **24**, 7635–7638.

171 T. Naota and H. Koori, Molecules that assemble by sound: An application to the instant gelation of stable organic fluids, *J. Am. Chem. Soc.*, 2005, **127**, 9324–9325.

172 X. Yu, Q. Liu, J. Wu, M. Zhang, X. Cao, S. Zhang, Q. Wang, L. Chen and T. Yi, Sonication-triggered instantaneous gel-to-gel transformation, *Chem. Eur. J.*, 2010, **16**, 9099–9106.

173 X. Yu, X. Cao, L. Chen, H. Lan, B. Liu and T. Yi, Thixotropic and self-healing triggered reversible rheology switching in a peptide-based organogel with a cross-linked nano-ring pattern, *Soft Matter*, 2012, **8**, 3329–3334.

174 A. Abalymov, B.-E. Pinchasik, R. A. Akasov, M. Lomova and B. V. Parakhonskiy, Strategies for Anisotropic Fibrillar Hydrogels: Design, Cell Alignment, and Applications in Tissue Engineering, *Biomacromolecules*, 2023, **24**, 4532–4552.

175 Md. A. Haque, G. Kamita, T. Kurokawa, K. Tsujii and J. P. Gong, Unidirectional Alignment of Lamellar Bilayer in Hydrogel: One-Dimensional Swelling, Anisotropic Modulus, and Stress/Strain Tunable Structural Color, *Adv. Mater.*, 2010, **22**, 5110–5114.

176 S. Zhang, M. A. Greenfield, A. Mata, L. C. Palmer, R. Bitton, J. R. Mantei, C. Aparicio, M. O. de la Cruz and S. I. Stupp, A self-assembly pathway to aligned monodomain gels, *Nat. Mater.*, 2010, **9**, 594–601.

177 B. D. Wall, S. R. Diegelmann, S. Zhang, T. J. Dawidczyk, W. L. Wilson, H. E. Katz, H. Mao and J. D. Tovar, Aligned Macroscopic Domains of Optoelectronic Nanostructures Prepared via Shear-Flow Assembly of Peptide Hydrogels, *Adv. Mater.*, 2011, **23**, 5009–5014.

178 A. H. Milani, L. A. Fielding, P. Greensmith, B. R. Saunders, D. J. Adlam, A. J. Freemont, J. A. Hoyland, N. W. Hodson, M. A. Elsawy, A. F. Miller, L. P. D. Ratcliffe, O. O. Mykhaylyk and S. P. Armes, Anisotropic pH-Responsive Hydrogels Containing Soft or Hard Rod-Like Particles Assembled Using Low Shear, *Chem. Mater.*, 2017, **29**, 3100–3110.

179 E. R. Draper, O. O. Mykhaylyk and D. J. Adams, Aligning self-assembled gelators by drying under shear, *Chem. Commun.*, 2016, **52**, 6934–6937.

180 S. Bianco, F. Hallam Stewart, S. Panja, A. Zyar, E. Bowley, M. Bek, R. Kádár, A. Terry, R. Appio, T. S. Plivelic, M. Maguire, H. Poptani, M. Marcello, R. R. Sonani, E. H. Egelman and D. J. Adams, Forging out-of-equilibrium supramolecular gels, *Nat. Synth.*, 2024, **3**, 1481–1489.

181 N. Smal and D. W. P. M. Löwik, *Magnetic fields to align natural and synthetic fibers*, Elsevier Ltd., 2018.

182 L. Pauling, The Diamagnetic Anisotropy of Aromatic Molecules, *J. Chem. Phys.*, 1936, **4**, 673–677.

183 D. L. Worcester, Structural origins of diamagnetic anisotropy in proteins., *Proc. Nat. Acad. Sci.*, 1978, **75**, 5475–5477.

184 Y. Jung, H. Kim, H.-K. Cheong and Y. Lim, Magnetic control of self-assembly and disassembly in organic materials, *Nat. Commun.*, 2023, **14**, 3081.

185 M. van den Heuvel, A. M. Prenen, J. C. Gielen, P. C. M. Christianen, D. J. Broer, D. W. P. M. Löwik and J. C. M. van Hest, Patterns of Diacetylene-Containing Peptide Amphiphiles Using Polarization Holography, *J. Am. Chem. Soc.*, 2009, **131**, 15014–15017.

186 D. W. P. M. Löwik, I. O. Shklyarevskiy, L. Ruizendaal, P. C. M. Christianen, J. C. Maan and J. C. M. van Hest, A Highly Ordered Material from Magnetically Aligned Peptide Amphiphile Nanofiber Assemblies, *Adv. Mater.*, 2007, **19**, 1191–1195.

187 M. Wallace, A. Z. Cardoso, W. J. Frith, J. A. Iggo and D. J. Adams, Magnetically Aligned Supramolecular Hydrogels, *Chem. Eur. J.*, 2014, **20**, 16484–16487.

188 E. Olivieri, G. Quintard, J.-V. Naubron and A. Quintard, Chemically Fueled Three-State Chiroptical Switching Supramolecular Gel with Temporal Control, *J. Am. Chem. Soc.*, 2021, **143**, 12650–12657.

189 K. Hu and S. S. Sheiko, Time programmable hydrogels: Regulating the onset time of network dissociation by a reaction relay, *Chem. Commun.*, 2018, **54**, 5899–5902.

190 M. J. Webber, E. A. Appel, E. W. Meijer and R. Langer, Supramolecular biomaterials, *Nat. Mater.*, 2015, **15**, 13–26.

191 A. Dawn and H. Kumari, Low Molecular Weight Supramolecular Gels Under Shear: Rheology as the Tool for Elucidating Structure–Function Correlation, *Chem. Eur. J.*, 2018, **24**, 762–776.

192 G. M. Kavanagh and S. B. Ross-Murphy, Rheological characterisation of polymer gels, *Prog. Polym. Sci.*, 1998, **23**, 533–562.

193 T. G. Mezger, *The Rheology Handbook*, Vincentz Network, Germany, 4th edn., 2012.

194 D. L. Blair, in *Molecular Gels: Structure and Dynamics*, 2018, pp. 28–56.

195 R. G. Weiss and P. Terech, *Molecular gels: Materials with self-assembled fibrillar networks*, Dordrecht, The Netherlands, 2006.

196 S. Sathaye, A. Mbi, C. Sonmez, Y. Chen, D. L. Blair, J. P. Schneider and D. J. Pochan, Rheology of peptide- and protein-based physical hydrogels: Are everyday measurements just scratching the surface?, *Wiley Interdiscip. Rev. Nanomed. Nanobiotechnol.*, 2015, **7**, 34–68.

197 C. E. Owens, A. J. Hart and G. H. McKinley, Improved rheometry of yield stress fluids using bespoke fractal 3D printed vanes, *J. Rheol.*, 2020, **64**, 643–662.

198 H. A. Barnes and Q. D. Nguyen, Rotating vane rheometry — a review, *J. Nonnewton Fluid Mech.*, 2001, **98**, 1–14.

199 J. M. Zuidema, C. J. Rivet, R. J. Gilbert and F. A. Morrison, A protocol for rheological characterization of hydrogels for tissue engineering strategies, *J. Biomed. Mater. Res. B Appl. Biomater.*, 2014, **102**, 1063–1073.

200 A. Y. Malkin and A. Isayev, *Rheology: concepts, methods, and applications*, ChemTec Publishing, Toronto, Ontario, Third., 2017.

201 L. Thomson, D. McDowall, L. Marshall, O. Marshall, H. Ng, W. J. A. Homer, D. Ghosh, W. Liu, A. M. Squires, E. Theodosiou, P. D. Topham, L. C. Serpell, R. J. Poole, A. Seddon and D. J. Adams, Transferring Micellar Changes to Bulk Properties via Tunable Self-Assembly and Hierarchical Ordering, *ACS Nano*, 2022, **16**, 20497–20509.

202 C. A. Dreiss, Wormlike micelles: where do we stand? Recent developments, linear rheology and scattering techniques, *Soft Matter*, 2007, **3**, 956.

203 G. S. Georgieva, S. E. Anachkov, I. Lieberwirth, K. Koynov and P. A. Kralchevsky, Synergistic Growth of Giant Wormlike Micelles in Ternary Mixed Surfactant Solutions: Effect of Octanoic Acid, *Langmuir*, 2016, **32**, 12885–12893.

204 O. O. Mykhaylyk, Time-resolved polarized light imaging of sheared materials: Application to polymer crystallization, *Soft Matter*, 2010, **6**, 4430–4440.

205 O. O. Mykhaylyk, N. J. Warren, A. J. Parnell, G. Pfeifer and J. Laeuger, Applications of shear-induced polarized light imaging (SIPLI) technique for mechano-optical

rheology of polymers and soft matter materials, *J. Polym. Sci. B Polym. Phys.*, 2016, **54**, 2151–2170.

206 D. McDowall, D. J. Adams and A. M. Seddon, Using small angle scattering to understand low molecular weight gels, *Soft Matter*, 2022, **18**, 1577–1590.

207 E. R. Draper, B. Dietrich, K. McAulay, C. Brasnett, H. Abdizadeh, I. Patmanidis, S. J. Marrink, H. Su, H. Cui, R. Schweins, A. Seddon and D. J. Adams, Using Small-Angle Scattering and Contrast Matching to Understand Molecular Packing in Low Molecular Weight Gels, *Matter*, 2020, **2**, 764–778.

208 C. J. Gommes, S. Jaksch and H. Frielinghaus, Small-angle scattering for beginners, *J. Appl. Crystallogr.*, 2021, **54**, 1832–1843.

209 J. B. Guilbaud and A. Saiani, Using small angle scattering (SAS) to structurally characterise peptide and protein self-assembled materials, *Chem. Soc. Rev.*, 2011, **40**, 1200–1210.

210 G. Ochbaum and R. Bitton, *Using small-angle X-ray scattering (SAXS) to study the structure of self-assembling biomaterials*, Elsevier Ltd., 2018.

211 K. McAulay, L. Thomson, L. Porcar, R. Schweins, N. Mahmoudi, D. J. Adams and E. R. Draper, Using Rheo-Small-Angle Neutron Scattering to Understand How Functionalised Dipeptides Form Gels, *Org. Mater.*, 2020, **2**, 108–115.

212 R. Ghanbari, A. Terry, S. Wojno, M. Bek, K. Sekar, A. K. Sonker, K. Nygård, V. Ghai, S. Bianco, M. Liebi, A. Matic, G. Westman, T. Nypelö and R. Kádár, Propagation of Orientation Across Lengthscales in Sheared Self-Assembling Hierarchical Suspensions via Rheo-PLI-SAXS, *Adv. Sci.*, 2025, **12**, 2410920.

213 S. Wojno, M. Fazilati, T. Nypelö, G. Westman and R. Kádár, Phase transitions of cellulose nanocrystal suspensions from nonlinear oscillatory shear, *Cellulose*, 2022, **29**, 3655–3673.

214 J. Royes, V. A. Bjørnestad, G. Brun, T. Narayanan, R. Lund and C. Tribet, Transition kinetics of mixed lipid:photosurfactant assemblies studied by time-resolved small angle X-ray scattering, *J. Colloid. Interface Sci.*, 2022, **610**, 830–841.

215 R. Lund, G. Brun, E. Chevallier, T. Narayanan and C. Tribet, Kinetics of Photocontrollable Micelles: Light-Induced Self-Assembly and Disassembly of

Azobenzene-Based Surfactants Revealed by TR-SAXS, *Langmuir*, 2016, **32**, 2539–2548.

216 R. I. Randle, A. M. Fuentes-Caparrós, L. P. Cavalcanti, R. Schweins, D. J. Adams and E. R. Draper, Investigating Aggregation Using In Situ Electrochemistry and Small-Angle Neutron Scattering, *J. Phys. Chem. C*, 2022, **126**, 13427–13432.

217 B. Escuder, M. LLusar and J. F. Miravet, Insight on the NMR study of supramolecular gels and its application to monitor molecular recognition on self-assembled fibers, *J. Org. Chem.*, 2006, **71**, 7747–7752.

218 M. Wallace, J. A. Iggo and D. J. Adams, Using solution state NMR spectroscopy to probe NMR invisible gelators, *Soft Matter*, 2015, **11**, 7739–7747.

219 E. R. Draper, M. Wallace, D. Honecker and D. J. Adams, Aligning self-assembled perylene bisimides in a magnetic field, *Chem. Commun.*, 2018, **54**, 10977–10980.

Chapter 2. Using Rheology to Understand Transient and Dynamic Gels

This Chapter is published as the following publication:

″Using Rheology to Understand Transient and Dynamic Gels″

S. Bianco, S. Panja and D.J. Adams, *Gels*, 2022, **8**, 132.

Author contributions

The author contributions are as follows: Conceptualization, D.J.A.; methodology, S.B., S.P. and D.J.A.; formal analysis, S.B., S.P. and D.J.A.; investigation, S.B. and S.P.; resources, D.J.A.; data curation, S.B. and S.P.; writing - original draft preparation, S.B., S.P. and D.J.A.; writing - review and editing, S.B., S.P. and D.J.A.; supervision, D.J.A.; project administration, D.J.A.; funding acquisition, D.J.A. All authors have read and agreed to the published version of the manuscript.

The manuscript has been included in the thesis as published. The molecule used in this work was synthesised by Prof. Dave J. Adams (University of Glasgow). All experiments shown in this work were performed, analysed and visualised by Simona Bianco.

2. Using Rheology to Understand Transient and Dynamic Gels

Simona Bianco,[a] Santanu Panja[a] and Dave J. Adams[a]*

[a] School of Chemistry, University of Glasgow, Glasgow G12 8QQ, UK

2.1 Abstract

Supramolecular gels can be designed such that pre-determined changes in state occur. For example, systems that go from a solution (sol) state to a gel state and then back to a sol state can be prepared using chemical processes to control the onset and duration of each change of state. Based on this, more complex systems such as gel-to-sol-to-gel and gel-to-gel-to-gel systems can be designed. Here, we show that we can provide additional insights into such systems by using rheological measurements at varying values of frequency or strain during the evolution of the systems. Since the different states are affected to different degrees by the frequency and/or strain applied, this allows us to better understand and follow the changes in state in such systems.

2.2 Introduction

In most cases when gels are prepared, their properties ideally do not change with time. However, there is an increasing interest in gels which have controllably changing properties. Transient gels as well as gels that are formed by fueled systems are a growing field, partially driven by a generic interest in systems chemistry as well as by potential analogy with biological systems.[1-5]

Several such systems have been reported that change phase with time.[6-18] There are examples where an initial solution (sol) state forms a gel in a pre-determined or programmable manner, then reverting to a sol state. Such sol-to-gel-to-sol systems can be driven by changes in pH, for example by using enzymatic methods that result in well controlled and predictable rates of pH change.[19-22] Alternatively, such sol-to-gel-to-sol systems can be driven by the addition of a fuel that converts a non-gelator to a gelator; when the fuel runs out, the gelator reverts to a non-gelator and hence the gel state only persists for as long as the fuel is available.[3, 23-26] Other examples of transient or dynamic systems include gel-to-sol-to-gel systems[17, 27] and gel-to-gel-to-gel[28] systems where changes in (for example) pH can result in the underlying network underpinning the gel changing.

Despite the number of examples of these transient and dynamic gels systems whereby changes in state occur, there is perhaps a surprising lack of rheological data showing the

properties of these systems (although there are of course many examples where more traditional sol-to-gel transitions have been examined). In some cases, photographs of upturned vials are provided as the only 'proof' of gel states.[29, 30]

Where rheological data are provided, these typically do not involve time-dependent measurements. For instance, these can be snapshots at some point during the process[24, 31] where a frequency sweep has been measured whilst the system was evolving, or show that some examples are perhaps not true gels on the basis of the storage modulus (G′) and loss modulus (G″) measured,[8] or for only G′ to be provided.[26, 27, 32] However, rheology should be a useful means of understanding the phase changes that occur during these sol-to-gel and gel-to-sol transitions over time.

We have previously found that using time sweep rheology can be an effective tool to monitor phase changes, but these are not always clear. For example, for a sol-to-gel-to-sol transition, we found that both G′ and G″ increased with time and then decreased again, with the overall trend agreeing with the visual observation as to when an invertible gel was formed.[16] However, during this entire process G′ remains greater than G″ with tan δ (defined as G″/G′) <0.15 throughout the sol-to-gel-to-sol transition.[16, 17, 33] Hence, from time sweep rheology, this could be defined as a gel throughout the transitions. Similar observations have been made elsewhere for gels that change to a sol state on irradiation.[34] Here, we show that useful insights into such transitions can be found by carrying out time sweep rheology at different frequencies and strains. This not only allows to correlate visual observations of the systems, but also enables to control final properties of the materials.

2.3 Results and Discussion

To exemplify the point, we chose a system we have described previously[17] whereby the gelator **1ThNapFF** (Figure 2.1a) is initially dissolved in DMSO at a concentration of 10 mg/mL. On addition of water such that the concentration of **1ThNapFF** is 2 mg/mL (DMSO-water solvent ratio is 20:80), a gel is formed due to the change in the properties of the solvent. Using this system, we can construct a gel-to-sol-to-gel process by incorporating urease (0.2 mg/mL), urea (0.01 M) and 100 μL of methyl formate. Within the first 20 minutes, the pH increases from the initial value of 4.43 to 7.52 driven by the conversion of urea to ammonia by urease.[35] Since **1ThNapFF** forms wormlike micelles at high pH, a sol phase transition from the initially formed gel at low pH occurs.[17] However, the hydrolysis of methyl formate becomes dominant at high pH, leading to a gradual pH decrease. Therefore, a pH-triggered gel is then formed once the pH falls below the apparent pK_a of the gelator (~6.3). After

regelation, the system reaches a final pH of 5.62. Hence overall we observe gel-to-sol-to-gel transitions (Figure 2.1 and Figure 2.2a shows photographs at different time points exemplifying this process).

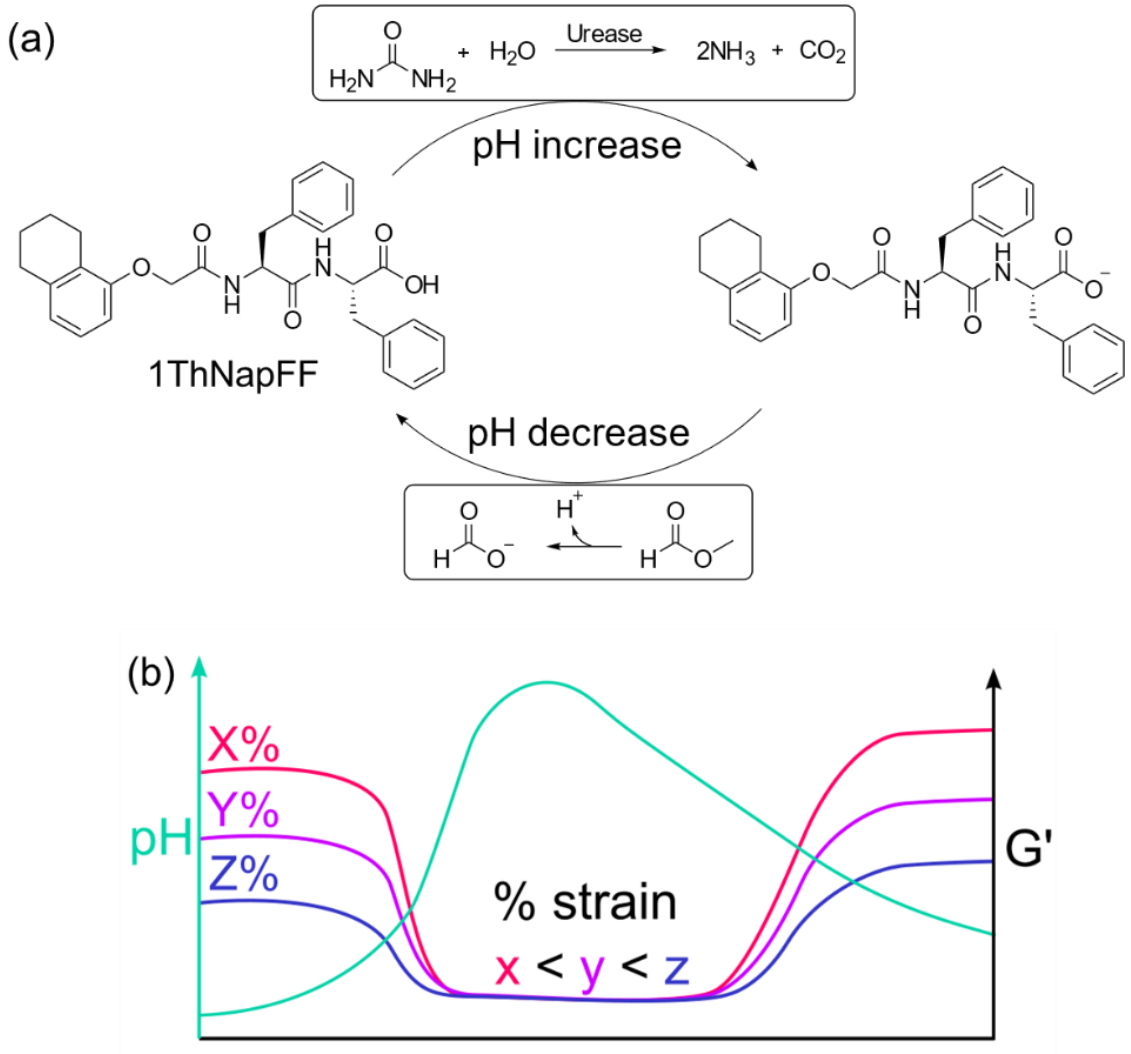

Figure 2.1. (a) Chemical structure of the gelator **1ThNapFF** used in the study. This compound undergoes deprotonation in presence of urea and urease due to production of ammonia. Base-catalysed hydrolysis of methyl formate reduces the pH and regenerates the structure of **1ThNapFF**. (b) Cartoon representing the effect of variation of strain on the G′ profile of a dynamic system undergoing gel-to-sol-to-gel transition. The final value of G′ decreases as the applied strain increases.

To monitor the gelation with time, rheological data are collected at a set frequency and strain. Typically, the storage and loss moduli should be frequency independent for a gel. However, in the sol phase there will likely be a strong frequency dependence. Hence, collection data for the same system at different values of frequency at a set strain would be expected to result in differences in the sol phase especially. The strain used would typically be low, since

the gels formed by such low molecular weight systems break at low strain; thus, to ensure data is within the linear viscoelastic region (LVE), one would typically use a value of <1 %. Rheological data for stable gels at low pH (i.e., formed using a solvent-switch only, with no urease, urea or methyl formate added to change the pH) show that the LVE region for the initial gel extends to 12.5 % (Figure 2.2b and Figure 2.2c).

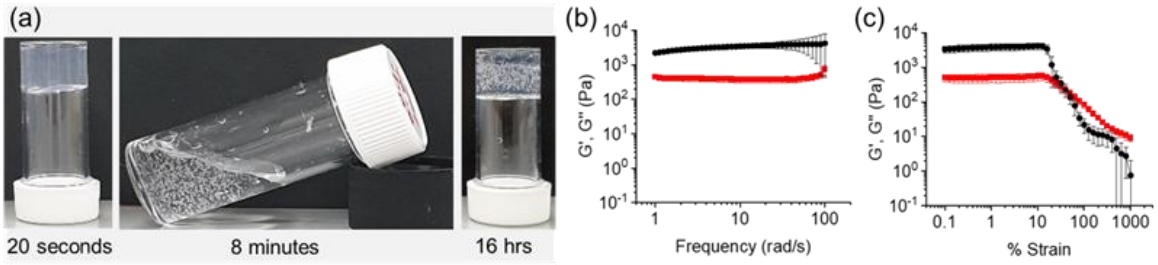

Figure 2.2. (a) Photograph of the gel-to-sol-to-gel transition brought about by the sequential increase and de-crease in pH. Note that bubbles appear during the phase transitions which can be seen in the sol and final gel state. Here, initial concentration of [**1ThNapFF**] = 2 mg/mL, [urea] = 0.01 M, [urease] = 0.2 mg/mL and volume of methyl formate is 100 μL. The black data represent G′ and the red data represent G″; (b) Frequency sweep for a stable gel formed at low pH; (c) Strain sweep for a stable gel formed at low pH. For both (b) and (c), no enzyme, urea or methyl formate were added and hence the solvent-triggered gel remains stable.

The time sweeps were collected at a value of 0.5% strain, while varying the frequency values, as shown in Figure 2.3 (the data are also shown with a linear x-axis scale in Figure 2.4). Overlaid are the pH data. By inspection of the time sweeps, initially there is a clear gel phase with G′> G″. As the pH reaches around 6, the pK_a of the terminal carboxylic acid is reached, resulting in sufficient deprotonation to lead formation of micellar structures. When these measurements are carried out at low frequency (1 rad/s, Figure 2.3a), a decrease in G′ and G″ is observed during this transition, but G′ dominates over G″ throughout and G′ never becomes less than 20 Pa. As the pH decreases once again, a two-stage increase in both G′ and G″ can be seen, which is not uncommon for these kinds of systems. Even though after 100 mins G′ is greater than G″, the system is still evolving which is evident from the further increase of rheological moduli with time. Hence, we performed the time sweeps for a longer time to allow the system to reach an equilibrium state where the values of G′ and G″ tend to reach a plateau. This was generally observed after almost 12 hours (Figure 2.3, Figure 2.4).

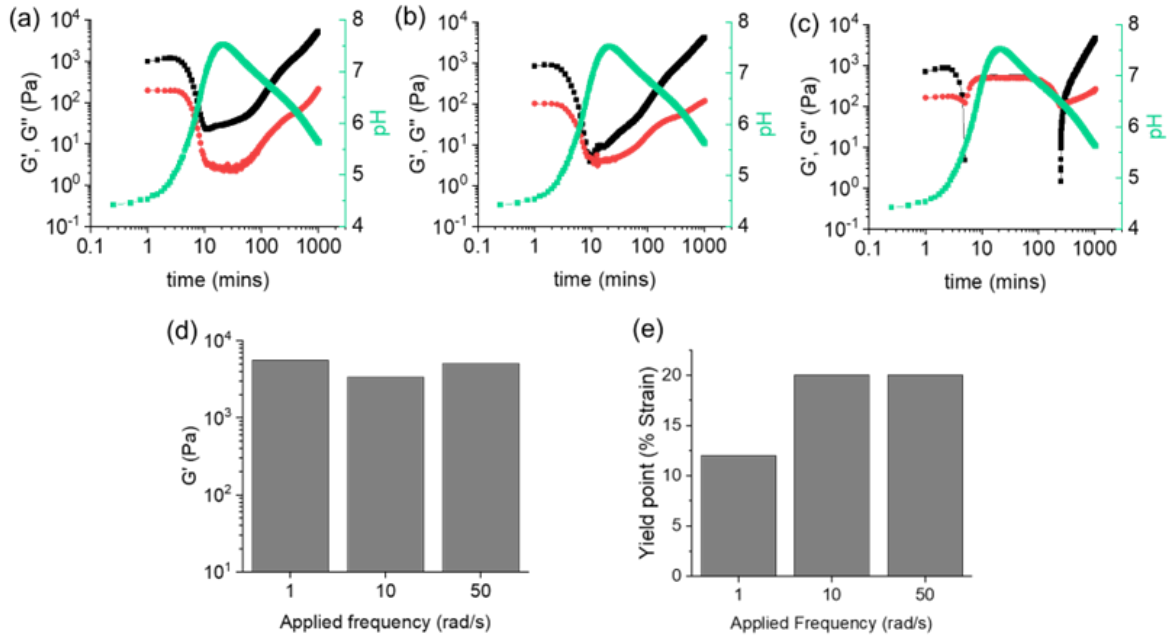

Figure 2.3. Variation of G′ (black), G″ (red), and pH (green) with time for **1ThNapFF** in presence of urea- urease reaction and methyl formate at (a) 1 rad/s, (b) 10 rad/s and (c) 50 rad/s. Throughout all measurements, the strain value was fixed at 0.5%. Comparisons of (d) initial G′ and (e) yield points of the three systems (considered as the strain value at which the gel starts to break and the G′ starts to decrease). For (d), the values of G′ at 0.5% strain from the strain sweeps are considered (see Figure 2.7). In all cases, initial concentration of [**1ThNapFF**] = 2 mg/mL, [urea] = 0.01 M, [urease] = 0.2 mg/mL and volume of methyl formate is 100 µL. Note that the pH and rheology measurements were performed with two different vials under identical conditions. The data were then compared to investigate the variation of rheological properties to that of the changes of pH with time.

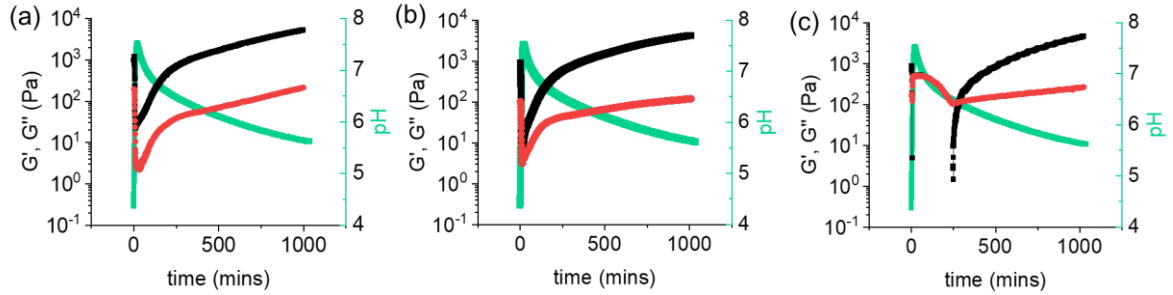

Figure 2.4. Variation of G′ (black), G″ (red), and pH (green) with time for **1ThNapFF** in presence of urea- urease reaction and methyl formate at (a) 1 rad/s, (b) 10 rad/s and (c) 50 rad/s. Throughout all measurements, the strain value was fixed at 0.5%. In all cases, initial concentration of [**1ThNapFF**] = 2 mg/mL, [urea] = 0.01 M, [urease] = 0.2 mg/mL and volume of methyl formate is 100 µL. Figure 2.4 represents Figure 2.3 above on a linear x-scale.

At a frequency of 10 rad/s (Figure 2.3b), G′ becomes approximately equal to G″ for a short period of time during pH increase, before regelation occurs in a similar two-stage increase of both rheological moduli. At 50 rad/s, a very different profile is seen (Figure 2.3c), whereby G′ quickly becomes less than G″ and drops below 0 Pa for a significant time period. Once the pH starts to decrease, G′ dominates again over G″. However, in this case, regelation occurs in a single stage increase of the rheological moduli. By time sweep rheology, different behaviours of G′ and G″ were noticed after the pH increase. We assign the overall transition to a gel-to-sol-to-gel. If we do not include methyl formate in the system such that there is a pH increase, but no further decrease, a solution phase is formed as confirmed visually and by rheology (Figure 2.5a). When methyl formate is also included, after 20 minutes the pH is above 7 and we would expect a solution phase to be formed. However, frequency sweeps of the intermediate materials after 20 minutes (Figures 2.5b, 2.5d, 2.5e and 2.5f) show complex behaviour with a low frequency region where G′ is greater than G″ (the data at higher frequency cannot be collected due to issues with the samples being below the minimum elastic torque for this measurement system). This could imply that a true solution phase is not formed and perhaps here a gel-to-gel-to-gel assignment would be more appropriate. However, we highlight that the system is evolving over the course of this experiment and an immediate repeat measurement shows different data (Figure 2.5c); this evolving over the course of the frequency sweep makes the assignment difficult.

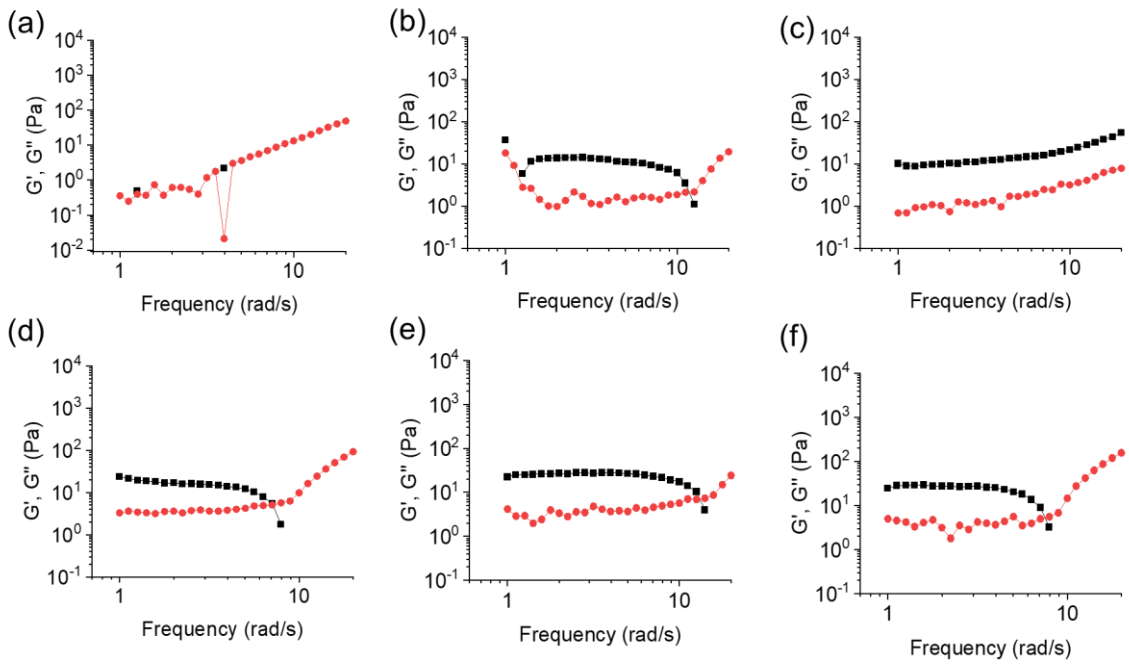

Figure 2.5. (a) Frequency sweep of the **1ThNapFF** system with no methyl formate after 45 minutes where the pH is 8.98. Visually, this system behaves as a liquid, and this is confirmed by the frequency sweep. (b) Frequency sweep of the **1ThNapFF** system obtained involving the enzymatic reaction in presence of methyl formate after initial gel-to-sol transition. The measurements were performed after running time sweeps for 20 mins at 0.5% strain at 10 rad/s. (c) Frequency sweep collected immediately after the data collection for (b) showing that the system has evolved over the timescale of the first frequency sweep. (d) Frequency sweep carried out after the system has evolved for 20 minutes at 0.5% strain and angular frequency of 1 rad/s; (e) Frequency sweep carried out after the system has evolved for 20 minutes at 0.5% strain and angular frequency of 10 rad/s; (f) Frequency sweep carried out after the system has evolved for 20 minutes at 0.5% strain and angular frequency of 50 rad/s. In all cases, initial concentration of [**1ThNapFF**] = 2 mg/mL, [urea] = 0.01 M, [urease] = 0.2 mg/mL. For (b)-(f), the volume of methyl formate is 100 µL. The black symbols represent G′, the red symbols G″. Data obtained in (b) and (c) was performed on the same sample, while (a), (d)-(f) were recorded on new samples each time.

Hence, it follows that we are able to pull out more clearly the phase behaviour by carrying out the time sweeps at different frequencies. For instance, more liquid-like response can be seen at higher frequencies. These results resemble the findings by Setz *et al*. who showed that for materials with liquid-like properties, increasing frequencies results in disappearance of the elastic component (G′).[36] In all cases, a gel was obtained at the end, further confirmed from the frequency independence of G′ for all materials (Figure 2.6). Interestingly, the final values of G′ and G″ were considerably higher than for the initially formed gels. We

previously suggested that the increase of stiffness in the final gel is due to annealing, which results in conversion of the initially formed kinetically trapped gel to a more homogeneous gel by establishing an optimal balance of the physical interactions between the molecules.[17] Further comparison of the final G′ (Figure 2.3d) shows very similar values, as would be expected considering we are in a gel phase at the end where these moduli should be frequency independent. However, collecting a strain sweep at the end of the time measurement shows some differences between the data collected on the gels, with the yield point (considered as the strain value at which the gel starts to break and the G′ starts to decrease) being affected by the frequency at which the time sweep was carried out (Figure 2.3e, Figure 2.7).

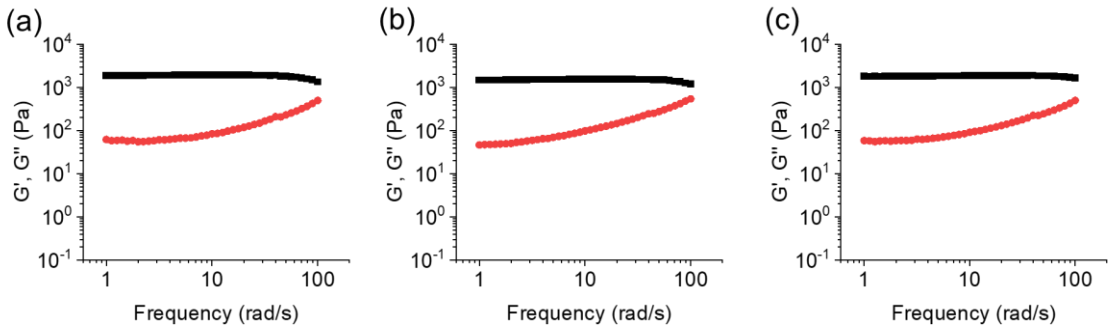

Figure 2.6. Frequency sweeps of the **1ThNapFF** system obtained involving the enzymatic reaction in presence of methyl formate. The gels are obtained after the time sweeps performed at 0.5% strain and angular frequency of (a) 1 rad/s, (b) 10 rad/s and (c) 50 rad/s. In all cases, initial concentration of [**1ThNapFF**] = 2 mg/mL, [urea] = 0.01 M, [urease] = 0.2 mg/mL and volume of methyl formate is 100 µL. The black symbols represent G′, the red symbols G″.

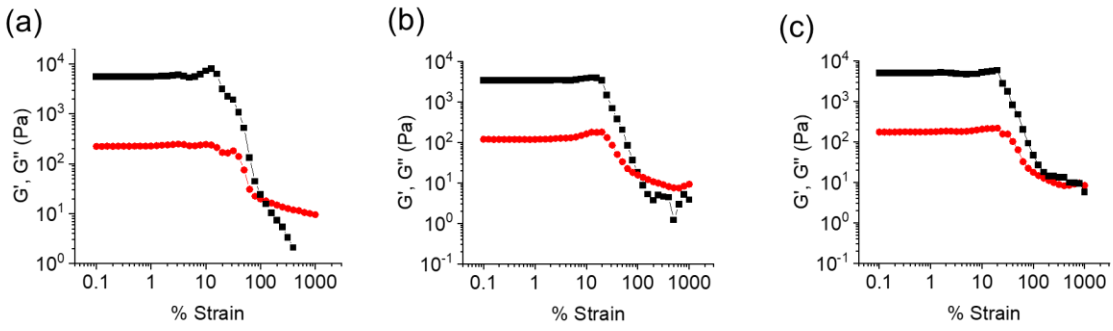

Figure 2.7. Strain sweeps of the hydrogels of **1ThNapFF** obtained involving the enzymatic reaction in presence of methyl formate. The gels are obtained after the time sweeps performed at 0.5% strain and angular frequency of (a) 1 rad/s, (b) 10 rad/s and (c) 50 rad/s. In all cases, initial concentration of [**1ThNapFF**] = 2 mg/mL, [urea] = 0.01 M, [urease] = 0.2 mg/mL and volume of methyl formate is 100 µL. The black symbols represent G′, the red symbols G″.

Indeed, it appears that the gel collapses at a higher strain when higher frequency is applied during the measurement. This needs to be considered when reporting data and therefore simply collecting data on the final gel after a time sweep may not be representative of the quiescent system.

As the gels are not strain independent outside the LVE region, we would expect to observe a change in gelation behaviour when the data are collected at a set frequency with different strain values (schematically shown in Figure 2.1b). The time sweeps performed at a constant frequency of 10 rad/s and varying strain are shown in Figure 2.8 and Figure 2.9. At low strain values of 0.05% and 0.5% (Figure 2.8a and 2.3b), G′ and G″ are observed to decrease and briefly become equal as the pH increases. Then, regelation occurs in a two-stage process again when the pH decreases. Note here that due to the low response at 0.05% strain, low signal to noise ratio leads to the presence of noisy data around 10 to 100 minutes.

At a value of 5% strain (Figure 2.8b), we should observe little difference in behaviour as the value is still within the LVE (Figure 2.2c). As the pH increases, G′ and G″ both decreases, though G′ and G″ never cross prior to regelation. The final G′ is lower than that observed when the data were collected at 0.05% and 0.5% strain, indicating that higher perturbation of the system affects the final properties. Therefore, we investigated the effect of applying higher strain to the system. At 10% strain (Figure 2.8c), a similar profile to 5% strain is seen with no crossover in G′ and G″. This is to be expected since this value is still below the yield point. Nevertheless, slight differences in the regelation profile are observed. In particular, the final G′ value was around 50% less compared to the value when the data were collected at a strain of 5%.

Different profiles were observed when we applied strain during the time sweep at values outside of the LVE region of the initial gel (Figure 2.2c). When the strain was increased to 20%, the initial G′ appeared at a lower value than for the low strain data due to increased perturbation of the gel network (Figure 2.8d). Both G′ and G″ decrease during pH uptake and overlap for a short period of time. However, no crossover point between the rheological moduli was observed and G′ > G″ throughout the rest of the measurement. Compared to the other samples, the two-stage increase in G′ and G″ was not observed upon regelation, with a more linear uptake of the values. A similar profile is observed for 50% strain with a significantly lower value for the final G′. This suggests that a weaker gel is formed under such conditions (Figure 2.8e). At 100% strain, G′ briefly drops below 0 Pa after 30 minutes (Figure 2.8f). As the pH decreases, regelation is observed, though the final G′ and G″ occur

at lower values than the initial ones, differently from all other measurements. To further test the strain limit of this system, a time sweep was performed at 200% strain (Figure 2.8g). Although a similar profile to 100% strain was observed within the first 10 minutes, the final G′ and G″ were seen at very close values (tanδ = 0.53, Figure 2.10).

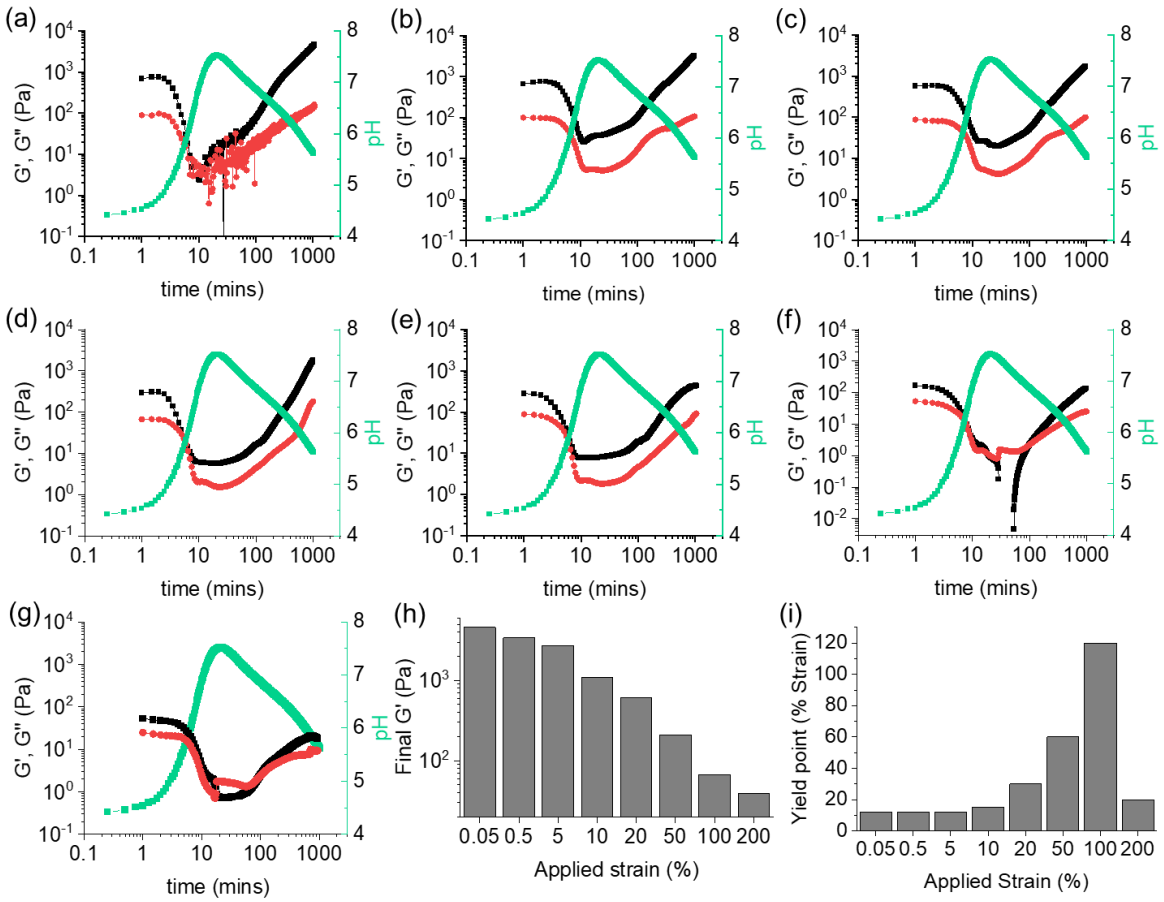

Figure 2.8. Variation of G′ (black), G″ (red), and pH (green) with time for **1ThNapFF** in presence of urea- urease reaction and methyl formate at strain values of (a) 0.05%, (b) 5%, (c) 10%, (d) 20%, (e) 50%, (f) 100% and (g) 200%. Throughout all measurements, the frequency value was fixed at 10 rad/s. Comparisons of (d) final G′ and (e) yield point of the systems. For (h), the values of G′ at 0.5% strain from the strain sweeps are considered. In all cases, initial concentration of [**1ThNapFF**] = 2 mg/mL, [urea] = 0.01 M, [urease] = 0.2 mg/mL and volume of methyl formate is 100 µL. Note that the pH and rheology measurements were performed with two different vials under identical conditions. The data were then compared to investigate the variation of rheological properties to that of the changes of pH with time.

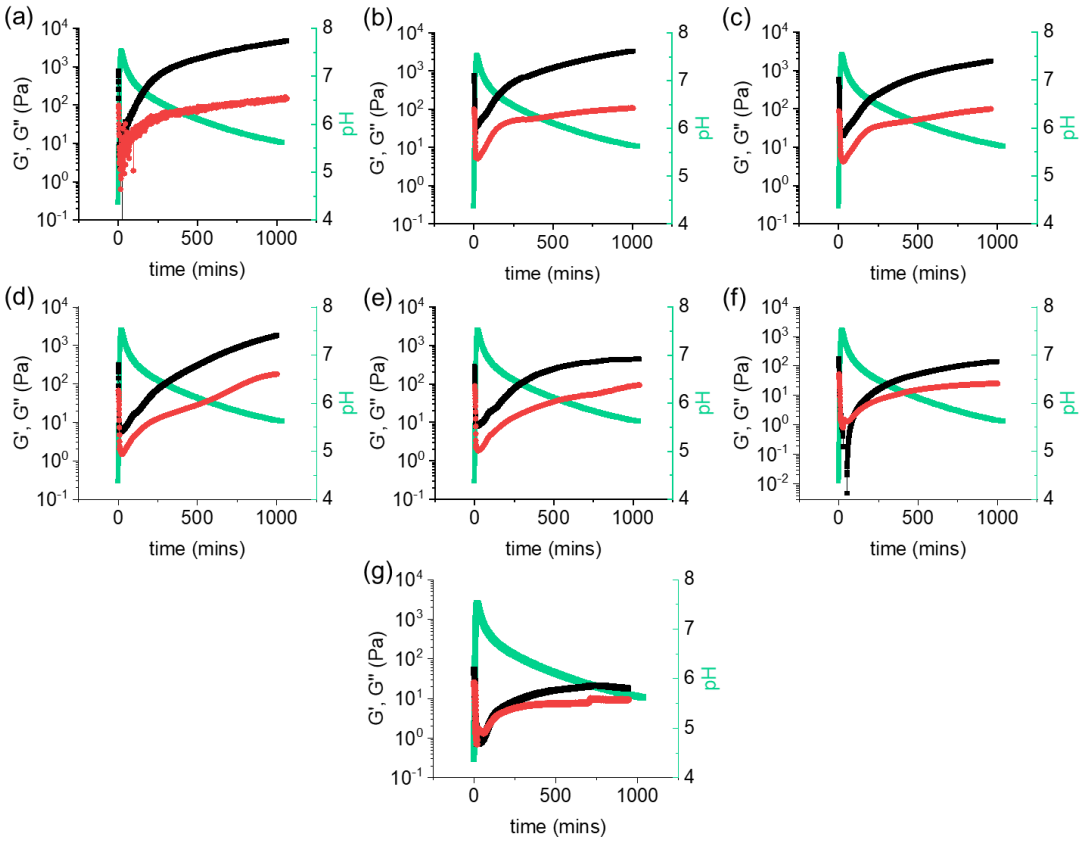

Figure 2.9. Variation of G′ (black), G″ (red), and pH (green) with time for **1ThNapFF** in presence of urea- urease reaction and methyl formate at strain values of (a) 0.05%, (b) 5%, (c) 10%, (d) 20%, (e) 50%, (f) 100% and (g) 200%. Throughout all measurements, the frequency value was fixed at 10 rad/s. In all cases, initial concentration of [**1ThNapFF**] = 2 mg/mL, [urea] = 0.01 M, [urease] = 0.2 mg/mL and volume of methyl formate is 100 µL. Figure 2.9 represents Figure 2.8 above on a linear x-scale.

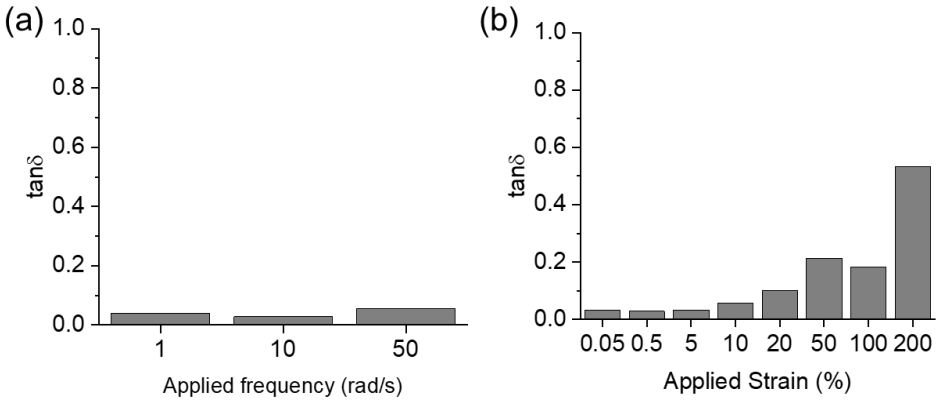

Figure 2.10. Bar graphs showing the final tanδ of **1ThNapFF** involving the enzymatic reaction in presence of methyl formate. The values were obtained from the last data point of the time sweeps performed at (a) 0.5% strain with varying frequency and (b) 10 rad/s frequency with varying strain values. In all cases, initial concentration of [**1ThNapFF**] = 2 mg/mL, [urea] = 0.01 M, [urease] = 0.2 mg/mL and volume of methyl formate is 100 µL.

Taken together, we again note that the behaviours of G′ and G″ absolutely depend on the applied strain during a gel-to-sol-to-gel transition. By conducting the time sweeps at high strain, one can pull out a crossover between the rheological moduli, even if the intermediate material is a sol for all strain values (Figure 2.11). The final materials obtained after the time sweeps were established to be gels from the frequency sweep (G′ > G″), although a slight frequency dependency of the G′ for the gels prepared outside the LVE region was noticed. (Figure 2.12). However, the final mechanical properties of the hydrogel are clearly influenced by applying different strain, with decreasing stiffness as the strain increases (Figure 2.8h). The applied strain is also found to affect the strain sweep behaviour of the gels, where a trend in the yield point is observed (Figure 2.8i, Figure 2.13). Thus, this needs to be further taken into consideration when characterizing these dynamic systems.

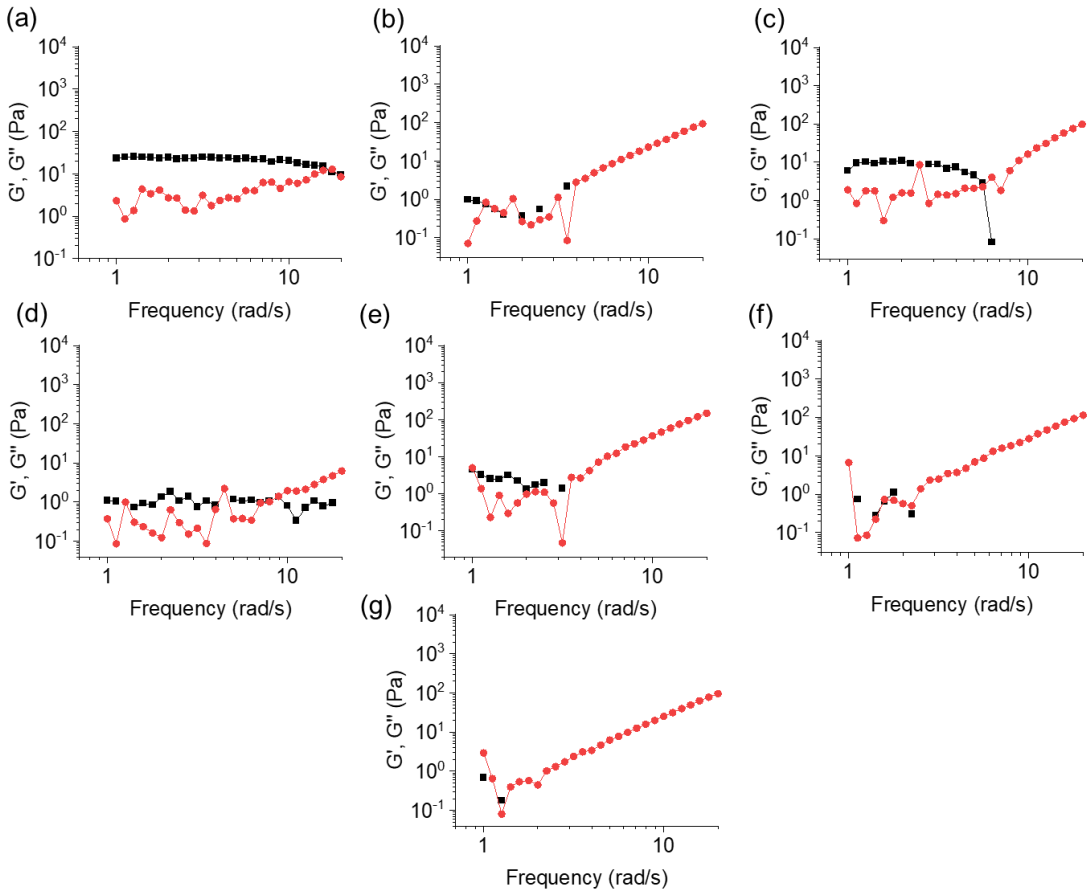

Figure 2.11. Frequency sweeps of the **1ThNapFF** system obtained involving the enzymatic reaction in presence of methyl formate after initial gel-to-sol transition. The measurements were performed after running time sweeps for 20 mins at an angular frequency of 10 rad/s and a strain of (a) 0.05%, (b) 5%, (c) 10%, (d) 20%, (e) 50%, (f) 100% and (g) 200%. In all cases, initial concentration of [**1ThNapFF**] = 2 mg/mL, [urea] = 0.01 M, [urease] = 0.2 mg/mL and volume of methyl formate is 100 µL. The black symbols represent G′, the red symbols G″.

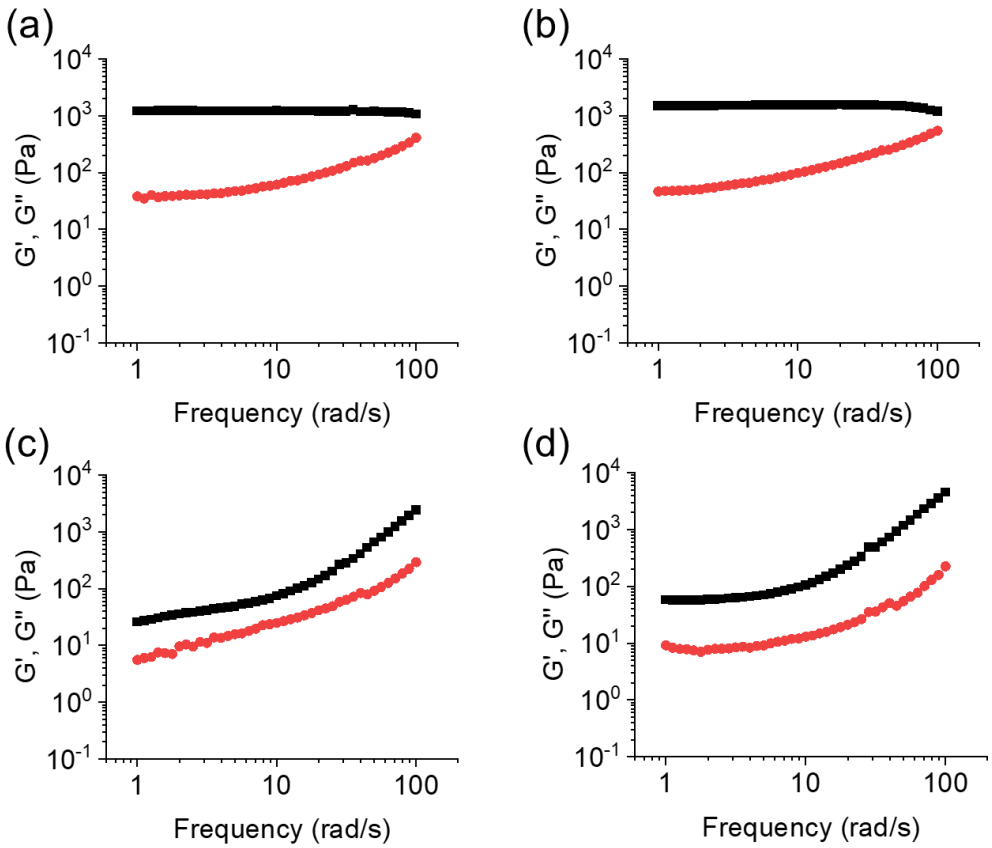

Figure 2.12. Frequency sweeps of the **1ThNapFF** system obtained involving the enzymatic reaction in presence of methyl formate. The gels are obtained after the time sweeps performed at an angular frequency of 10 rad/s and a strain of (a) 0.05%, (b) 0.5%, (c) 100%, (d) 200%. In all cases, initial concentration of [**1ThNapFF**] = 2 mg/mL, [urea] = 0.01 M, [urease] = 0.2 mg/mL and volume of methyl formate is 100 µL. The black symbols represent G′, the red symbols G″.

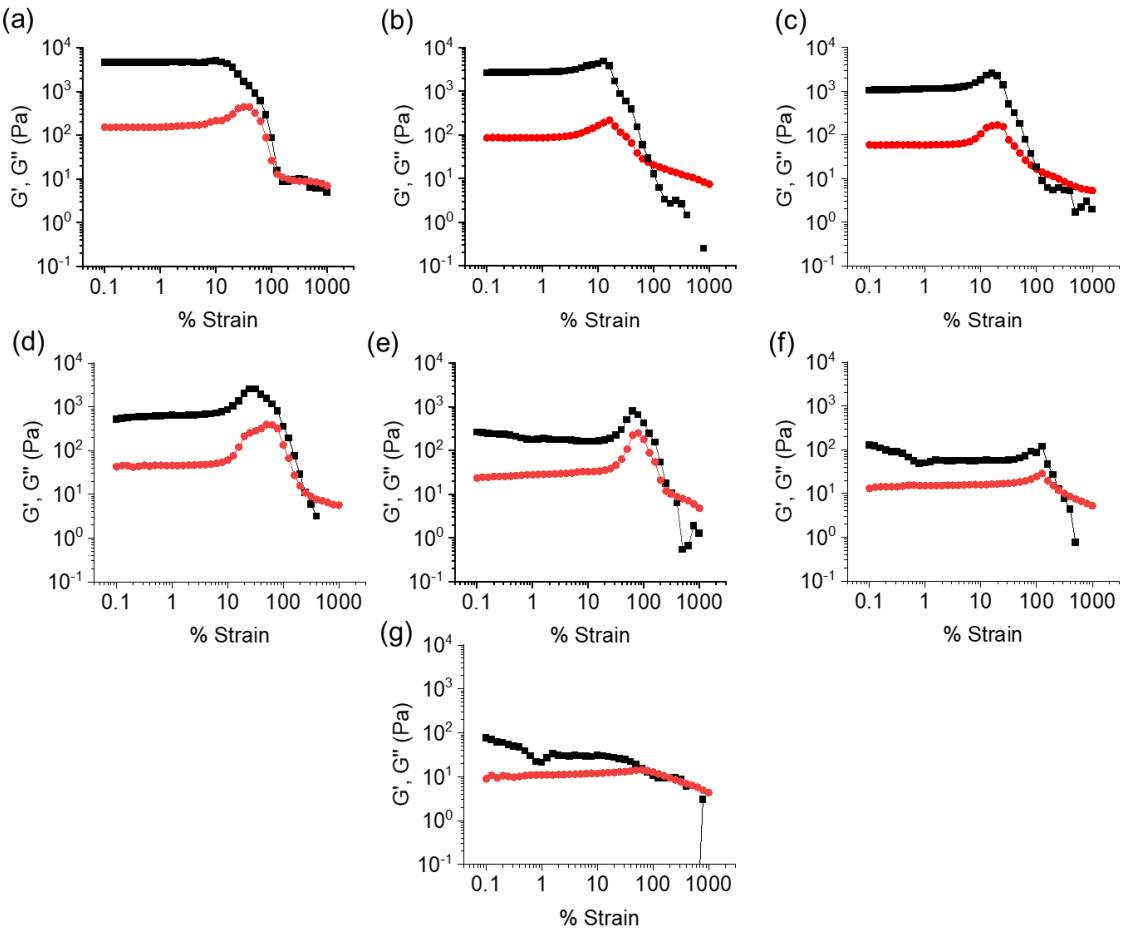

Figure 2.13. Strain sweeps of the hydrogels of **1ThNapFF** obtained involving the enzymatic reaction in presence of methyl formate. The gels are obtained after the time sweeps performed at an angular frequency of 10 rad/s and a strain of (a) 0.05%, (b) 5%, (c) 10%, (d) 20%, (e) 50%, (f) 100% and (g) 200%. In all cases, initial concentration of [**1ThNapFF**] = 2 mg/mL, [urea] = 0.01 M, [urease] = 0.2 mg/mL and volume of methyl formate is 100 μL. The black symbols represent G′, the red symbols G″.

2.4 Conclusions

Overall, we have shown here that systems that evolve between solution and gel states can be probed effectively using time sweep rheology. The data collected depend on the absolute frequency and strain at which the data are collected as gels and solutions have a different frequency dependence. Depending on the values at which the rheology is collected, it is therefore possible for the system to appear as if there is a gel phase present throughout (when the data are collected at low frequencies) with G′>G″ at all times, even though visual observation shows that a solution phase is present. Collecting data at higher frequencies more effectively pulls out the phase transitions with a crossover between G′ and G″. Collecting data at different strains shows that there can be effects on the mechanical properties even when the measurement is carried out at a strain within the initial LVE. Here,

the system evolves from a gel to a sol to a gel; as the gel starts to break apart, presumably the system′s response to strain is highly dependent on the time and hence phase present. Moreover, for such pH-driven dynamic systems the final material properties are typically controlled by varying the rate of pH change.[17] Here for the first time, we showed that the properties of the final gels can also be controlled by varying the applied rheological conditions under a fixed rate of pH change. Self-regulating dynamic reconfiguration of gel properties often leads to materials that cannot be prepared directly.[17, 37] In this endeavor, the insights provided in this work would not only be helpful to understand the self-regulating dynamic systems but also enable to prepare a wide variety of materials from a single starting gel using rheology.

2.5 Materials and Methods

2.5.1 Materials

The **1ThNapFF** gelator was synthesized as described previously.[38] Methyl formate (anhydrous, 99%) was purchased from Sigma Aldrich. Dimethyl sulfoxide (>= 99%) was purchased from Fischer Scientific. Urease (U4002-100KU, Jack Beans, 100,000 units/g solid) and urea (ultrapure 99%) were purchased from Alfa Aesar. Deionised water was employed in all the experiments.

2.5.2 Solution preparation

To prepare the stock solution of **1ThNapFF**, the gelator powder was dissolved by stirring in a quantity of dimethyl sulfoxide (DMSO) to reach a concentration of 10 mg/mL. Stock solutions of urea and urease were prepared in H_2O, at concentrations of 2 M and 0.253 mg/mL, respectively. For the urease stock solution, the concentration was determined by taking the mass of the enzyme powder (in mg) dissolved in a known volume of H_2O. Both urea and urease were highly soluble in water and hence did not require stirring.

2.5.3 Hydrogel preparation

1ThNapFF hydrogels were firstly prepared in absence of enzyme, urea and methyl formate. For these samples, 1.6 mL of H_2O were transferred to 0.4 mL of the gelator solution in DMSO. Hence, the final concentration of gelator was 2 mg/mL in a 20:80 ratio of DMSO and H_2O. The samples were left overnight prior to any measurements.

To induce the gel-to-sol-to-gel transitions, **1ThNapFF** gels were prepared in presence of urea, urease and methyl formate. For these gels, 400 µL of the gelator solution, 10 µL of urea and 100 µL of methyl formate were first mixed into a 7 mL Sterilin vial. 1.580 mL of

the urease solution was then added to the mixture in one aliquot and the system was left undisturbed for 16 hours. The solvent ratio of DMSO and H_2O was kept at 20:80 as for the stable hydrogels. Initial concentrations of the components were as follows: **1ThNapFF** = 2 mg/mL, urea = 0.01 M, urease = 0.2 mg/mL and volume of methyl formate was 100 µL.

To compare the properties of the final gel to the initially formed one, a gel sample was prepared with **1ThNapFF** and only urease enzyme. For this method, 1.6 mL of urease solution were pipetted in one aliquot to 0.4 mL gelator solution in DMSO. The system was left undisturbed overnight prior to measurements. Due to the absence of urea and methyl formate, the gel remained stable throughout.

2.5.4 Rheological measurements

All rheological experiments were carried out on an Anton Paar Physica MCR 301 rheometer at a constant temperature of 25 °C. For all measurements, a vane and cup geometry (ST10-4V-8.8/97.5-SN42404) was employed at a measuring distance of 2.1 mm.

Strain sweeps were performed over the range of 0.01% to 1000% strain at a frequency of 10 rad/s. Frequency sweeps were taken at 0.5% strain while increasing the frequency from 1 rad/s to 100 rad/s. Time sweeps were performed overnight with variable parameters for strain and frequency. The samples were prepared immediately before positioning the vial in the rheometer cup system. In the first set of measurements, the strain was kept constant at 0.5% and time sweeps were collected at frequency values of 1 rad/s, 10 rad/s and 50 rad/s. Then, time sweeps were performed while keeping the frequency constant at 10 rad/s and at strain values of 0.05%, 0.5%, 5%, 10%, 20%, 50%, 100%, 200%. Strain sweeps for the gels obtained after gel-to-sol-to-gel transitions under different mechanical conditions were conducted just after the time sweeps, without lifting the vane from the system. The angular frequency was kept at 10 rad/s for all strain sweeps, while the strain was increased from 0.01% to 1000%.

To confirm the nature of the materials obtained after the initial decrease of G′ and G″ during time sweeps, we performed frequency sweep experiments on the samples after 20 minutes of running the time sweeps without lifting the vane from the system. Throughout all frequency sweeps, the strain value was 0.5% and the frequency was ramped up from 1 rad/s to 100 rad/s.

2.5.5 pH measurements

pH measurements were performed using a HANNA FC200 pH probe with a 6 mm × 10 mm conical tip. The accuracy of the pH values was ±0.1. To monitor the pH change of the system with urea-urease and methyl formate, the reaction mixture was prepared as above (Section 2.5.2) immediately before measurement. The temperature was kept at 25 °C by using a circulating water bath.

2.6 References

1 Q. Wang, Z. Qi, M. Chen and D.-H. Qu, Out-of-equilibrium supramolecular self-assembling systems driven by chemical fuel, *Aggregate*, 2021, **2**, e110.

2 B. Rieß, R. K. Grötsch and J. Boekhoven, The Design of Dissipative Molecular Assemblies Driven by Chemical Reaction Cycles, *Chem*, 2020, **6**, 552-578.

3 Z. Leng, F. Peng and X. Hao, Chemical-Fuel-Driven Assembly in Macromolecular Science: Recent Advances and Challenges, *ChemPlusChem*, 2020, **85**, 1190-1199.

4 F. della Sala, S. Neri, S. Maiti, J. L. Y. Chen and L. J. Prins, Transient self-assembly of molecular nanostructures driven by chemical fuels, *Curr. Opin. Biotechnol.*, 2017, **46**, 27-33.

5 S. A. P. van Rossum, M. Tena-Solsona, J. H. van Esch, R. Eelkema and J. Boekhoven, Dissipative out-of-equilibrium assembly of man-made supramolecular materials, *Chem. Soc. Rev.*, 2017, **46**, 5519-5535.

6 S. P. Afrose, S. Bal, A. Chatterjee, K. Das and D. Das, Designed Negative Feedback from Transiently Formed Catalytic Nanostructures, *Angew. Chem. Int. Ed.*, 2019, **58**, 15783-15787.

7 S. Pal, A. Reja, S. Bal, B. Tikader and D. Das, Emergence of a Promiscuous Peroxidase Under Non-Equilibrium Conditions**, *Angew. Chem. Int. Ed.*, 2022, **61**, e202111857.

8 J. Boekhoven, W. E. Hendriksen, G. J. M. Koper, R. Eelkema and J. H. v. Esch, Transient assembly of active materials fueled by a chemical reaction, *Science*, 2015, **349**, 1075-1079.

9 G. Panzarasa, T. Sai, A. L. Torzynski, K. Smith-Mannschott and E. R. Dufresne, Supramolecular assembly by time-programmed acid autocatalysis, *Mol. Syst. Des. Eng.*, 2020, **5**, 445-448.

10 R. Chevigny, J. Schirmer, C. C. Piras, A. Johansson, E. Kalenius, D. K. Smith, M. Pettersson, E. D. Sitsanidis and M. Nissinen, Triggering a transient organo-gelation system in a chemically active solvent, *Chem. Commun.*, 2021, **57**, 10375-10378.

11 K. Nakamura, W. Tanaka, K. Sada, R. Kubota, T. Aoyama, K. Urayama and I. Hamachi, Phototriggered Spatially Controlled Out-of-Equilibrium Patterns of Peptide Nanofibers in a Self-Sorting Double Network Hydrogel, *J. Am. Chem. Soc.*, 2021, **143**, 19532-19541.

12 F. Schnitter, A. M. Bergmann, B. Winkeljann, J. Rodon Fores, O. Lieleg and J. Boekhoven, Synthesis and characterization of chemically fueled supramolecular materials driven by carbodiimide-based fuels, *Nat. Protoc.*, 2021, **16**, 3901-3932.

13 M. Kretschmer, B. Winkeljann, B. A. K. Kriebisch, J. Boekhoven and O. Lieleg, Viscoelastic behavior of chemically fueled supramolecular hydrogels under load and influence of reaction side products, *Commun. Mater.*, 2021, **2**, 97.

14 M. Tena-Solsona, B. Rieß, R. K. Grötsch, F. C. Löhrer, C. Wanzke, B. Käsdorf, A. R. Bausch, P. Müller-Buschbaum, O. Lieleg and J. Boekhoven, Non-equilibrium dissipative supramolecular materials with a tunable lifetime, *Nat. Commun.*, 2017, **8**, 15895.

15 M. Kumar, N. L. Ing, V. Narang, N. K. Wijerathne, A. I. Hochbaum and R. V. Ulijn, Amino-acid-encoded biocatalytic self-assembly enables the formation of transient conducting nanostructures, *Nat. Chem.*, 2018, **10**, 696-703.

16 S. Panja, C. Patterson and D. J. Adams, Temporally-Programmed Transient Supramolecular Gels, *Macromol. Rapid Commun.*, 2019, **40**, 1900251.

17 S. Panja, A. M. Fuentes-Caparrós, E. R. Cross, L. Cavalcanti and D. J. Adams, Annealing Supramolecular Gels by a Reaction Relay, *Chem. Mater.*, 2020, **32**, 5264-5271.

18 H. Wang, L. Liu, S. Bai, X. Guo, R. Eelkema, J. H. van Esch and Y. Wang, Transient supramolecular hydrogels formed by catalytic control over molecular self-assembly, *Soft Matter*, 2020, **16**, 9406-9409.

19 E. Jee, T. Bánsági Jr., A. F. Taylor and J. A. Pojman, Temporal Control of Gelation and Polymerization Fronts Driven by an Autocatalytic Enzyme Reaction, *Angew. Chem. Int. Ed.*, 2016, **55**, 2127-2131.

20 S. Panja and D. J. Adams, Urea-Urease Reaction in Controlling Properties of Supramolecular Hydrogels: Pros and Cons, *Chem. Eur. J.*, 2021, **27**, 8928-8939.

21 T. Heuser, E. Weyandt and A. Walther, Biocatalytic Feedback-Driven Temporal Programming of Self-Regulating Peptide Hydrogels, *Angew. Chem. Int. Ed.*, 2015, **54**, 13258-13262.

22 X. Fan and A. Walther, Autonomous Transient pH Flips Shaped by Layered Compartmentalization of Antagonistic Enzymatic Reactions, *Angew. Chem. Int. Ed.*, 2021, **60**, 3619-3624.

23 M. Kumar, D. Sementa, V. Narang, E. Riedo and R. V. Ulijn, Self-Assembly Propensity Dictates Lifetimes in Transient Naphthalimide–Dipeptide Nanofibers, *Chem. Eur. J.*, 2020, **26**, 8372-8376.

24 S. Debnath, S. Roy and R. V. Ulijn, Peptide nanofibers with dynamic instability through nonequilibrium biocatalytic assembly, *J. Am. Chem. Soc.*, 2013, **135**, 16789-16792.

25 S. Dhiman, K. Jalani and S. J. George, Redox-Mediated, Transient Supramolecular Charge-Transfer Gel and Ink, *ACS Appl. Mater. Interfaces*, 2020, **12**, 5259-5264.

26 W. A. Ogden and Z. Guan, Redox Chemical-Fueled Dissipative Self-Assembly of Active Materials, *ChemSystemsChem*, 2020, **2**, e1900030.

27 N. Singh, B. Lainer, G. J. M. Formon, S. De Piccoli and T. M. Hermans, Re-programming Hydrogel Properties Using a Fuel-Driven Reaction Cycle, *J. Am. Chem. Soc.*, 2020, **142**, 4083-4087.

28 S. Panja and D. J. Adams, Mimicking evolution of 'mini-homeostatic' modules in supramolecular systems, *Giant*, 2021, **5**, 100041.

29 M. Liu, C. N. Creemer, T. J. Reardon and J. R. Parquette, Light-driven dissipative self-assembly of a peptide hydrogel, *Chem. Commun*., 2021, **57**, 13776–13779**.**

30 C. A. Angulo-Pachón and J. F. Miravet, Sucrose-fueled, energy dissipative, transient formation of molecular hydrogels mediated by yeast activity, *Chem. Commun.*, 2016, **52**, 5398-5401.

31 S. Bal, K. Das, S. Ahmed and D. Das, Chemically Fueled Dissipative Self-Assembly that Exploits Cooperative Catalysis, *Angew. Chem. Int. Ed.*, 2019, **58**, 244-247.

32 J. P. Wojciechowski, A. D. Martin and P. Thordarson, Kinetically Controlled Lifetimes in Redox-Responsive Transient Supramolecular Hydrogels, *J. Am. Chem. Soc.*, 2018, **140**, 2869-2874.

33 S. Panja, B. Dietrich and D. J. Adams, Chemically Fuelled Self-Regulating Gel-to-Gel Transition, *ChemSystemsChem*, 2020, **2**, e1900038.

34 F. A. Larik, L. L. Fillbrook, S. S. Nurttila, A. D. Martin, R. P. Kuchel, K. Al Taief, M. Bhadbhade, J. E. Beves and P. Thordarson, Ultra-Low Molecular Weight Photoswitchable Hydrogelators, *Angew. Chem. Int. Ed.*, 2021, **60**, 6764-6770.

35 G. Hu, J. A. Pojman, S. K. Scott, M. M. Wrobel and A. F. Taylor, Base-Catalyzed Feedback in the Urea−Urease Reaction, *J. Phys. Chem. B*, 2010, **114**, 14059-14063.

36 L. F. G. Setz, A. C. Silva, S. C. Santos, S. R. H. Mello-Castanho and M. R. Morelli, A viscoelastic approach from α-Al_2O_3 suspensions with high solids content, *J. Eur. Ceram. Soc.*, 2013, **33**, 3211-3219.

37 N. Singh, A. Lopez-Acosta, G. J. M. Formon and T. M. Hermans, Chemically Fueled Self-Sorted Hydrogels, *J. Am. Chem. Soc.*, 2022, **144**, 410-415.

38 S. Panja, B. Dietrich, A. Trabold, A. Zydel, A. Qadir and D. J. Adams, Varying the hydrophobic spacer to influence multicomponent gelation, *Chem. Commun.*, 2021, **57**, 7898-7901.

Chapter 3. Forging Out-of-Equilibrium Supramolecular Gels

This Chapter is published as the following publication:

"Forging Out-of-Equilibrium Supramolecular Gels"

S. Bianco, F. Hallam Stewart, S. Panja, A. Zyar, E. Bowley, M. Bek, R. Kádár, A. Terry, R. Appio, T. S. Plivelic, M. Maguire, H. Poptani, M. Marcello, R. R. Sonani, E. H. Egelman and D. J. Adams, *Nature Synthesis*, 2024, **3**, 1481 – 1489. https://doi.org/10.1038/s44160-024-00623-4.

Author contributions

The author contributions are as follows: Conceptualization: D.J.A., S.B. and S.P. Methodology: S.B., F.H.S., E.B., M.B., R.K., A.T., R.A., T.S.P. and D.J.A. Validation: S.B., F.H.S. and E.B. Formal analysis: S.B., F.H.S., M.B. and R.K. Investigation: S.B., F.H.S., A.Z., E.B., M.B., R.K., M. Marcello, R.R.S., E.H.E. and D.J.A. Resources: S.B., M.B., R.K., A.T., R.A., T.S.P., M. Maguire, H.P., M. Marcello, R.R.S., E.H.E. and D.J.A. Data curation: S.B., F.H.S. and R.K. Writing—original draft: S.B., F.H.S. and D.J.A. Writing—review and editing: all. Visualization: S.B., F.H.S. and R.K. Supervision: D.J.A. Project administration: D.J.A. Funding acquisition: D.J.A.

The manuscript has been included in this thesis as published. The molecule used in this chapter was synthesised by Dr. Qingwen Guan (University of Glasgow). Rheological experiments have been collected by Fin Hallam Stewart (University of Glasgow) and Simona Bianco. Rheo-PLI-SAXS data was collected by Simona Bianco with the help of Emma Bowley (University of Glasgow) and the SAXS data was analysed by Simona Bianco. The Rheo-PLI-SAXS data was processed and visualised by Prof. Roland Kádár and Dr. Marko Bek (Chalmers University). Cryo-EM data was performed and processed by Dr. Ravi R. Sonani and Prof. Edward H. Egelman (University of Virginia). Acknowledgements have been provided in the Figure captions where necessary. The rest of the presented data has been collected, visualised and analysed by Simona Bianco.

3. Forging Out-of-Equilibrium Supramolecular Gels

Simona Bianco,[a] Fin Hallam Stewart,[a] Santanu Panja,[a] Asra Zyar,[a] Emma Bowley,[a] Marko Bek,[b] Roland Kádár,[b,c] Ann Terry,[c] Roberto Appio,[c] Tomás S. Plivelic,[c] Mahon Maguire,[d] Harish Poptani,[d] Marco Marcello,[e] Ravi R. Sonani,[f] Edward H. Egelman[f] and Dave J. Adams[a,*]

[a] School of Chemistry, University of Glasgow, Glasgow, G12 8QQ, UK

[b] Chalmers University of Technology, Department of Industrial and Materials Science, Göteborg, 41296, Sweden

[c] MAX IV Laboratory, Lund University, Lund, 22484, Sweden

[d] Centre for Preclinical Imaging, Department of Molecular and Clinical Cancer Medicine, University of Liverpool, Liverpool, L69 3BX, UK

[e] Centre for Cell Imaging, University of Liverpool, Liverpool, L69 3BX, UK

[f] Department of Biochemistry and Molecular Genetics, University of Virginia, Charlottesville, VA 22903, USA

3.1 Abstract

The design of supramolecular hydrogels comprising aligned domains is important for the fabrication of biomimetic materials and applications in optoelectronics. One way to access such materials is by the self-assembly of small molecules into long fibres, which can be aligned using an external stimulus. Out-of-equilibrium supramolecular gels can also be designed, where pre-programmed changes of state can be induced by the addition of chemical fuels. Here we exploit these dynamic properties to form materials with aligned domains through a 'forging′ approach: an external force is used to rearrange the underlying network from random to aligned fibres as the system undergoes a pre-programmed gel-to-sol-to-gel transition. We show that we can predictably organize the supramolecular fibres, leading to controllable formation of materials with aligned domains through a high degree of temporal control.

3.2 Introduction

Transient, dynamic, and dissipative supramolecular systems have recently gained significant interest.[1–9] In such systems, supramolecular structures form and change in a pre-programmed manner, controlled by external stimuli such as chemical or light triggers, and typically result

in changes in molecular structure.[10–12] These transient and dynamic systems have been investigated in the bulk, as well as within droplets.[13,14] The processes occurring in these systems are often comparable or analogous to those found within cells, especially when confined within droplets. For example, van Esch's group have shown how a gel with a pre-programmed lifetime can be formed by the addition of a chemical fuel.[15] Addition of the fuel results in a chemical reaction, leading to the formation of a low molecular weight gelator, a molecule that self-assembles into supramolecular fibers to immobilize the solvent. Once the fuel has been used up, a second chemical reaction dominates, leading to the molecule being converted back to the starting compound which can no longer act as a gelator. Overall, this process leads to a sol-to-gel-to-sol transition with controllable gel lifetimes. There are many examples now of similar processes resulting in changes of state based on a range of different reactions, as well as the use of light or electrochemical stimuli to modify molecular structure and hence alter the aggregation type.[16–28]

However, almost all the reported systems operate within a static environment; external conditions are typically kept constant whilst the chemical processes are ongoing. There is no reason why this needs to be the case. External forces could be applied to manipulate these systems as they are evolving chemically, and it is possible to imagine how the supramolecular structures formed at different times could be affected by an external force to a greater or lesser extent. In particular, mechanical forces can be used as directional stimuli to impart anisotropy in supramolecular gels,[29–32] and shaking has been used to mix components and lead to changes in dynamic systems in a closed system.[33] Long-range alignment is often found within biological systems and the design of soft materials comprising of aligned fibrils is attractive for tissue engineering applications.[34] For this purpose, extrusion techniques have been used to achieve aligned nanomaterials,[32,35] and xerogels containing aligned fibers have been formed under shear.[36] It is worth noting that a range of forces have been used to affect supramolecular systems including ultrasound,[37,38] sound waves,[39–41] and magnetic fields.[42–47]

We have previously described systems undergoing pre-programmed gel-to-sol-to-gel transitions by incorporating two competing pH triggers, resulting in a pH increase and subsequent decrease to anneal a supramolecular gel.[48,49] Following initial gelation at low pH, a conversion to a free-flowing micellar state is achieved at high pH, before a gel is reformed as the pH gradually decreases. Critically, the final gel exhibits improved mechanical properties underpinned by a change in the self-assembled structures driven by the pH cycle.

Here, we describe what we call a "forging" approach, inspired by how blacksmiths work heated metal into desired shapes. We report supramolecular systems which change with time in a pre-programmed manner whilst simultaneously an external force is applied; this contrasts with previous examples where the system is quiescent (Figure 3.1). Due to the pre-programmable nature of the system, the force can be applied with a high level of temporal control. We show how the application of the force results in changes to the mesoscale organization of the supramolecular structures present, leading to the formation of aligned fibrillar domains while also changing the mechanical properties of the resulting gel. We further show how anisotropy in these systems can be achieved non-invasively by evolution of these materials within a strong magnetic field.

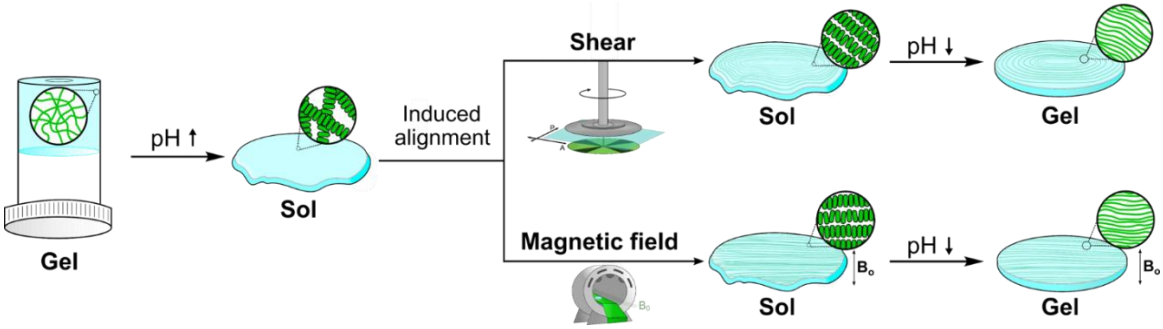

Figure 3.1. Cartoon of the work described in this paper: alignment is induced in a system undergoing a chemically triggered gel-to-sol-to-gel cycle by applying external invasive (shear) and non-invasive (magnetic field) stimuli to impart changes in the organisation of the self-assembled fibres. Cartoon prepared by Simona Bianco and Fin Hallam Stewart, University of Glasgow.

3.3 Results and Discussion

We focus on a transient gel-to-sol-gel system. L,D-2NapFF (Figure 3.2a) is an effective low molecular weight gelator.[50] On dilution of a high concentration solution of L,D-2NapFF in DMSO with water to give a final water:DMSO ratio of 90:10, a gel is formed at a final concentration of L,D-2NapFF of 5 mg/mL at a pH of 4.0. At this point, the gels are formed by spherulitic domains of supramolecular fibers that jam together.[48] Such solvent-triggered gels are stable for extended periods of time. Small angle X-ray scattering (SAXS) shows that the structures underpinning the gel network are thin-walled nanotubes with a radius of 14.7 nm and a wall thickness of 3.4 nm (Figure 3.3, Table 3.1).

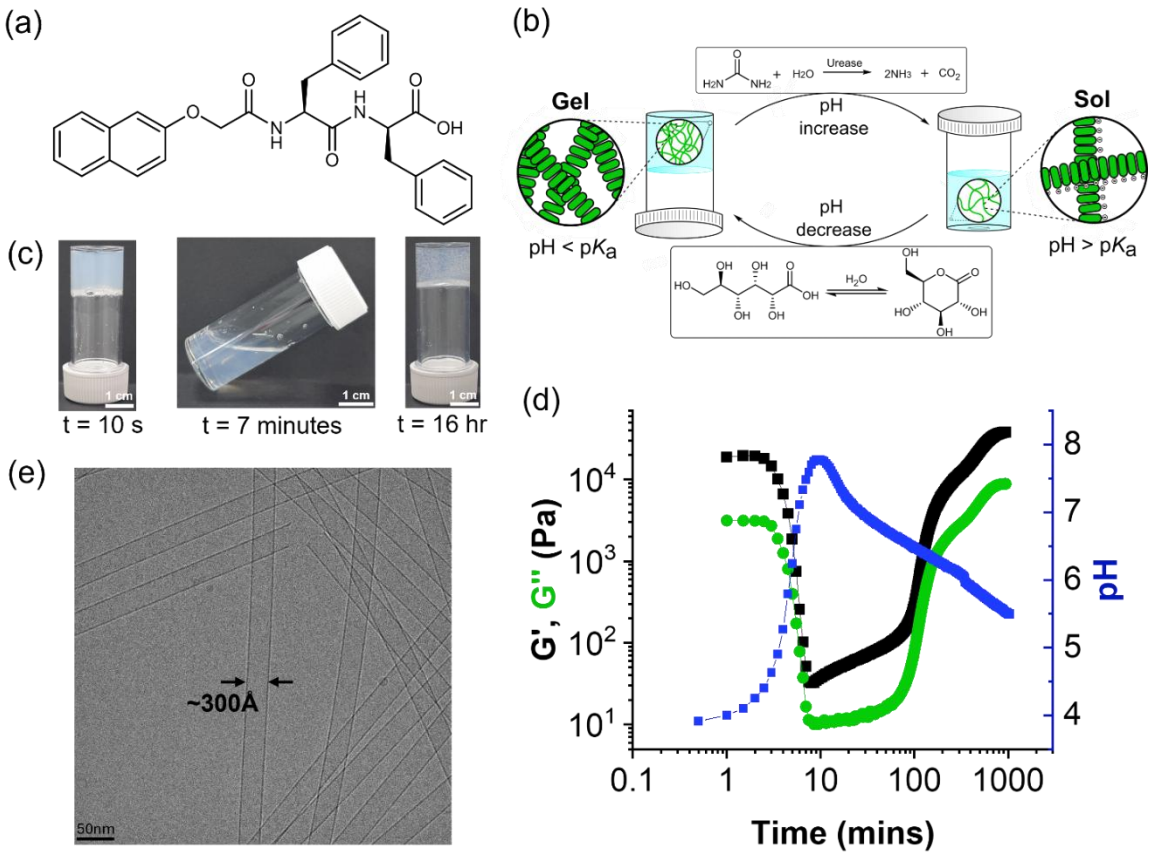

Figure 3.2. (a) Chemical structure of L,D-2NapFF; (b) Cartoon of the gel-to-sol-to-gel process; (c) Photographs of the system at 10 seconds, 7 minutes and 16 hours (scale bar represents 1 cm); (d) Change in rheology and pH with time for a system containing L,D-2NapFF in presence of urea, urease and GdL. Note, the colors of the lines and circles have been color-coded to match the colored axis titles; (e) cryo-EM of L,D-2NapFF (scale bar represents 50 nm). In (c)-(d), [L,D-2NapFF] = 5 mg/mL, [urea] = 0.04 M, [urease] = 0.4 mg/mL and [GdL] = 14.3 mg/mL. Cryo-EM data collected and analysed by Ravi R. Sonani and Edward H. Egelman, University of Virginia.

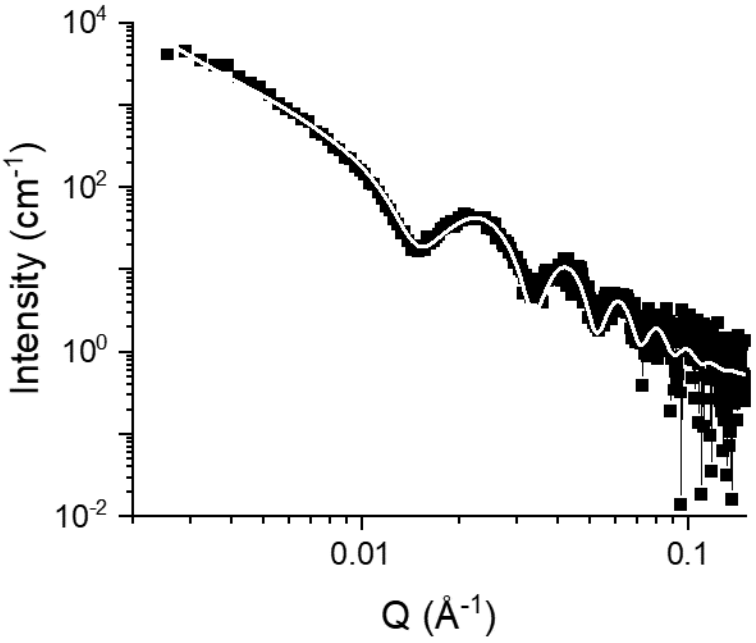

Figure 3.3. Small angle X-ray scattering data of a L,D-2NapFF gel in absence of urea and GdL. The gel was formed in presence of urease (0.4 mg/mL) to allow comparison with the evolving systems. The white line indicates model fit through Sasview (Table 3.1).

Table 3.1. Fitting parameters for SAXS data in Figure 3.3. The data was fit to a hollow cylinder model (A) combined with a power law model (B). Values that were manually added and fixed have been labelled with *.

	(L,D)-2NapFF static gel	
	Value	**Error**
Scale	1	
Background (cm^{-1})	0.5*	
A_scale	2.44×10^{-2}	6.63×10^{-4}
A_radius (Å)	147	0.66
A_thickness (Å)	34.2	1.04
A_length (Å)	1000*	/
B_scale	1.89×10^{-5}	4.74×10^{-6}
B_power	3.2	0.04
χ^2	7.03	

To induce a pre-programmed phase transition, dilution can be carried out with an aqueous solution of urease, urea and glucono-δ-lactone (GdL) instead of pure water. Initially, a solvent-triggered gel is formed at low pH (~4). As the pH increases driven by the production of ammonia through the reaction between urea and urease, the gel converts to a micellar solution of nanotubes due to the deprotonation of the terminal carboxylic acid.[51–53] At high pH, the nanotubes will be charged and hence direct interactions will be unlikely. When the pH reaches a sufficiently high value, the hydrolysis of GdL to gluconic acid becomes predominant, leading to a slow decrease in pH and regelation once the pH drops below the apparent pK_a of the gelator (~ 6.0).[50] Hence, overall we have a gel-to-sol-to-gel transition (Figure 3.2b), with the timescales of each stage being determined by the concentrations of urease, urea and GdL used. Whilst direct addition of acid and bases can be used to achieve such changes, irreproducible and inhomogeneous systems are often obtained in this way due to fast mixing.[54] Further, using a pre-programmable pH cycle allows highly reproducible temporal control over the phase changes.

This process can be followed by eye (Figure 3.2c) and by rheology (Figure 3.2d and Figure 3.4a). Initially, a gel is formed as shown by the storage modulus (G′) being an order of magnitude higher than the loss modulus (G″). As the pH increases, both G′ and G″ decrease, showing that a micellar solution is formed. This is further supported by the observation of a G′ and G″ cross-over when the data is collected with a frequency of 50 rad/s (Figure 3.4a), in line with our previous data.[55] Once the hydrolysis of GdL becomes more dominant and the pH decreases, gelation reoccurs, represented by an increase of both rheological moduli. As we have shown for related systems,[48] this can be thought of as a pH-induced “annealing″ process, which often results in improvement of the final mechanical properties of the material compared to the original system.

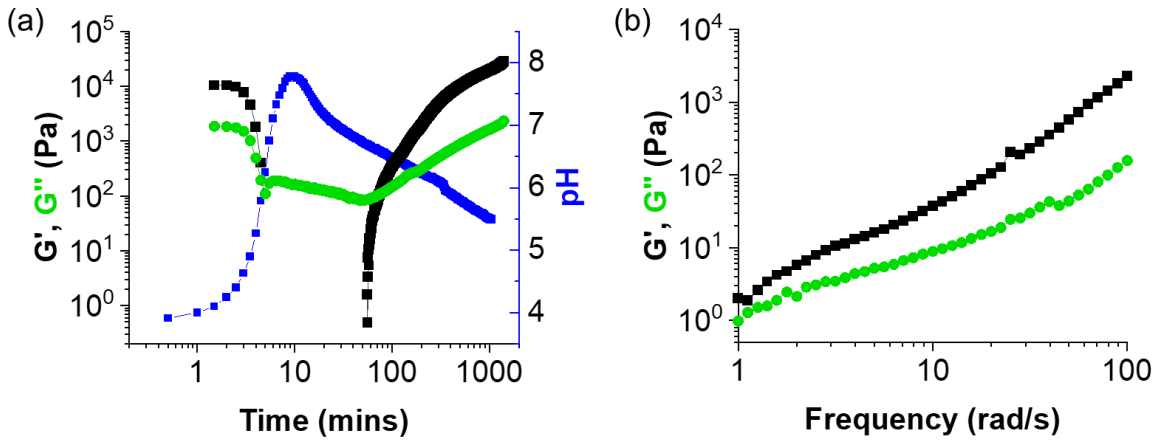

Figure 3.4. (a) Change in rheology and pH with time for a system containing L,D-2NapFF in presence of urea, urease and GdL at ω = 50 rad/s, showing a cross-over in G′ and G″ in the sol phase. (b) Frequency sweep for the solution phase of a system containing L,D-2NapFF in presence of urea, urease and GdL. In all cases, [L,D-2NapFF] = 5 mg/mL, [urea] = 0.04 M, [urease] = 0.4 mg/mL and [GdL] = 14.3 mg/mL.

The solution phase obtained at high pH contains self-assembled aggregates formed by L,D-2NapFF with a deprotonated terminal carboxylic acid. In this phase, L,D-2NapFF forms well-defined nanotubes at high pH as shown by SAXS[50] and cryo-EM (Figure 3.2e, Figure 3.5)[56] that exhibit shear-thinning behavior under shear (Figure 3.6b). Here, the nanotube formation is primarily driven by π-π stacking between the aromatic rings of the L,D-2NapFF molecules, which then twist in a left-handed helical manner to form the large, hollow structures.[56] Interestingly, related nanotubes can be aligned using shear or in a magnetic field.[42,57] Alignment under shear is expected for long anisotropic structures.[36,58] Alignment in a magnetic field is possible owing to high diamagnetic anisotropy resulting from their anisotropic shape and abundance of aromatic rings.[42] We therefore hypothesized that we should be able to tune the outcome of the pre-programmed temporal phase changes by the application of a shear force during the annealing process. We refer to this as "forging". Since the chemical changes are determined by the composition of the mixture, it is simple to carry out the pH changes in a highly reproducible manner in a range of sample environments.

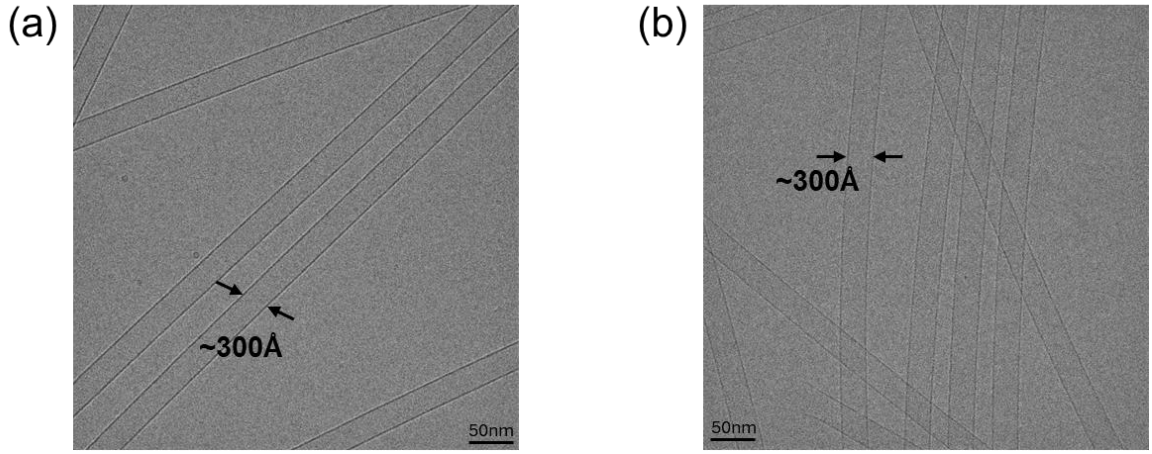

Figure 3.5. Additional cryo-EM images of L,D-2NapFF (scale bar 50 nm), showing the presence of hollow nanotubes within the sample. Cryo-EM data collected and analysed by Ravi R. Sonani and Edward H. Egelman, University of Virginia.

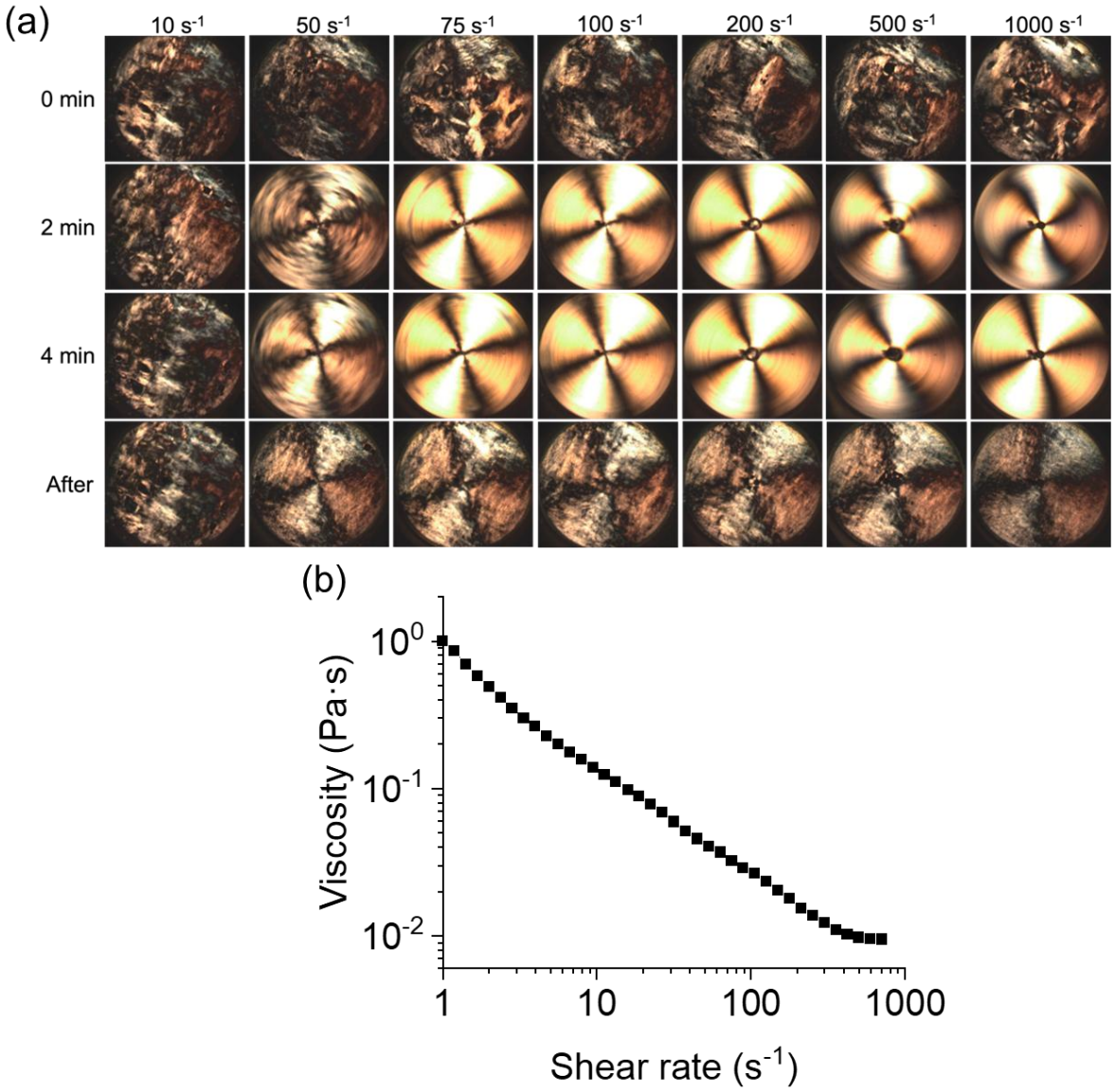

Figure 3.6. (a) Shear-induced Polarised Light Imaging (SIPLI) images of solutions for a system containing L,D-2NapFF in presence of urea, urease and GdL at a range of different constant shear rates (left). Measurements were taken on different samples immediately after the solution phase was formed to best represent the system. All images were taken with the same brightness. (b) Dynamic viscosity measurement for a system containing L,D-2NapFF in presence of urea, urease and GdL in the solution phase. All data presented in this Figure has been collected by Fin Hallam Stewart, University of Glasgow.

To forge the system, we apply a shear force to induce alignment. We used a unidirectional shear at specific times during the process using a rheometer. To measure the evolution of G′ and G″, oscillatory shear was used during the gel-to-sol transition, followed by a unidirectional shear of 100 s^{-1} starting at 7 minutes for 93 minutes. The shear rate of 100 s^{-1} was chosen due to optimal observation of alignment in the sol phase (Figure 3.6a). The time under shear was carefully chosen based on the initial values obtained by rheology and pH

(Figure 3.2d), to ensure full dispersion of the micellar aggregates in solution as well as to avoid disruption of the final gel. An oscillatory shear was then re-applied to follow the increase of G′ and G″ as the sample regelled. To observe the effect of shear on the macroscopic scale of the evolving system, a rheo-optics set-up was used: here, alignment can be determined by the observation of a Maltese cross pattern.[59,60] The Maltese cross pattern arises when a structure is preferentially aligned in the flow direction, with the four dark fringes corresponding to the areas where one of the refractive indices of the material under shear coincides with the plane of polarization of the polarizer.[59] If no unidirectional shear is applied, no Maltese cross is observed over the entire process (Figure 3.7a, insert, Figure 3.9c). However, application of unidirectional shear at 7 minutes results in the immediate observation of a Maltese cross, showing that the nanotubes are aligning along the direction of shear. If the unidirectional shear is stopped at 100 minutes, alignment is shown to persist as the pH decreases, with the final system still showing the presence of a Maltese cross (Figure 3.7b, insert, Figure 3.9d). Stopping the shear only after 18 minutes results in the formation of stiffer materials that exhibit alignment (Figure 3.10), but with a lower intensity of the Maltese cross (Figure 3.10c). We hypothesize that the alignment in the sol phase is maintained due to aromatic inter-fiber interactions,[61] allowing the system to lock in the alignment during regelation. If instead the unidirectional shear is maintained up to 300 minutes, where the apparent pK_a of the gelator is reached (around 6.0),[50] no regelation occurs, and no Maltese cross is observed after 16 hours (Figure 3.11). This shows that the self-assembly process leading to gelation starts to take place earlier than the apparent pK_a of L,D-2NapFF and careful consideration of timescales is vital in allowing regelation of the system while locking in the alignment of the fibers. We note that a similar result can be obtained by application of unidirectional shear starting at 10 minutes (Figure 3.12) when the pH reaches the highest value. However, 7 minutes was chosen throughout the rest of this study to account for any time loss due to sample loading and measurement start.

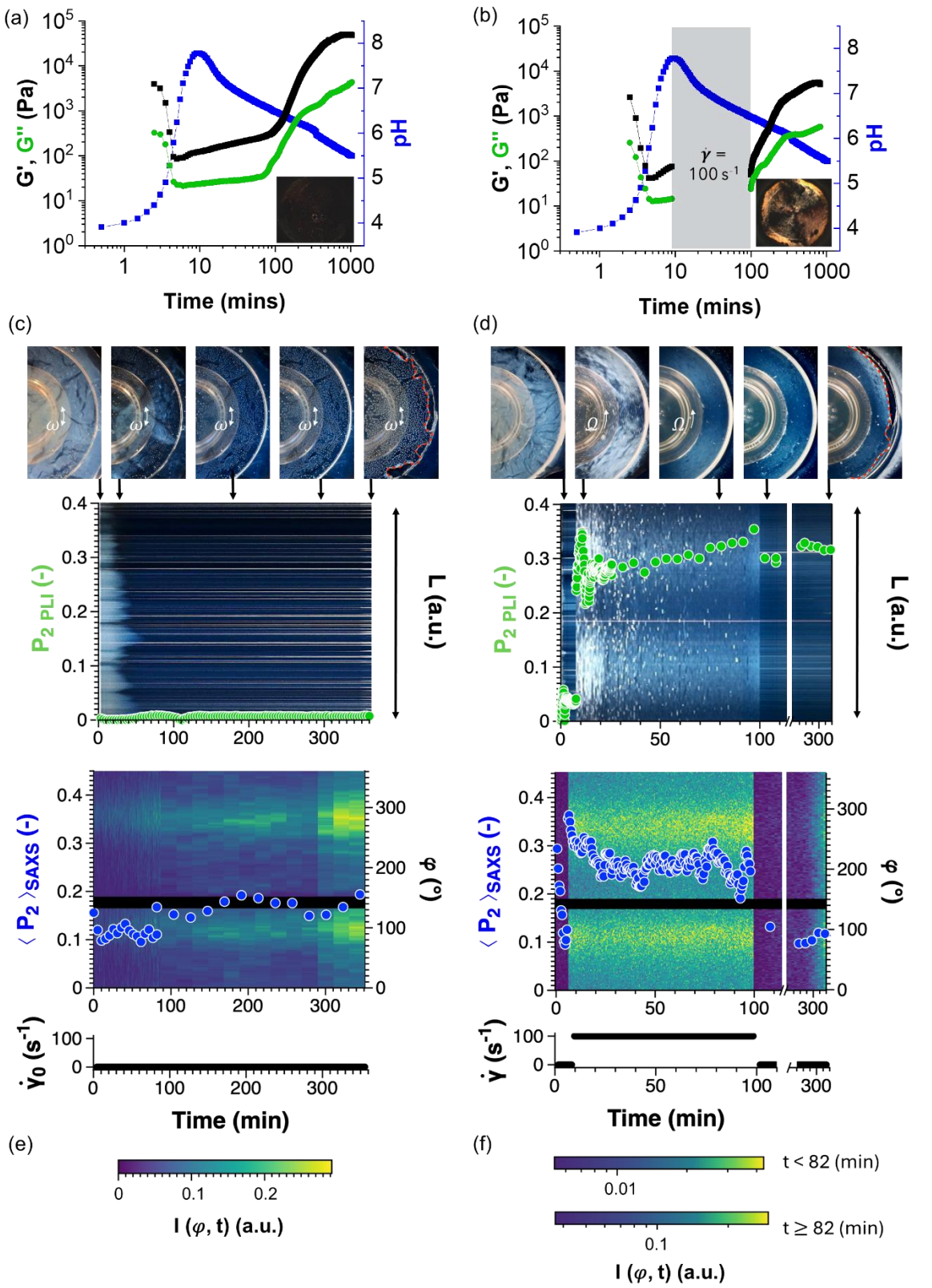

Figure 3.7. (a) Change in rheology and pH with time for a system containing L,D-2NapFF in presence of urea, urease and GdL with no unidirectional shear. The inserted photograph shows the sample after 16 hours using the rheo-optics system. Note here and for the remainder of this Figure, the colors of the lines and circles have been color-coded to match the colored axis titles; (b) Change in rheology and pH with time for a system containing L,D-

2NapFF in presence of urea, urease and GdL with unidirectional shear starting at 7 mins and finishing at 100 mins. The inserted photograph shows the sample after 16 hours using the rheo-optics system. Multi-scale analysis for a system with (c) no shear-alignment; (d) unidirectional shear starting at 7 mins and finishing at 100 mins. For (c) and (d), top: photographs of the sample at specific timepoints during the shearing process, indicated with an arrow. The red dashed line in the final image highlights the perimeter of the gel as it dried; upper-middle: time-space diagram of PLI using Hermans algorithm to detect the presence of the Maltese-cross pattern (green); lower-middle: time-space diagram of azimuthally-integrated SAXS data with Hermans Orientation Parameter (blue); bottom: imposed shear rate amplitude (oscillatory shear, c) or shear rate (steady shear, d). Scalar plot scattering intensity for the azimuthal integration scalar plots in Figure 3.7c (e) and Figure 3.7d (f). Full description of the calculations to obtain the orientation parameters can be found in the experimental section. Time sweep rheology data during Rheo-PLI-SAXS can be found in Figure 3.8. In all cases; [L,D-2NapFF] = 5 mg/mL, [urea] = 0.04 M, [urease] = 0.4 mg/mL and [GdL] = 14.3 mg/mL. Rheo-PLI-SAXS data was processed and analyzed by Roland Kádár and Marko Bek, Chalmers University.

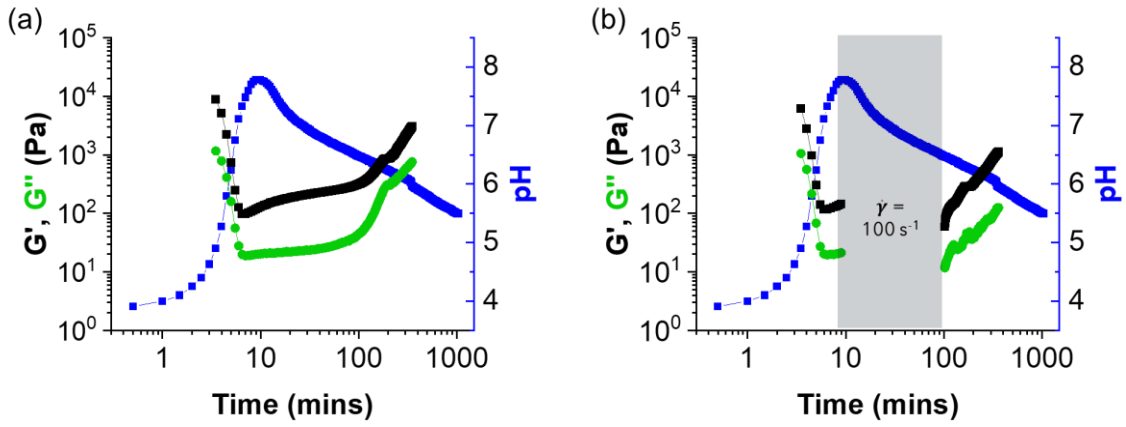

Figure 3.8. Time sweeps for a system containing L,D-2NapFF in presence of urea, urease and GdL with (a) no unidirectional shear and (b) shear applied from 7 minutes to 100 minutes during SAXS collection in the Rheo-PLI-SAXS set-up. In all cases, [L,D-2NapFF] = 5 mg/mL, [urea] = 0.04 M, [urease] = 0.4 mg/mL and [GdL] = 14.3 mg/mL.

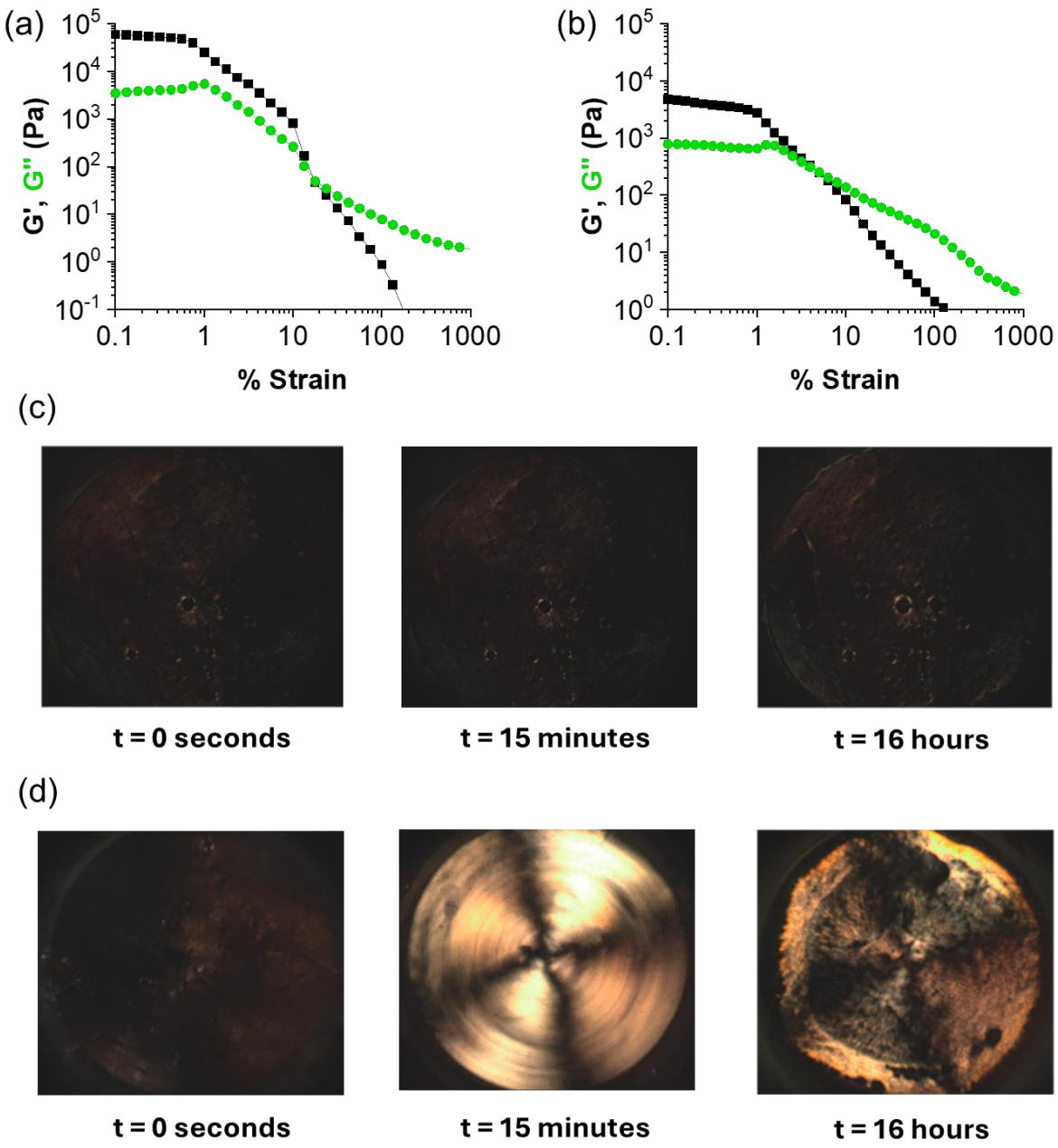

Figure 3.9. Strain sweeps collected after 16 hours for a system containing L,D-2NapFF in presence of urea, urease and GdL with (a) no unidirectional shear and (b) shear applied from 7 minutes to 100 minutes. SIPLI images collected at 0 seconds, 15 minutes and 16 hours a system containing L,D-2NapFF in presence of urea, urease and GdL with (c) no unidirectional shear and (d) shear applied from 7 minutes to 100 minutes In all cases, [L,D-2NapFF] = 5 mg/mL, [urea] = 0.04 M, [urease] = 0.4 mg/mL and [GdL] = 14.3 mg/mL. The data presented in this Figure was collected by Fin Hallam Stewart, University of Glasgow.

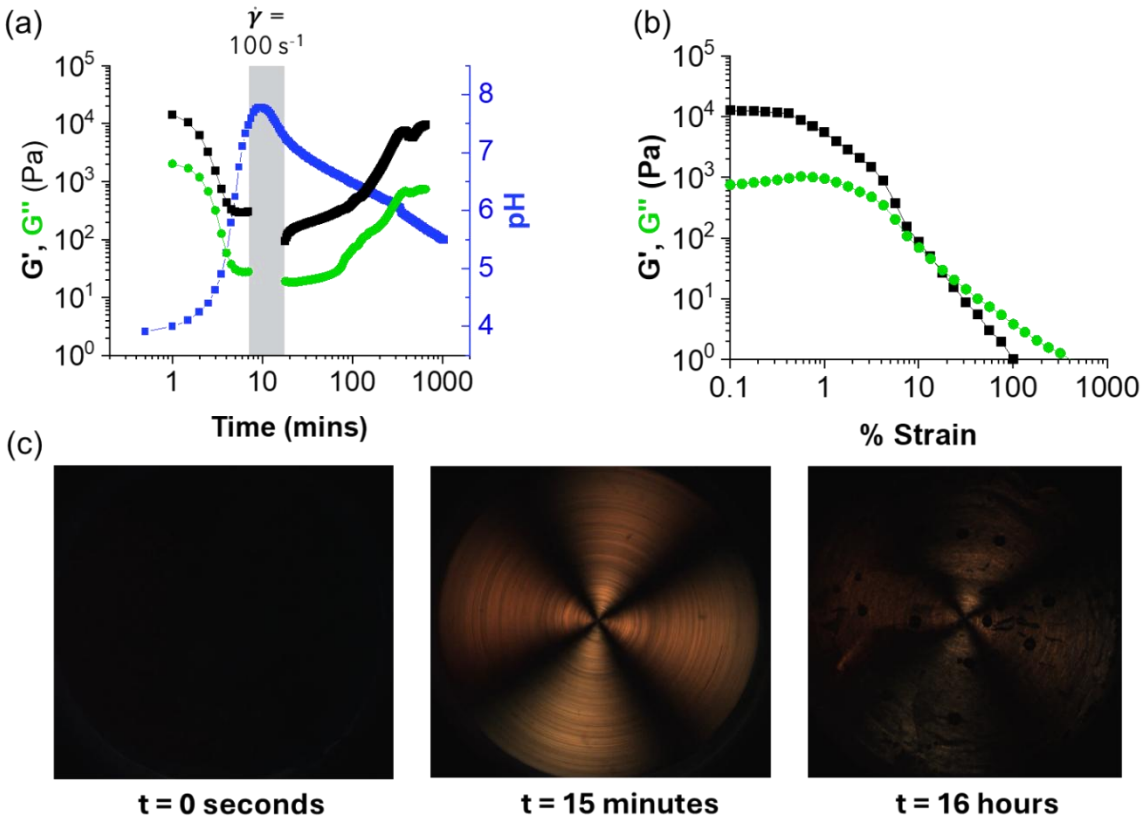

Figure 3.10. (a) Change in rheology and pH with time for a system containing L,D-2NapFF in presence of urea, urease and GdL with unidirectional shear applied from 7 minutes to 18 minutes. (b) Strain sweep collected for the system in (a) after 16 hours. (c) SIPLI images collected at 0 seconds, 15 minutes and 16 hours for a system containing L,D-2NapFF in presence of urea, urease and GdL with shear applied from 7 to 18 minutes. In all cases, [L,D-2NapFF] = 5 mg/mL, [urea] = 0.04 M, [urease] = 0.4 mg/mL and [GdL] = 14.3 mg/mL.

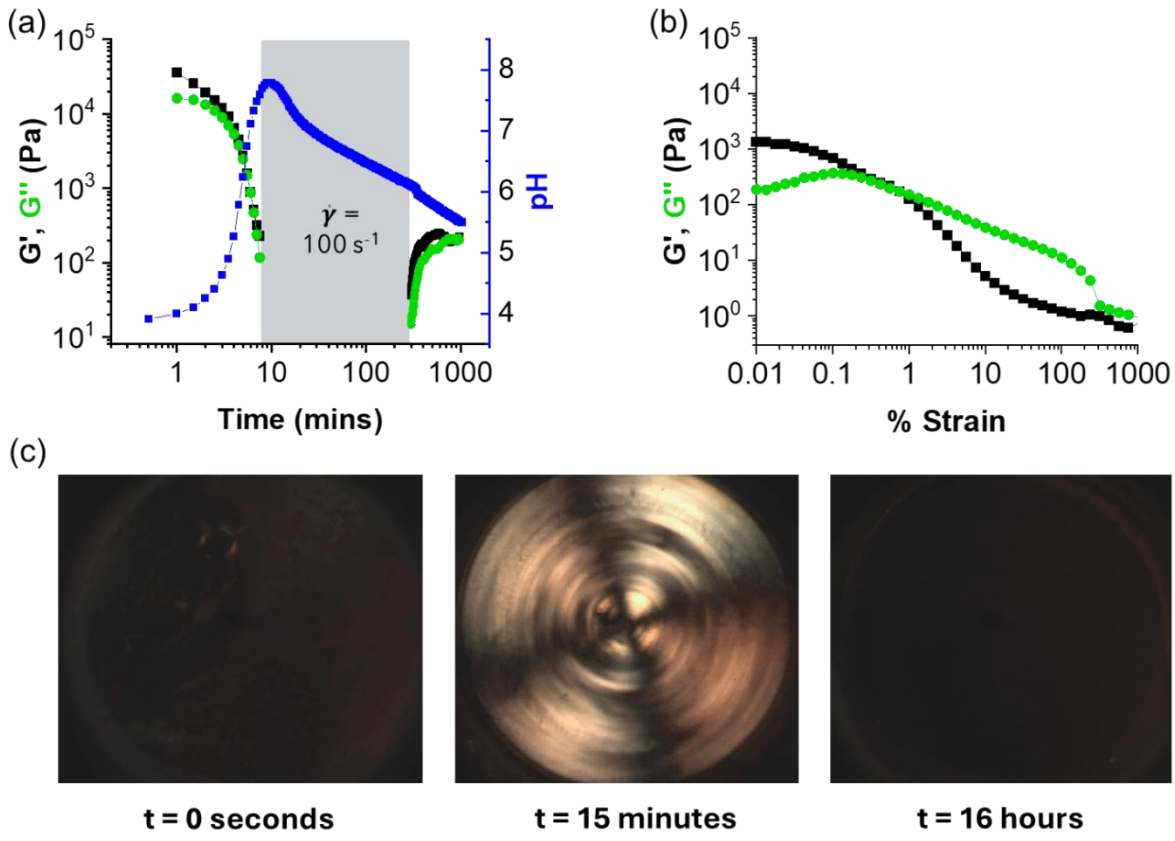

Figure 3.11. (a) Change in rheology and pH with time for a system containing L,D-2NapFF in presence of urea, urease and GdL with unidirectional shear applied from 7 minutes to 300 minutes. (b) Strain sweep collected for the system in (a) after 16 hours. (c) SIPLI images collected at 0 seconds, 15 minutes and 16 hours for a system containing L,D-2NapFF in presence of urea, urease and GdL with shear applied from 7 to 300 minutes. In all cases, [L,D-2NapFF] = 5 mg/mL, [urea] = 0.04 M, [urease] = 0.4 mg/mL and [GdL] = 14.3 mg/mL. All the data presented in this Figure was collected by Fin Hallam Stewart, University of Glasgow.

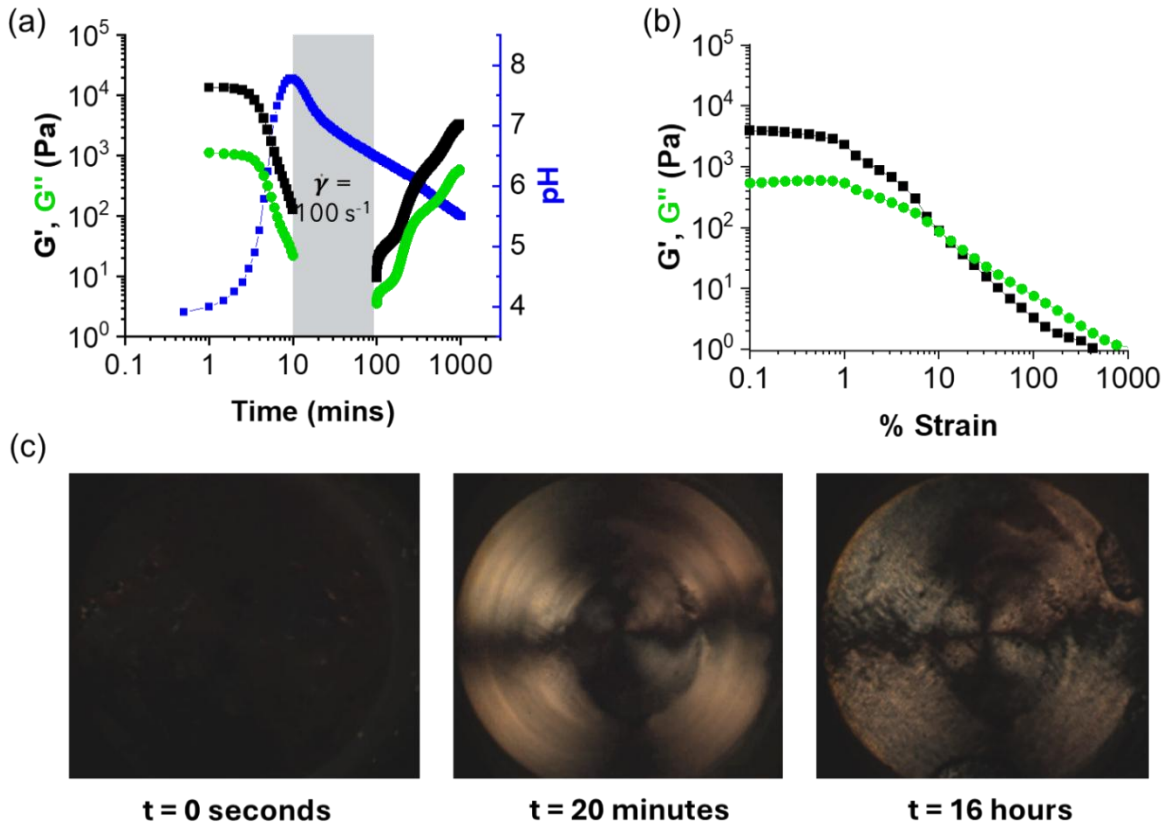

Figure 3.12. (a) Change in rheology and pH with time for a system containing L,D-2NapFF in presence of urea, urease and GdL with unidirectional shear applied from 10 minutes to 100 minutes. (b) Strain sweep collected for the system in (a) after 16 hours. (c) SIPLI images collected at 0 seconds, 20 minutes and 16 hours for a system containing L,D-2NapFF in presence of urea, urease and GdL with shear applied from 10 to 100 minutes. In all cases, [L,D-2NapFF] = 5 mg/mL, [urea] = 0.04 M, [urease] = 0.4 mg/mL and [GdL] = 14.3 mg/mL. All the data presented in this Figure was collected by Fin Hallam Stewart, University of Glasgow.

To understand how shear-alignment affects the nanostructures in solution, rheo-SAXS was performed on the sample. This allowed us to gain information on both the evolution of the mechanical properties of the system and the changes in the underlying self-assembled structures. Alignment of the self-assembled structures in SAXS can be observed by the presence of anisotropy in the 2D scattering patterns. To expand on this, a novel custom set-up was used to collect polarized light imaging (PLI) data while performing rheo-SAXS, i.e. Rheo-PLI-SAXS. By doing so, we could further assess the relationship between alignment on the meso- (PLI) and nanoscale (SAXS) under shear. The rheo-SAXS data showed that thin-walled nanotube structures are present throughout the evolution of the system (Figures 3.13 and 3.14). When no shear is applied to the system, the PLI data shows no Maltese cross

across the whole measurement, agreeing with our previous data (Figure 3.7a) and indicating no mesoscale alignment (Figure 3.7c, green circles). The 2D SAXS pattern shows an initial anisotropy potentially due to sample preparation in the rheometer and squeeze flow to gap. However, the anisotropy immediately drops during measurement, suggesting that no nanoscale orientation is present in the system as it evolves (Figure 3.7c, blue circles). A slight increase in nanoscale anisotropy is observed for this sample as it regels. This can be ascribed to confinement of the sample with increased bubble formation and drying (Figure 3.7c, top, red dashed line). Conversely, a Maltese cross is immediately observed if monodirectional shear is started at 7 minutes (Figure 3.7d, green circles), accompanied by a sudden increase in anisotropy in the 2D SAXS pattern of the system (Figure 3.7d, blue circles). A decrease in color of the Maltese cross can be seen over the shearing window. As the pH of the sample decreases, a slight decrease in radius of the nanotubes is observed (Figure 3.13c, Table 3.2) and higher interactions between the structures within the system are expected to occur. Such changes can be related to the differences in intensity of the Maltese cross pattern. However, as the sample regels, the Maltese cross pattern persists, indicating formation of aligned domains within the final material at the mesoscale level (Figure 3.7d, green circles). Interestingly, the nanoscale anisotropy drops once the shear is stopped (Figure 3.7d, blue circles). It is likely that, on the nanoscale, entanglements and further aggregations between the self-assembled structures are occurring to allow regelation, resulting in relaxation of the anisotropy at this length scale. The 1D scattering patterns of the system do not appear to change significantly between the sheared material and the one with no shear applied, with the presence of thin-walled nanotubes observed in both final materials (Figures 3.13, 3.14 and Tables 3.2 and 3.3). A slight decrease of about 1.0 nm in radius is only observed for the final gel obtained under shear, which could result from tighter packing of the gelator molecules upon reduction of bubbles during shearing (Figure 3.13 and Table 3.2). As the SAXS data shown here extend up to 240 nm, we should expect to observe any rupture of the fibers at this length scale. Hence, as no differences at low q can be seen, our data overall suggest that the shearing process does not break the self-assembled structures under application of mechanical stimuli.

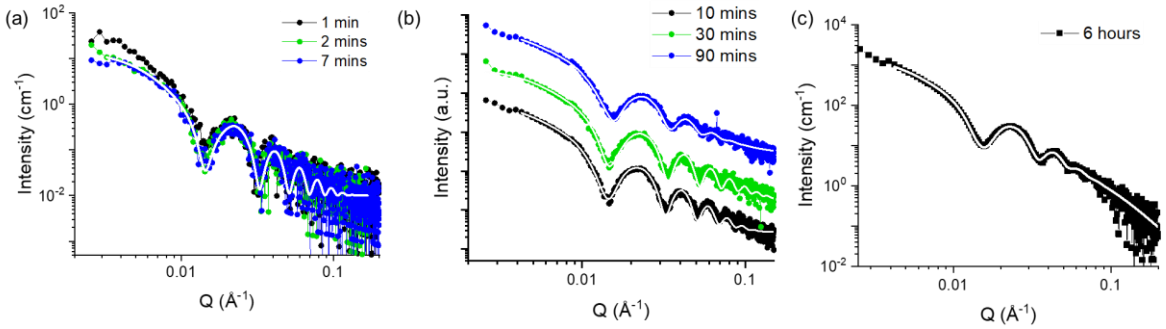

Figure 3.13. Small angle X-ray scattering data of a system containing L,D-2NapFF in presence of urea, urease and GdL with shear applied from 7 minutes to 100 minutes. (a) Data obtained at 1 minute (black data), 2 minutes (green data) and 7 minutes (blue data) under oscillatory shear; (b) data obtained at 10 minutes (black data), 30 minutes (green data) and 90 minutes (blue data) under unidirectional shear; (c) data obtained after 6 hours under oscillatory shear. In all cases, the white line indicates the model fit obtained using Sasview (Table 3.2). In (b), SAXS data has been offset for clarity.

Table 3.2. Fitting parameters for SAXS data in Figure 3.13. All the data was fit to a hollow cylinder model. Values that were manually added and fixed have been labelled with *.

	(L,D)-2NapFF shear-aligned									
	1 – 7.5 mins		10 mins		30 mins		100 mins		6 hours	
	Value	Error	Value	Error	Value	Error	Value	Error	Value	Error
Scale	0.00025*	/	0.12	0.0017	0.11	0.002	0.11	0.002	0.036	0.0003
Background (cm^{-1})	0.008*	/	1.36*	/	1.4*	/	1.89*	/	0.045*	/
Radius (Å)	155	0.55	160.7	0.19	155.9	0.22	147.1	0.27	146	0.13
Thickness (Å)	25*	/	19.4	0.28	17.7	0.35	18	0.33	20.6	0.22
Length (Å)	1250*	/	1254	17.1	1059.2	16.464	1094.2	21.765	1093	6.99
Radius polydispersity	/	/	0.05*	/	0.05*	/	0.1*	/	0.12*	/
χ^2	2.9313		5.80		6.83		11.58		6.96	

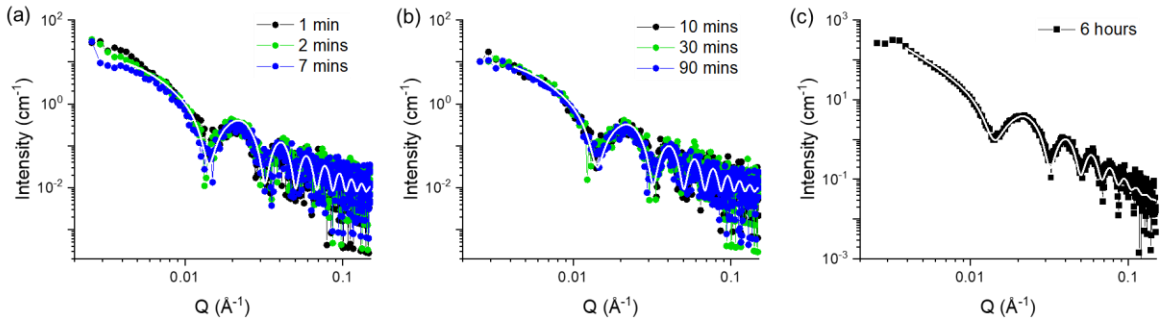

Figure 3.14. Small angle X-ray scattering data of a system containing L,D-2NapFF in presence of urea, urease and GdL with no unidirectional shear applied (a) Data obtained at 1 minute (black data), 2 minutes (green data) and 7 minutes (blue data) under oscillatory shear; (b) data obtained at 10 minutes (black data), 30 minutes (green data) and 90 minutes (blue data) under oscillatory shear; (c) data obtained after 6 hours under oscillatory shear. In all cases, the white line indicates model fit obtained using Sasview (Table 3.3).

Table 3.3. Fitting parameters for SAXS data in Figure 3.14. The data was fit either to a hollow cylinder model (A) or a combination of hollow cylinder (A) and a power law (B). Values that were manually added and fixed have been labelled with *.

	(L,D)-2NapFF no shear					
	1 – 7.5 mins		10 – 30 mins		6 hours	
	Value	Error	Value	Error	Value	Error
Scale	$3 \times 10^{-4*}$		2.44×10^{-4}	1.47×10^{-5}	1	
Background (cm^{-1})	0.008*		0.008*		0.02	
A_scale	/	/	/	/	2.66×10^{-3}	4.65×10^{-5}
A_radius (Å)	160*	/	160*	/	159.3	0.35
A_thickness (Å)	25*	/	25*	/	27.3	0.56
A_length (Å)	1000*	/	1000*	/	1031.8	21.55
B_scale	/	/	/	/	1.78×10^{-08}	4.56×10^{-09}
B_power	/	/	/	/	4.1	0.05
χ^2	3.814		3.6		8.48	

We can therefore use an external force to influence the outcome of our transient system. A consequence of this is that the mechanical properties of the system are affected by the alignment, with the absolute values of G′ and G″ being lower as compared to the ones obtained when no unidirectional shear is applied (Figures 3.7a and 3.7b, Figure 3.9). These changes are only due to the application of shear, as the structures that underpin the final gel

phase are unaffected by the shearing process. Although materials with aligned domains can also be formed directly by gelation under shear,[36] our forging method provides a further level of structural control: here, a variety of gels with different mechanical properties can be obtained from a single starting gel by application of shear.

Whilst effective, the application of shear requires use of an external invasive stimulus. Use of a magnetic field can also be used to induce alignment for such systems in a non-invasive manner. In the context of this thesis, we define as non-invasive the techniques that are not directly in physical contact with the material and cannot cause rupture in the materials upon application. Previously, our group has successfully aligned self-assembled structures of nanotubes within a magnetic field in an NMR magnet.[42] The behavior of LD-2NapFF within a magnetic field has further been studied using a magnetic sample environment for *in situ* SAXS, showing that the nanotubes can be successfully oriented using low and moderate magnetic fields (Figure 3.15) NMR has also been previously used to quantify the extent of alignment of self-assembled oligopeptide nanofibers.[62] ^{2}H NMR spectrum of a L,D-2NapFF gel formed in absence of urea/urease/GdL within an NMR tube indicated lack of magnetic alignment in the gel phase (Figure 3.16).

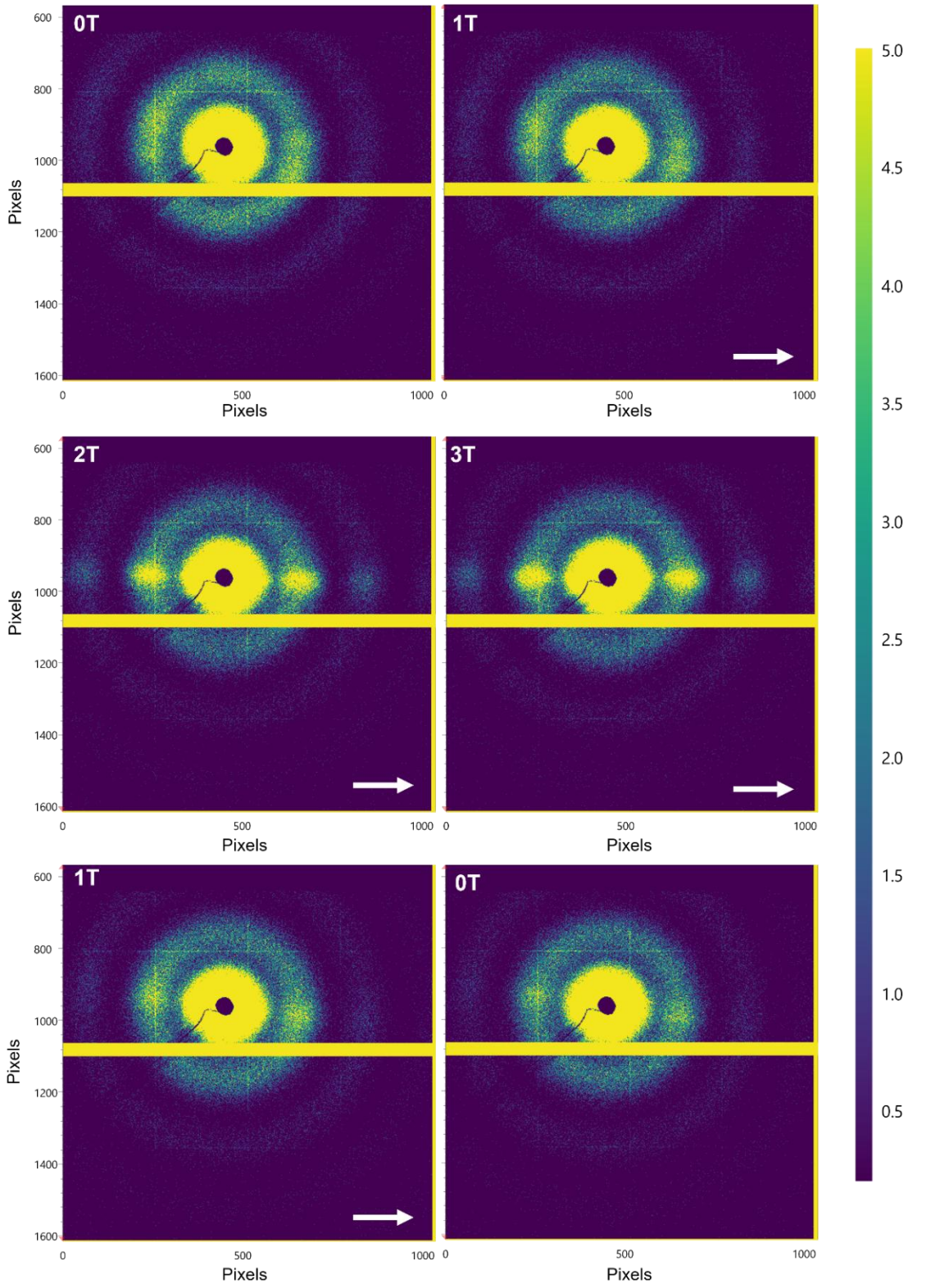

Figure 3.15. Scattering patterns of a 10 mg/mL solution of LD-2NapFF at different strength of applied horizontal magnetic field (white arrow), from 0T to 3T and after relaxation back to 0T. Anisotropy of the scattering pattern in the horizontal field direction at 2T and 3T is indicative of magnetically induced orientation.

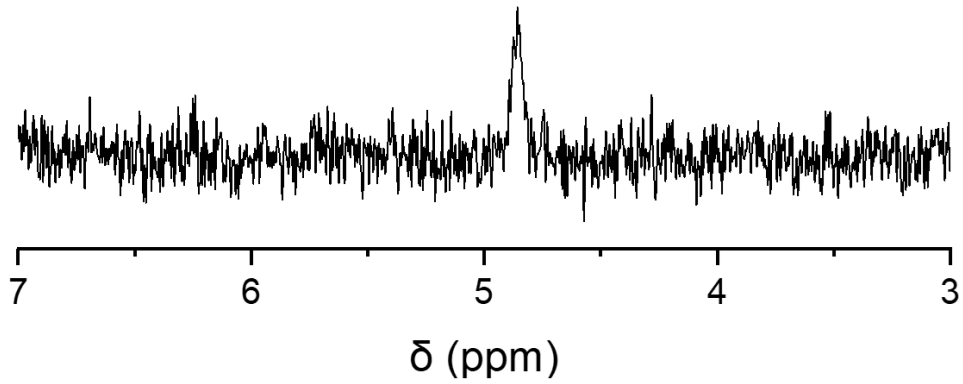

Figure 3.16. ^{2}H NMR spectra of a L,D-2NapFF DMSO/H_2O gel (10/90, v/v) formed in the presence of a magnetic field of 9.4T within an NMR tube. No splitting of the peak can be observed, indicating lack of magnetic alignment.

For the transient system shown here, the NMR approach was not possible, as the small size of the NMR tube did not allow homogeneous preparation of the gel incorporating the three triggers, affecting the kinetics. However, we hypothesized that magnetic alignment could be achieved if the sample was allowed to evolve within a larger vessel. Hence, samples of L,D-2NapFF containing the competing pH triggers were prepared inside an MRI scanner with a magnetic field strength of 9.4 T. To test the effect of the magnetic alignment, samples were allowed to form in the MRI scanner. Identical systems were prepared outside the MRI as a control. After being left for 16 hours, cross-polarized microscopy and SEM of the resulting samples showed unidirectional alignment of the final structures orthogonal to the field, both in the gel state (Figure 3.17a) and in the dried state (Figure 3.17b). Conversely, samples left outside of the MRI magnet showed random orientation of fibers (Figures 3.17c and 3.17d). As the Rheo-PLI-SAXS data shows the tendency of such structures to align on the mesoscale, we hypothesize that the periodicity observed in the dried state (Figure 3.17b) could result from longer-range alignment between bundles of smaller fibers, as well as clumping of the fibers during drying.

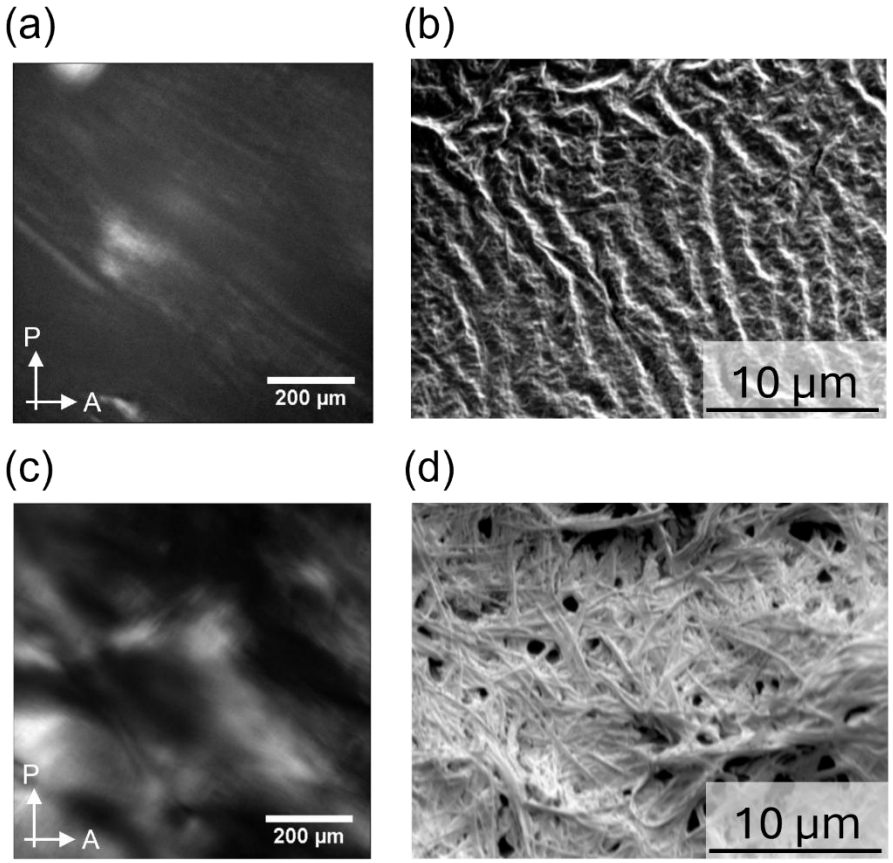

Figure 3.17. Cross-polarised optical image (a) and SEM (b) for a system containing L,D-2NapFF in presence of urea, urease and GdL allowed to evolve overnight in an MRI magnet; cross-polarised optical image (c) and SEM (d) for a system containing L,D-2NapFF in presence of urea, urease and GdL allowed to evolve overnight outside of the magnet. Note that all the samples were kept in the same room with controlled humidity and temperature. In all cases; [L,D-2NapFF] = 5 mg/mL, [urea] = 0.04 M, [urease] = 0.4 mg/mL and [GdL] = 14.3 mg/mL.

3.4 Conclusions

Here, we present a method to obtain anisotropic materials by changing the organization of the supramolecular fibers using external stimuli as the sample evolves through pre-programmed phase changes. Material properties can be directed through a forging approach, where external force is used to direct alignment of the supramolecular fibers and impart different mechanical responses. This method allows tunable, temporal control over network and final material properties. Dynamic systems are of wide interest, and here we provide a method for further controlling systems beyond the previous quiescent systems. Whilst we have exemplified this for a single system, many functionalized dipeptides and other gelators form gels under one set of conditions and micellar phases under other conditions and hence

we see no reason why this approach is not generalizable. There is a wider contextual interest here too, as many dynamic biological systems adapt in a flowing environment. We also show that our system is versatile, and that anisotropy can be further introduced in the sample by application of a magnetic field, enabling changes in network in a non-invasive manner. Aligned peptide fibers and nanotubes have applications in directing cell growth.[63] Additionally, aligning fibers and tubes has potential usefulness in optoelectronic applications.[64,65] We envisage that our approach may be used to design adaptive materials for these applications.

3.5 Experimental

3.5.1 Materials

L,D-2NapFF was synthesised as described previously.[50] Dimethyl sulfoxide (≥ 99 %) was purchased from Fischer Scientific. Urease (U4002-100KU, Jack Beans, 100,000 units/g solid), urea (ultrapure 99 %) and glucono-δ-lactone (99 %) were purchased from Alfa Aesar. All chemicals were used as received. Deionised water was used throughout all experiments.

3.5.2 Methodology

3.5.2.1 Solution preparation

To prepare the stock solution of L,D-2NapFF, the gelator powder was dissolved in dimethyl sulfoxide (DMSO) to reach a concentration of 200 mg/mL. Stock solutions of urea and urease were prepared in H_2O, at concentrations of 4 M and 0.450 mg/mL, respectively. The concentration of the urease stock solution was determined by taking the mass of the enzyme powder (in mg) dissolved in a known volume of H_2O. Both urea and urease were highly soluble in water and hence did not require stirring. Stock solutions of GdL were prepared freshly on the day by dissolving GdL in DMSO under stirring to achieve a final concentration of 286 mg/mL.

3.5.2.2 Hydrogel preparation

LD-2NapFF gels that did not evolve over time were prepared without adding urea, urease and GdL. For these samples, 50 μL of L,D-2NapFF 200 mg/mL stock solution was diluted with 150 μL of DMSO in a 7 mL Sterilin vial. 1.8 mL of H_2O was then added to this in one aliquot, achieving a final gelator concentration of 5 mg/mL and a DMSO:H_2O ratio of 10:90.

L,D-2NapFF gels pre-programmed to undergo gel-to-sol-to-gel transitions were prepared in the presence of urea, urease and GdL. For preparation of these gels, 50 μL of L,D-2NapFF

200 mg/mL stock solution was further diluted with 50 μL of DMSO in a 7 mL Sterilin vial. To this, 20 μL of aqueous urea (4 M) and 100 μL of GdL solution (286 mg/mL) were added and mixed by briefly swirling the vial. Finally, 1.78 mL of aqueous urease stock solution (0.45 mg/mL) was added to the mixture in one aliquot to induce gelation. The solvent ratio of DMSO and H_2O was kept at 10:90 for all samples. The final concentrations of the components were as follows; [L,D-2NapFF] = 5 mg/mL, [urea] = 0.04 M, [urease] = 0.4 mg/mL and [GdL] = 14.3 mg/mL.

3.5.3 Characterisation

3.5.3.1 Rheological measurements

Time sweeps. To initially observe the kinetics of the system, time sweeps were performed on an Anton Paar Physica MCR301 rheometer. A cup and vane measuring system was used, set at a measuring distance of 2.1 mm. The test was performed by preparing the sample in a 7 mL Sterilin vial immediately before positioning the vial in the rheometer cup. The tests were performed at a frequency of 10 rad/s and strain of 0.5% over 16 hours.

Rheo-Optics. All time sweeps were performed on an Anton Paar Physica MCR302 coupled with the shear-induced polarised light imaging (SIPLI) technique, as previously reported.[36,59,60] For all experiments, a PP25 geometry was used at a measuring distance of 1.0 mm. The gels were prepared directly on the plate by mixing solution of the gelator in DMSO and water (10/90, v/v) in presence of urea, urease and GdL and pouring the sample onto the quartz plate. To contain the sample during the gel-to-sol-to-gel transitions, a circular mould with a 32 mm diameter was used. A custom workbook was designed on RheoCompass to apply a constant shear (shear rate of 100 s^{-1}) on the system at variable time intervals, while collecting oscillatory shear rheology on the system when no shear was being applied. For all these, oscillatory shear rheology measurements were run at a frequency of 10 rad/s and strain of 0.5%. To prevent evaporation, wet blue-roll was placed around the sample overnight. Cross-polarised images of the materials were taken within the first 20 minutes and after 16 hours to observe the presence of a Maltese-cross pattern. A halogen lamp (white light source) was used to illuminate the sample.

Strain sweeps for the gels obtained after the gel-to-sol-to-gel transitions were conducted just after the time sweeps, without lifting the geometry from the surface of the gel. These were performed over the range of 0.1% to 1000% strain at a constant frequency of 10 rad/s.

Rheo-PLI-SAXS. Combined rheological measurements (Rheo), polarised light imaging (PLI) and small-angle X-ray scattering (SAXS), or rheo-PLI-SAXS, have been performed using a newly developed custom setup,[66] Figure 3.18, adapted from previous custom set-ups used to observe birefringence under flow.[67–69] The setup is based on a glass parallel plate measuring geometry in a separate motor-transducer configuration. The diameter of the upper plate was 43 mm, with region (i) in the Figure 3.18 being opaque due to the steel shaft of the geometry, and region (ii) being see-through, Figure 3.18a. The custom setup was adapted on an Anton Paar MCR702 MultiDrive rotational rheometer. Here, the samples were prepared similarly as described in the Rheo-Optics section, using the same custom RheoCompass workbook to apply a constant shear on the system.

The SAXS part consists of a radial incident configuration (R), meaning that the scattering pattern corresponds to the (1)-(2) plane, where (1) is the velocity direction, and (2) is the velocity gradient direction. To assess the flow induced orientation at nanoscale length scale, the scattering patterns were azimuthally integrated within $q \in [1.4,3.4] \cdot 10^{-2}$ Å-1, region of interest identified based on radial integration curves. Furthermore, as a quantitative measure of orientation the azimuthally-integrated data was fitted with an element series of even Legendre polynomials to determine the Hermans Orientation Parameter:

$$\langle P_2 \rangle_{SAXS} = \frac{\int_{-\frac{\pi}{2}}^{\frac{\pi}{2}} 1/2\ (3\cos^2\varphi - 1) I(\varphi) \sin\varphi\, d\varphi}{\int_{-\frac{\pi}{2}}^{\frac{\pi}{2}} I(\varphi) \sin\varphi\, d\varphi}$$

Where φ is the azimuthal angle. We note that within the integration limits chosen $\langle P_2 \rangle_{SAXS} = 0$ signifies random orientation whereas $\langle P_2 \rangle_{SAXS} = 1$ corresponds to full orientation in the flow direction.

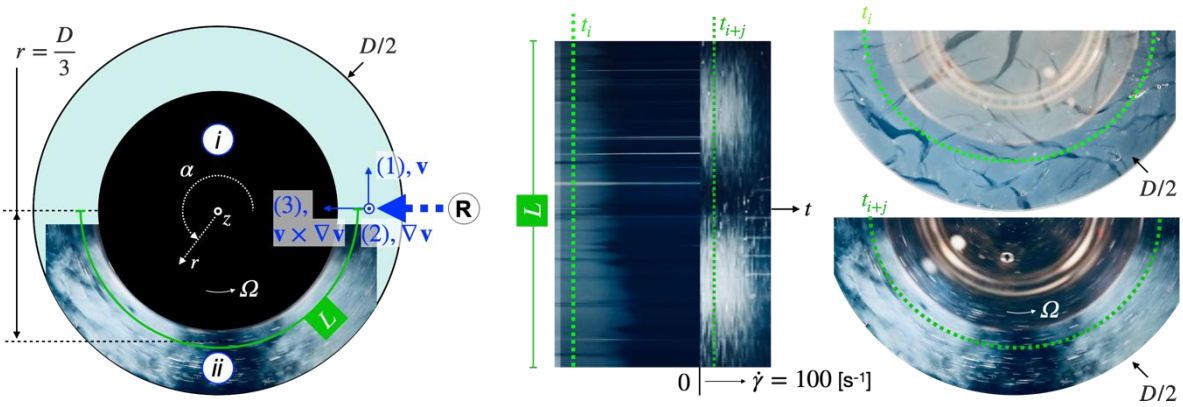

(a) (b) (c)

Figure 3.18. (a) Illustration of the rheo-PLI-SAXS setup. (b) Example of space-time diagram. (c) Examples of PLI visualizations acquired during the experiments at rest and during shear, the latter showing a Maltese-cross pattern, and their correspondence to the space-time diagram in (b).

A PLI optical train was positioned perpendicular to the shear plane. The optical train consisted of a cross-polarized setup operating in transmission mode. A DSLR Canon 90D camera (Canon, Japan) equipped with a 100 mm Canon L-series Macro lens was used to perform the PLI flow visualizations. The visualized area corresponds to region (ii) in Figure 3.19a, which allows to identify the onset of the Maltese-cross pattern. Due to the extended testing times, images (2440 x 1344 px resolution) were acquired at a frequency of 1/5 Hz (every 5 seconds). Out of each frame, a pixel-arc of length L was extracted from each frame and was added to a newly created so called space-time image, Figure 3.18a. Thus, the y-axis of the image corresponds to the arc L while the x-axis corresponds to the experimental time, t. Based on the similitude between the azimuthally integrated scattering data and the grayscale intensity of the space time-diagrams, Hermans algorithm was used to also quantify the onset of the Maltese-cross pattern by replacing $I(\varphi)$ with the grayscale intensity of the PLI images, $I_g(\alpha)$, where α is the angular coordinate along the arc L. We note that in this case the resulting $P_{2\,PLI}$ does not have the same meaning as for SAXS, rather the same mathematical framework is used to assess azimuthal uniformity of the flow field as viewed through the PLI: $P_{2\,PLI} > 0$ detects the onset of the Maltese-cross pattern, i.e. there is unidirectional orientation of optical indicatrixes in the shear direction. We note that while the notion of optical indicatrix does not specify an associated material lengthscale, it captures contributions from mesoscale which complements SAXS orientation ~nm material lengthscales. Finally, the radius corresponding to the arc of length L was $r = D/3$ from the

centre of the geometry which corresponds to the radius at which the nominal shear rate was calculated.[68]

3.5.3.2 pH measurements

pH measurements were taken with a HANNA FC200 pH probe using a 6 mm × 10 mm conical tip with a ± 0.1 accuracy. To monitor the pH changes of the evolving system, the gels were prepared as above immediately before starting the measurement. To keep the temperature constant at 25 °C, the sample was kept in a circulating water bath.

3.5.3.3 Small angle X-ray scattering

Small angle X-ray scattering data was collected at the CoSAXS beamline at the diffraction limited 3 GeV storage ring at the MAX IV Laboratory in Sweden. For the Rheo-PLI-SAXS measurements, a novel custom set-up was used, as described above. An X-ray beam of 15 keV was used, with the camera length set at 4.7 m to achieve a q-range of 0.0026 – 0.3 $Å^{-1}$ (where $q= 4\pi/\lambda \sin(\theta)$, $\lambda=0.8267$ Å and 2θ the scattering angle). The data was collected using an EIGER2 4M hybrid photon-counting pixel detector (Dectris AG). The gel samples were prepared directly on the rheometer plate as described before. For all samples, Rheo-PLI-SAXS data was collected over six hours to ensure that gelation had occurred. For the sheared sample, 0.1 s exposures were collected every 30 seconds within the first 6 minutes to observe any information on the gel-to-sol transition. As the sample was being sheared, 2 s exposures were recorded every 30 seconds for 90 minutes. Finally, 0.1 s frames were collected every 10 minutes as the sample regelled until the end of the run. For the control sample with no shear, shorter exposures were required to avoid X-ray damage. Hence, 0.1 s frames were collected every 30 seconds within the first 100 minutes, followed by 0.5 s frames every 20 minutes until the end of the 6 hours. Rheological data and images were collected every 30 seconds over the course of each run.

SAXS data of LD-2NapFF within a magnetic field was collected using the electromagnetism set-up of the CoSAXS beamline. The X-ray beam used had an energy of 15 keV and the sample-detector distance was set at 4.5 m. The GMW 3480 dipole electromagnet magnet with 5 mm diameter poles was used for the experiments. The poles distance was set at 2 mm distance to achieve a 3T maximum magnetic field. The samples were measured in 1.5 mm diameter borosilicate glass capillaries supported by an Aluminium frame between the magnetic poles. The magnetic field was swept up from 0 to 3T in 40 minutes, holding the sample at 0T, 1T and 2T for 10 minutes respectively. Then, the sample was kept at 3T for 1 hour, before lowering the magnetic field down to 0T. To investigate if loss of anisotropy

occurred immediately below 3T or over different values, the field was lowered stepwise, holding the sample at 2T and 1T for 10 minutes before reaching 0T. Then, the sample was held at 0 T for another hour. SAXS data was collected every 5 minutes with 0.5 s exposure time across the whole magnetic field program.

3.5.3.4 Alignment in the MRI

To align the samples in the MRI, a Bruker 9.4 T MR scanner was used at the Centre for Pre-Clinical Imaging at the University of Liverpool. For these experiments, samples undergoing gel-to-sol-to-gel transitions in presence of urea, urease and GdL were prepared within the magnet and outside the MRI. All samples were prepared as described before and immediately poured from the vial into a borosilicate glass cell-culture dish prior to gelation. In both cases, six samples were prepared: three were kept sealed and three were left without the lid to allow to dry overnight. The direction of the magnetic field was written on each of the dishes within the magnet. For the MRI samples, the glass dishes were moved into the centre of the magnetic field. The samples prepared outside of the magnet were kept in the same room as the MRI to ensure the samples were subjected to similar environmental conditions. The room was kept at a controlled temperature of 25 °C. After 16 hours, the samples were removed from the MRI and directly measured under the microscope.

3.5.3.5 Scanning electron microscopy

SEM images were collected on a PC controlled TESCAN CLARA Ultra High-Resolution Scanning Electron Microscope (UHR-SEM) with a Field Emission Gun electron source (accelerating voltage 0.5 keV – 30keV). The hydrogels were prepared in glass dishes as described in the MRI section and left to dry for minimum 24 hours. The glass dishes were scored and cut without perturbing the xerogels into ca. 1 cm x 2 cm slides. To prevent charging and obtain better images, the dried hydrogels attached to the glass were sputter coated prior to imaging using a PolaronSC7640 auto/manual high resolution sputter coater with a Gold/Palladium target.

3.5.3.6 Optical Microscopy under cross-polarised light

Optical microscope images were collected at the Centre for Cell Imaging at the University of Liverpool. The images were recorded using a Zeiss (Zeiss, Jena, Germany) Axio Observer Z.1 with a 10x/0.3 lens and plane-polarising filters. An Andor (ANDOR technology, Belfast, Northern Ireland, UK) iXon Ultra 897 camera was used to image the samples. All images

were acquired using Micro-Manager1.4.15 open-source software (http://www.micro-manager.org/)

3.5.3.7 Cryo-EM data collection and image processing

The sample was vitrified on lacey carbon grid using Vitrobot Mark IV (Thermo Fisher Scientific). First, the surface of lacey carbon grid was made hydrophilic by glow-discharging it in the GloQube (Quorum Technologies). ~3uL of sample was applied on the glow-discharged grid, excess sample was blotted away by Whatman filter paper (1001-055) leaving the thin film of sample on grid, which was plunge frozen in liquid ethane. The frozen grid was imaged on a 200 keV cryo-electron microscope (Glacios, Thermo Fisher Scientific) equipped with a cryo-autoloader, XFEG electron source and Falcon4 direct electron detector, housed in the University of Virginia Molecular Electron Microscopy Core facility.

3.6 References

1 J. H. van Esch, R. Klajn and S. Otto, Chemical systems out of equilibrium, *Chem. Soc. Rev.*, 2017, **46**, 5474–5475.

2 F. della Sala, S. Neri, S. Maiti, J. L. Y. Chen and L. J. Prins, Transient self-assembly of molecular nanostructures driven by chemical fuels, *Curr. Opin. Biotechnol.*, 2017, **46**, 27–33.

3 G. Ragazzon and L. J. Prins, Energy consumption in chemical fuel-driven self-assembly, *Nat. Nanotechnol.*, 2018, **13**, 882–889.

4 B. Rieß, R. K. Grötsch and J. Boekhoven, The Design of Dissipative Molecular Assemblies Driven by Chemical Reaction Cycles, *Chem*, 2020, **6**, 552–578.

5 A. Sharko, D. Livitz, S. De Piccoli, K. J. M. Bishop and T. M. Hermans, Insights into Chemically Fueled Supramolecular Polymers, *Chem. Rev.*, 2022, **122**, 11759–11777.

6 V. A. Ranganath and I. Maity, Artificial Homeostasis Systems Based on Feedback Reaction Networks: Design Principles and Future Promises, *Angew. Chem. Int. Ed.*, 2024, **63**, e202318134.

7 Z. Leng, F. Peng and X. Hao, Chemical-Fuel-Driven Assembly in Macromolecular Science: Recent Advances and Challenges, *Chempluschem*, 2020, **85**, 1190–1199.

8 S. Bal, C. Ghosh, P. Parvin and D. Das, Temporal Self-Regulation of Mechanical Properties via Catalytic Amyloid Polymers of a Short Peptide, *Nano Lett.*, 2023, **23**, 9988–9994.

9 S. A. P. van Rossum, M. Tena-Solsona, J. H. van Esch, R. Eelkema and J. Boekhoven, Dissipative out-of-equilibrium assembly of man-made supramolecular materials, *Chem. Soc. Rev.*, 2017, **46**, 5519–5535.

10 J. Chen, H. Wang, F. Long, S. Bai and Y. Wang, Dynamic supramolecular hydrogels mediated by chemical reactions, *Chem. Commun.*, 2023, **59**, 14236–14248.

11 C. Sharma, I. Maity and A. Walther, pH-feedback systems to program autonomous self-assembly and material lifecycles, *Chem. Commun.*, 2023, **59**, 1125–1144.

12 J. P. Wojciechowski, A. D. Martin and P. Thordarson, Kinetically Controlled Lifetimes in Redox-Responsive Transient Supramolecular Hydrogels, *J. Am. Chem. Soc.*, 2018, **140**, 2869–2874.

13 C. Donau, F. Späth, M. Stasi, A. M. Bergmann and J. Boekhoven, Phase Transitions in Chemically Fueled, Multiphase Complex Coacervate Droplets, *Angew. Chem. Int. Ed.*, 2022, **61**, e202211905.

14 S. Li, Y. Zhao, S. Wu, X. Zhang, B. Yang, L. Tian and X. Han, Regulation of species metabolism in synthetic community systems by environmental pH oscillations, *Nat. Commun.*, 2023, **14**, 7507.

15 J. Boekhoven, W. E. Hendriksen, G. J. M. Koper, R. Eelkema and J. H. van Esch, Transient assembly of active materials fueled by a chemical reaction, *Science (1979)*, 2015, **349**, 1075–1079.

16 M. Tena-Solsona, B. Rieß, R. K. Grötsch, F. C. Löhrer, C. Wanzke, B. Käsdorf, A. R. Bausch, P. Müller-Buschbaum, O. Lieleg and J. Boekhoven, Non-equilibrium dissipative supramolecular materials with a tunable lifetime, *Nat. Commun.*, 2017, **8**, 15895.

17 T. Heuser, A.-K. Steppert, C. Molano Lopez, B. Zhu and A. Walther, Generic Concept to Program the Time Domain of Self-Assemblies with a Self-Regulation Mechanism, *Nano Lett.*, 2015, **15**, 2213–2219.

18 T. Heuser, E. Weyandt and A. Walther, Biocatalytic Feedback-Driven Temporal Programming of Self-Regulating Peptide Hydrogels, *Angew. Chem. Int. Ed.*, 2015, **54**, 13258–13262.

19 C. G. Pappas, I. R. Sasselli and R. V Ulijn, Biocatalytic Pathway Selection in Transient Tripeptide Nanostructures, *Angew. Chem. Int. Ed.*, 2015, **54**, 8119–8123.

20 S. Toledano, R. J. Williams, V. Jayawarna and R. V. Ulijn, Enzyme-Triggered Self-Assembly of Peptide Hydrogels via Reversed Hydrolysis, *J. Am. Chem. Soc.*, 2006, **128**, 1070–1071.

21 N. Singh, B. Lainer, G. J. M. Formon, S. De Piccoli and T. M. Hermans, Re-programming Hydrogel Properties Using a Fuel-Driven Reaction Cycle, *J. Am. Chem. Soc.*, 2020, **142**, 4083–4087.

22 N. Singh, A. Lopez-Acosta, G. J. M. Formon and T. M. Hermans, Chemically Fueled Self-Sorted Hydrogels, *J. Am. Chem. Soc.*, 2022, **144**, 410–415.

23 M. Liu, C. N. Creemer, T. J. Reardon and J. R. Parquette, Light-driven dissipative self-assembly of a peptide hydrogel, *Chem. Commun.*, 2021, **57**, 13776–13779.

24 H. Xu, S. Bai, G. Gu, Y. Gao, X. Sun, X. Guo, F. Xuan and Y. Wang, Bioinspired Self-Resettable Hydrogel Actuators Powered by a Chemical Fuel, *ACS Appl. Mater. Interfaces*, 2022, **14**, 43825–43832.

25 B. Xue, M. Qin, T. Wang, J. Wu, D. Luo, Q. Jiang, Y. Li, Y. Cao and W. Wang, Electrically Controllable Actuators Based on Supramolecular Peptide Hydrogels, *Adv. Funct. Mater.*, 2016, **26**, 9053–9062.

26 W. A. Ogden and Z. Guan, Redox Chemical-Fueled Dissipative Self-Assembly of Active Materials, *ChemSystemsChem*, *ChemSystemsChem*, 2020, **2**, e1900030.

27 R. Kubota, M. Makuta, R. Suzuki, M. Ichikawa, M. Tanaka and I. Hamachi, Force generation by a propagating wave of supramolecular nanofibers, *Nat. Commun.*, 2020, **11**, 3541.

28 J. Leira-Iglesias, A. Sorrenti, A. Sato, P. A. Dunne and T. M. Hermans, Supramolecular pathway selection of perylenediimides mediated by chemical fuels, *Chem. Commun.*, 2016, **52**, 9009–9012.

29 Md. A. Haque, G. Kamita, T. Kurokawa, K. Tsujii and J. P. Gong, Unidirectional Alignment of Lamellar Bilayer in Hydrogel: One-Dimensional Swelling, Anisotropic Modulus, and Stress/Strain Tunable Structural Color, *Adv. Mater.*, 2010, **22**, 5110–5114.

30 A. H. Milani, L. A. Fielding, P. Greensmith, B. R. Saunders, D. J. Adlam, A. J. Freemont, J. A. Hoyland, N. W. Hodson, M. A. Elsawy, A. F. Miller, L. P. D. Ratcliffe, O. O. Mykhaylyk and S. P. Armes, Anisotropic pH-Responsive Hydrogels Containing Soft or Hard Rod-Like Particles Assembled Using Low Shear, *Chem. Mater.*, 2017, **29**, 3100–3110.

31 A. Franceschini, E. Filippidi, E. Guazzelli and D. J. Pine, Transverse Alignment of Fibers in a Periodically Sheared Suspension: An Absorbing Phase Transition with a Slowly Varying Control Parameter, *Phys. Rev. Lett.*, 2011, **107**, 250603.

32 S. Zhang, M. A. Greenfield, A. Mata, L. C. Palmer, R. Bitton, J. R. Mantei, C. Aparicio, M. O. de la Cruz and S. I. Stupp, A self-assembly pathway to aligned monodomain gels, *Nat. Mater.*, 2010, **9**, 594–601.

33 X. Lang, Y. Huang, L. He, Y. Wang, U. Thumu, Z. Chu, W. T. S. Huck and H. Zhao, Mechanosensitive non-equilibrium supramolecular polymerization in closed chemical systems, *Nat. Commun.*, 2023, **14**, 3084.

34 A. Abalymov, B.-E. Pinchasik, R. A. Akasov, M. Lomova and B. V. Parakhonskiy, Strategies for Anisotropic Fibrillar Hydrogels: Design, Cell Alignment, and Applications in Tissue Engineering, *Biomacromolecules*, 2023, **24**, 4532–4552.

35 B. D. Wall, S. R. Diegelmann, S. Zhang, T. J. Dawidczyk, W. L. Wilson, H. E. Katz, H. Mao and J. D. Tovar, Aligned Macroscopic Domains of Optoelectronic Nanostructures Prepared via Shear-Flow Assembly of Peptide Hydrogels, *Adv. Mater.*, 2011, **23**, 5009–5014.

36 E. R. Draper, O. O. Mykhaylyk and D. J. Adams, Aligning self-assembled gelators by drying under shear, *Chem. Commun.*, 2016, **52**, 6934–6937.

37 C. G. Pappas, T. Mutasa, P. W. J. M. Frederix, S. Fleming, S. Bai, S. Debnath, S. M. Kelly, A. Gachagan and R. V. Ulijn, Transient supramolecular reconfiguration of peptide nanostructures using ultrasound, *Mater. Horiz.*, 2014, **2**, 198–202.

38 Y. Wang, C. Zhan, H. Fu, X. Li, X. Sheng, Y. Zhao, D. Xiao, Y. Ma, J. S. Ma and J. Yao, Switch from intra- to intermolecular H-bonds by ultrasound: Induced gelation and distinct nanoscale morphologies, *Langmuir*, 2008, **24**, 7635–7638.

39 A. Tsuda, Y. Nagamine, R. Watanabe, Y. Nagatani, N. Ishii and T. Aida, Spectroscopic visualization of sound-induced liquid vibrations using a supramolecular nanofibre, *Nat. Chem.*, 2010, **2**, 977–983.

40 Y. Hotta, S. Fukushima, J. Motoyanagi and A. Tsuda, Photochromism in sound-induced alignment of a diarylethene supramolecular nanofibre, *Chem. Commun.*, 2015, **51**, 2790–2793.

41 R. Miura, Y. Ando, Y. Hotta, Y. Nagatani and A. Tsuda, Acoustic Alignment of a Supramolecular Nanofiber in Harmony with the Sound of Music, *Chempluschem*, 2014, **79**, 516–523.

42 M. Wallace, A. Z. Cardoso, W. J. Frith, J. A. Iggo and D. J. Adams, Magnetically Aligned Supramolecular Hydrogels, *Chem. Eur. J.*, 2014, **20**, 16484–16487.

43 D. W. P. M. Löwik, I. O. Shklyarevskiy, L. Ruizendaal, P. C. M. Christianen, J. C. Maan and J. C. M. van Hest, A Highly Ordered Material from Magnetically Aligned Peptide Amphiphile Nanofiber Assemblies, *Adv. Mater.*, 2007, **19**, 1191–1195.

44 M. van den Heuvel, A. M. Prenen, J. C. Gielen, P. C. M. Christianen, D. J. Broer, D. W. P. M. Löwik and J. C. M. van Hest, Patterns of Diacetylene-Containing Peptide Amphiphiles Using Polarization Holography, *J. Am. Chem. Soc.*, 2009, **131**, 15014–15017.

45 I. O. Shklyarevskiy, P. Jonkheijm, P. C. M. Christianen, A. P. H. J. Schenning, A. Del Guerzo, J.-P. Desvergne, E. W. Meijer and J. C. Maan, Magnetic Alignment of Self-Assembled Anthracene Organogel Fibers, *Langmuir*, 2005, **21**, 2108–2112.

46 Y. Jung, H. Kim, H.-K. Cheong and Y. Lim, Magnetic control of self-assembly and disassembly in organic materials, *Nat. Commun.*, 2023, **14**, 3081.

47 N. Y. Patrawalla, R. Raj, V. Nazar and V. Kishore, Magnetic Alignment of Collagen: Principles, Methods, Applications, and Fiber Alignment Analyses, *Tissue Eng. Part B Rev.*, 2024, **30**, 405–422.

48 S. Panja, A. M. Fuentes-Caparrós, E. R. Cross, L. Cavalcanti and D. J. Adams, Annealing Supramolecular Gels by a Reaction Relay, *Chem. Mater.*, 2020, **32**, 5264–5271.

49 S. Panja and D. J. Adams, Gel to gel transitions by dynamic self-assembly, *Chem. Commun.*, 2019, **55**, 10154–10157.

50 K. McAulay, B. Dietrich, H. Su, M. T. Scott, S. Rogers, Y. K. Al-Hilaly, H. Cui, L. C. Serpell, A. M. Seddon, E. R. Draper and D. J. Adams, Using chirality to influence supramolecular gelation, *Chem. Sci.*, 2019, **10**, 7801–7806.

51 E. Jee, T. Bánsági, A. F. Taylor and J. A. Pojman, Temporal Control of Gelation and Polymerization Fronts Driven by an Autocatalytic Enzyme Reaction, *Angew. Chem. Int. Ed.*, 2016, **128**, 2167–2171.

52 T. Heuser, E. Weyandt and A. Walther, Biocatalytic Feedback-Driven Temporal Programming of Self-Regulating Peptide Hydrogels, *Angew. Chem. Int. Ed.*, 2015, **54**, 13258–13262.

53 L. Heinen, T. Heuser, A. Steinschulte and A. Walther, Antagonistic enzymes in a biocatalytic ph feedback system program autonomous DNA hydrogel life cycles, *Nano Lett.*, 2017, **17**, 4989–4995.

54 D. J. Adams, M. F. Butler, W. J. Frith, M. Kirkland, L. Mullen and P. Sanderson, A new method for maintaining homogeneity during liquid–hydrogel transitions using low molecular weight hydrogelators, *Soft Matter*, 2009, **5**, 1856–1862.

55 S. Bianco, S. Panja and D. J. Adams, Using Rheology to Understand Transient and Dynamic Gels, *Gels*, 2022, **8**, 132.

56 R. R. Sonani, S. Bianco, B. Dietrich, J. Doutch, E. R. Draper, D. J. Adams and E. H. Egelman, Atomic structures of naphthalene dipeptide micelles unravel mechanisms of assembly and gelation, *Cell. Rep. Phys. Sci.*, 2024, **5**, 101812.

57 L. Chen, G. Pont, K. Morris, G. Lotze, A. Squires, L. C. Serpell and D. J. Adams, Salt-induced hydrogelation of functionalised-dipeptides at high pH, *Chem. Commun.*, 2011, **47**, 12071–12073.

58 S. Förster, M. Konrad and P. Lindner, Shear Thinning and Orientational Ordering of Wormlike Micelles, *Phys. Rev. Lett.*, 2005, **94**, 017803.

59 O. O. Mykhaylyk, Time-resolved polarized light imaging of sheared materials: Application to polymer crystallization, *Soft Matter*, 2010, **6**, 4430–4440.

60 O. O. Mykhaylyk, N. J. Warren, A. J. Parnell, G. Pfeifer and J. Laeuger, Applications of shear-induced polarized light imaging (SIPLI) technique for mechano-optical rheology of polymers and soft matter materials, *J. Polym. Sci. B Polym. Phys.*, 2016, **54**, 2151–2170.

61 B. D. Frounfelker, G. C. Kalur, B. H. Cipriano, D. Danino and S. R. Raghavan, Persistence of birefringence in sheared solutions of wormlike micelles, *Langmuir*, 2009, **25**, 167–172.

62 S. Y. Qin, W. Q. Ding, Z. W. Jiang, X. Lei and A. Q. Zhang, Directing an oligopeptide amphiphile into an aligned nanofiber matrix for elucidating molecular structures, *Chem. Commun.*, 2019, **55**, 1659–1662.

63 C. M. Rubert Pérez, N. Stephanopoulos, S. Sur, S. S. Lee, C. Newcomb and S. I. Stupp, The Powerful Functions of Peptide-Based Bioactive Matrices for Regenerative Medicine, *Ann. Biomed. Eng.*, 2015, **43**, 501–514.

64 S. R. Diegelmann, N. Hartman, N. Markovic and J. D. Tovar, Synthesis and Alignment of Discrete Polydiacetylene-Peptide Nanostructures, *J. Am. Chem. Soc.*, 2012, **134**, 2028–2031.

65 J. López-Andarias, M. J. Rodriguez, C. Atienza, J. L. López, T. Mikie, S. Casado, S. Seki, J. L. Carrascosa and N. Martín, Highly Ordered *n* / *p* -Co-assembled Materials with Remarkable Charge Mobilities, *J. Am. Chem. Soc.*, 2015, **137**, 893–897.

66 K. Nygård, S. A. McDonald, J. B. González, V. Haghighat, C. Appel, E. Larsson, R. Ghanbari, M. Viljanen, J. Silva, S. Malki, Y. Li, V. Silva, C. Weninger, F. Engelmann, T. Jeppsson, G. Felcsuti, T. Rosén, K. Gordeyeva, L. D. Söderberg, H. Dierks, Y. Zhang, Z. Yao, R. Yang, E. M. Asimakopoulou, J. K. Rogalinski, J. Wallentin, P. Villanueva-Perez, R. Krüger, T. Dreier, M. Bech, M. Liebi, M. Bek, R. Kádár, A. E. Terry, H. Tarawneh, P. Ilinski, J. Malmqvist and Y. Cerenius, ForMAX – a beamline for multiscale and multimodal structural characterization of hierarchical materials, *J. Synchrotron Radiat.*, 2024, **31**, 363–377.

67 S. Wojno, M. Fazilati, T. Nypelö, G. Westman and R. Kádár, Phase transitions of cellulose nanocrystal suspensions from nonlinear oscillatory shear, *Cellulose*, 2022, **29**, 3655–3673.

68 R. Kádár, M. Fazilati and T. Nypelö, Unexpected microphase transitions in flow towards nematic order of cellulose nanocrystals, *Cellulose*, 2020, **27**, 2003–2014.

69 R. Kádár, S. Spirk and T. Nypelö, Cellulose Nanocrystal Liquid Crystal Phases: Progress and Challenges in Characterization Using Rheology Coupled to Optics, Scattering, and Spectroscopy, *ACS Nano*, 2021, **15**, 7931–7945.

Chapter 4. Reversibly Tuning the Viscosity of Peptide-Based Solutions Using Visible Light

This Chapter is published as the following publication:

"Reversibly Tuning the Viscosity of Peptide-Based Solutions Using Visible Light"

S. Bianco, L. Wimberger, Y. Ben‐Tal, G. T. Williams, A. J. Smith, J. E. Beves and D. J. Adams, *Chemistry – A European Journal*, 2024, **30**, e202400544.

Author contributions

The author contributions are as follows: Conceptualization, D.J.A. and S.B.; methodology, S.B., Y.B-T, G.T.W., A.J.S. and D.J.A; Validation: S.B., Y.B-T, G.T.W.; Formal analysis: S.B., Y.B-T, G.T.W.; Investigation: S.B., Y.B-T, G.T.W., A.J.S.; Resources: S.B., L.W., Y.B-T, G.T.W., A.J.S., J.E.B. and D.J.A.; Data curation: S.B., G.T.W.; Writing—original draft: S.B. and D.J.A. Writing—review and editing: all. Visualization: S.B., Supervision: D.J.A. Project administration: D.J.A. Funding acquisition: D.J.A.

The manuscript has been included in the thesis as published and additional discussion from the ESI has been included *verbatim* in the main text of this Chapter for further clarity. The dipeptide molecule used in this chapter was synthesised by Prof. Dave J. Adams (University of Glasgow), while the photoacid molecule was synthesised and provided by Dr. Laura Wimberger and Prof. Jonathon E. Beves (UNSW). ^{1}H NMR measurements were collected by Dr. Yaen Ben-Tal and Dr. George T. Williams (University of Southampton) and analysed by Simona Bianco. Where necessary, acknowledgements have been provided in the Figure captions. SAXS data was collected by Simona Bianco with the help of Dr. Libby J. Marshall (University of Glasgow), Dr. Max J. S. Hill (University of Glasgow) and Dr. Chloe M. Wallace (University of Glasgow) and the data was analysed and processed by Simona Bianco. The rest of the presented data has been collected, visualised and analysed by Simona Bianco.

4. Reversibly Tuning the Viscosity of Peptide-Based Solutions Using Visible Light

Simona Bianco,[a] Laura Wimberger,[b] Yael Ben-Tal,[c] George T. Williams,[c,d] Andrew J. Smith,[e] Jonathon E. Beves,[b] Dave J. Adams*[a]

[a] School of Chemistry, University of Glasgow, Glasgow G12 8QQ, UK

[b] School of Chemistry, UNSW Sydney, Sydney NSW 2052 (Australia)

[c] School of Chemistry, University of Southampton, Southampton SO17 1BJ (UK)

[d] Institute for Life sciences, University of Southampton, Southampton SO17 1BJ (UK)

[e] Diamond Light Source Ltd., Diamond House, Harwell Science and Innovation Campus, Didcot, Oxfordshire OX11 0DE (UK)

4.1 Abstract

Light can be used to design stimuli-responsive systems. We induce transient changes in the assembly of a low molecular weight gelator solution using a merocyanine photoacid. Through our approach, reversible viscosity changes can be achieved *via* irradiation, delivering systems where flow can be controlled non-invasively on demand.

4.2 Manuscript

Driven by inspiration of biological systems that operate out-of-equilibrium, the design of systems capable of undergoing transient changes in self-assembly have gained significant interest in the field of systems chemistry.[1–3] Peptide-based low molecular weight gelators (LMWGs) are interesting candidates for such systems due to their stimuli-responsive behaviour.[4,5] At high pH, these materials self-assemble through non-covalent interactions to form micellar aggregates, such as worm-like micelles, spherical micelles, nanotubes, or fibrils.[6,7] Due to the nature of their interactions, reversible changes in self-assembly or morphology can be obtained upon application of a variety of external triggers, such as light, electricity, pH or temperature.[8–10] Specifically, light is an attractive trigger to induce stimuli-responsive behaviour as it is non-invasive and can be applied with high spatiotemporal control, allowing the formation of patterned materials or surfaces. Photo-responsive systems comprising of LMWGs can be designed by appending photo-responsive moieties to the molecule or by introducing photo-responsive molecules in presence of the LMWG in solution.[11] For this purpose, photoacids can be used to trigger gelation or aggregation

responses by protonating pH-responsive end groups under irradiation. For instance, metastable photoacids have been used to produce light-triggered supramolecular gels,[12–14] form supramolecular gels on photo-patterned surfaces,[15] induce light-triggered reversible gel-to-sol transitions[16–19] or generate reversible changes in supramolecular self-assembly or functionality for surfactant systems[20] and DNA-based systems.[21,22]

Here, we used a merocyanine photoacid **1** (Figure 4.1)[23] to induce transient pH changes in a functionalised dipeptide solution and achieve reversible changes in viscosity. Under irradiation with visible light, merocyanine photoacids like **1** can isomerise to the ring-closed spiropyran form **2**, releasing a proton and leading to a significant pH drop.[23–25] In the case of photoacid **1**, this process can be repeated for at least 10 cycles, with minimal changes to the pH-switching properties of the system.[23] Based on these observations, we investigated the pH-switching behaviour of photoacid **1** in the presence of functionalised dipeptide **1ThNapFF** (Figure 4.1).

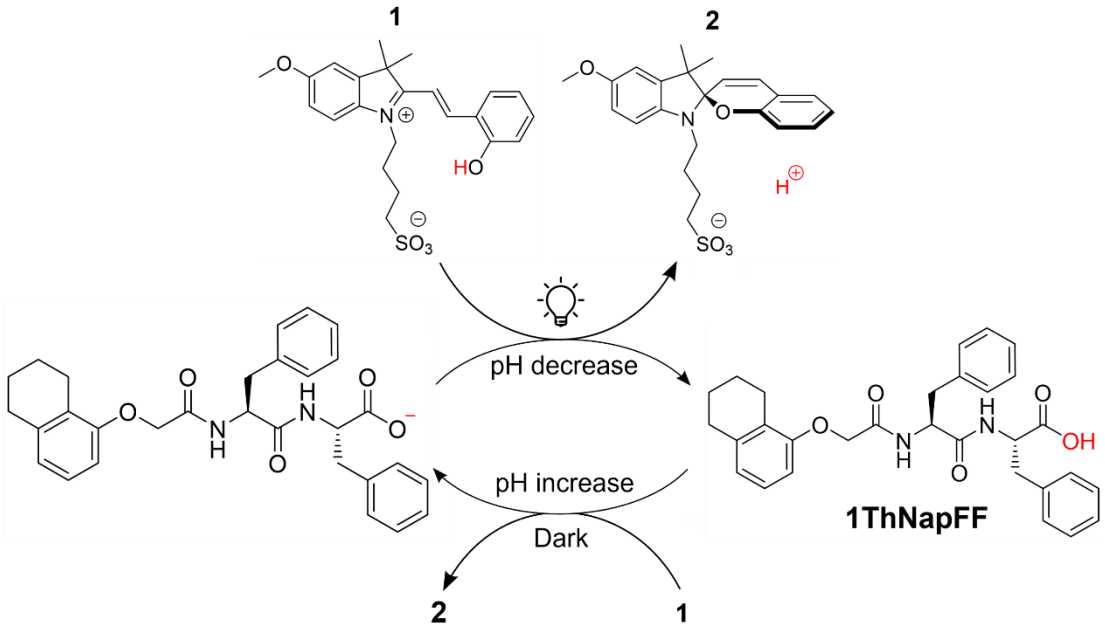

Figure 4.1. Schematic representation of the dynamic system presented in this work. Light-triggered isomerisation of merocyanine photoacid **1** to spiropyran **2** in presence of deprotonated **1ThNapFF** leads to a decrease in pH and protonation of the carboxylic acid moiety. In the dark, the system relaxes back to the initial pH, deprotonating **1ThNapFF** once more.

At high pH, **1ThNapFF** self-assembles into worm-like micellar structures.[26,27] When the pH is decreased below the apparent pK_a of the gelator (~6.3)[28], protonation of the carboxylic acid end leads to the formation of a network of fibres, often resulting in gelation.[29] We show

that photoacid **1** can be used to reversibly change the pH of the solution, leading to controllable dynamic changes in viscosity. A similar method of inducing reversible gel-to-sol transitions for a small dipeptide (**FF**) has been previously reported using a merocyanine photoacid.[16] Compared to the previous system, here we show a system capable of switching viscosity in water-based solutions instead of organogels. Further, the presence of a solution phase throughout allows this system to be easily loaded in microfluidic cells, where the flow can be controlled on-demand using light. The pH switch here is induced within a larger window from a basic pH, allowing the system to be applicable to a wider range of materials. We have also shown characterisation of the system *in situ* across different length scales using a variety of techniques.

Solutions of **1ThNapFF** were prepared at 1.5 mg/mL (3 mM) at pH 7.2, followed by addition of photoacid **1** (1.5 mM) and KCl (20 mM, added to mimic preparation of photoacid solution as previously reported).[23] The salt does not significantly affect the gelator behaviour (Figure 4.2).

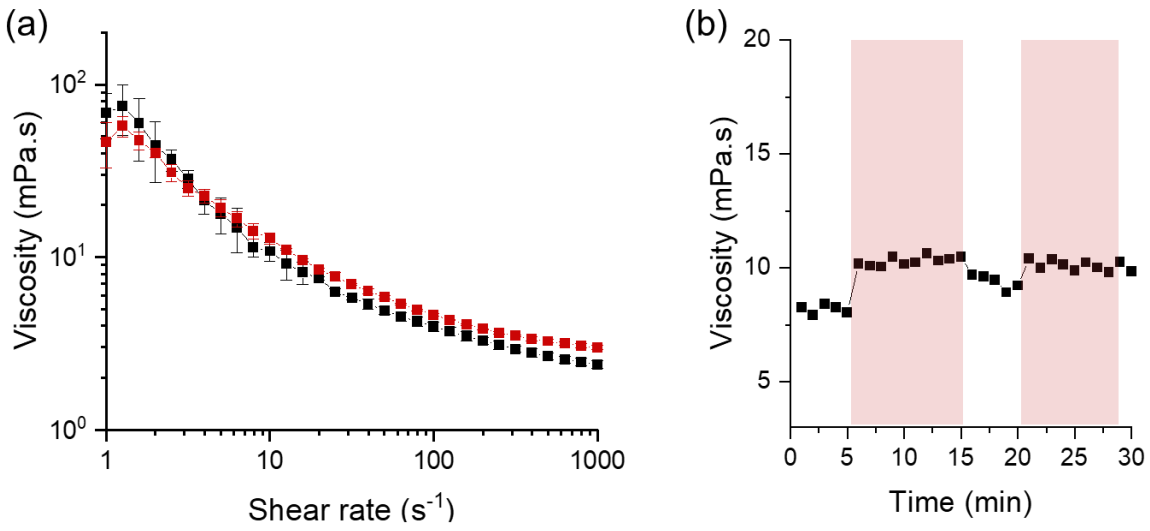

Figure 4.2. (a) Shear viscosity data for a solution of **1ThNapFF** (1.5 mg/mL) at pH 7.2 in presence of 20 mM KCl (red data) and 0 mM KCl (black data). (b) Constant shear viscosity measurement under irradiation of a solution of **1ThNapFF** (1.5 mg/mL) and **1** (1.5 mM) with 0 mM KCl. The red-shaded areas indicate irradiation with 450 nm light.

The dipeptide concentration in this work was chosen due to the limit of solubility of photoacid **1** (3mM), ensuring dissolution of the photoacid up to 1 equivalent with respect to **1ThNapFF**. We note that this is lower compared to the concentration typically used for gelation of **1ThNapFF** (concentrations of 2 mg/mL and greater).[26] Two concentrations of photoacid **1** were initially investigated to test the effect of the amount of protonation within

the sample. With a photoacid **1** concentration of 1 equivalent with respect to the gelator (3 mM), reversible viscosity increase was observed (Figure 4.3). However, localised gelation domains did not allow homogeneous irradiation of the sample (Figure 4.3), resulting in low control over the system light-triggered response as well as re-usability.

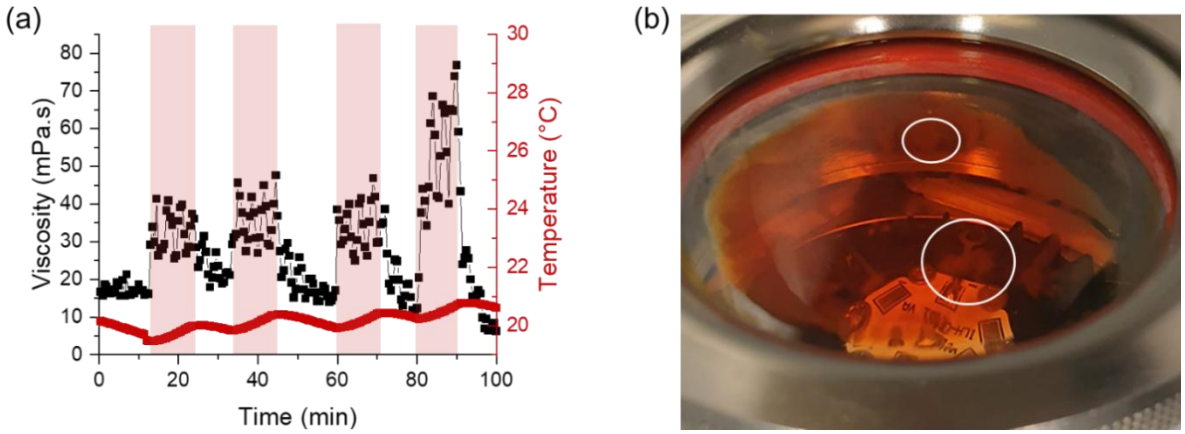

Figure 4.3. (a) Constant shear viscosity measurement recorded under irradiation for a solution **1ThNapFF** (1.5 mg/mL) and **1** (3 mM). The red shaded areas indicate irradiation of the sample with 450 nm light. (b) Image of a solution of **1ThNapFF** (1.5 mg/mL) and **1** (3 mM) after the irradiation cycles, highlighting the presence of localised gel domains within the solution (white circles).

Because of this, a lower concentration of 1.5 mM (0.5 eq. to the gelator) was used throughout the rest of this work. A decrease in viscosity was observed upon addition of photoacid **1** to the solution compared to **1ThNapFF** alone (Figure 4.4a). This suggests a potential interaction between the two components, leading to higher dissolution of the **1ThNapFF** molecule. This is further shown by small angle X-ray scattering (SAXS, Figure 4.4b). At pH 7.2, an increase in the fibre radius from 10 nm to 12 nm is observed in the solutions containing the photoacid (Figure 4.4b, red data) compared to solutions without (Figure 4.4b, black data). In particular, the fits to the data show a decrease in lateral association of the fibres upon addition of **1**, indicating that the additive is potentially getting incorporated in the micellar structures and affecting the molecular packing of the dipeptide (Figures 4.6 and 4.7, Tables 4.1 and 4.2).

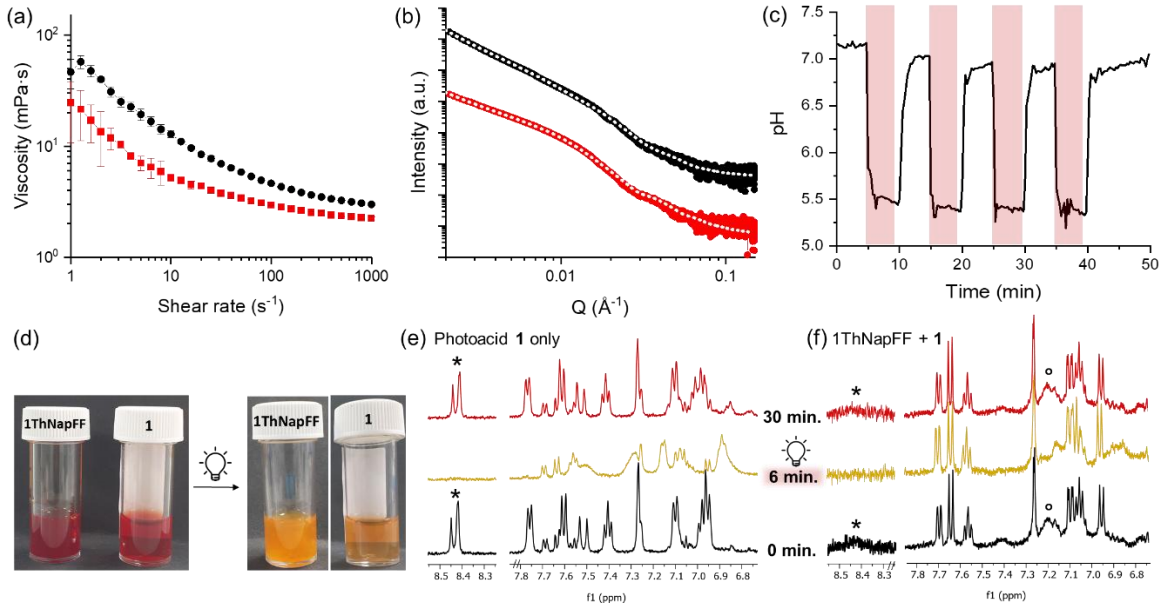

Figure 4.4. Viscosity (a) and SAXS data (b) of solutions of **1ThNapFF** (1.5 mg/mL) with photoacid **1** (1.5 mM) (red square) and without (black circle). Fits to the SAXS data (white dots) have been overlayed on the respective dataset. The SAXS patterns have been offset for clarity. (c) pH-switching behaviour for a solution of **1ThNapFF** (1.5 mg/mL) in presence of photoacid **1** (1.5 mM) over 4 irradiation cycles. The red-shaded areas indicate illumination with 450 nm LED; (d) photographs of solutions before and after irradiation of photoacid **1** (1.5 mM) with **1ThNapFF** (1.5 mg/mL) (left vial) and without (right vial); (e) NMR spectra of photoacid **1** in D_2O (1.5 mM) prior to irradiation (black), after 6 minutes of irradiation (yellow) and after 30 minutes of relaxation in the dark (red), the peak corresponding to the characteristic alkene peak of **1** (*) is highlighted to show the change upon irradiation; (f) NMR spectra of a D_2O solution of **1ThNapFF** (1.5 mg/mL) and photoacid **1** (1.5 mM) prior to irradiation (black), after 6 minutes of irradiation (yellow) and after 30 minutes of relaxation in the dark (red). The broad peaks corresponding to the characteristic alkene peak of **1** (*) and broad peak related to **1ThNapFF** (°) have been labelled. Full NMR spectra can be found in Figures 4.9 – 4.13. The data presented in (e) and (f) has been collected by Yael Ben-Tal and George T. Williams, University of Southampton.

We then investigated the pH-switching behaviour of the composite solution under irradiation with LED light at 450 nm. The pH drops from 7.2 to 5.3 upon turning on the light (Figure 4.4c), accompanied by a change in colour from red to yellow (Figure 4.4d). The **1ThNapFF** solution appears more turbid after irradiation (Figure 4.4d, left vial), suggesting further aggregation of the self-assembled structure. The pH drop can be cycled for at least 4 consecutive cycles of 5-minute irradiations (Figure 4.4c), with a similar pH reached in all

repetitions (≈5.3). In the dark, the kinetics of pH recovery are slower than the light-induced pH drop, and the pH was found not to increase back to the initial value of 7.2 over the cycles. Longer relaxation times (30 minutes) are required for the pH to recover to values close to the initial pH, and a slightly lower pH is typically recorded (pH 7.1). The pH switching behaviour of a solution of just photoacid (1.5 mM) was tested to observe the behaviour of the solution within the same irradiation times as the composite solution (Figure 4.5). The solution was irradiated in the same set-up, by switching the light on after 5 minutes in the dark, irradiating the sample for 5 minutes and allowing the system to relax for 5 minutes in the dark. The process is cyclable and reaches a lower pH than the one reached with **1ThNapFF** (Figure 4.4c), suggesting that aggregation or interactions between the dipeptide and **1** might impede the photoacid to fully isomerise under irradiation. In this case, the pH is found to still not fully relax back to the initial 7.2 ± 0.1 over the course the irradiation cycles, indicating that longer times are required to obtain this. This was also previously observed by for light-responsive DNA assemblies with photoacid **1**.[30]

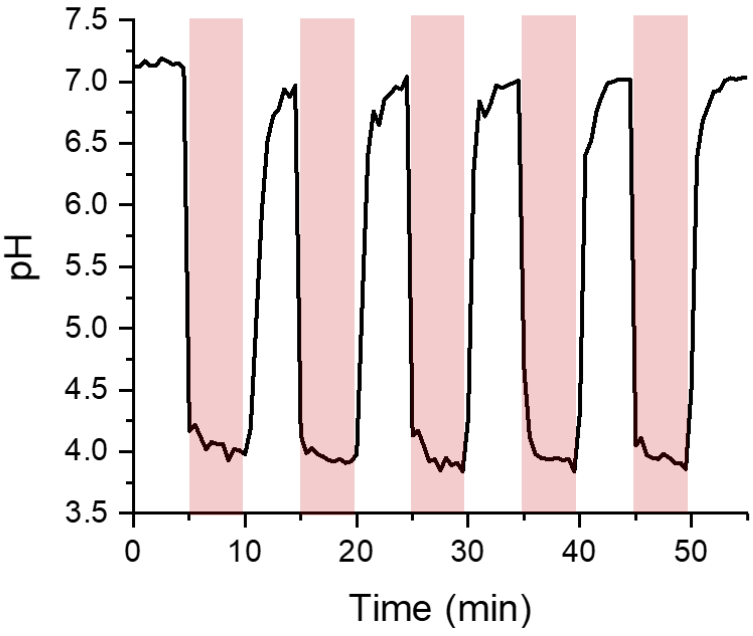

Figure 4.5. pH measurement of a solution of photoacid **1** (1.5 mM) at pH 7.2 under 5 cycles of 5-minute irradiation with a 450 nm LEDs.

Potential interactions between the spiropyran **2** and the dipeptide could cause this slower relaxation. We note, however, that the pH is observed to fully recover to its initial value after overnight relaxation in the dark. Interestingly, no gelation was observed in the sample upon lowering the pH. This is likely because the kinetics of the ring-closing are faster than gelation kinetics or due to the low concentration of **1ThNapFF** used in this study. Nonetheless, a

visual increase in viscosity was observed immediately after irradiation, indicating that the pH drop is leading to changes in aggregation.

To further understand this behaviour on the molecular and structural level, *in situ* irradiation measurements during NMR and SAXS were performed (Figures 4.6 – 4.13). In the dark, the NMR spectrum of the **1ThNapFF** and **1** solution shows several changes compared to the spectrum of **1** by itself (Figure 4.4e and 4.4f, black spectra). The characteristic alkene doublet of photoacid **1** at 8.45 ppm broadens significantly in the presence of **1ThNapFF** (Figure 4.4f, *), suggesting interactions between **1** and **1ThNapFF**. Due to the low number of scans, the characteristic peak from the spiropyran **2** at 5.80 ppm was too low to distinguish within the noise. Furthermore, a doublet centred at 6.95 ppm can be observed instead of a multiplet around 7.00 – 6.97 ppm. The doublet can be correlated to the signal of the alkene in spiropyran form **2**.[23] It is therefore possible that **1** is significantly interacting with the dipeptide, resulting in more intense peaks from **2**, which might interact less with **1ThNapFF**. Upon irradiation, signals related to **1** disappear (Figures 4.4e, 4.4f, yellow spectra, Figures 4.10, 4.12), agreeing with the literature data.[23] Additionally, a broad peak assigned to **1ThNapFF** at 7.15 ppm in the composite solution is observed to disappear under irradiation (Figure 4.4f, °, Figure 4.12). The data suggest that fewer interactions between the photoacid molecule and the dipeptide occur when there is less **1** present in solution at low pH. As a result, **1ThNapFF** can aggregate further with itself, becoming NMR invisible. This is likely because less interactions with merocyanine **1** can occur under irradiation, favouring more interactions between the dipeptide molecules and leading to an increase in viscosity. The NMR data show that this switch in assembly is reversible, as the peaks recover their intensity in the dark (Figures 4.4e, 4.4f, red spectra, Figures 4.10, 4.12). To further prove that the changes are related to the presence of the two interacting species in the system, the spectra of just **1ThNapFF** (1.5 mg/mL) was collected under in situ irradiation at pD 7.2. As expected, no changes in the spectra can be seen upon irradiation, confirming that the aggregation changes are brought about by the light-induced pH switch in presence of photoacid **1** (Figure 4.13).

Interestingly, SAXS data of the same solution showed no change in pattern under irradiation and in the dark (Figure 4.14a, yellow and red data, Figures 4.6, 4.7 and Tables 4.1, 4.2). All datasets were fit to the same fit curve to highlight the similarities in scattering data. Minor decreases in intensity of the data can be observed over time, which could be ascribed to X-ray damaging over the course of the measurements. The SAXS data here extends to around 300 nm, which is below the length of the fibres (< 500 nm). It is likely that the interactions

between the molecules are occurring at the network level and ultra-small angle X-ray scattering is required to assess them.

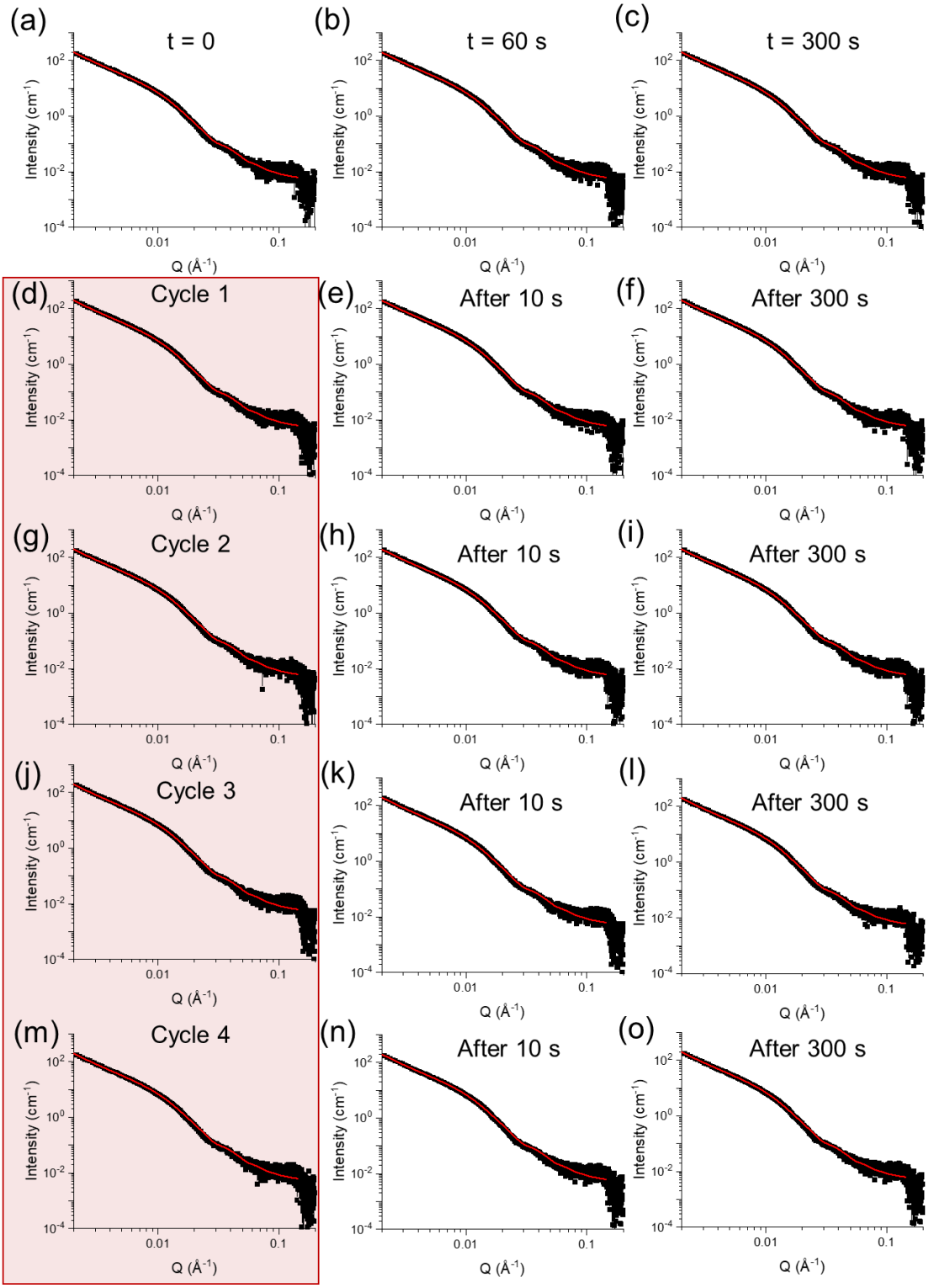

Figure 4.6. SAXS data (black squares) with model fits (red lines) for a solution **1ThNapFF** (1.5 mg/mL) and photoacid **1** (1.5 mM) in the dark at pH 7.2 (a) – (c), after 30 seconds of irradiation (d), (g), (j), (m) and after 5 minutes of relaxation (e) - (f), (h) – (i), (n) – (o) over 4 cycles. The red square indicates samples that were measured under irradiation.

Table 4.1. Fitting parameters for SAXS data in Figure 4.6. The data was fit to an elliptical cylinder (A) combined with a power law model (B). Values that were manually added and fixed have been labelled with *.

1ThNapFF + **1**	**Value**	**Error**
Background / cm^{-1}	0.0063*	/
A_scale	$2.18x10^{-4}$	$1.74x10^{-6}$
A_radius_minor / Å	119.7	0.63
A_axis_ratio	2.1	0.018
A_length / Å	5000*	/
B_scale	$5.77x10^{-6}$	$3.19x10^{-7}$
B_power	2.7	0.009
χ^2	1.12	

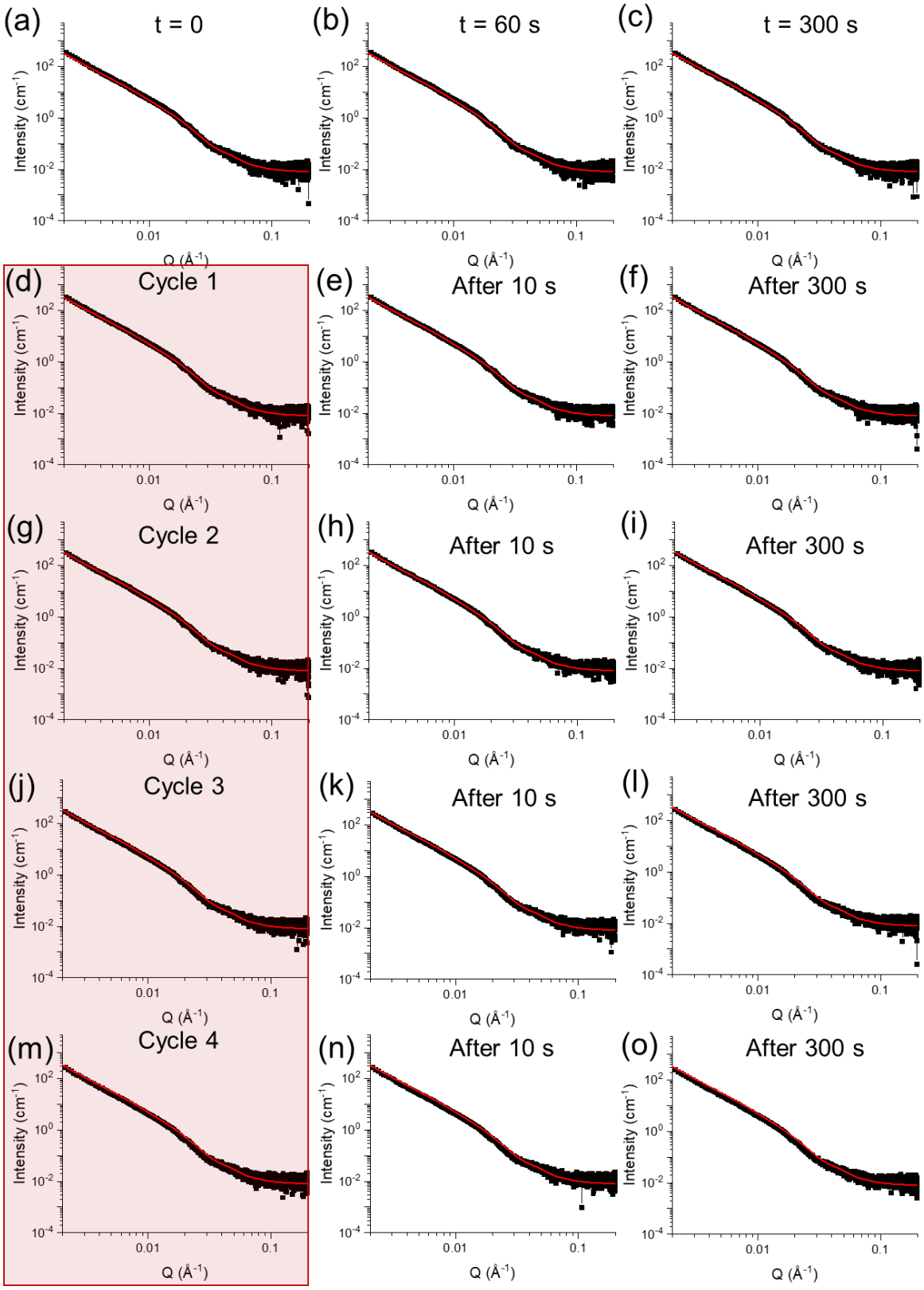

Figure 4.7. SAXS data (black squares) with model fits (red lines) for a solution **1ThNapFF** (1.5 mg/mL) in the dark at pH 7.2 (a) – (c), after 30 seconds of irradiation (d), (g), (j), (m) and after 5 minutes of relaxation (e) - (f), (h) – (i), (n) – (o) over 4 cycles. The red square indicates samples that were measured under irradiation.

Table 4.2. Fitting parameters for SAXS data in Figure 4.7. The data was fit to an elliptical cylinder (A) combined with a power law model (B). Values that were manually added and fixed have been labelled with *. We note that the data for the solution containing just **1ThNapFF** was difficult to fit, as Sasview would converge to models that were not able to fully capture the bump in the data at around 0.03 $Å^{-1}$. Hence, values were manually added to the fit to obtain data that best followed the scattering curve, which resulted in an elliptical cylinder model with a radius of 10.0 nm. An axis ratio between 3 and 4 provided a good fit to the data, with the value of 3.5 capturing the data well. This can be related to some polydispersity in the system and the size of the aggregates formed in solution.

1ThNapFF	**Value**	**Error**
Background / cm^{-1}	0.008*	/
A_scale	$1.40x10^{-4}$	$3.30x10^{-7}$
A_radius_minor / Å	100*	/
A_axis_ratio	3.5*	/
A_length / Å	5000*	/
B_scale	$1.49x10^{-6}$	$1.90x10^{-9}$
B_power	3.1*	/
χ^2	1.73	

No significant scattering was instead observed for the sample containing just photoacid **1** and the data could be simply fit to a power law model (Figure 4.8, Table 4.3).

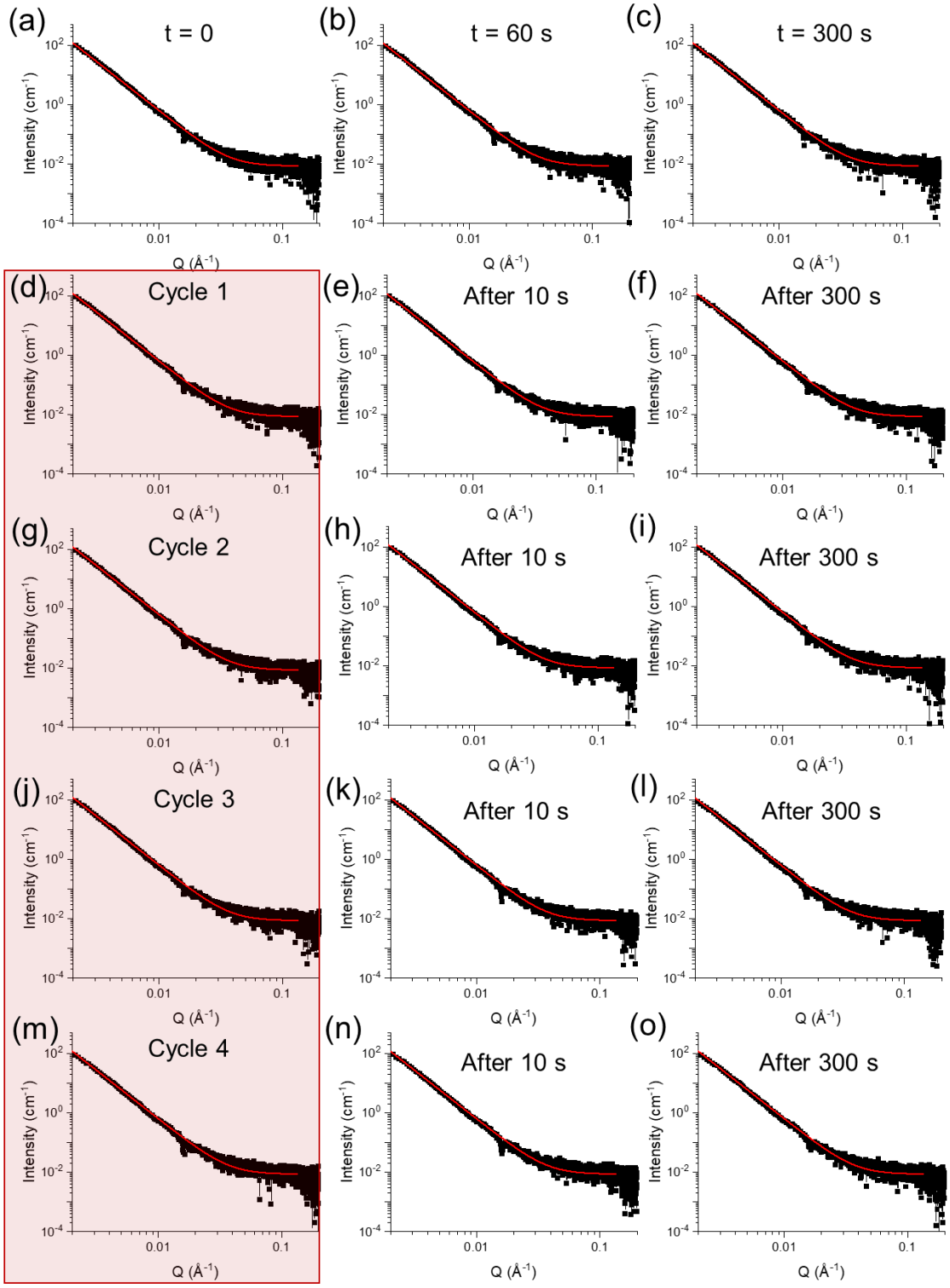

Figure 4.8. SAXS data (black squares) with model fits (red lines) for a solution of photoacid **1** (1.5 mM) in the dark at pH 7.2 (a) – (c), after 30 seconds of irradiation (d), (g), (j), (m) and after 5 minutes of relaxation (e) - (f), (h) – (i), (n) – (o) over 4 cycles. The red square indicates samples that were measured under irradiation.

Table 4.3. Fitting parameters for SAXS data in Figure 4.8. The data was fit to a power law model. Values that were manually added and fixed have been labelled with *.

Photoacid 1	**Value**	**Error**
Scale	1.92×10^{-7}	4.48×10^{-9}
Background / cm^{-1}	0.009*	/
Power	3.6	0.004
χ^2	1.06	

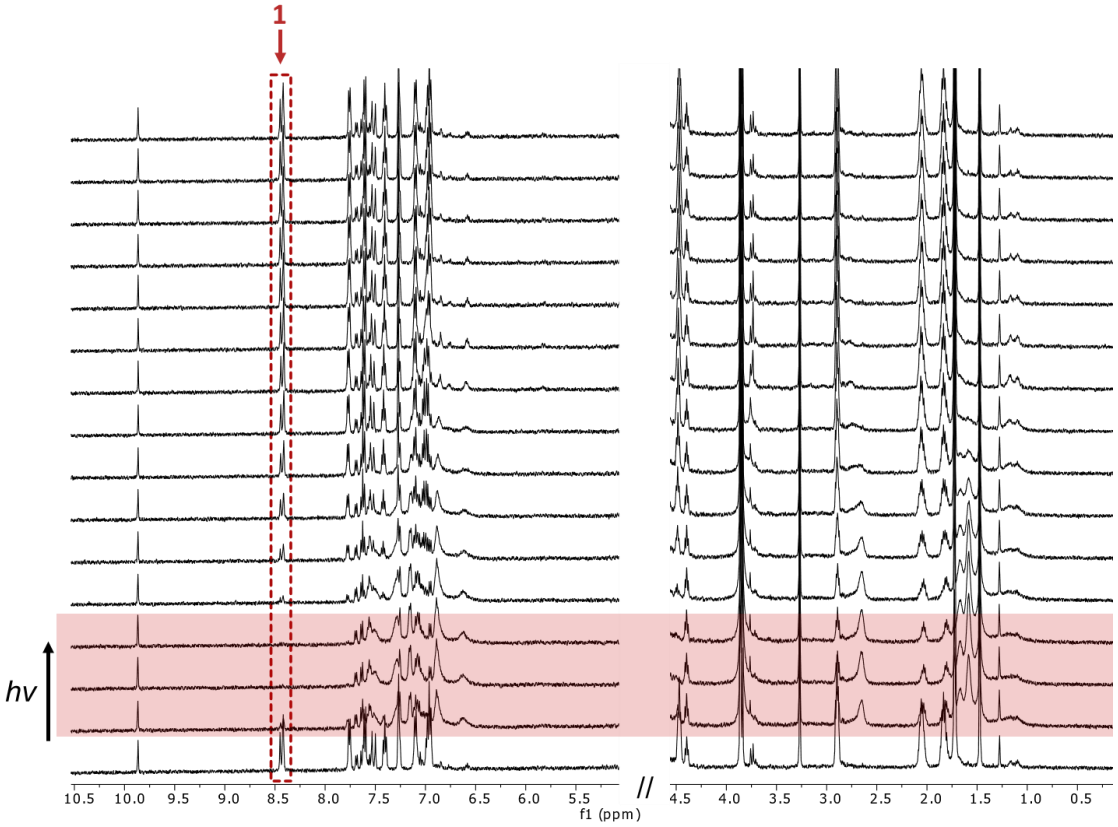

Figure 4.9. ^{1}H NMR spectra of **1** at pD 7.2 (1.5 mM) under irradiation and relaxation. The bottom spectrum was collected in the dark without irradiation, the three spectra above show the sample under irradiation. The remaining spectra show the sample recovering in the dark. The top spectrum was collected after 30 minutes of relaxation. The red shaded area indicates irradiation. The red dashed square indicates the characteristic peak of **1**. The data presented has been collected by Yael Ben-Tal and George T. Williams, University of Southampton.

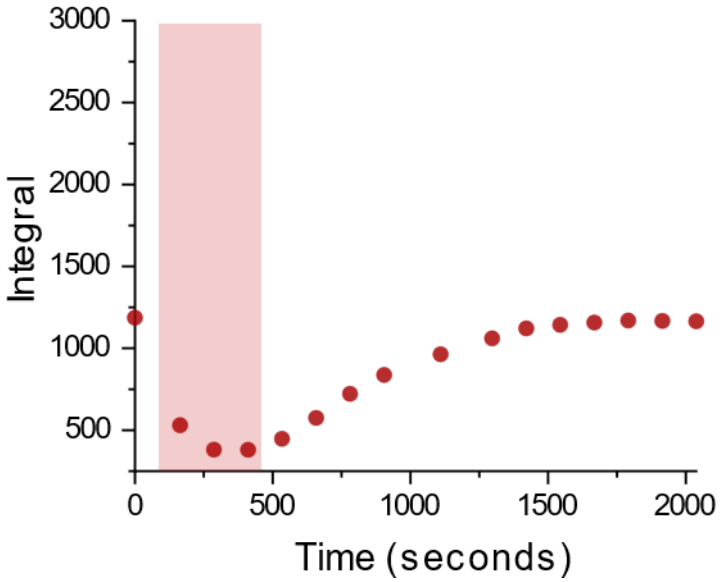

Figure 4.10. Trace following the absolute integral of the merocyanine characteristic peak at 8.42 ppm under in situ irradiation in the NMR at pD 7.2. The data was extracted from the red-dashed rectangle in the ^{1}H NMR spectra in Figure 4.9. The red-shaded area indicates irradiation.

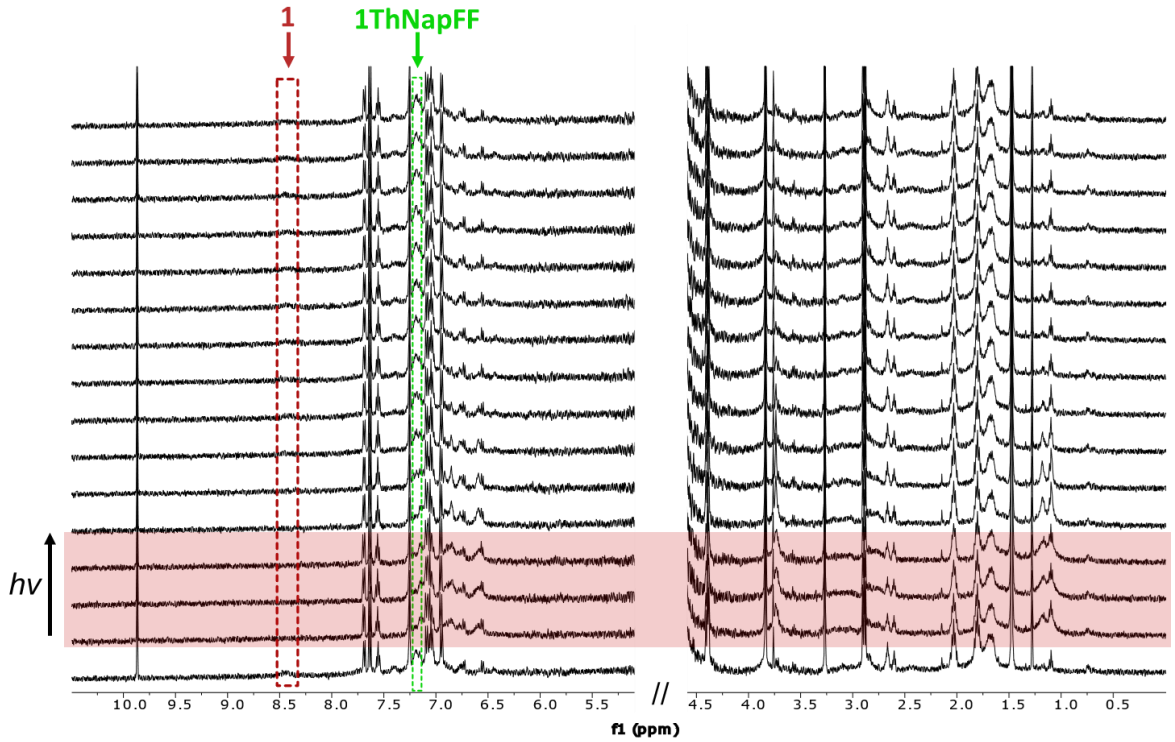

Figure 4.11. ^{1}H NMR spectra of **1** (1.5 mM) and **1ThNapFF** (1.5 mg/mL) at pD 7.2 under irradiation and relaxation. The bottom spectrum was collected in the dark without irradiation, the three spectra above show the NMR spectra of the sample under irradiation. The remaining spectra show the sample recovering in the dark. The top spectrum was collected after 30 minutes of relaxation. The red shaded area indicates irradiation. The red dashed square indicates the characteristic peak of **1**, the green dashed square indicates the **1ThNapFF** peak. The data presented has been collected by Yael Ben-Tal and George T. Williams, University of Southampton.

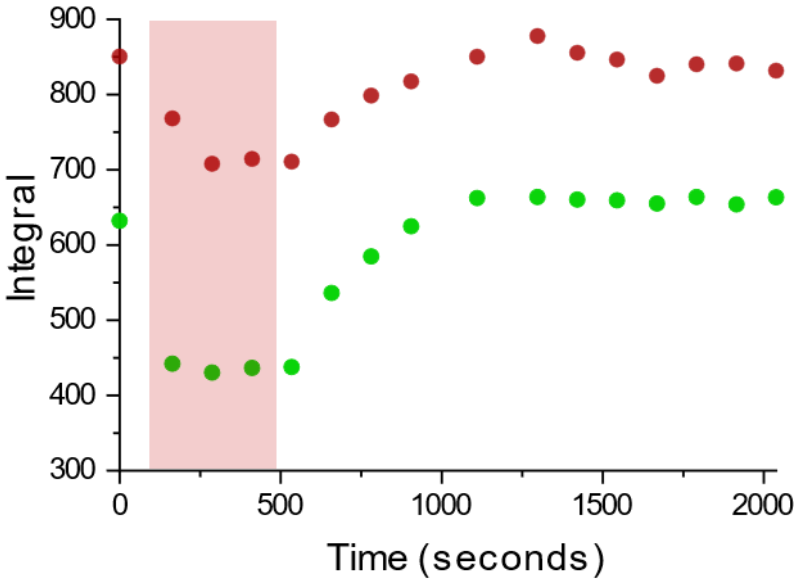

Figure 4.12. Trace following the absolute integral of the merocyanine characteristic peak at 8.42 ppm and the **1ThNapFF** peak at 7.21 ppm under in situ irradiation in the NMR at pD 7.2. The data was extracted from the red-dashed rectangle and the green-dashed rectangle in the ^{1}H NMR spectra in Figure 4.11. The red-shaded area indicates irradiation.

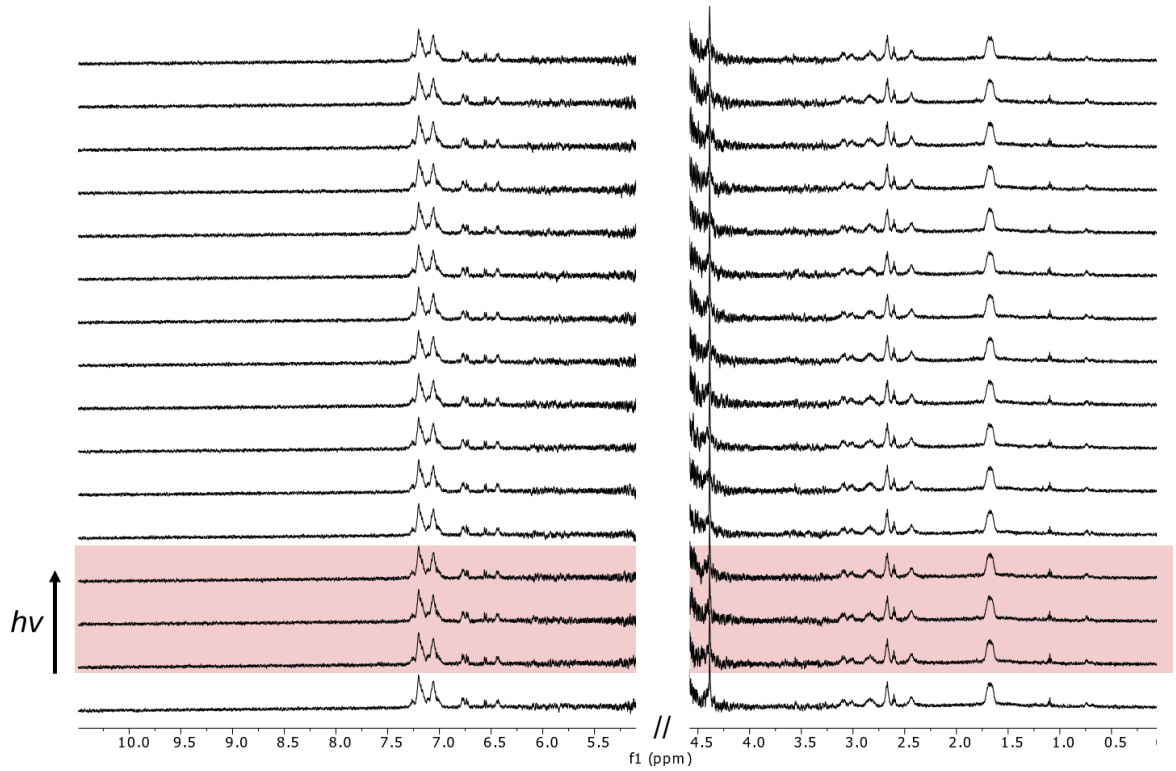

Figure 4.13. ^{1}H NMR spectra of **1ThNapFF** (1.5 mg/mL) at pD 7.2 under irradiation and relaxation. The bottom spectrum was collected in the dark without irradiation, the three spectra above show the NMR spectra of the sample under irradiation. The top spectrum was collected after 30 minutes of relaxation. The remaining spectra show the sample recovering in the dark. The red shaded area indicates irradiation. The data presented has been collected by Yael Ben-Tal and George T. Williams, University of Southampton.

To observe the changes in viscosity over time, constant shear viscosity measurements were performed under irradiation using a rheo-irradiation set-up with a quartz glass bottom plate and a bespoke 3D-printed LED holder (Section 4.3.3.1 in Experimental). The set-up was optimised to ensure that the sample measured was being irradiated with the light homogeneously. The sample was measured during 5 minutes of irradiation and then while recovering for 5 minutes in the dark. Under irradiation, the viscosity of the sample increases immediately (Figure 4.14b), staying at similar values until the LED is turned off. As the sample relaxes in the dark, the viscosity decreases back to values close to the initial value. The viscosity in the dark further increases over the course of the experiment. This can be ascribed to the fact that the de-aggregation of **1ThNapFF** might be slower than the pH recovery, resulting in higher protonation and aggregation over subsequent cycles. When no photoacid is added to a **1ThNapFF** solution, no changes in viscosity can be observed under irradiation (Figure 4.14c and Figure 4.15b). Similarly, no viscosity changes are seen in a photoacid-only solution upon irradiation (Figures 4.15a, 4.16c). To test the reproducibility

of the viscosity increase, viscosity measurements on the **1ThNapFF** and **1** solution were run during irradiation (Figure 4.14d). In all cases, shear-thinning behaviour can be observed, consistent with the presence of worm-like micellar structures in all samples. The viscosity under irradiation increases (Figure 4.14d, yellow) and it relaxes back to its original value in the dark (Figure 4.14d, red). This confirms that the viscosity changes are due to the large light-induced pH drop.

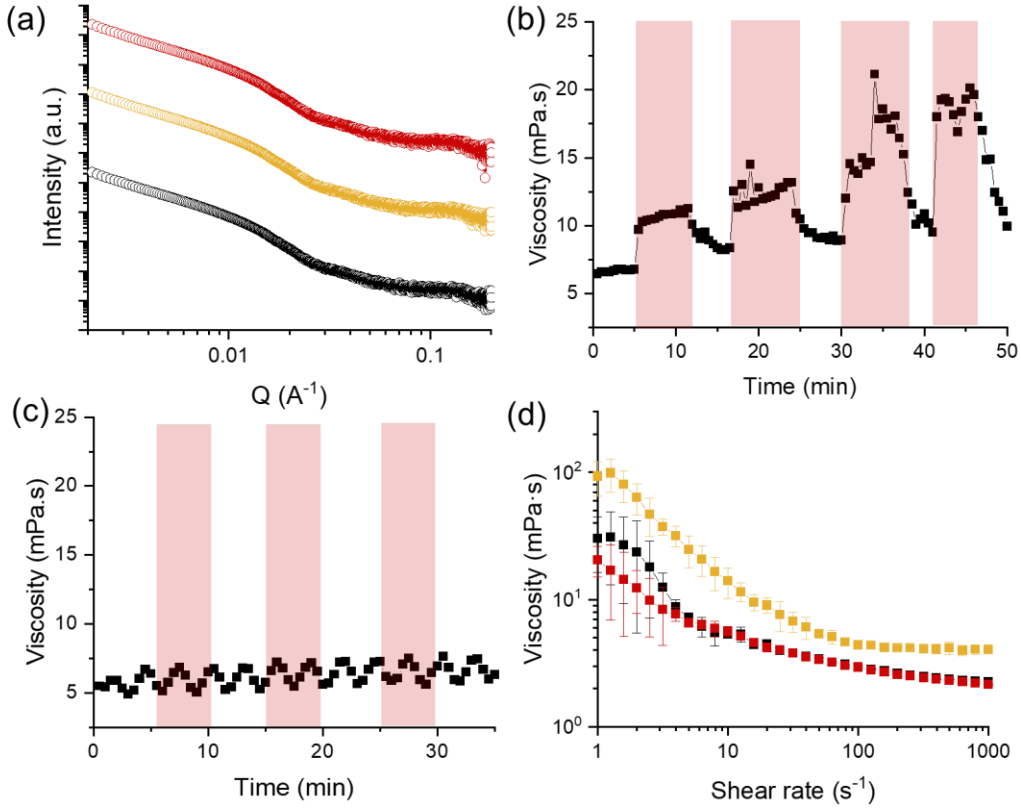

Figure 4.14. (a) SAXS data for a solution of **1ThNapFF** (1.5 mg/mL) with photoacid **1** (1.5 mM) in the dark (black), during irradiation (yellow), after relaxation (red). SAXS data has been offset for clarity. Constant shear viscosity under irradiation for a solution of **1ThNapFF** (1.5 mg/mL) (b) in presence of **1** 1.5 mM) and (c) without. (d) Viscosity data of solution of **1ThNapFF** (1.5 mg/mL) with photoacid **1** (1.5 mM) in the dark (black), during irradiation (yellow) and after relaxation (red). In all cases, red shaded areas indicate irradiation with 450 nm LED.

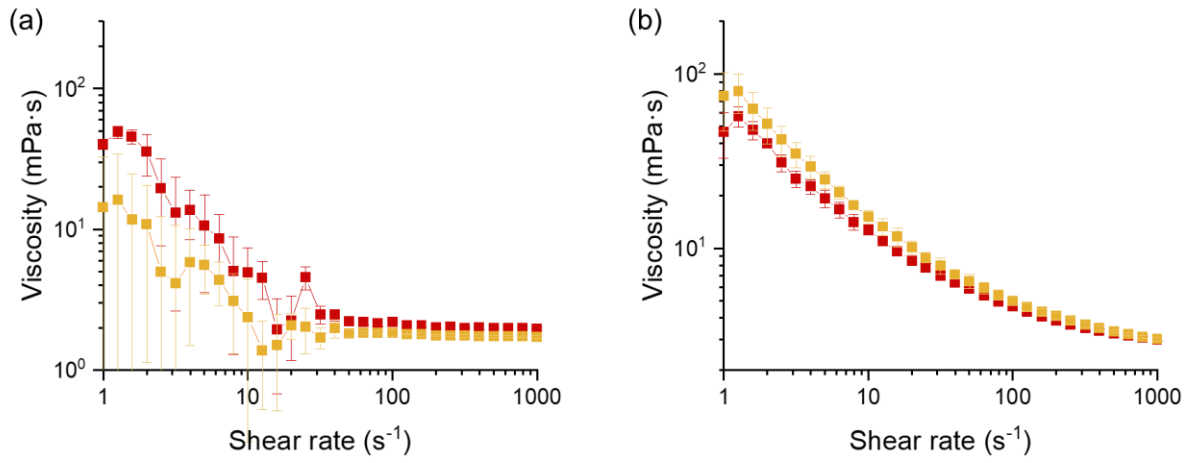

Figure 4.15. Viscosity measurements of a solution containing (a) only photoacid **1** (1.5 mM) and (b) only **1ThNapFF** (1.5 mg/mL). The red squares indicate the data prior to irradiation and the yellow squares indicate data after irradiation. The error bars are calculated from triplicate experiments.

Overall, the data indicate that we can reversibly induce increases in viscosity quickly and reversibly for 4 cycles on short timescales. By monitoring the temperature of the bottom plate of the rheometer, we can rule-out that such changes are induced by the increase in temperature upon irradiation (Figure 4.16).

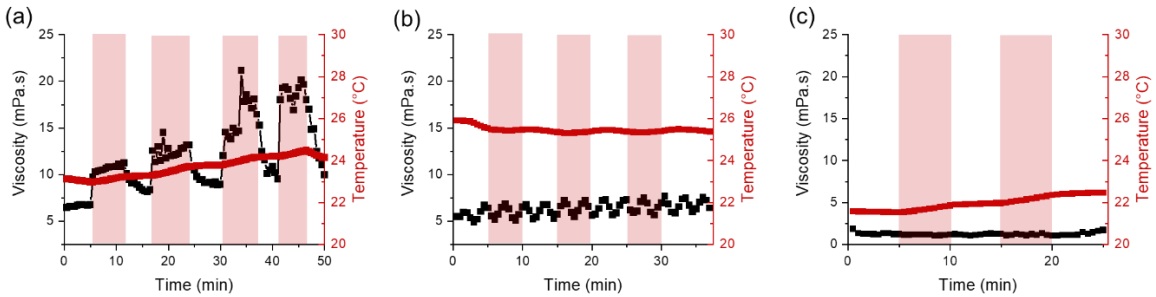

Figure 4.16. Constant shear viscosity measurements recorded under irradiation for (a) a solution of **1ThNapFF** and **1**, (b) **1ThNapFF** only and (c) photoacid **1** only. In all cases, final concentrations of **1ThNapFF** and **1** are 1.5 mg/mL and 1.5 mM. The red shaded areas indicate irradiation of the sample with 450 nm light, the black squares indicate the viscosity and red squares indicate temperature.

The observed behaviour can be used to control flow non-invasively by irradiation at specific locations. In this endeavour, a custom set-up was built to monitor changes in flow under irradiation (Figures 4.17, 4.18 and Section 4.3.3.4 in Experimental). The set-up consists of a syringe pump fitted with transparent tubing, connected to a pressure gauge *via* a t-piece. The pressure gauge is placed before the LEDs, allowing us to measure the pressure of the

solution as it flows prior to irradiation. At rest with no sample flowing, the pressure gauge detects a pressure of 0.7 mbar (Figure 4.17b). When the sample is pumped through the system (1 mL/min) in the dark, an increase in the detected pressure is observed to a constant value of around 1.8 mbar. Upon irradiation, a rapid increase in pressure is detected to 4.4 mbar (Figure 4.17b, red shaded area), ascribed to the increase in viscosity of the solution. In the dark, the pressure slowly reverts to 1.9 mbar as the sample relaxes. Using the same solution, a similar increase in pressure under irradiation was observed for at least two repeats (Figure 4.18), indicating the reproducibility of this set-up.

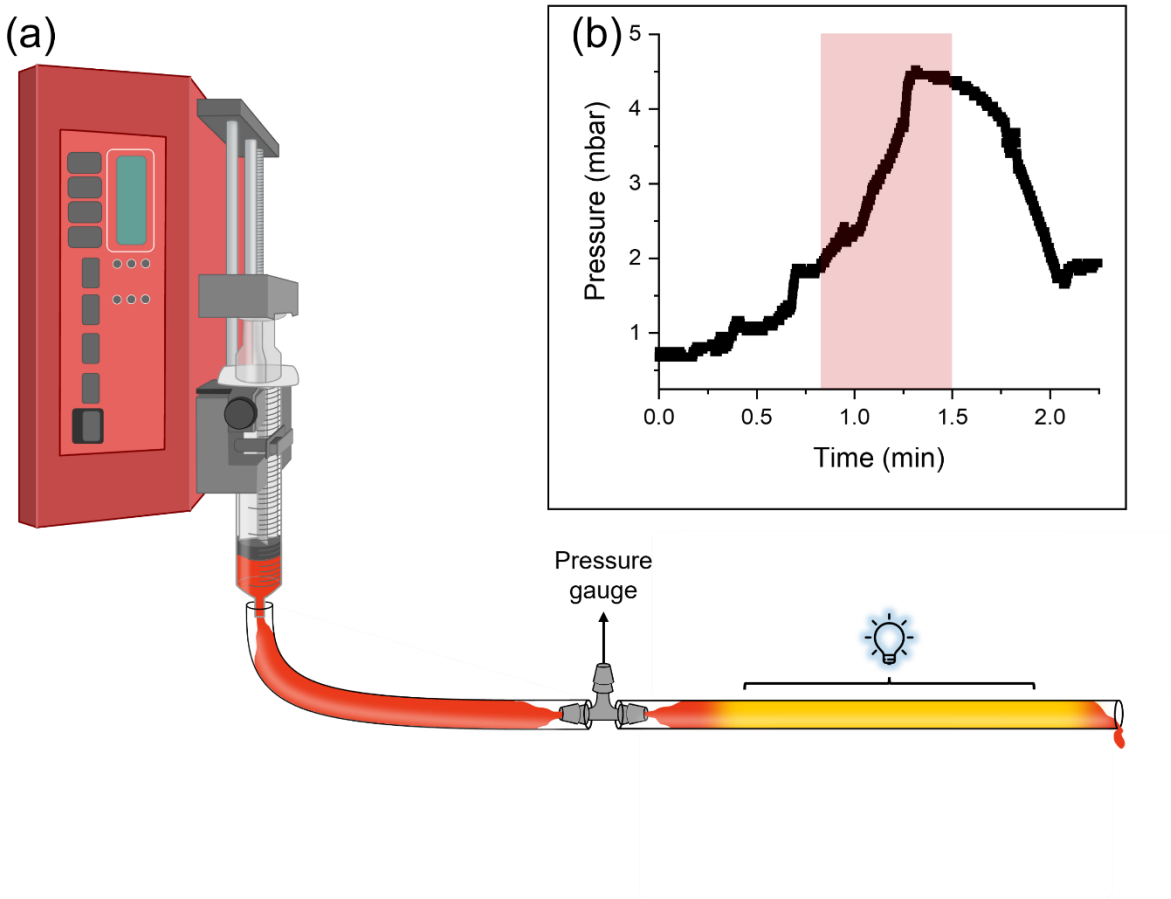

Figure 4.17. (a) Schematic representing the custom set-up to detect changes in pressure under irradiation used in this work. (b) Data collected for a solution of **1ThNapFF** (1.5 mg/mL) and **1** (1.5 mM) using the custom set-up. The red shaded area indicates irradiation with LED light (λ = 450 nm).

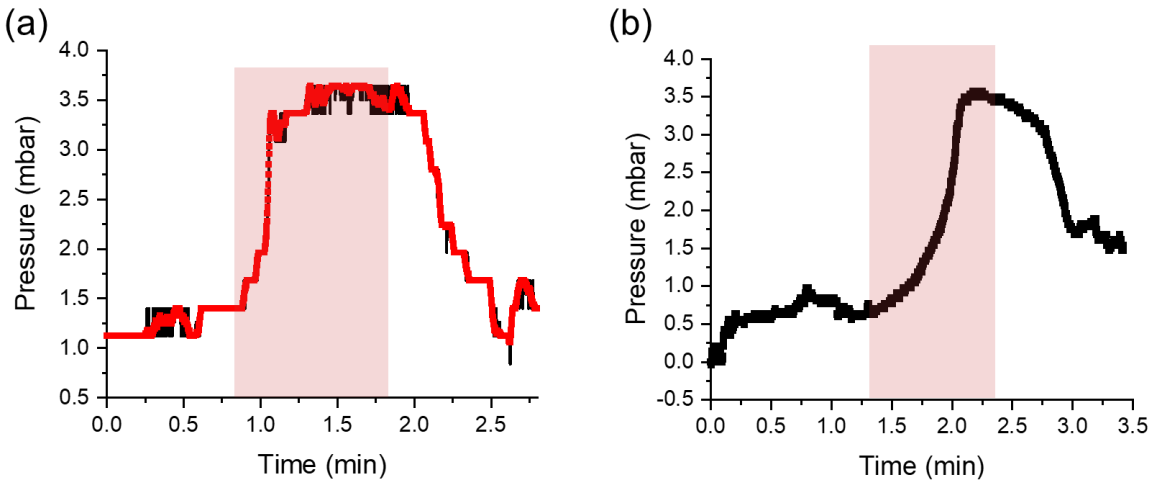

Figure 4.18. Data collected for a solution of **1ThNapFF** (1.5 mg/mL) and **1** (1.5 mM) using the custom set-up to detect pressure over two cycles. The red shaded area indicates irradiation with LED light (λ = 450 nm). In (a), black data is data collected at lower resolution and red data is the smoothed data for ease of comparison. The smoothed data was obtained using Origin with the Adjacent-Averaging.

In conclusion, we can combine the stimuli-responsive behaviour of a functionalised dipeptide with a photoacid capable of fast pH-switching. This allowed us to design a system capable of reversible changes in viscosity. Our data show that interactions between the dipeptide and the photoacid are responsible for a decrease in viscosity, which in turn increases once the merocyanine photoacid isomerises to its ring-closed form. The change in pH as well as viscosity is reversible and reproducible for at least 4 irradiation cycles, with the sample relaxing to a lower viscosity in the dark. This method provides a facile way to design systems where flow can be controlled non-invasively and with a high level of spatial control. Such systems showing reversible viscosity changes are interesting for applications within microscale devices. For instance, these responsive systems can be used to direct flow within a microfluidic environment and, specifically, generate photoresponsive microvalves that can be controlled by localised light-irradiation of the solution.[31,32] The fast kinetics of the system shown here would allow precise control of the opening and closing of the valves. The current challenge within these two-component systems is related to the solubility of the photoacid molecule, as it can limit the concentration of self-assembling molecules that can be added to induce the changes. Improving the solubility of the photoacid would allow applications of such system to a wider variety of small self-assembling molecules with different limits of dissolutions to achieve larger changes in viscosity. As a final point, the self-assembled structures formed by **1ThNapFF** persist at higher temperatures and heating

and cooling can be used to modify the viscosity of these systems[33], meaning that there is the potential for using these self-assembled systems at higher temperatures.

4.3 Experimental

4.3.1 Materials

1ThNapFF was synthesised as previously reported. [34–39] The merocyanine photoacid **1** was synthesised as previously reported.[23] All other reagents and solvents were purchased from Sigma-Aldrich and Alfa Aesar and used as received without further purification. De-ionised water was used throughout

4.3.2 Methodology

4.3.2.1 Solution Preparation

To prepare aqueous solutions of **1ThNapFF** without photoacid, **1ThNapFF** was weighed into a 7 mL Sterilin vial, followed by deionised water and 1 equivalent of 0.1M KOH to achieve a final concentration of 1.5 mg/mL. Typically, 5 mL of solution were prepared for ease of handling. The solutions were stirred overnight at 1000 rpm. The pH of the solution was adjusted up to 11.0 ± 0.1 using 1M KOH to ensure dissolution of any micellar aggregates. Then, the pH was brought down to 7.2 ± 0.1 using 1M HCl. During pH adjusting, the solutions were stirred for at least 30 minutes after addition of acid to ensure homogeneity as insufficient mixing could result in localised pH differences. If localised gelation occurred, samples were left to stir for at least 1 hour until full dissolution could be observed. KCl was added to the solution under stirring to achieve a final concentration of 20 mM. Solutions were prepared fresh every day for each measurement and the pH was checked before use to ensure a starting pH of 7.2 ± 0.1.

1ThNapFF solutions in presence of photoacid were prepared in a similar way. The solution was then added to a pre-weighed amount of photoacid **1** to achieve a final concentration of 1.5 mM. The solution was stirred at 1000 rpm for 30 minutes or until full dissolution of **1**. The pH was then checked to ensure an initial pH of 7.2 ± 0.1 and adjusted if needed. The pH did not change significantly after addition of **1**. For solutions of **1** without **1ThNapFF**, **1** was weighed in 7 mL Sterilin vials, followed by addition of 20 mM aqueous KCl solution (H_2O) to a final concentration of 1.5 mM. The solution was stirred for 30 minutes or until full dissolution at 1000 rpm. The pH was checked and adjusted to an initial pH of 7.2 ± 0.1 using either 0.1M KOH or 0.1M HCl. In all cases, to avoid interaction with light, the solutions were wrapped in tinfoil.

4.3.3 Characterisation

4.3.3.1 Viscosity measurements

Viscosity measurements of the samples prior to irradiation and during irradiation were performed using an Anton Paar Physica MCR302 rheometer with a temperature-controlled quartz bottom plate. To irradiate the sample, a 450 nm LED (0.7 A, RS Components Ltd) was held in place under the quartz bottom plate using a bespoke 3D-printed holder (Figure 4.19b). The set-up is shown in Figure 4.19a and 4.19b below. The intensity of the light was measured using a Thorlabs Optical Power Meter PM100D and Thorlabs sensor S/N: 16100711 to test the intensity of the light across the quartz plate. Based on the results, the intensity of the light was homogeneous at around 21 mW across a diameter of 30 mm. Hence, a CP25 geometry (cone angle 1°) was used to measure the viscosity of the samples in this study. As an example, a picture of the sample after irradiation is shown in Figure 4.19c, which looks yellow throughout, indicating homogeneous irradiation.

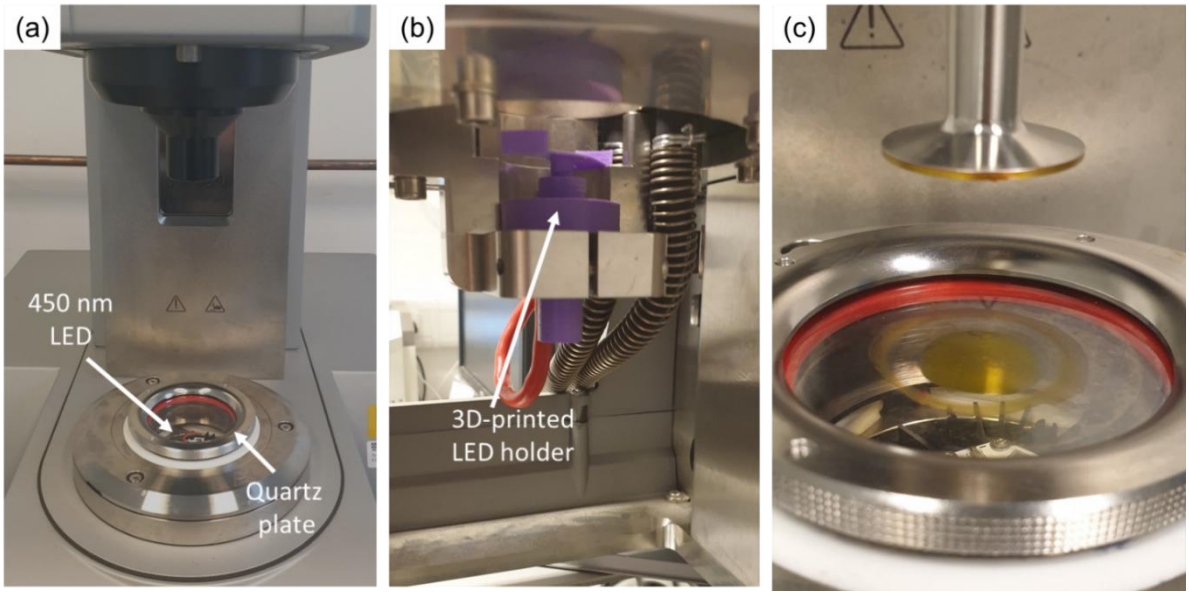

Figure 4.19. (a), (b) Irradiation set-up on the Anton Paar Physica MCR302 rheometer with a 450 nm LED powered by a constant-current power source. The pictures show the bespoke 3D-printed LED holder placed under the quartz plate. (c) Picture of a solution of **1ThNapFF** (1.5 mg/mL) and **1** (1.5 mM) after 30 seconds of irradiation under the CP25 geometry showing a homogeneous colour throughout.

For all viscosity measurements, all solutions were poured on the quartz bottom plate to avoid any shear-thinning. The top plate was lowered on the solution at a gap height of 0.047 mm and any excess was gently dabbed away with a small amount of paper towel. Dynamic viscosity was measured by collecting viscosity data at shear rates from 1 s^{-1} to 1000 s^{-1}. For

the constant viscosity measurements under irradiation, data points were collected every 30 seconds at a constant shear rate of 10 s^{-1}. The LED was manually turned on after 5 minutes in the dark and then turned off after 5 minutes of irradiation. Care was taken in observing the temperature of the rheometer bottom plate to observe any sharp increases under irradiation.

4.3.3.2 pH measurements

pH measurements under irradiation were performed using a HANNA FC200 pH probe with a 6 mm x 10 mm conical tip with an accuracy of ± 0.1. The pH change of the system was monitored under irradiation using a custom-made set-up in a dark box, shown below (Figure 4.20). The sample was positioned on a bespoke 3D-printed holder, with two LEDs (450 nm, 0.7 A, RS Components Ltd) placed at 1 cm away from the sample.

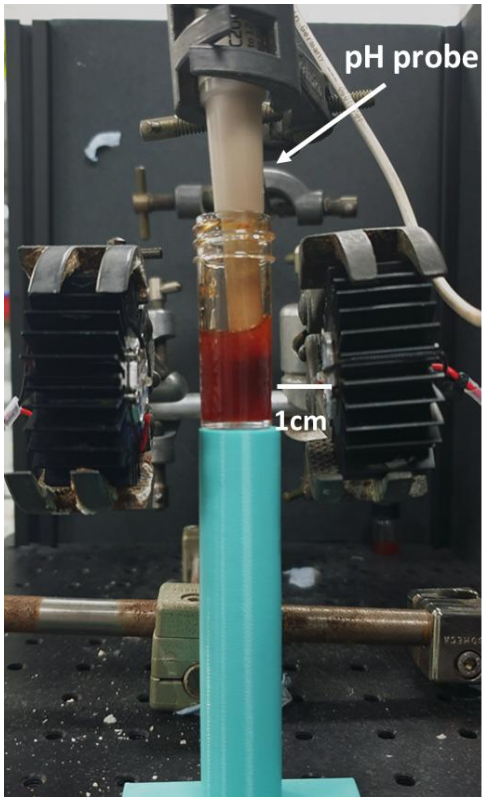

Figure 4.20. Custom set-up to measure pH changes under irradiation in a dark box. The sample is placed on a bespoke 3D-printed holder. The LEDs are placed at 1 cm away from the sample and a pH probe is inserted in the vial.

4.3.3.3 ^{1}H NMR measurements

In situ ^{1}H NMR irradiation experiments were performed using a Bruker AVIIIHD500 FT-NMR spectrometer equipped with a Bruker BBFO CryoProbe at a constant temperature of 298 K, using an irradiation set-up based on a previous design by Gshwind and co-workers

and closely resembling one previously reported by Ben-Tal and Lloyd-Jones.[35,36] A Thorlabs mounted LED (470 nm maxima, M470L5), powered by Thorlabs T-cube LED driver was coupled to a length of FP1500URT cable, the other end of which was stripped to a length of ≈ 3 cm and roughened with sandpaper to ensure even light distribution. The stripped end was placed inside a quartz coaxial insert (Norrel scientific), which was then inserted into 280 μL of the experimental solution inside an amberized 5 mm NMR tube; this corresponds to a light pathlength of 0.44 mm.[36] The T-cube power source was set to the maximum current for the M470L5 LED. The LED source and NMR console were connected *via* a split BNC cable to a Prizmatic PulserPlus TTL signal generator, which was activated *via* an external trigger switch, to ensure that spectra collection and illumination began simultaneously.

^{1}H NMR spectra of solutions of just **1ThNapFF** (1.5 mg/mL), photoacid **1** (1.5 mM) and of the composite solution of **1ThNapFF** and **1** (1.5 mg/mL and 1.5 mM) were collected under irradiation. All samples were prepared similarly to the ones in H_2O by using D_2O and 0.1 M KOD. The pD of the samples was adjusted to 7.2 by addition of 1M DCl and 1M KOD.

The changes under irradiation were monitored by ^{1}H NMR experiments (32 scans per spectra). A first spectrum was collected in the dark, followed by 5 minutes of irradiation *in situ*, then 30 minutes of recovery in the dark. Due to the fast changes in the system, it was not possible to use a higher number of scans per spectra.

4.3.3.4 Syringe pump set-up

A ProSense single channel syringe pump was used to monitor the flow of the **1ThNapFF** and **1** solution. A 12 mL syringe was used, attached *via* Luer lock fittings to a PVC tubing with a 3mm inner diameter. The tubing was cut in the middle and connected to a custom-built manometer *via* a t-piece and rubber tubing. The high precision manometer "Cavitation Rheometer Analyser Box (CRAB)" [37] has data logging capability to record the pressure in the system. The syringe was loaded directly with the gelator solution by removing the plunger and pouring the sample in to avoid any shear-thinning of the solution. The syringe was then placed in the syringe pump and attached to the tubing. Note here that, although not pictured, the tubing was held by a bespoke 3D-printed holder to ensure that the tubing was at the same height throughout. At the end of the tubing, a beaker was placed to collect the solution. To keep the sample in the dark, a large box was used to cover the whole set-up. The collection of pressure data points was started prior to any flow. Next, the solution was allowed to flow through the system at a rate of 1 mL/min. Once the solution travelled through the whole system, the LEDs were turned on to collect the data during irradiation.

Figure 4.21. Custom set-up to measure changes in pressure under irradiation with 450 nm LEDs as the sample flows through a tubing system.

4.3.3.5 Small angle X-ray scattering

Small angle X-ray scattering experiments were conducted at the I22 beamline at Diamond Light Source (Didcot, UK) with experiment number SM33006-1. The beamline operates at an energy of 12.4 keV and the camera length was set at 8.756 m to achieve a q range of 0.00174 – 0.2036 $Å^{-1}$. The solutions were prepared as previously described and loaded in quartz capillaries using a 1 mL syringe and 21G needle. The capillaries were then capped and wrapped in tinfoil prior to beamtime. To measure the samples under irradiation, an *in situ* irradiation sample environment was designed (Figure 4.22a and 4.22b). The set-up consisted in a LED holder positioned at a fixed height (Figure 4.22a), which was placed under a capillary holder (Figure 4.22c). The distance between the LED and the capillary could be adjusted and it was fixed at 1 cm. This allowed the sample to be irradiated homogeneously, with a change in colour observed throughout the capillary for at least 30 seconds of irradiation. However, we note that longer irradiations (5 minutes) combined with the X-ray data collection appeared to cause bleaching of the photoacid: the sample was not able to relax back to the initial state in the position of the data collection (Figure 4.22c, yellow area) even after leaving the sample for 16 hours in the dark.

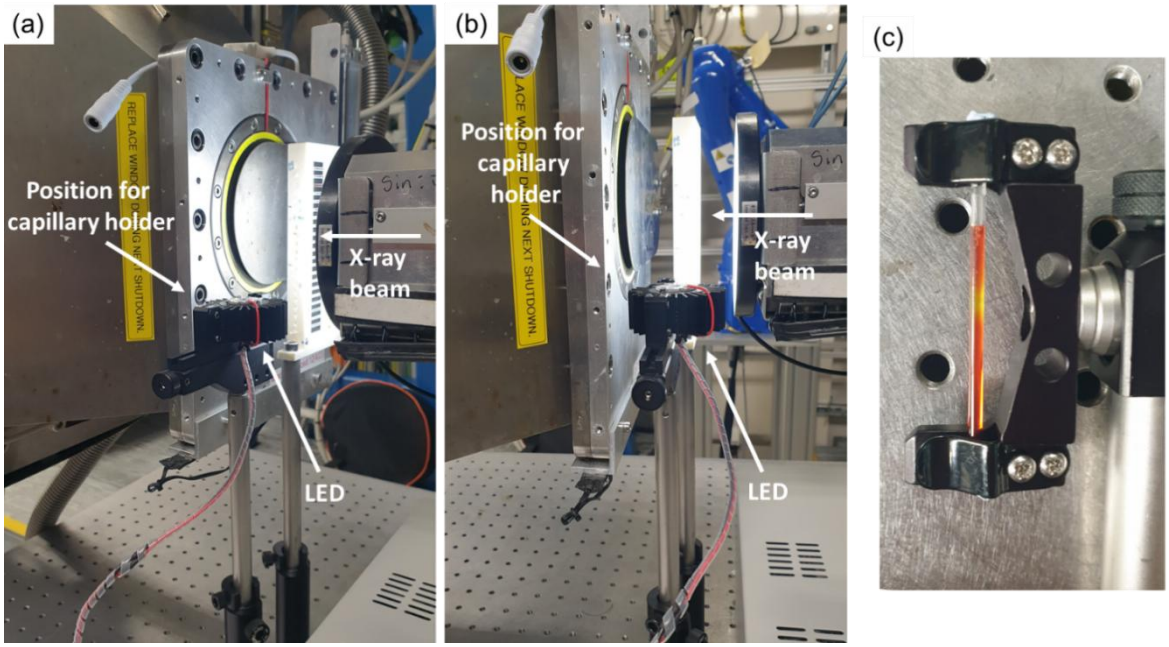

Figure 4.22. (a), (b) Photographs of the sample environment used at Diamond Light Source to test morphology changes under irradiation. The LED is held on a mount at a fixed height with a capillary holder placed above it. The distance between capillary and LED could be fixed by changing the fixed height of the post collar. (c) Picture of the capillary holder used in this set-up. The capillary contains a solution of **1ThNapFF** and **1** after repeated irradiation cycles (5 minutes). The sample shows inhomogeneity in colour due to bleaching of the photoacid in the area where data collection was performed. After 16 hours, the sample was not able to relax back to the initial colour. This did not occur for irradiation periods of 30 seconds.

For all samples, 100 x 10 ms frames were collected and averaged. All samples were kept in the dark for 5 minutes, irradiated for 30 seconds and left to relax for 5 minutes. This was repeated for 4 cycles for all solutions. Note here that measurements were also carried out for a sample of **1ThNapFF** and **1** with a longer irradiation time of 5 minutes. However, no significant changes were observed for this sample (Figure 4.23 and Table 4.4), with an area of the sample not being able to relax back within the capillary even after prolonged times of 16 hours (Figure 4.20c). To avoid this, shorter irradiation times were used for the samples, as the viscosity changes can be already observed within 30 seconds of irradiation.

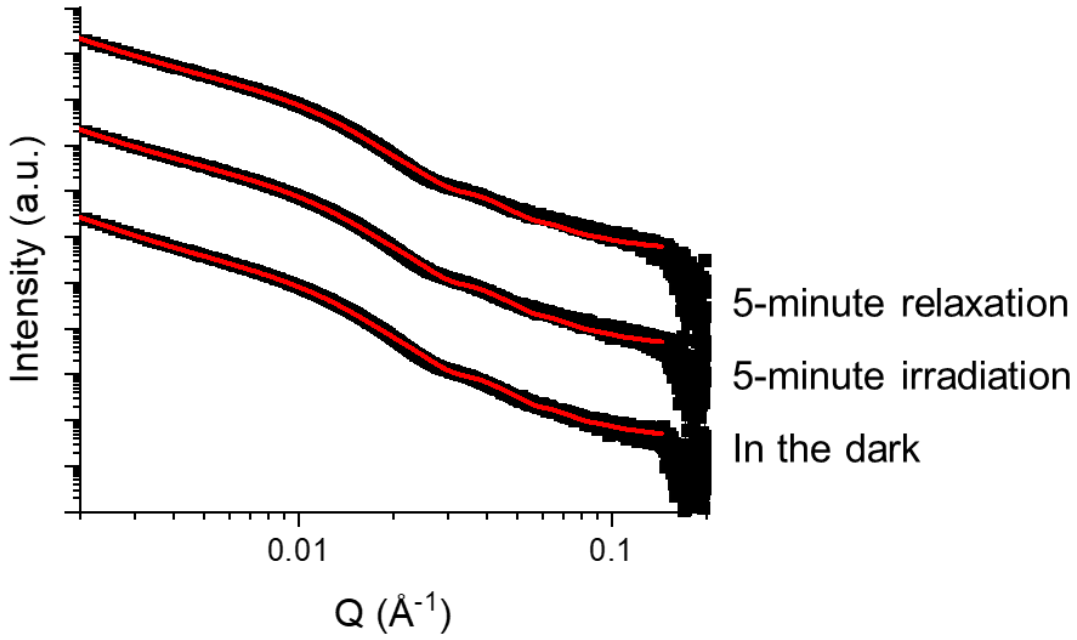

Figure 4.23. Small angle scattering data (black squares) and model fits (red line) for a solution of **1ThNapFF** and **1** in the dark (bottom), after 5 minutes of irradiation (middle) and 5 minutes of relaxation (top). SAXS patterns have been offset for clarity.

Table 4.4. Fitting parameters for the small angle scattering data shown in Figure 4.23. All data was fit to an elliptical cylinder model (A) combined with a power law model (B). Values that were manually added and fixed have been labelled with *.

Sample	**In the dark**	**5-minute irradiation**	**5-minute relaxation**
Background / cm^{-1}	0.004*	0.004*	0.005*
Background error / cm^{-1}	/	/	/
A_scale	$2.56x10^{-4}$	$2.39x10^{-4}$	$2.34x10^{-4}$
A_scale error	$5.94x10^{-7}$	$5.72x10^{-7}$	$5.46x10^{-7}$
A_radius_minor / Å	118.3	118.7	120.6
A_radius_minor error / Å	0.18	0.18	0.20
A_axis_ratio	2.0	2.0	1.9
A_axis_ratio error	0.005	0.005	0.005
A_length / Å	5000*	5000*	5000*
A_length error / Å	/	/	/
B_scale	$4.05x10^{-6}$	$4.95x10^{-6}$	$5.79x10^{-6}$
B_scale error	$6.59x10^{-8}$	$8.75x10^{-8}$	$9.49x10^{-8}$
B_power	2.9	2.8	2.8
B_power error	0.003	0.003	0.003
χ^2	3.95	3.24	2.59

The data was processed using Dawn Science (version 2.27),[38] according to a standard I22 pipeline. [39] As part of the processing, the solvent background (H_2O) was subtracted and a full azimuthal integration was performed to yield I vs *q* plots, which were fitted to models using SasView (version 5.0.2). For this, scattering length densities (SLDs) were calculated using the NIST neutron activation and scattering calculator (https://www.ncnr.nist.gov/resources/activation/), assuming a density of 1.58 g/cm^3 for the dipeptide. For **1ThNapFF**, an SLD of 14.025x10^{-6} Å^2 was used, while for H_2O a solvent SLD of 9.469x10^{-6} Å^2 was used.

4.4 References

1 S. De and R. Klajn, Dissipative Self-Assembly Driven by the Consumption of Chemical Fuels, *Adv. Mater.*, 2018, **30**, 1706750.

2 S. A. P. Van Rossum, M. Tena-Solsona, J. H. Van Esch, R. Eelkema and J. Boekhoven, Dissipative out-of-equilibrium assembly of man-made supramolecular materials, *Chem. Soc. Rev.*, 2017, **46**, 5519–5535.

3 M. Tena-Solsona, B. Rieß, R. K. Grötsch, F. C. Löhrer, C. Wanzke, B. Käsdorf, A. R. Bausch, P. Müller-Buschbaum, O. Lieleg and J. Boekhoven, Non-equilibrium dissipative supramolecular materials with a tunable lifetime, *Nat. Commun.*, 2017, **8**, 15895.

4 C. D. Jones and J. W. Steed, Gels with sense: Supramolecular materials that respond to heat, light and sound, *Chem. Soc. Rev.*, 2016, **45**, 6546–6596.

5 R. J. Mart, R. D. Osborne, M. M. Stevens and R. V. Ulijn, Peptide-based stimuli-responsive biomaterials, *Soft Matter*, 2006, **2**, 822–835.

6 K. McAulay, B. Dietrich, H. Su, M. T. Scott, S. Rogers, Y. K. Al-Hilaly, H. Cui, L. C. Serpell, A. M. Seddon, E. R. Draper and D. J. Adams, Using chirality to influence supramolecular gelation, *Chem. Sci.*, 2019, **10**, 7801–7806.

7 C. J. C. Edwards-Gayle and I. W. Hamley, Self-assembly of bioactive peptides, peptide conjugates, and peptide mimetic materials, *Org. Biomol. Chem.*, 2017, **15**, 5867–5876.

8 B. Xue, M. Qin, T. Wang, J. Wu, D. Luo, Q. Jiang, Y. Li, Y. Cao and W. Wang, Electrically Controllable Actuators Based on Supramolecular Peptide Hydrogels, *Adv. Funct. Mater.*, 2016, **26**, 9053–9062.

9 T. Heuser, E. Weyandt and A. Walther, Biocatalytic Feedback-Driven Temporal Programming of Self-Regulating Peptide Hydrogels, *Angew. Chem. Int. Ed.*, 2015, **54**, 13258–13262.

10 S. Xian and M. J. Webber, Temperature-responsive supramolecular hydrogels, *J. Mater. Chem. B*, 2020, **8**, 9197–9211.

11 E. R. Draper and D. J. Adams, Photoresponsive gelators, *Chem. Commun.*, 2016, **52**, 8196–8206.

12 J. Raeburn, T. O. Mc Donald and D. J. Adams, Dipeptide hydrogelation triggered via ultraviolet light, *Chem. Commun.*, 2012, **48**, 9355–9357.

13 C. Maity, W. E. Hendriksen, J. H. Van Esch and R. Eelkema, Spatial structuring of a supramolecular hydrogel by using a visible-light triggered catalyst, *Angew. Chem. Int. Ed.*, 2015, **54**, 998–1001.

14 M. Liu, C. N. Creemer, T. J. Reardon and J. R. Parquette, Light-driven dissipative self-assembly of a peptide hydrogel, *Chem. Commun.*, 2021, **57**, 13776–13779.

15 B. Yang, M. Lledos, R. Akhtar, G. Ciccone, L. Jiang, E. Russo, S. Rajput, C. Jin, M. G. F. Angelereou, T. Arnold, J. Rawle, M. Vassalli, M. Marlow, D. J. Adams and M. Zelzer, Surface-controlled spatially heterogeneous physical properties of a supramolecular gel with homogeneous chemical composition, *Chem. Sci.*, 2021, **12**, 14260–14269.

16 X. Li, J. Fei, Y. Xu, D. Li, T. Yuan, G. Li, C. Wang and J. Li, A Photoinduced Reversible Phase Transition in a Dipeptide Supramolecular Assembly, *Angew. Chem. Int. Ed.*, 2018, **57**, 1903–1907.

17 Z. Qiu, H. Yu, J. Li, Y. Wang and Y. Zhang, Spiropyran-linked dipeptide forms supramolecular hydrogel with dual responses to light and to ligand–receptor interaction, *Chem. Commun.*, 2009, **7345**, 3342–3344.

18 T. M. Doran, D. M. Ryan and B. L. Nilsson, Reversible photocontrol of self-assembled peptide hydrogel viscoelasticity, *Polym. Chem.*, 2014, **5**, 241–248.

19 F. A. Larik, L. L. Fillbrook, S. S. Nurttila, A. D. Martin, R. P. Kuchel, K. Al Taief, M. Bhadbhade, J. E. Beves and P. Thordarson, Ultra-Low Molecular Weight Photoswitchable Hydrogelators, *Angew. Chem. Int. Ed.*, 2021, **60**, 6764–6770.

20 A. L. Fameau, A. Arnould, M. Lehmann and R. Von Klitzing, Photoresponsive self-assemblies based on fatty acids, *Chem. Commun.*, 2015, **51**, 2907–2910.

21 V. J. Périllat, E. Del Grosso, C. Berton, F. Ricci and C. Pezzato, Controlling DNA nanodevices with light-switchable buffers, *Chem. Commun.*, 2023, **59**, 2146–2149.

22 F. J. Rizzuto, C. M. Platnich, X. Luo, Y. Shen, M. D. Dore, C. Lachance-Brais, A. Guarné, G. Cosa and H. F. Sleiman, A dissipative pathway for the structural evolution of DNA fibres, *Nat. Chem.*, 2021, **13**, 843–849.

23 L. Wimberger, J. Andréasson and J. E. Beves, Basic-to-acidic reversible pH switching with a merocyanine photoacid, *Chem. Commun.*, 2022, **58**, 5610–5613.

24 L. Wimberger, S. K. K. Prasad, M. D. Peeks, J. Andreásson, T. W. Schmidt and J. E. Beves, Large, Tunable, and Reversible pH Changes by Merocyanine Photoacids, *J. Am. Chem. Soc.*, 2021, **143**, 20758–20768.

25 L. Kortekaas, J. Chen, D. Jacquemin and W. R. Browne, Proton-Stabilized Photochemically Reversible E/ Z Isomerization of Spiropyrans, *J. Phys. Chem. B*, 2018, **122**, 6423–6430.

26 D. McDowall, M. Walker, M. Vassalli, M. Cantini, N. Khunti, C. J. C. Edwards-Gayle, N. Cowieson and D. J. Adams, Controlling the formation and alignment of low molecular weight gel ‘noodles’, *Chem. Commun.*, 2021, **57**, 8782–8785.

27 R. R. Sonani, S. Bianco, B. Dietrich, J. Doutch, E. R. Draper, D. J. Adams and E. H. Egelman, Atomic structures of naphthalene dipeptide micelles unravel mechanisms of assembly and gelation, *Cell. Rep. Phys. Sci.*, 2024, **5**, 101812.

28 S. Panja and D. J. Adams, Mimicking evolution of ‘ mini-homeostatic ’ modules in supramolecular systems, *Giant*, 2021, **5**, 100041.

29 E. R. Draper, B. Dietrich, K. McAulay, C. Brasnett, H. Abdizadeh, I. Patmanidis, S. J. Marrink, H. Su, H. Cui, R. Schweins, A. Seddon and D. J. Adams, Using Small-Angle Scattering and Contrast Matching to Understand Molecular Packing in Low Molecular Weight Gels, *Matter*, 2020, **2**, 764–778.

30 L. Wimberger, F. J. Rizzuto and J. E. Beves, Modulating the Lifetime of DNA Motifs Using Visible Light and Small Molecules, *J. Am. Chem. Soc.*, 2023, **145**, 2088–2092.

31 C. Delaney, P. McCluskey, S. Coleman, J. Whyte, N. Kent and D. Diamond, Precision control of flow rate in microfluidic channels using photoresponsive soft polymer actuators, *Lab Chip*, 2017, **17**, 2013–2021.

32 S. Coleman, J. ter Schiphorst, A. Azouz, S. Ben Bakker, A. P. H. J. Schenning and D. Diamond, Tuning microfluidic flow by pulsed light oscillating spiropyran-based polymer hydrogel valves, *Sens. Actuators B Chem.*, 2017, **245**, 81–86.

33 E. R. Draper, H. Su, C. Brasnett, R. J. Poole, S. Rogers, H. Cui, A. Seddon and D. J. Adams, Opening a Can of Worm(-like Micelle)s: The Effect of Temperature of Solutions of Functionalized Dipeptides, *Angew. Chem. Int. Ed.*, 2017, **56**, 10467–10470.

34 M. C. Nolan, A. M. Fuentes Caparrós, B. Dietrich, M. Barrow, E. R. Cross, M. Bleuel, S. M. King and D. J. Adams, Optimising low molecular weight hydrogels for automated 3D printing, *Soft Matter*, 2017, **13**, 8426–8432.

35 C. Feldmeier, H. Bartling, E. Riedle and R. M. Gschwind, LED based NMR illumination device for mechanistic studies on photochemical reactions – Versatile and simple, yet surprisingly powerful, *J. Magn. Reson.*, 2013, **232**, 39–44.

36 Y. Ben-Tal and G. C. Lloyd-Jones, Kinetics of a Ni/Ir-Photocatalyzed Coupling of ArBr with RBr: Intermediacy of ArNi II (L)Br and Rate/Selectivity Factors, *J. Am. Chem. Soc.*, 2022, **144**, 15372–15382.

37 A. M. Fuentes-Caparrós, B. Dietrich, L. Thomson, C. Chauveau and D. J. Adams, Using cavitation rheology to understand dipeptide-based low molecular weight gels, *Soft Matter*, 2019, **15**, 6340–6347.

38 J. Filik, A. W. Ashton, P. C. Y. Chang, P. A. Chater, S. J. Day, M. Drakopoulos, M. W. Gerring, M. L. Hart, O. V. Magdysyuk, S. Michalik, A. Smith, C. C. Tang, N. J. Terrill, M. T. Wharmby and H. Wilhelm, Processing two-dimensional X-ray diffraction and small-angle scattering data in DAWN 2, *J. Appl. Crystallogr.*, 2017, **50**, 959–966.

39 B. R. Pauw, A. J. Smith, T. Snow, N. J. Terrill and A. F. Thünemann, The modular small-angle X-ray scattering data correction sequence, *J. Appl. Crystallogr.*, 2017, **50**, 1800–1811.

Chapter 5. Designing mechanically releasable supramolecular gels to store and recover intact proteins

This Chapter is adapted from the following publication:

"Mechanical release of homogeneous proteins from supramolecular gels"

S. Bianco,* M. Hasan,* A. Ahmad, S.-J. Richards, B. Dietrich, M. Wallace, Q. Tang, A. J. Smith, M. I. Gibson and D. J. Adams, *Nature*, 2024, **631**, 544–548.

*Joint authors.

Author Contributions

M.I.G. and D.J.A. conceived this work. S.B., Q.T., S.-J.R., B.D., M.H., A.A., A.J.S. and M.W. undertook data curation. S.B., M.H., M.I.G. and D.J.A. were responsible for formal analysis. S.B., Q.T., M.H., S.-J.R., B.D., A.A., M.W. and A.J.S. carried out the investigations. S.B., M.H., B.D., A.J.S., M.W., M.I.G. and D.J.A. developed the methodology. S.B., M.H. and M.I.G. produced the visualizations. M.I.G. and D.J.A. acquired funding. M.I.G. and D.J.A. carried out project administration. M.I.G. and D.J.A. supervised the work. M.I.G. and D.J.A. wrote the original draft. S.B., M.H., M.I.G., D.J.A., S.-J.R., A.A., M.W. and Q.T. were involved in reviewing and editing the final manuscript.

The dipeptide molecules used in this chapter were synthesised by Dr. Bart Dietrich (University of Glasgow) and Prof. Dave J. Adams. The STD-NMR data shown in this Chapter was collected and analysed by Dr. Matthew Wallace. Acknowledgements have been provided in the Figure captions where necessary. SAXS data presented in this work was collected by Simona Bianco with the help of Dr. Valentina Gauci (University of Glasgow), Connor MacDonald (University of Glasgow), Dr. Libby J. Marshall (University of Glasgow) and Dr. Alex Loch (University of Glasgow) and the data was analysed and processed by Simona Bianco. The rest of the data presented in this Chapter has been collected, visualised and analysed by Simona Bianco.

5. Designing mechanically releasable supramolecular gels to store and recover intact proteins

5.1 Introduction

In Chapter 1, we discussed the way gels can be formed *via* the self-assembly of low molecular weight gelators (LMWG) by applying a variety of gelation triggers.[1,2] Often, these gels are shown to be very stiff but break at low strain. This behavior at low strain has been widely described as a drawback of supramolecular gel systems.[3,4] However, this perceived "failing" can be exploited as a unique benefit, allowing the design of systems capable of responding to a mechanical trigger for homogeneous protein delivery that is not possible with conventional gels.

Biological macromolecules and additives including proteins can be easily encapsulated in supramolecular gels formed by LMWG.[5-7] Upon gelation, the additive is trapped in the gel network between the fibres (Figure 5.1, left). If the gel network is sufficiently permanent and the network pores are small enough, molecules such as proteins are not able to diffuse easily within the gel matrix and hence are not able to aggregate.[8] Indeed, controlled release experiments have previously shown that restricted diffusion occurs in LWMG gels.[9,10] By combining this concept and the ability of supramolecular gels to break at low strain, we can form gels containing encapsulated molecules in syringes. By applying a mechanical stimulus and pushing the gel through an in-line filter, release of pure, excipient free additive can be achieved (Figure 5.1, right). Because of the extended supramolecular network, all the gel components are retained in the filter.

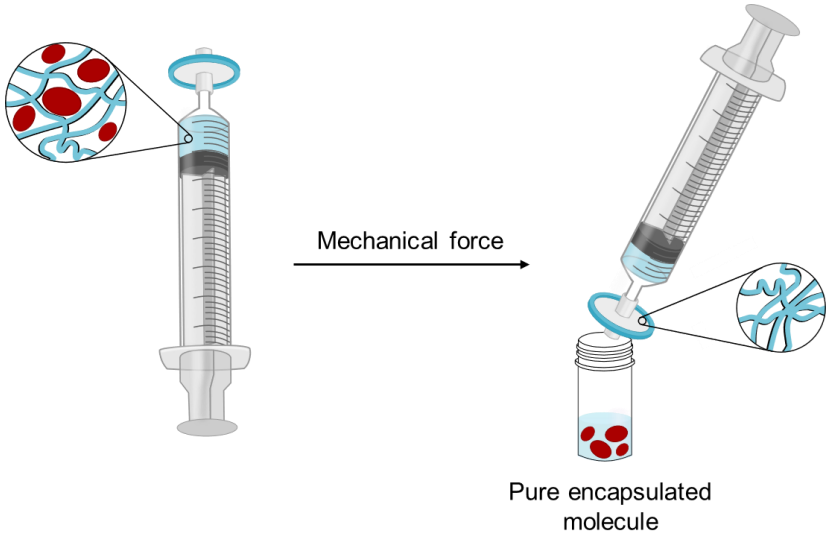

Figure 5.1. Cartoon summarising the approach used in this Chapter. The supramolecular gel is loaded with a cargo molecule (red) and prepared within a syringe fitted with an in-line filter. Mechanical stimulus is used to release the molecule, while the extended supramolecular network is kept in the filter.

There have been several examples of systems used to stabilise proteins against aggregation. For instance, Maynard *et al*. have developed synthetic polymers with trehalose side chains for protein stabilization, enabling both freeze-drying and heating stabilization, but the conjugation reduces activity.[11] Fully reversible hydrogels based on PEG (polyethylene glycol) have emerged to protect diverse proteins against thermal stress[12,13] and mRNA formulations have been stabilized in a dissolvable matrix.[14] Similarly, frozen formulations to prevent ice crystal growth suppress protein aggregation.[15] Despite the strengths of these approaches, these strategies often result in the release of stored protein mixed with its stabilization agents or gel components. As such, these materials will also require separate approval and evaluation of their safety profile before being deemed suitable for human use. Even materials based on PEG have also immunological concerns for frequent exposure.[12,13,16] Furthermore, for most of these gels, a chemical stimulus may be required to release the protein, which will then in practice be dosed by the user.

An optimal solution and ideal material to store and release encapsulated molecules would firstly require to be stable at room temperature to avoid cold chain requirements. The desired material would have to be easily and broadly applicable and thus not require complex chemical triggers to release the stored molecule. Finally, it would release zero or minimal stabilization components in the delivered solution, while still releasing non-aggregated additive.

In this Chapter, we aim to investigate the design of low molecular weight supramolecular gel networks that can physically entrap model cargo macromolecules and insulin to prevent irreversible aggregation at room temperature. Through this approach, we will provide a protocol for the formation of stiff gels to store encapsulated additives in syringes and show how we can release pure, excipient free molecules in buffer by application of a simple mechanical stimulus. Compared to the Chapters presented in this Thesis so far, here the stimulus response does not induce a change in structure, but rather it is used to induce a reproducible response from the gel network to break and release the encapsulated molecules. To further understand how mechanical stimuli affect gelation properties and their ability to release stored molecules, we will examine gelators formed *via* two different triggers: pH trigger and a buffer trigger. By comparing their properties across different length scales, we aim to generate a robust approach for the design of releasable gels, examining several factors such as initial sample morphology, gel mechanical properties and storage stability.

5.2 Results and discussion

To design hybrid gels for drug loading and release, several LMWG were investigated, formed by a pH trigger and a buffer trigger. This approach was used to understand meaningful relationships between mechanical properties, morphology and gelation method on gel stability and releasability. To probe impact on gel structure, function and release, a model macromolecule was loaded into the gels. For this purpose, dextran (M_r 6000 Da, hydrodynamic radius = 1.6 nm[17]) was chosen as a non-interacting additive with a similar size to insulin,[18] as well as due to its high solubility in water. Previously, our group has shown that hybrid LMWG gels formed in presence of dextran can be formed at concentrations up to 33 wt%, resulting in materials with tailored mechanical properties.[6] Here, the gels were loaded with dextran at concentrations up to 10 wt%, which is far above loadings generally required for real-world drug storage.

5.2.1 pH-triggered gels

A variety of LMWG capable of forming pH-triggered gels were used, shown in Figure 5.2: **2NapIF**, **1Br2NapLFF** (referred to as **BrNapLFF** for the rest of this chapter) and **2NapFV**. Gels were obtained through the slow hydrolysis of glucono-δ-lactone (GdL) to gluconic acid, allowing a uniform change in pH within the system and formation of homogeneous gels.[19] The gelators were chosen based on previous screening tests to cover different initial values of stiffness (G′) and yield point,[21] namely the point at which G′ deviates from linearity.

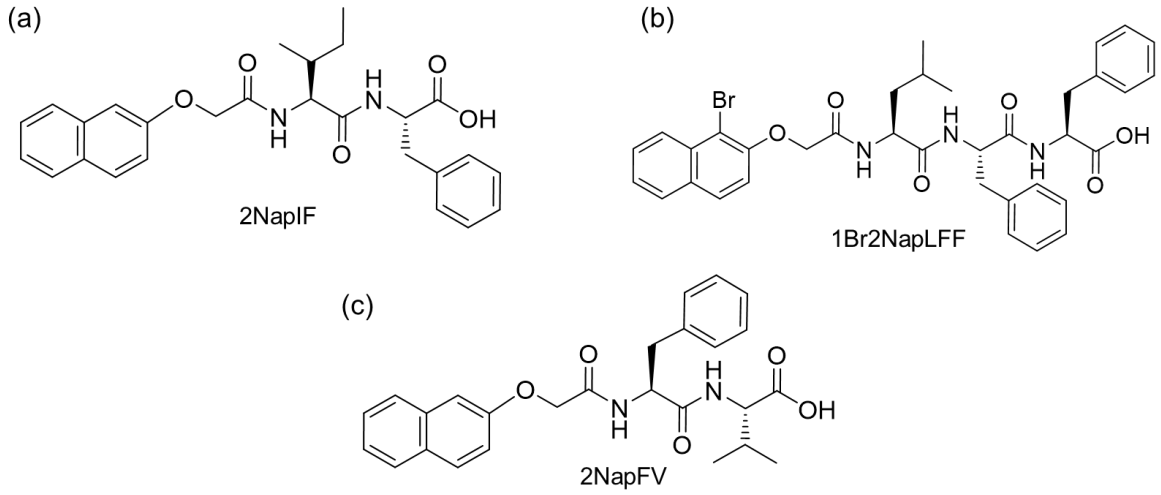

Figure 5.2. Chemical structures for pH-triggered gelators used in this work: (a) **2NapIF**, (b) **BrNapLFF** and (c) **2NapFV**.

Firstly, we investigated the rheological properties of the gels formed in absence and in presence of model cargo molecule dextran (Figure 5.3) at a high loading of 10 wt%. In all cases, self-supporting materials were formed (Figures 5.3a, 5.3d and 5.3g) at pH values in the range of 3.00 – 3.50. Gels formed from gelator **2NapIF** were clear, while turbid gels were obtained from **2NapFV** and **BrNapLFF**. Gels obtained from **BrNapLFF** appeared to undergo minimal syneresis after overnight stabilization, where contraction of the gel occurs with expulsion of water. This phenomenon is often driven by change in hydrophobicity of the gelator.[21] Interestingly, no significant changes could be visually observed in the samples containing 10 wt% dextran (Figure 5.3a, 5.3d and 5.3g, right). In all cases, the materials showed G′ higher than G″ by an order of magnitude and frequency independent behaviour, confirming the formation of true gels both in absence (Figure 5.3, black data) and in presence of dextran (Figure 5.3, red data). **2NapFV** formed the stiffest gels (highest G′) compared to gels obtained from **2NapIF** and **BrNapLFF**. However, the **2NapFV** gels showed a very small linear viscoelastic region (LVER), the region at which the gel is independent of strain, showing a yield point at around 0.6% strain. Conversely, strong gels were formed by **BrNapLFF**, with a LVER that extended up to 6.8% strain. The rheological properties of **2NapIF** gels instead exhibited a yield point at 1.4% strain. For most of the gels obtained, the rheological properties were not affected by the presence of 10 wt% dextran, with the samples showing similar G′, G″ and LVER (Figures 5.3b and 5.3h). Based on this, we hypothesise that the dextran is encapsulated within the gel network and therefore not interacting with the primary fibres making up the gel. An increase in stiffness was only observed for gelator **2NapFV** (Figure 5.3e), accompanied by a slight reduction in the LVER.

This behaviour could result from potential interactions between the fibres of the gels and the macromolecule or due to the presence of a smaller mesh in the gel network, which is likely perturbed when the large macromolecule is present.

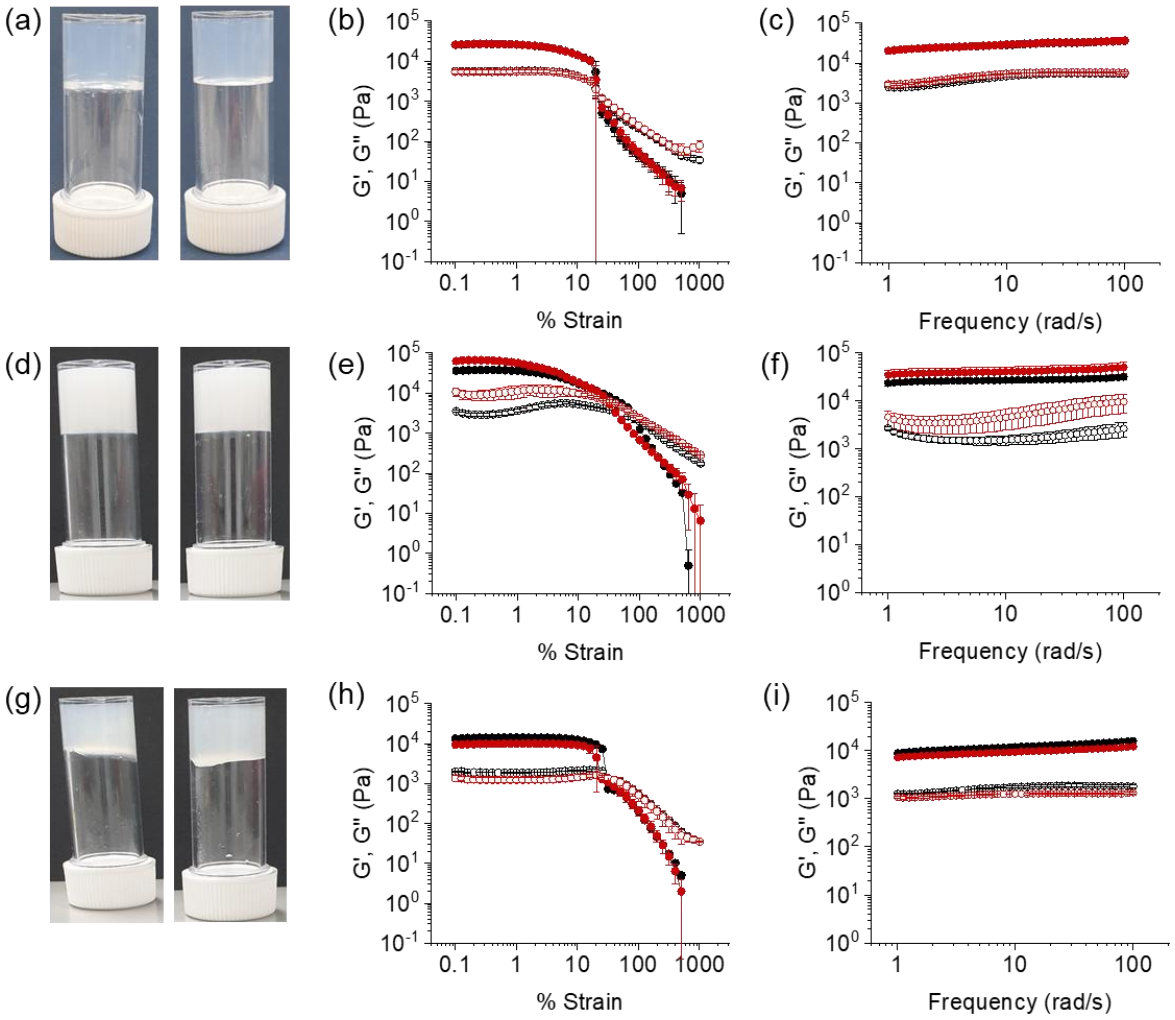

Figure 5.3. Photographs of inverted gels formed from (a) **2NapIF** (5 mg/mL), (d) **2NapFV** (5 mg/mL) and (g) **BrNapLFF** (10 mg/mL). Strain sweeps and frequency sweeps obtained for (b)-(c) **2NapIF** (5 mg/mL), (e)-(f) **2NapFV** (5 mg/mL) and (h) and (i) **BrNapLFF** (10 mg/mL) in absence (black data) and presence (red data) of 10 wt% dextran. In all cases, closed circles indicate G′ and open circles indicate G″.

To further understand this, the morphology of the gels in absence and presence of dextran was studied using small angle X-ray scattering (SAXS) (Figure 5.4). In all cases, the data could be fitted to cylinder models, indicative of the presence of long fibres making up the gel network. In absence of dextran, the data from **2NapIF** and **2NapFV** gels were fitted to flexible elliptical cylinders, suggesting the presence of either tape-like fibres or cylindrical fibres that are laterally associating and scattering as an elliptical object (Tables 5.1 and 5.2).[22]

In the case of **2NapIF**, the data was fit to a model with a radius of 4.5 nm and an axis ratio of 2, with lengths exceeding the length scales that could be observed in this SAXS measurement (> 300 nm). The **2NapFV** gels were instead fitted to flexible elliptical cylinders with a larger radius of 10.4 nm and an axis ratio of around 3. To obtain a better fit of the data, it was necessary to add a polydispersity of 0.3 to the value of the radius, indicating inhomogeneity in the radii of the fibres. A power law was also added to capture best the scattering coming from the gel network at low *q*. Finally, gels obtained from **BrNapLFF** were fitted to a simple cylinder model with a radius of 4.3 nm and lengths larger than 300 nm (Table 5.3). Overall, the data highlights the formation of a wide range of gel networks in the materials, allowing us to investigate the effect of morphology on the ability of storing and releasing the additive.

All the gels formed in the presence of dextran could be fit to similar models to the original gels, with all models requiring the addition of a sphere model (Tables 5.1, 5.2 and 5.3). This spherical model was necessary to account for the presence of dextran in the system. Indeed, in all cases, the sphere model was fit to the same value in all three gelators, showing a radius of around 2.0 nm, which is in line with the expected hydrodynamic radius for the dextran used.[18] A slight decrease in radius of the fibres was observed for **2NapIF** and **BrNapLFF**, from 4.3 nm down to around 3.9 nm. This can be due to model fitting requirements to allow the fit of the spherical model or can be ascribed to the formation of slightly smaller fibres to accommodate the bulky macromolecule. Overall, the minimal changes observed in presence of the macromolecule further indicate that the dextran is encapsulated within the gel network and not interacting with the primary fibres for gelators **2NapIF** and **BrNapLFF**. In line with the rheological data, the gels formed from **2NapFV** in the presence of dextran showed larger differences in the fits compared to the original gels. A decrease of around 1 nm in radius was observed, accompanied by an increase in the axis ratio from 3 to 4. This suggests that the dextran molecule is inducing increased lateral association between the fibres upon gel formation, resulting in the increased stiffness observed (Figure 5.3e).

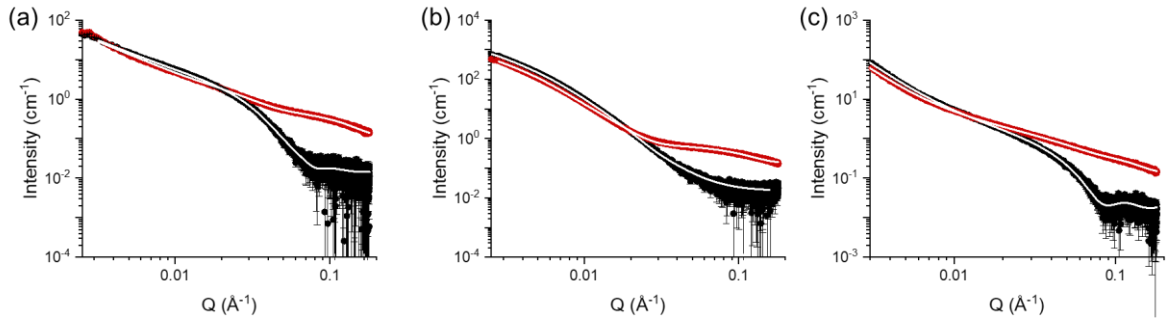

Figure 5.4. Small angle X-ray scattering patterns for gels of (a) **2NapIF** (5 mg/mL), (b) **2NapFV** (5 mg/mL) and (c) **BrNapLFF** (10 mg/mL) in absence (black data) and presence (red data) of 10 wt% dextran. In all cases, the white line represents the model fit.

Table 5.1. Fitting parameters for SAXS data in Figure 5.4a. The data was fitted to a flexible elliptical cylinder (FCE) combined with a sphere model. Values that were manually added and fixed have been labelled with *.

	2NapIF (5 mg/mL)			
Sample	**0 wt% Dextran**		**10 wt% Dextran**	
Model	**FCE**		**FCE+Sphere**	
	Value	**Error**	**Value**	**Error**
Scale	0.0036	1.55×10^{-6}	1	/
Background (cm^{-1})	0.014*		0.12*	
A_scale	/	/	0.0003	1.05×10^{-6}
A_radius (Å)	42.6	0.11	38.7	0.12
A_axis_ratio	2.1	0.01	2*	/
A_Kuhn_length (Å)	545.4	5.13	304.0	2.38
A_length (Å)	6952.4	316.79	7593.5	374.52
B_scale	/	/	0.0574	0.0001
B_radius	/	/	19.1	0.23
χ^2	1.73		2.47	

Table 5.2. Fitting parameters for SAXS data in Figure 5.4b. The data was fitted to a flexible elliptical cylinder (FCE) combined with a power law (PL) model or a sphere model. Values that were manually added and fixed have been labelled with *.

	2NapFV (5 mg/mL)			
Sample	**0 wt% Dextran**		**10 wt% Dextran**	
Model	**FCE+PL**		**FCE+Sphere**	
	Value	**Error**	**Value**	**Error**
Scale	1		1	
Background (cm^{-1})	0.017*		0.16	0.0005
A_scale	0.0024	5.06×10^{-5}	0.00014	1.43×10^{-6}
A_radius (Å)	104.1	0.48	90.6	0.39
Radius Pd	0.3		0.2	
A_axis_ratio	3.0	0.01	4.1	0.02
A_Kuhn_length (Å)	215.4	5.54	233.5	3.26
A_length (Å)	10000*	/	10000*	/
B_scale	1.02×10^{-5}	6.46×10^{-7}	/	/
B_power	2.7	0.02	/	/
C_scale	/	/	0.04	0.00023
C_radius	/	/	22.1	0.04
χ^2	3.68		6.078	

Table 5.3. Fitting parameters for SAXS data in Figure 5.4c. The data was fitted to a cylinder (C) combined with a power law (PL) model or a sphere model. Values that were manually added and fixed have been labelled with *.

	BrNapLFF (10 mg/mL)			
Sample	**0 wt% Dextran**		**10 wt% Dextran**	
Model	**C+PL**		**C+PL+Sphere**	
	Value	**Error**	**Value**	**Error**
Scale	1		1	
Background (cm^{-1})	0.017	0.00015	0.014*	
A_scale	0.0008	1.86×10^{-6}	0.00097	5.24×10^{-6}
A_radius (Å)	43.6	0.06	39.2	0.11
A_length (Å)	6280.1	48.46	4165.5	78.06
B_scale	2.52×10^{-6}	7.50×10^{-8}	2.04×10^{-6}	8.83×10^{-8}
B_power	3.0	0.005	2.9	0.008
C_scale	/	/	0.048	0.0001
C_radius		/	20.3	0.03
χ^2	2.89		2.23	

To test the ability of the samples to release the macromolecule, gels were formed in a 12 mL propylene syringe, fitted with a 2.7 μm filter. Due to the slow formation of gels over 16 hours, the solutions could be easily transferred from the vial after addition of GdL to the syringe and allowed to form overnight in the syringe. The gels were then extruded by pushing through the filter to release clear solutions. Gels formed from **BrNapLFF** were harder to push through the filter, whilst **2NapFV** gels were the easiest to push through, corroborating with the lower yield point observed in the rheological data (Figures 5.3e and 5.3h). To test whether any gelator was pushed through and to confirm the presence of dextran in the extrudate, ^{1}H NMR was carried out on the collected solution after freeze-drying and re-dissolving in d6-DMSO. As all gelators used in this section contain aromatic peptides as well as aromatic moieties, the NMR spectra have been also presented by expanding the

aromatic region (Figures 5.5b, 5.6b and 5.7b) to investigate the presence of gelator in the extrudate. The data has been presented against the NMR data for dextran (green data) and for the original gelator (black data) dissolved in d6-DMSO. For ease of comparison, the NMR spectrum of GdL in deionised H_2O after extrusion through a syringe and freeze-drying is presented in Figure 5.8.

For all three gels, the GdL hydrolysis product peaks can be observed, in particular in the gels extruded in absence of dextran (0 wt%, orange data). At this concentration, a small amount of gelator can be seen in the NMR spectra in the aromatic region (7.2 ppm), suggesting that some gelator passes through the filter. In presence of 10 wt% of dextran, the ^{1}H NMR data for all three gelators exhibits the characteristic peaks from dextran, confirming the presence of the extrudate in the solution, whilst the gelator peaks are not visible in these samples. This could be due to very small changes in the network in presence of dextran or to the larger quantity of dextran in the sample with respect to small amounts of gelator passing through.

It is relevant to note that, in all cases, the 0 wt% data required large scaling in order to observe the gelator peaks, so the data is presented with different intensities to best compare the spectra (right hand side).

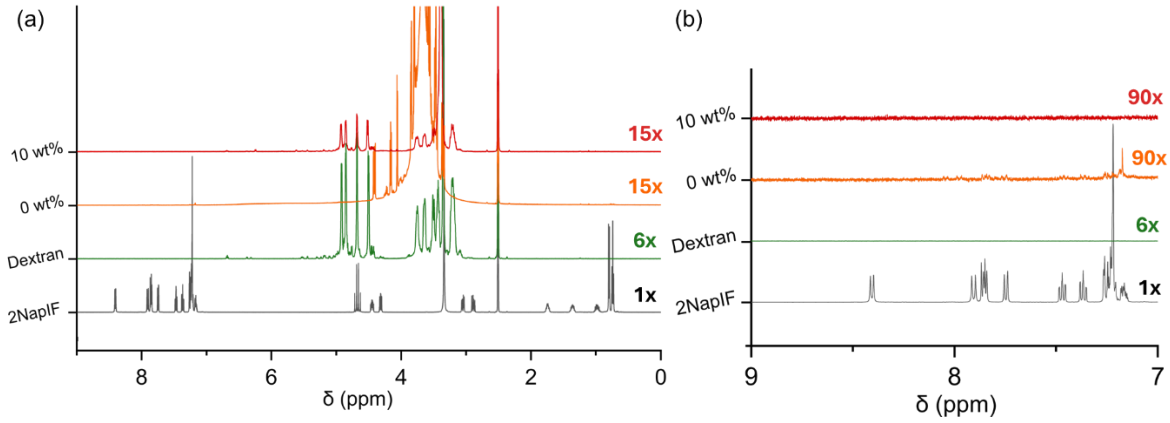

Figure 5.5. NMR data in d6-DMSO for liquid released through the syringe filter showing the presence of the hydrolysis products of GdL (used to change the pH) in both cases and the presence of dextran from the gel containing dextran. The full chemical range is shown in (a), while an expansion of the aromatic region is shown in (b), to further highlight the absence of gelator passing through. The sample collected from the gel formed in the presence of dextran shows the absence of any peaks that can be attributed to the **2NapIF** gelator. For the gel formed without dextran, a very small amount of the gelator can be detected on passing through the filter. Scaling of the data with respect to each other has been added for clarity.

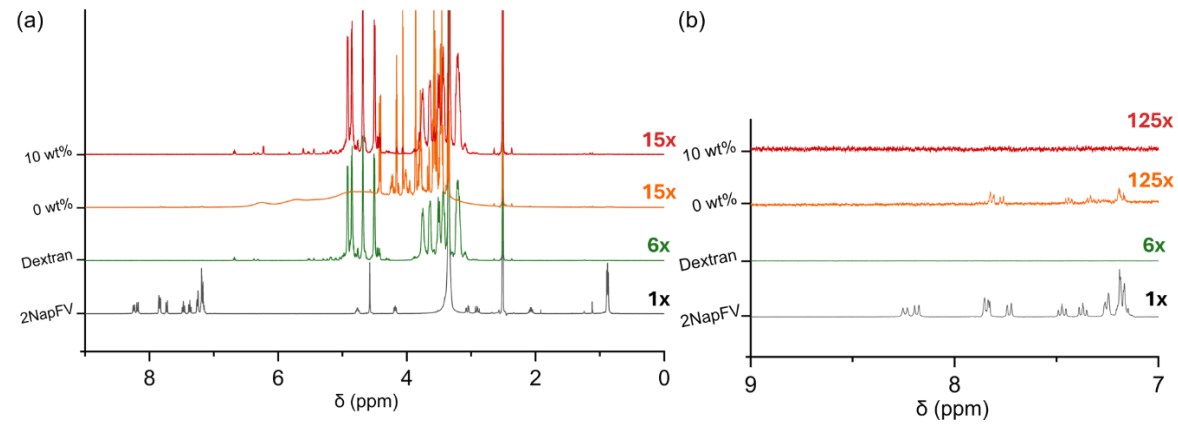

Figure 5.6. NMR data in d6-DMSO for liquid released through the syringe filter showing the presence of the hydrolysis products of GdL (used to change the pH) in both cases and the presence of dextran from the gel containing dextran. The full chemical range is shown in (a), while an expansion of the aromatic region is shown in (b), to further highlight the absence of gelator passing through. The sample collected from the gel formed in the presence of dextran shows the absence of any peaks that can be attributed to the **2NapFV** gelator. For the gel formed without dextran, a very small amount of the gelator can be detected on passing through the filter. Scaling of the data with respect to each other has been added for clarity.

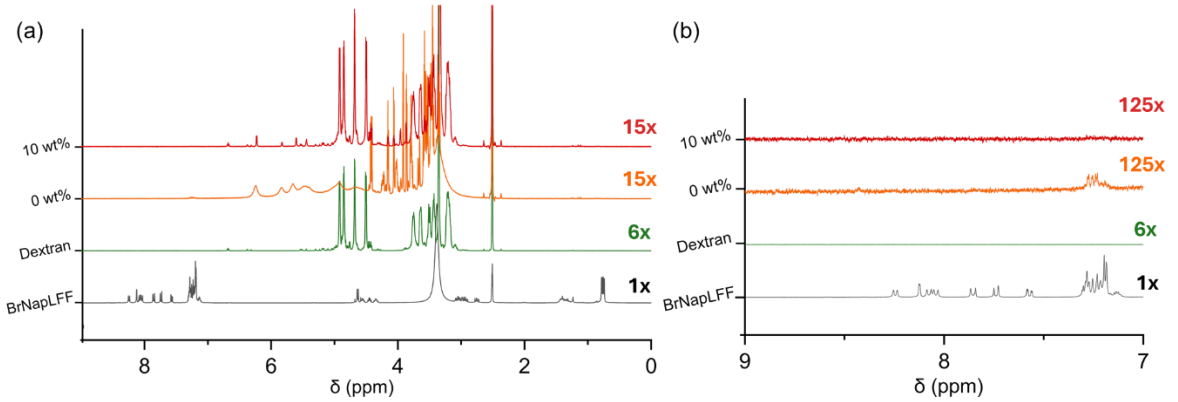

Figure 5.7. NMR data in d6-DMSO for liquid released through the syringe filter showing the presence of the hydrolysis products of GdL (used to change the pH) in both cases and the presence of dextran from the gel containing dextran. The full chemical range is shown in (a), while an expansion of the aromatic region is shown in (b), to further highlight the absence of gelator passing through. The sample collected from the gel formed in the presence of dextran shows the absence of any peaks that can be attributed to the **BrNapLFF** gelator. For the gel formed without dextran, a very small amount of the gelator can be detected on passing through the filter. Scaling of the data with respect to each other has been added for clarity.

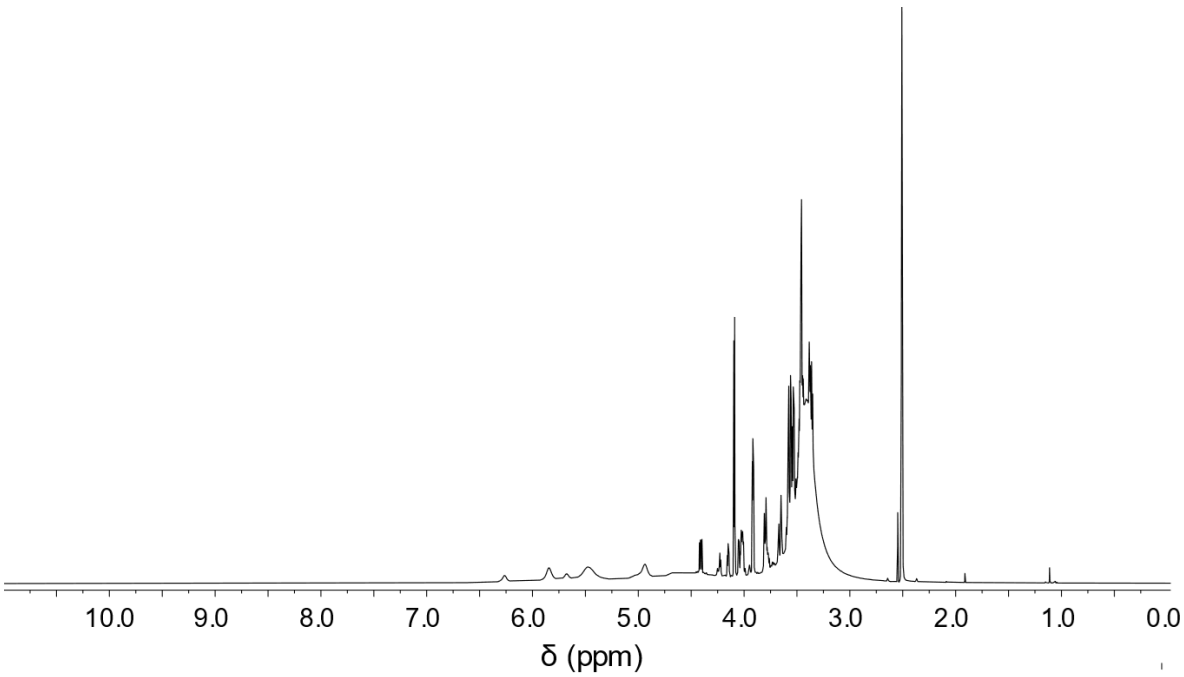

Figure 5.8. NMR data in d6-DMSO of GdL after being dispersed in H_2O and released through the syringe filter to show the peaks related to GdL hydrolysis used to lower the pH.

Overall, the data suggests that the morphology of the network on the nanoscale level, the bulk network and the mechanical properties (stiffness, yield point) of the material do not greatly influence the ability of the gel to store and, particularly, release the cargo macromolecule from the network. The data suggests that the main requirement for such systems to work for release applications is to possess a persistent and extended supramolecular network, capable of being left in the filter as the gel is pushed through. For potential release applications, a gel that can be pushed through more easily while maintaining its network structure would be more ideal. As such, based on rheology, gelator **2NapIF** was used for the rest of this work as a model dipeptide to further quantify the storage and release abilities of pH-triggered gels.

5.2.1.1 Investigating gel loading and releasability

To fully understand the releasability and loading capabilities of pH-triggered gels, a variety of **2NapIF** gels were formed in presence of 0.1, 1, 2, 3, 4, 5, 6, 7, 8 and 9 wt% dextran. In all cases, very clear gels were obtained (Figure 5.9a), with very similar rheological properties (Figures 5.9b, 5.9c and 5.9d) and final pH values (3.40 – 3.55). The rheological data suggests that the bulk properties of the material are independent on loading, indicating that the dextran is simply included in the pores rather than interacting with the gelator in all cases. Higher loadings of dextran were not tested due to the hygroscopic nature of the material, which could affect the rheological data after sitting overnight.

As exemplary samples, SAXS was performed on 0.1 wt% and 1 wt% dextran and compared with the 0 wt% and 10 wt% data (Figure 5.10 and Table 5.4). The data for 0.1 wt% (Figure 5.10, brown) was very similar to the 0 wt% data, likely due to the fact that the small amount of dextran did not contribute to the scattering. The data for the gels formed in presence of 1 wt% dextran (Figure 5.10, orange) could be fit in a similar way than to the 10 wt%, using a flexible elliptical cylinder model combined with a sphere with a 1.9 nm radius (Table 5.4). Compared to the 10 wt%, the scale of the spherical model for 1 wt% is much lower, in line with the smaller amount of dextran in the material.

The releasability of all the dextran loadings was also tested using ^{1}H NMR on the freeze-dried extrudate solutions (Figures 5.11 and 5.12). All the samples show the GdL hydrolysis peaks and the characteristic dextran peaks could be observed from as little as 1 wt% loading. Interestingly, gelator was only observed in the solutions at 0.1 wt% and 0 wt% (Figures 5.11 and 5.12). This is either due to small changes in the network at higher dextran loadings or due to the larger quantity of dextran with respect to little gelator passing through.

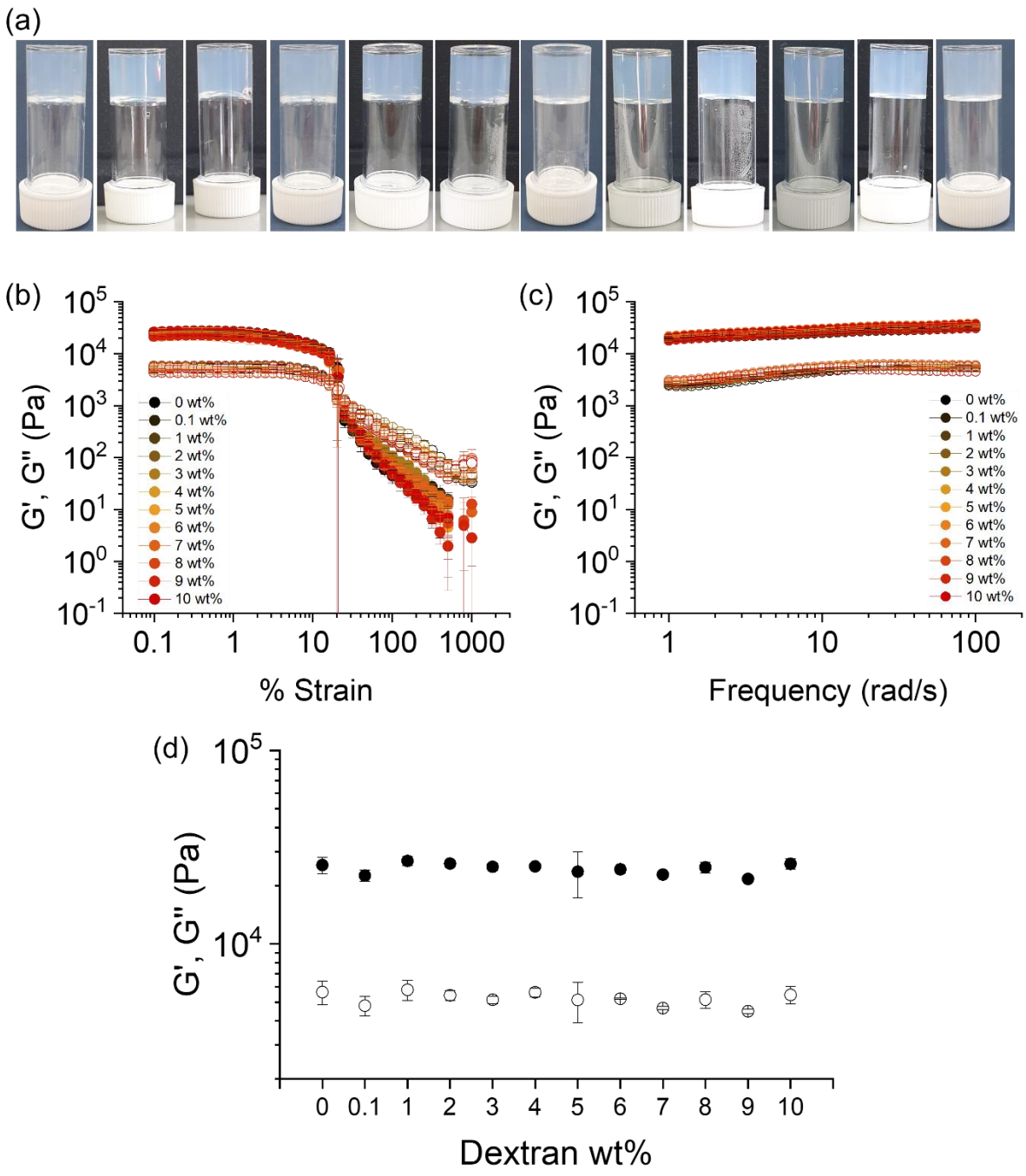

Figure 5.9. (a) Photographs of **2NapIF** gels (5 mg/mL) formed *via* a pH trigger with dextran loadings ranging from 0 wt% to 10 wt%. (b) and (c) Strain sweeps and frequency sweeps for **2NapIF** gels (5 mg/mL) formed in presence of dextran from 0 wt% to 10 wt%. (d) Comparison of G′ and G″ for gels obtained at different dextran loadings from (b) and (c). The data was taken from the strain sweeps at 0.1% strain. In all cases, the closed circles represent G′ and the open circles represent G″.

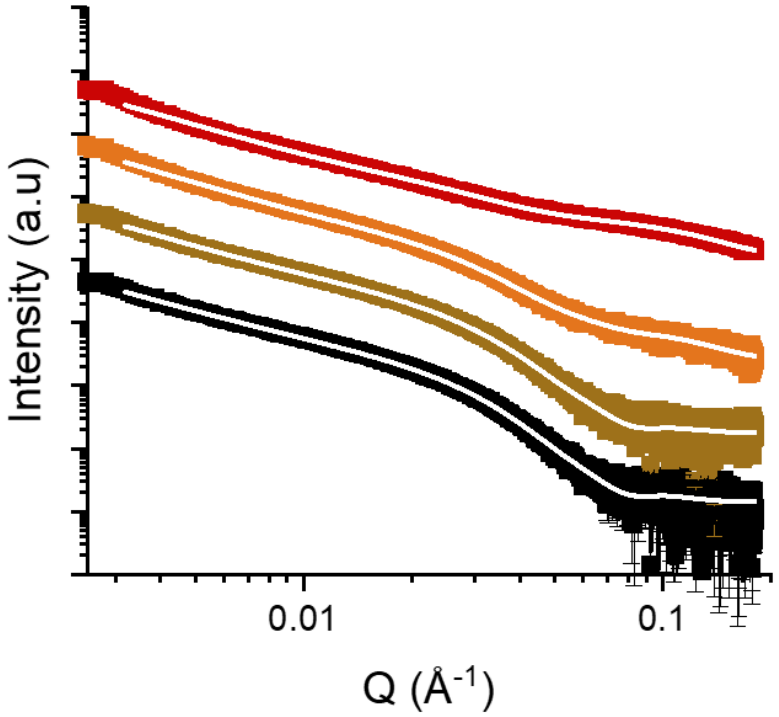

Figure 5.10. Small angle X-ray data for **2NapIF** gels (5 mg/mL) obtained in presence of 0 wt% dextran (black), 0.1 wt% dextran (brown), 1 wt% (orange) and 10 wt% (red). The white data represents model fits, summarised in Table 5.4. Data has been offset for clarity.

Table 5.4. Fitting parameters for SAXS data in Figure 5.10. The data was fit to a flexible elliptical cylinder (FCE) combined with a sphere model. Values that were manually added and fixed have been labelled with *.

	2NapIF (5 mg/mL)			
Sample	**0.1 wt% Dextran**		**1 wt% Dextran**	
Model	**FCE**		**FCE+Sphere**	
	Value	**Error**	**Value**	**Error**
Scale	0.0040	1.62×10^{-6}	1	/
Background (cm^{-1})	0.018	0.0001	0.026*	
A_scale	/	/	0.0003	1.72×10^{-6}
A_radius (Å)	40.5	0.10	40.1	0.19
A_axis_ratio	2.1	0.01	2.1	0.02
A_Kuhn_length (Å)	479.5	3.02	385.5	2.15
A_length (Å)	7902.9	342.33	10000*	/
B_scale	/	/	0.01	0.0001
B_radius	/	/	19.2	0.13
χ^2	1.79		1.81	

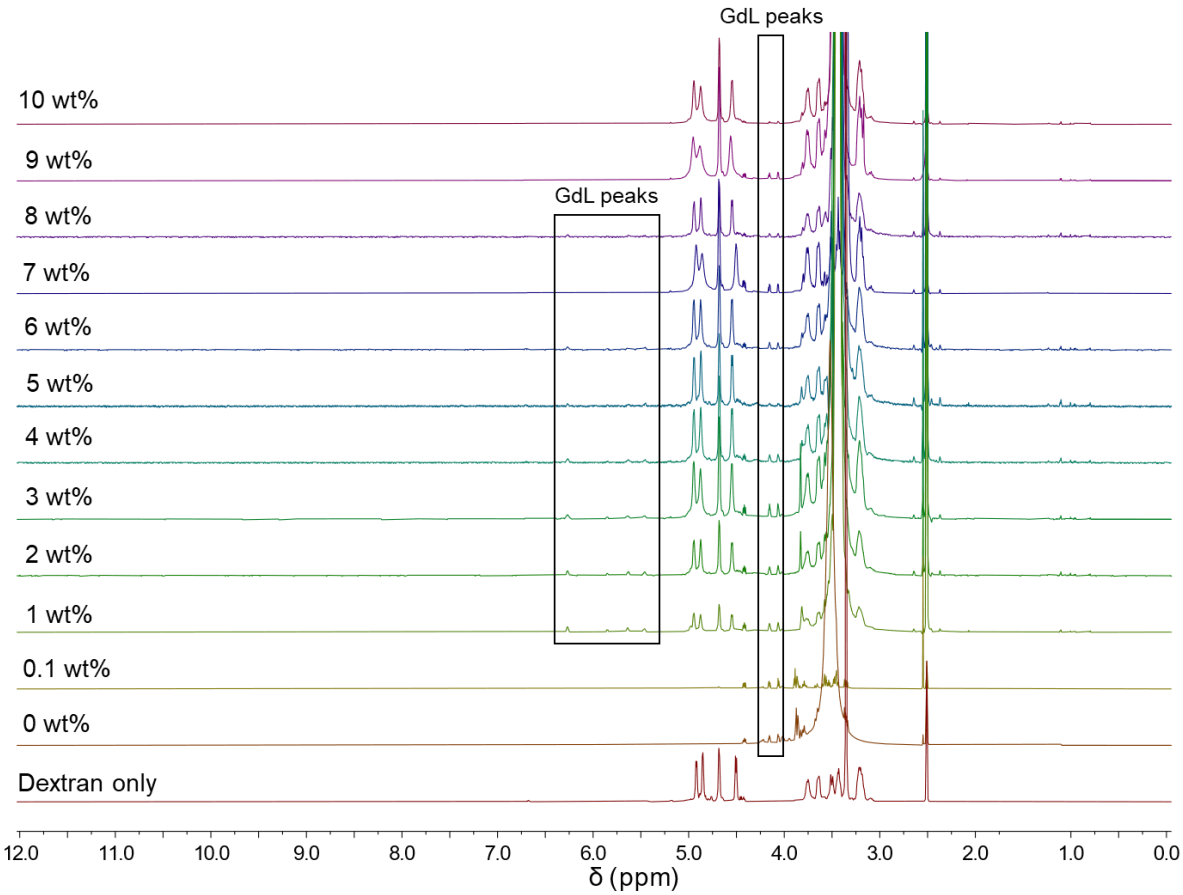

Figure 5.11. Full NMR data in d6-DMSO for liquid released through the syringe filter for **2NapIF** gels formed in presence of dextran at loadings ranging from 0 wt% to 10 wt%. The data shows the presence of the hydrolysis products of GdL and the presence of dextran in all gel loadings.

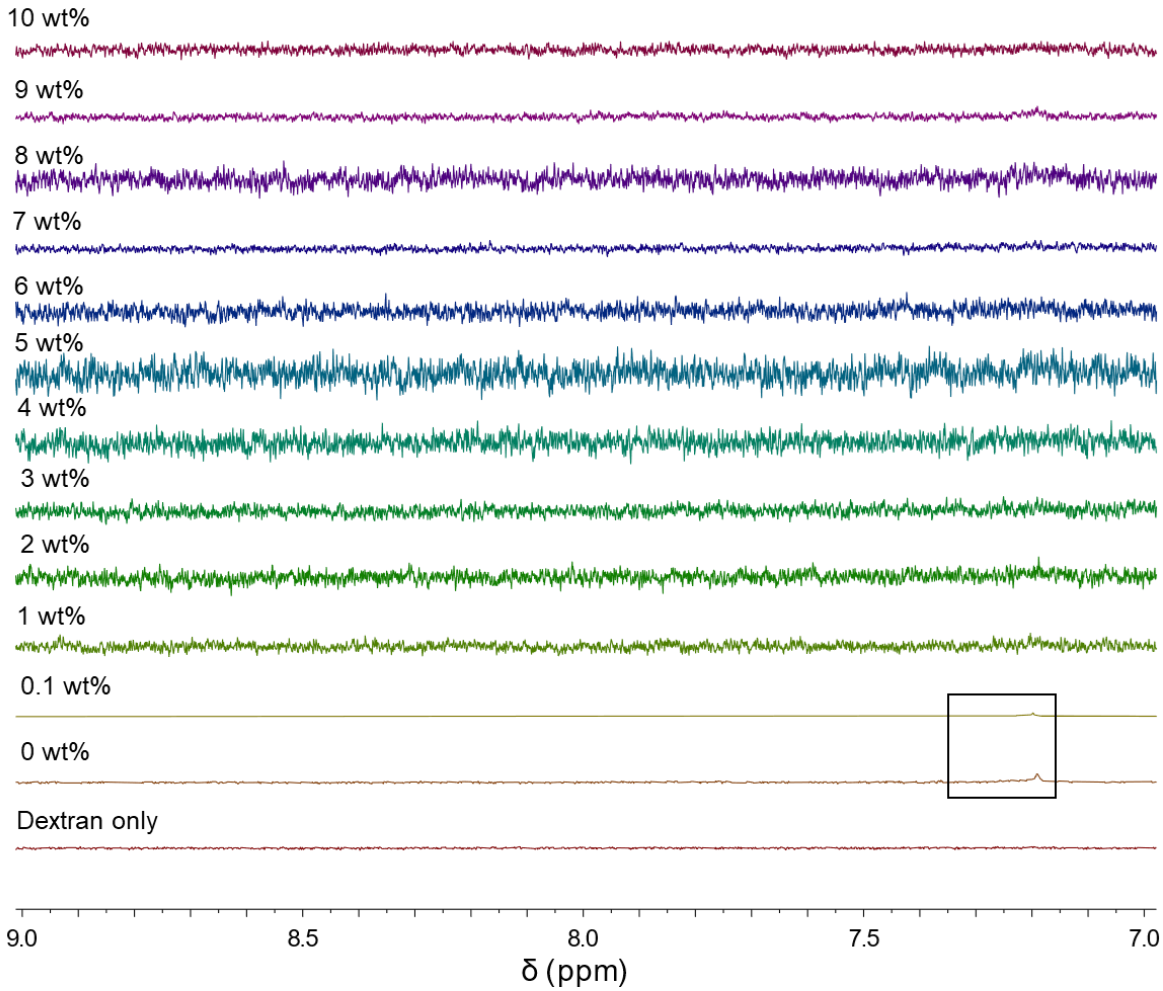

Figure 5.12. Expanded aromatic region for Figure 5.11 to further highlight the presence or absence of gelator passing through. The sample collected from the gels containing higher loadings of dextran show the absence of gelator peaks, while very small amount of gelator can be observed at 0 wt% and 0.1 wt%.

To quantify the gelator present in the extruded solution, fluorescence was used, taking advantage of the inherent fluorescence of the naphthalene moiety in **2NapIF**. Firstly, a calibration curve was obtained in DMSO by using a variety of dilutions of **2NapIF** and taking the intensity value at 351 nm (Figure 5.13). The curve was then fitted using a linear fitting function, obtaining the following equation:

$$y = 18.04 + 57594.42x \qquad Equation\ 5.1$$

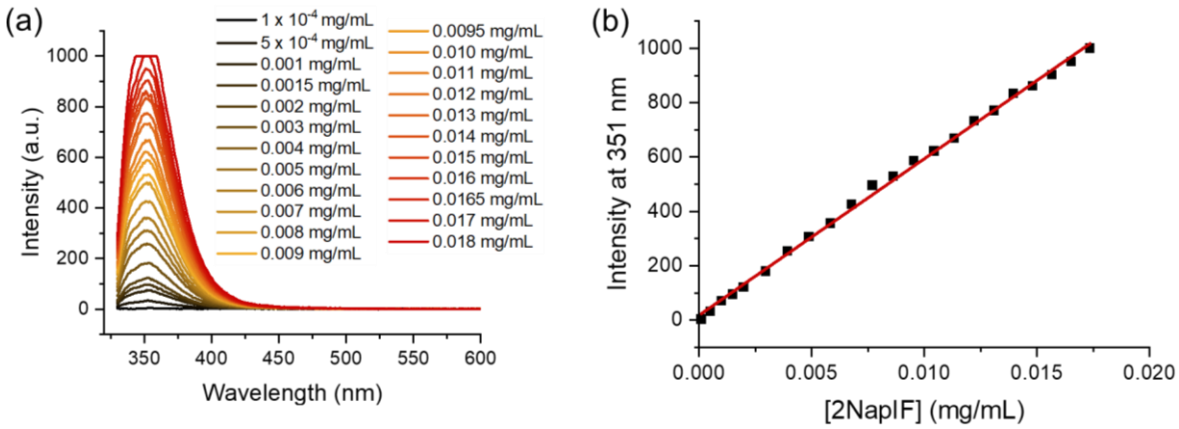

Figure 5.13. (a) Fluorescence spectra of a solution of **2NapIF** in DMSO at different concentrations. (b) Calibration curve obtained from the intensity at 351 in (a). The calibration curve was fitted using the Linear fitting function on Origin v2020b.

Then, fluorescence spectra were obtained from 1 mL of extrudate solution after freeze-drying and dissolving in 2 mL of DMSO for 0 wt% (Figure 5.14, red data), 1 wt% (Figure 5.14, orange data) and 10 wt% dextran (Figure 5.14, brown data). The data was also compared to the fluorescence spectra of **2NapIF** (Figure 5.14, black data) and dextran (Figure 5.14, green data) for clarity. The fluorescence intensity was recorded at 351 nm and plugged into the equation to provide exact concentrations of **2NapIF** in the extruded solutions, showing that only a maximum of 0.36% of the expected **2NapIF** amount is present (Table 5.5).

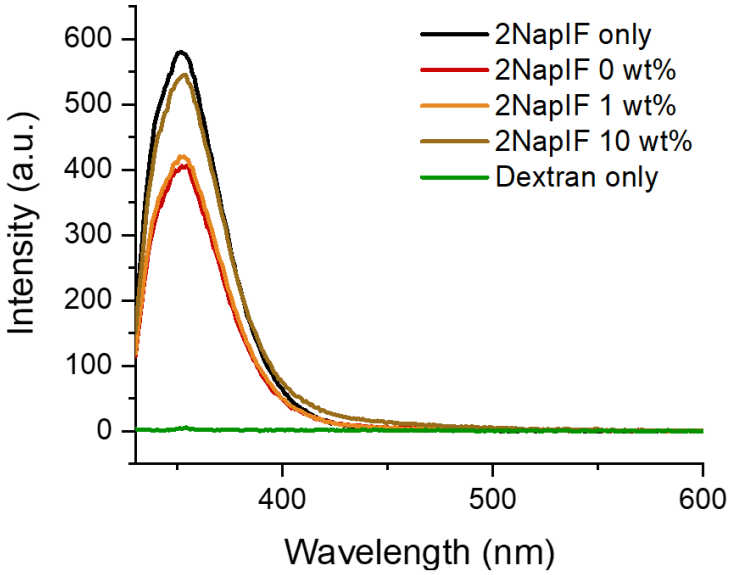

Figure 5.14. Fluorescence spectra of a solution of **2NapIF** (black), a solution of just dextran (green) and solutions of extrudates obtained at different dextran concentrations recovered after filtration of the gel through a syringe filter.

Table 5.5. Summary of the results obtained from comparing the fluorescence spectra of the extrudates and the calibration curve to quantify amount of gelator passing through the filter.

	Concentration extruded	% extruded
2NapIF 0 wt% dextran	0.0067 mg/mL	0.26 %
2NapIF 1 wt% dextran	0.007 mg/mL	0.28 %
2NapIF 10 wt% dextran	0.009 mg/mL	0.36 %

Although pH-triggered gelation at low pH is a useful method to obtain homogeneous gels, the pH reached by these materials is too low for any applications in the human body. One way to overcome this is to form gels at values near physiological pH (7.4) by using buffer as a gelation trigger.

5.2.2 Buffer-triggered gels

For buffer-triggered gels, we focused on one system, called **CD-005** for the rest of this Chapter (Figure 5.15). **CD-005** forms gels after addition of a 1.5M Tris-HCl buffer solution (pH 6.8) to a concentrated solution of the LMWG, giving self-supporting materials at pH 6.9 within 5-10 minutes (Figure 5.16a). However, to allow the gelation to reach completion, all the gels were left undisturbed overnight prior to any measurements.

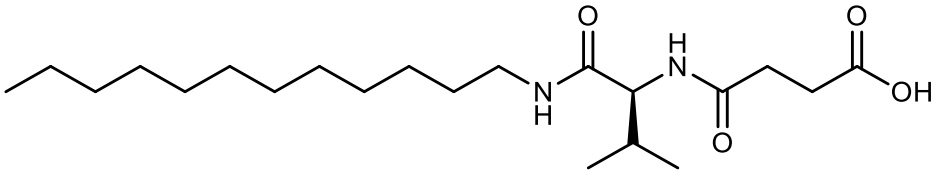

Figure 5.15. Chemical structure of gelator **CD-005** capable of forming gels *via* buffer triggered gelation.

CD-005 gels formed through this method were visually very clear (Figure 5.16a, left), with poor mechanical properties (Figure 5.16b, red data). Here, the system had relatively low G′ and G″ and started breaking at very low strain (<1%). The material also showed frequency dependence on G′ and G″, indicating the formation of not true gels (Figure 5.16c, red data). To improve material properties, a calcium salt was added ($CaCl_2$). In the presence of 1 equivalent of $CaCl_2$, opaque gels were formed (Figure 5.16a, right), with higher G′ (Figure 5.16b, black data) and more frequency independent behaviour (Figure 5.16c, black data). The LVER was also improved, but crucially the material still breaks at lower strain, allowing the system to still be used successfully for release.

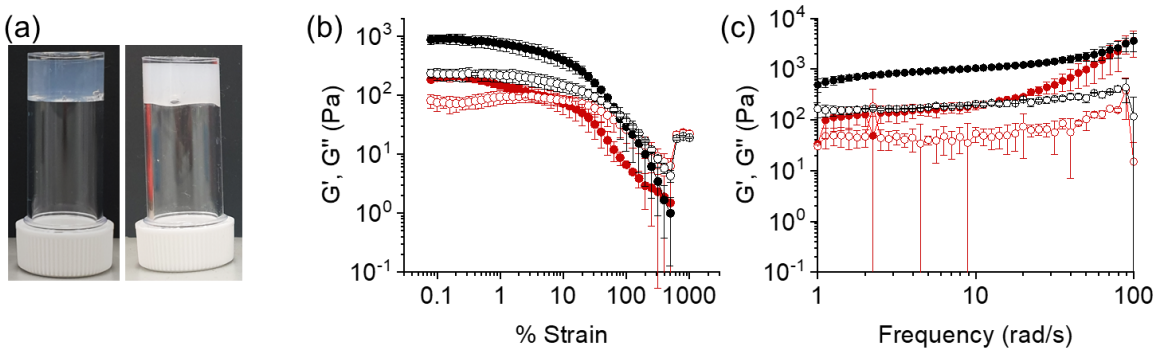

Figure 5.16. (a) Photographs of gels obtained using a buffer trigger at pH 6.8 without (left) and in presence of 1 eq. $CaCl_2$ (right). Strain sweeps (b) and frequency sweeps (c) for **CD-005** gels obtained without (red data) and in presence of 1 eq. $CaCl_2$ (black data). In all cases, closed circles represent G′ and open circles represent G″.

For both gels, the yield stress was also determined to investigate the way the gel network breaks. This was done by performing strain sweeps at a frequency of 1 rad/s and plotting the elastic stress (G′ x γ_0) versus the strain, as previously used for other systems.[23-27] Both **CD-005** gels showed an initial linear increase, related to the elastic response of the gel network to low amplitude. For the gels prepared in presence of salt, a single yielding process at a strain amplitude of 63% (38 Pa) was observed (Figure 5.17b, black data), which agrees with the crossover point of G′ and G″ in the strain sweep (Figure 5.17a, black data). Gels obtained in absence of calcium instead showed two maxima in the elastic stress curve, with the first occurring at a strain of 1.6% (1.4 Pa) and the second one at 126% (4.06 Pa) (Figure 5.17b, red data). The first yield point occurs within the values of the crossover strain in the amplitude sweep (Figure 5.17a, red data), while the second one can be related to a maximum peak in G″, the maxima of energy dissipation. In this case, the first yield could be ascribed to initial breaking of the self-assembled network into smaller disconnected clusters, which are further disrupted at the second yield stress.[25]

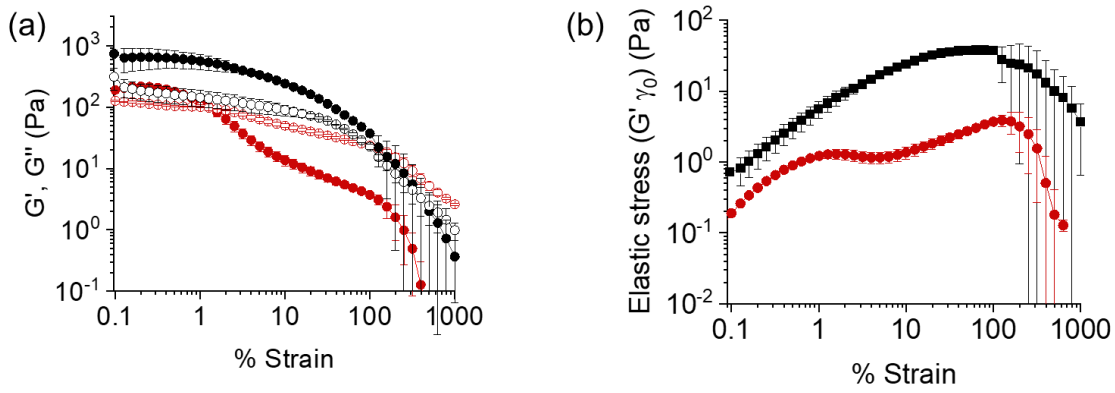

Figure 5.17. Determination of dynamic yield stress. (a) Amplitude sweeps for gels formed from **CD-005** with (black data) and without (red data) addition of $CaCl_2$ at 1 rad/s. (b) Dynamic yield stress plot for gels formed from **CD-005** with (black data) and without (red data) addition of $CaCl_2$ using the data from (a). In all cases, full circles represent G′ and open circles represent G″.

Small angle X-ray scattering was used to probe the morphology of the gels. Without salt, the scattering data was fitted to a power law model (Figure 5.18a, red, Table 5.6), indicative of the presence of large heterogeneities in the network or irregular aggregates in the gel. The SAXS data for the **CD-005** in presence of $CaCl_2$ instead showed a stronger scattering which was fit to an elliptical cylinder model combined with a power law (Figure 5.18a, black, Table 5.6). Interestingly, the data presents a peak at q = 0.154 Å (d = 40.8 Å), which suggests that the gelator fibers are part of a periodic arrangement in the structure with a crystalline character.

To further investigate this, circular dichroism (CD) was performed on the gels in absence of calcium (Figure 5.18b and 5.18c, red data) and in presence of 1 eq. of $CaCl_2$ (Figure 5.18b and 5.18c, black data). The CD data showed different arrangements in the secondary structures between the two systems. The gel formed without any salt exhibits a negative band with a shoulder in the range of 200-240 nm (Figure 5.18b, red data). The sample with $CaCl_2$ showed a negative band around 235 nm and a positive band occurring near 190 nm, which could be indicative of a β-sheet-like arrangement (Figure 5.18b, black data).

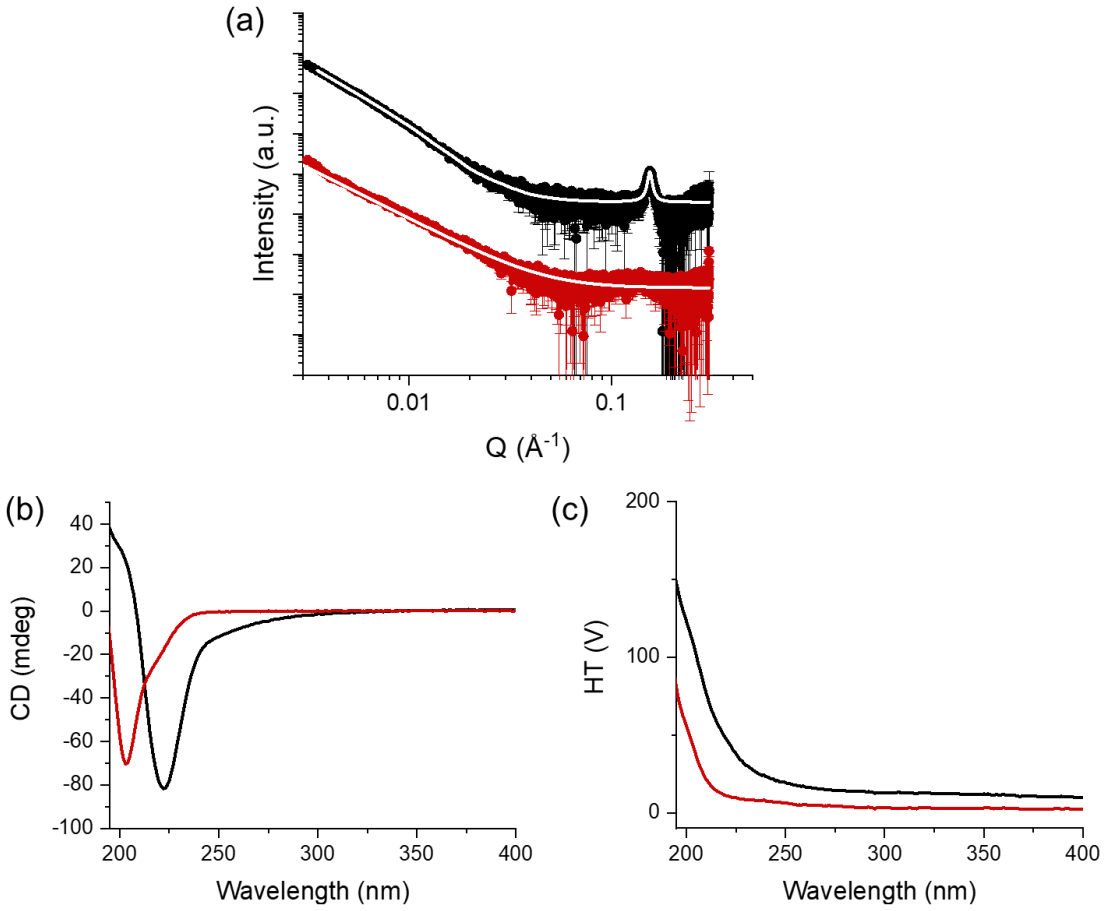

Figure 5.18. (a) Small angle X-ray patterns of **CD-005** gels obtained without (red data) and in presence of $CaCl_2$ (black data). The white lines represent the model fits. Data has been offset for clarity. Circular dichroism (b) and HT (c) of the **CD-005** gels obtained without (red data) and in presence of 1 eq. of $CaCl_2$ (black data).

Table 5.6. Fitting parameters for SAXS data in Figure 5.18a. The data was fit to either a power law model (PL) or an elliptical cylinder model (EC) combined with a Lorentzian Peak model (Peak) and a power law (PL). Values that were manually added and fixed have been labelled with *.

Sample	**CD-005 0 eq. CaCl2**			**CD-005 1 eq. CaCl2**	
Model	**PL**			**EC+Peak+PL**	
	Value	**Error**		**Value**	**Error**
Scale	4.30×10^{-6}	1.63×10^{-7}	**Scale**	1	
Background (cm^{-1})	0.02*	/	**Background (cm^{-1})**	0.02*	/
Power	2.6	0.01	**A_scale**	1.78×10^{-5}	7.85×10^{-7}
			A_radius (Å)	159.3	3.11
			A_axis_ratio	2.2	0.09
			A_length (Å)	1000*	/
			B_scale	0.09	0.001
			B_peak_pos	0.154	4.96×10^{-5}
			B_peak_HWHM	0.004	7.01×10^{-5}
			C_scale	2.36×10^{-7}	1.66×10^{-8}
			C_power	3.3	0.01
χ^2	2.28		χ^2	2.73	

Similarly, as for **2NapIF**, different loadings of dextran were tested in the **CD-005** gels (0.1 wt%, 1 wt% and 10 wt%), both without and with a calcium salt. Differences in the stiffness and strength in the materials were observed when the gels were prepared without calcium (Figure 5.19, red data), with the gels possessing higher G′ and yield points at higher dextran loadings. This is likely due to a stabilisation of the gel network in presence of the bulky macromolecule. Conversely, very similar datasets could be observed for **CD-005** gels formed in presence of 1 eq. of $CaCl_2$, with a slight increase in stiffness in presence of 1 wt% and 10 wt% dextran (Figure 5.19, black data). This suggests that the more fibrous structures formed in presence of the calcium salt can form stronger networks with larger pores that can accommodate the dextran.

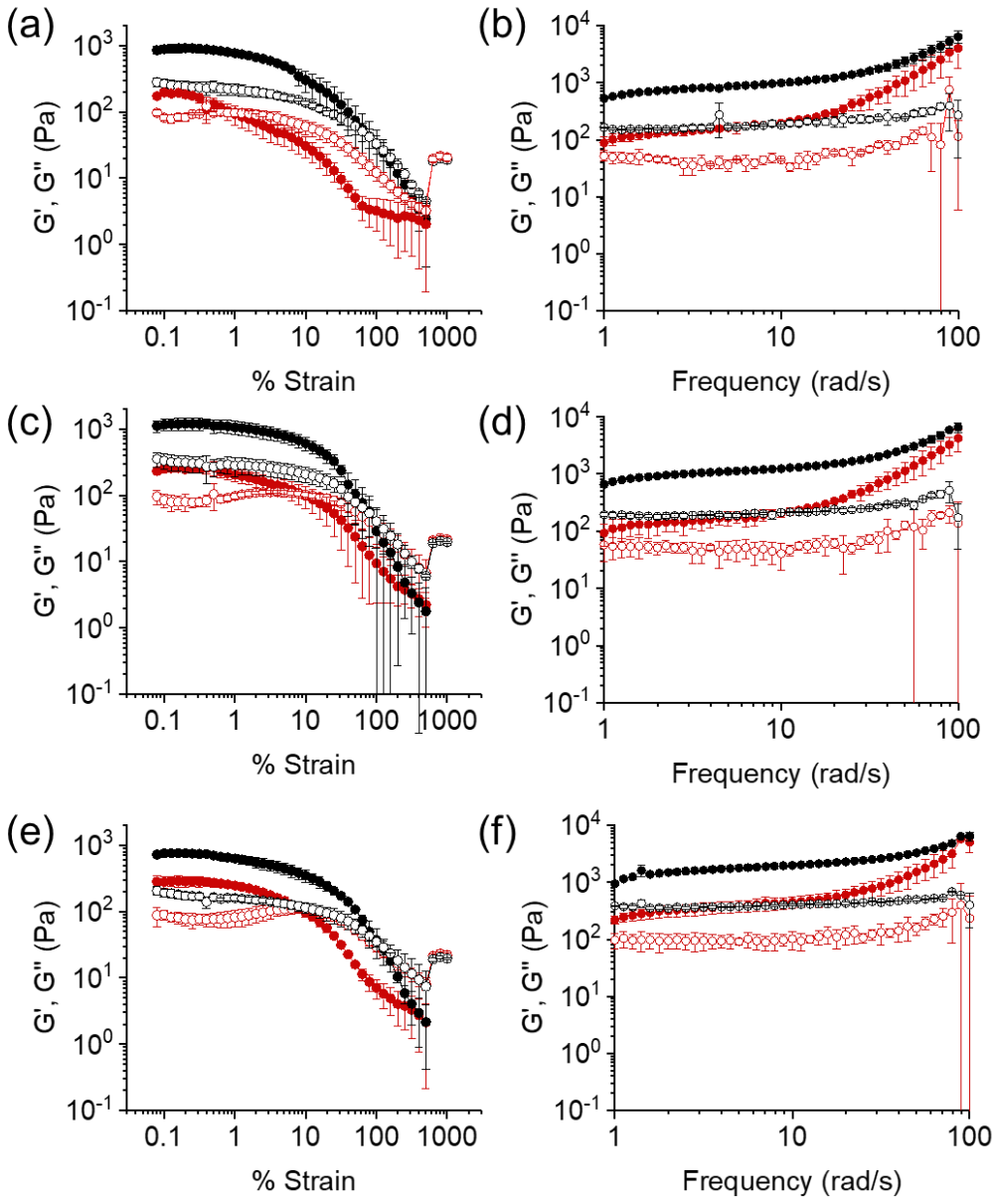

Figure 5.19. Strain sweeps (a) and frequency sweeps (b) obtained for **CD-005** gels formed in presence of 0.1 wt% dextran without (red data) and with 1 eq. of $CaCl_2$ (black data). Strain sweeps (b) and frequency sweeps (c) obtained for **CD-005** gels formed in presence of 1 wt% dextran without (red data) and with 1 eq. of $CaCl_2$ (black data). Strain sweeps (e) and frequency sweeps (f) obtained for **CD-005** gels formed in presence of 10 wt% dextran without (red data) and with 1 eq. of $CaCl_2$ (black data). In all cases, full circles represent G′ and open circles represent G″.

SAXS was also performed on the different gels to assess any effect of the dextran on the morphology of the final materials (Figure 5.20). Similarly as before, the data for both **CD-005** gels was fitted to similar models to the data with no dextran for 0.1 wt% dextran (Figure 5.20, brown data, Tables 5.7 and 5.8), while for 1 wt% (Figure 5.20, orange data) and 10 wt% (Figure 5.20, red data), a spherical model needed to be included to capture the dextran

scattering at high *q* (Tables 5.7 and 5.8). For the **CD-005** gel formed with 1 eq. $CaCl_2$ in presence of 10 wt% dextran, addition of an elliptical cylinder model would not change the fit to the data. This is likely due to the large amount of dextran compared to the low concentration of gelator, which then dominates the scattering pattern. Interestingly, for both **CD-005** gels, the data at 10 wt% was fit to spherical models with a radius of around 2.0 nm, whilst the data at 1 wt% suggested the presence of spheres with radii of around 3.0 nm. This may suggest that at 1 wt%, more dextran molecules are packed within the pores. However, as there are multiple models being added for fits to the **CD-005** gels formed in presence of salt, changes in values can also result from the need to accommodate four different models.

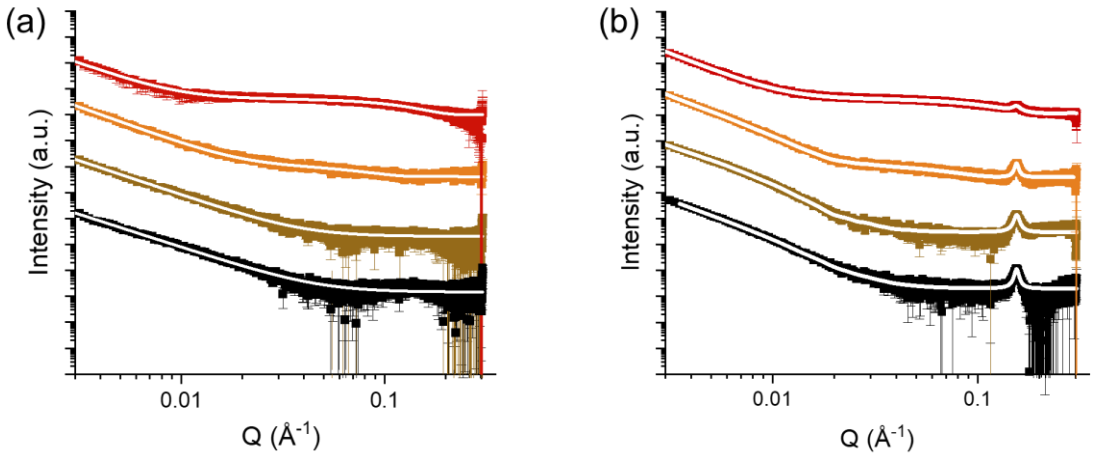

Figure 5.20. (a) Small angle X-ray scattering patterns for gels of **CD-005** formed in presence of 0 wt% (black data), 0.1 wt% (brown data), 1 wt% (orange data) and 10 wt% (red data) without calcium salts. (b) (a) Small angle X-ray scattering patterns for gels of **CD-005** formed in presence of 0 wt% (black data), 0.1 wt% (brown data), 1 wt% (orange data) and 10 wt% (red data) after addition of 1 eq. $CaCl_2$. In all cases, white lines represent model fits to the data. Patterns offset for clarity.

Table 5.7. Fitting parameters for SAXS data in Figure 5.20a. The data was fit to a power law model (PL) combined with a sphere. Values that were manually added and fixed have been labelled with *.

CD-005, 0 eq. CaCl2						
Sample	**0.1 wt% dextran**		**1 wt% dextran**		**10 wt% dextran**	
Model	**PL**		**PL+Sphere**		**PL+Sphere**	
	Value	**Error**	**Value**	**Error**	**Value**	**Error**
Scale	4.51×10^{-6}	1.37×10^{-7}	1		1	
Background (cm^{-1})	0.02*	/	0.041*		0.099*	/
A_scale	2.6	0.01	2.17×10^{-4}	4.55×10^{-6}	4.92×10^{-3}	1.43×10^{-5}
A_radius (Å)	/	/	29.2	0.29	17.6	0.02
B_scale	/	/	1.67×10^{-6}	7.51×10^{-8}	1.23×10^{-6}	9.50×10^{-8}
B_power	/	/	2.8	8.55×10^{-3}	2.7	0.02
χ^2	2.04		2.07		4.74	

Table 5.8. Fitting parameters for SAXS data in Figure 5.20b. The data was fit to an elliptical cylinder model (EC) combined with a Lorentzian Peak model (Peak), a power law model (PL) and sphere. Values that were manually added and fixed have been labelled with *.

CD-005, 1 eq. CaCl2						
Sample	**0.1 wt% dextran**		**1 wt% dextran**		**10 wt% dextran**	
Model	**EC+Peak+PL**		**EC+Peak+PL+Sphere**		**Peak+PL+Sphere**	
	Value	**Error**	**Value**	**Error**	**Value**	**Error**
Scale	1		1		1	
Background (cm^{-1})	0.02*	/	0.04*		0.11*	/
A_scale	4.33×10^{-5}	7.15×10^{-7}	2.69×10^{-5}	1.28×10^{-8}	/	/
A_radius (Å)	165.7	1.18	158.6	1.94	/	/
A_axis_ratio	2.4	0.04	2.5	0.07	/	/
A_length (Å)	1000*	/	1000*	/	/	/
B_scale	0.11	0.001	0.097	8.38×10^{-4}	0.081	9.41×10^{-4}
B_peak_pos	0.154	4.51×10^{-5}	0.154*	/	0.154*	/
B_peak_HWHM	0.005	6.36×10^{-5}	0.004*	/	0.008	1.54×10^{-4}
C_scale	1.67×10^{-7}	8.56×10^{-9}	3.49×10^{-8}	7.11×10^{-9}	4.41×10^{-7}	2.07×10^{-8}
C_power	3.4	0.01	3.6	0.03	3.1	0.01
D_scale	/	/	0.003	5.35×10^{-5}	0.003	1.75×10^{-5}
D_radius (Å)	/	/	32.1	0.29	20.0	0.05
χ^2	4.62		2.20		1.74	

CD was also performed on both gels with various dextran loadings, which show similar spectra as the ones obtained in absence of the macromolecule (Figure 5.21). Overall, these data suggest that the primary fibres and the secondary structures that are forming the gel network do not appear to be significantly affected by the presence of dextran, indicating that the macromolecule is likely residing within the pores of the gel network.

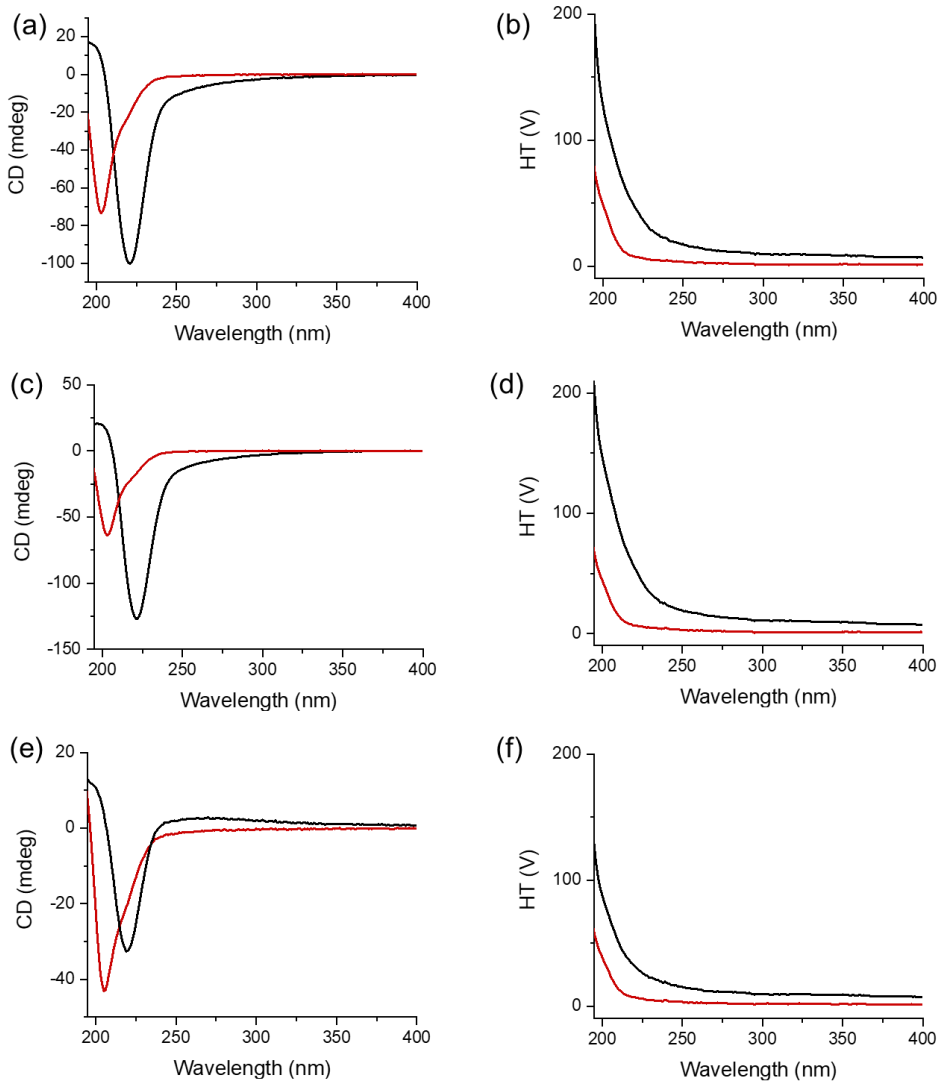

Figure 5.21. (a) Circular dichroism and (b) HV for **CD-005** gels obtained in presence of 0.1 wt% of dextran without (red data) and with 1 eq. $CaCl_2$ (black data). (c) Circular dichroism and (d) HV for **CD-005** gels obtained in presence of 1 wt% of dextran without (red data) and with 1 eq. $CaCl_2$ (black data). (e) Circular dichroism and (f) HT for **CD-005** gels obtained in presence of 10 wt% of dextran without (red data) and with 1 eq. $CaCl_2$ (black data).

5.2.3 Investigating the releasability of buffer-trigger gels

To test the ability of the **CD-005** gels to be released *via* a mechanical trigger, the gels were prepared in syringes fitted with 2.7 μm filters. Compared to the pH-triggered gels, these gels form relatively fast once the buffer is added to the gelator solution. Therefore, the materials were prepared directly in 12 mL propylene syringes by loading the gelator solution through the syringe nozzle using a 1 mL syringe, followed by addition of the buffer solution in a similar way using a 3 mL syringe. This method allowed formation of homogeneous gels directly in the syringe, minimising volume losses. The samples were allowed to stabilise

overnight then syringed through the filter, giving clear solutions (Figure 5.22). Compared to the pH-triggered gels, both **CD-005** gels were easier to push through, due to the lower stiffness and yield points of the materials.

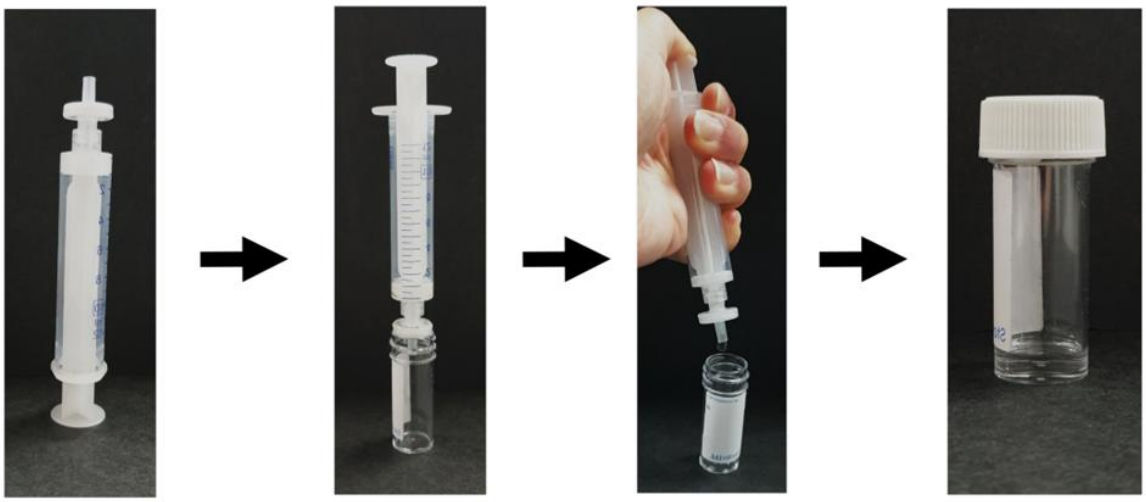

Figure 5.22. Photographs showing the release process for **CD-005** gels *via* mechanical trigger. The opaque gel is first formed in the syringe (left) and then pushed through the in-line filter to release a clear solution (right).

The extrudate solution was freeze-dried and then analysed using ^{1}H NMR. The resulting spectra were compared to the NMR spectrum of **CD-005** (Figure 5.23, black data). As this gelator does not possess any aromatic moieties, the presence of gelator was studied by observing peaks in the aliphatic region within 1.2 – 1.5 ppm. Broad peaks at 5.0 ppm and 7.5 ppm were observed in all samples, which can be ascribed to peaks arising from the buffer solution used to prepare the gels (Figure 5.23, green data). The NMR data shows the presence of **CD-005** peaks in the gels prepared in absence of calcium salt (Figure 5.23, red data), whilst these peaks were not observed in the **CD-005** gels prepared with 1 eq. $CaCl_2$ (Figure 5.23, orange data). This suggests that the **CD-005** gels obtained with no calcium were likely not suitable for the mechanical release of model molecules and therefore only gels with 1 eq. $CaCl_2$ were used to test the release of dextran.

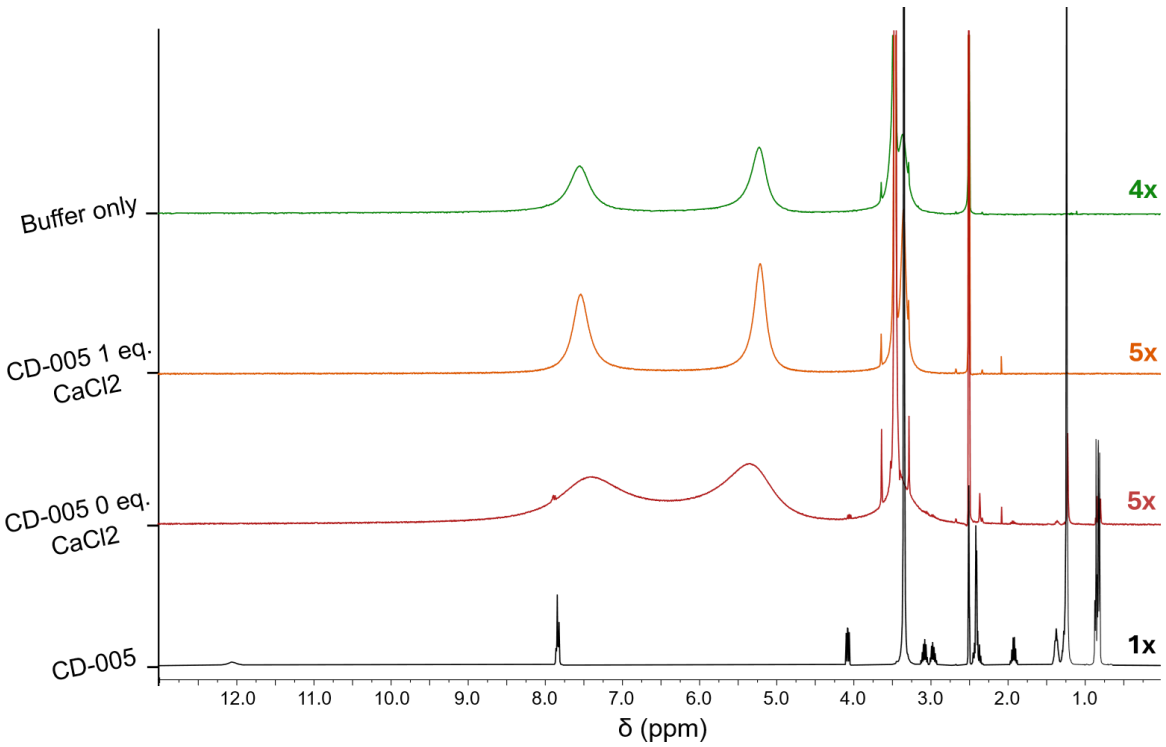

Figure 5.23. Full NMR spectra in d6-DMSO for **CD-005** (black data) compared to liquid released through the syringe filter for **CD-005** gels formed without (red data) and with 1 eq. $CaCl_2$ (orange data). To clarify the presence of broad peaks at 5.0 ppm and 7.5 ppm, the full NMR spectra obtained from the buffer solution after release and freeze-drying is shown (green data). Scaling of the data with respect to each other has been added for clarity.

To further prove the presence of the **CD-005** network in the syringe filter after gel filtration, a syringe filter after extrusion was tested using FTIR and compared to the infrared spectra of a clean filter (Figure 5.24a) and the **CD-005** powder as synthesised (Figure 5.24c). Excitingly, the data from the syringe filter (Figure 5.24b) exhibits the **CD-005** peaks, confirming the ability of the gelator to be retained in the syringe filter and not extruded.

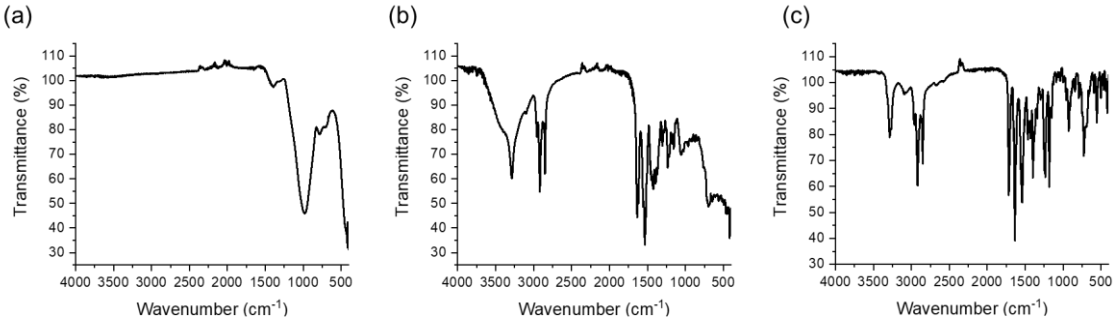

Figure 5.24. Infrared spectra of (a) clean 2.7 µm syringe filter, (b) 2.7 µm syringe filter after extrusion of **CD-005** gel using the filter, (c) **CD-005** powder as synthesised. The syringe filter after extrusion presents peaks coming from the gelator molecule, which are not visible in the clean filter spectra.

5.2.3.1 Release of model compound dextran

CD-005 gels with calcium were prepared in presence of 0.1 wt%, 1 wt% and 10 wt% of dextran in 12 mL propylene syringes as previously described. ^{1}H NMR was then performed on the extruded samples after freeze-drying (Figure 5.25). The data is plotted in comparison with the spectra of just **CD-005** (Figure 5.25, black data) and dextran (Figure 5.25, green data). For all dextran concentrations, no peaks from the gelator were observed in the NMR data and dextran peaks were observed for the samples at 1 wt% and 10 wt% (Figure 5.25, orange and red data). Due to overlapping with the wide peaks arising from the buffer, the dextran peaks observed at 1 wt% (Figure 5.25, orange data) are broadened.

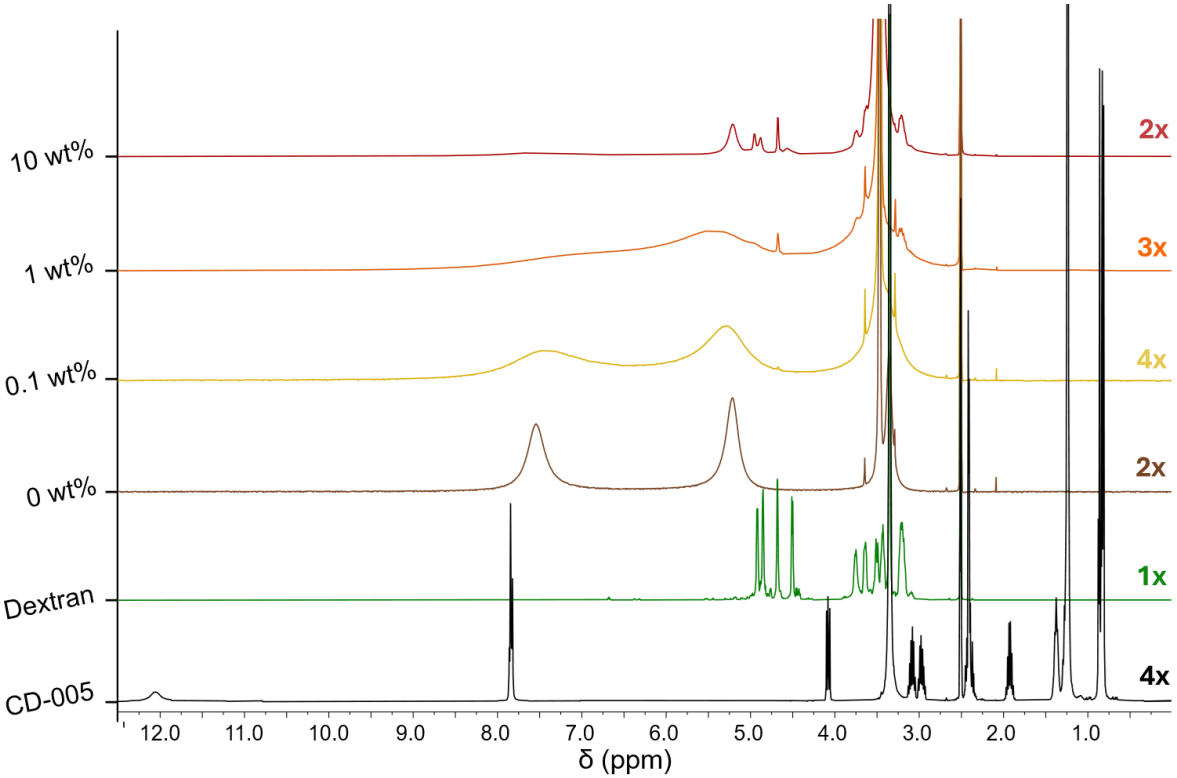

Figure 5.25. Full NMR spectra in d6-DMSO for **CD-005** (black data) compared to liquid released through the syringe filter for **CD-005** gels formed with 1 eq. $CaCl_2$ in presence of 0 wt% (brown), 0.1 wt% (yellow), 1 wt% (orange) and 10 wt% (red) dextran. The spectrum of dextran is also shown for comparison (green). Broad peaks at around 5.0 and 7.5 ppm are ascribed to the buffer (Figure 5.23, green data). Scaling of the data with respect to each other has been added for clarity.

To understand if the storing and release of the macromolecule had any effect on the macromolecule itself, SAXS data was collected on fresh solutions of 1 wt% and 10 wt% dextran and compared to the SAXS data obtained on the solutions after pushing the loaded gels through the filter. The data is also compared to the scattering pattern obtained after

pushing an unloaded gel through the filter (Figure 5.26, black data). This showed very little scattering, suggesting that only buffer is released, which is then subtracted. The SAXS data shows the same scattering pattern from the fresh dextran solutions (Figure 5.26, brown data) and the dextran solution after syringing (Figure 5.26, orange and red data), indicating that the macromolecule is not affected by the storing and releasing from the gel.

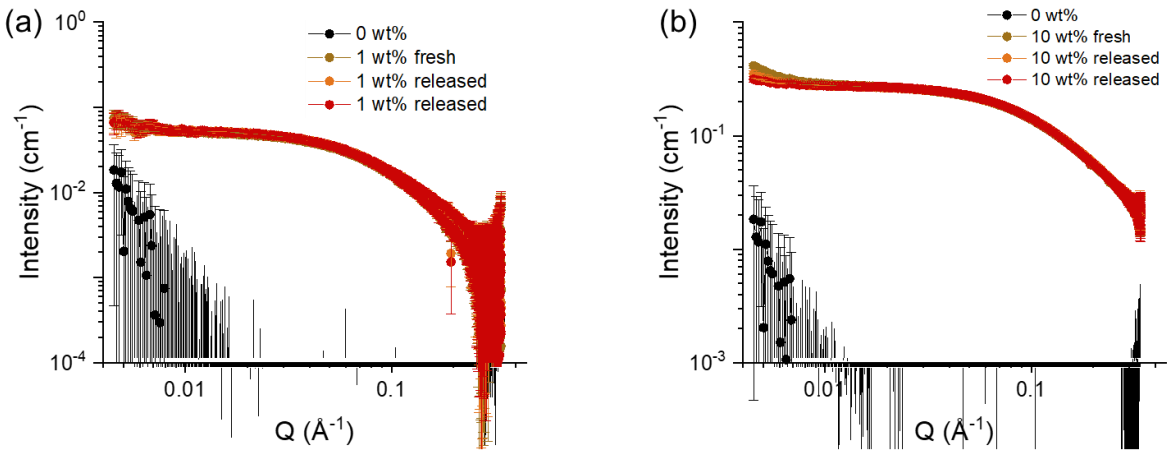

Figure 5.26. Small angle X-ray scattering data obtained for fresh solutions of dextran (brown data) and solutions obtained after being released from the gel (orange and red data) at 1 wt% (a) and 10 wt% (b) dextran loadings.

To quantify the released dextran from the gel, fluorescein isothiocyanate-Dextran (FITC-D) was used to prepare gels at a loading of 1 mg/mL. A calibration curve was first obtained in TRIS buffer by preparing FITC-D at different dilutions using UV-Vis (Figures 5.27a and 5.27b). The absorbance at 293 nm was plotted and fitted using a linear fitting to obtain the following equation:

$$y = -(0.0027 \pm 2.9E-4) + (0.64 \pm 0.0015)x \qquad Equation\ 5.2$$

Then, UV-Vis was performed on buffer solutions obtained from syringing the gel through the filter (Figure 5.27c) and compared to the calibration curve data (Figure 5.27d). The absorption at 493 nm was then recorded and plugged into the equation to quantify the concentration of dextran. Overall, 92% ± 2 of the expected dextran was recovered. We hypothesise that the remaining dextran is likely trapped in the syringe filter, as the syringe filter shows a yellow tint after release (Figure 5.27c, right).

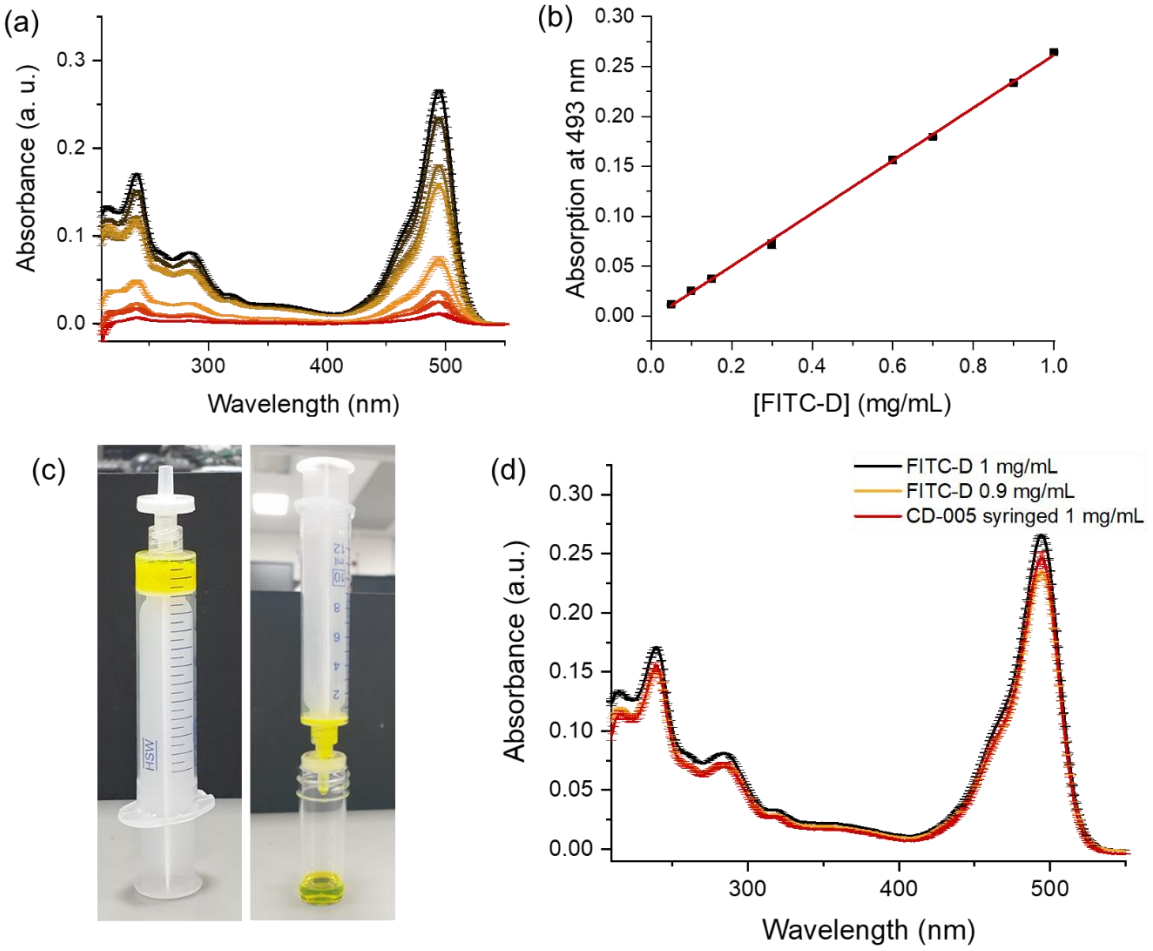

Figure 5.27. (a) Spectra of FITC-Dextran at different concentrations in buffer. (b) Calibration curve obtained from (a). The data was fit using the Linear fitting function on Origin v2020b. (c) Photographs showing the release of FITC-D dextran from a **CD-005** gel (1 eq. $CaCl_2$). From the opaque gel, a clear yellow solution is released. Some dextran can be observed in the filter. (d) Data for solutions of FITC-Dextran at 1 mg/mL (black), 0.9 mg/mL (orange) and data from solution of extruded gel (red) where the solution is expected to be at 1 mg/mL of FITC-Dextran.

5.2.4 Using supramolecular gels to store and release insulin

With confirmation that macromolecules can be encapsulated and selectively released by mechanical trigger, protein storage was studied to demonstrate recovery and the mode of action (preventing aggregation). As an exemplary molecule, we chose to encapsulate (bovine) insulin as a model therapeutic protein. Insulin is one of the most widely used protein drugs in the world but must be stored cool or freeze-dried requiring the user to self-prepare the solution prior to injection.[28] The instructions for insulin are very specific not to shake, as it is prone to aggregate into extended amyloid fibers losing efficacy and bioavailability.

Insulin was loaded into **CD-005** gels with no calcium at concentrations of 0.2 mg/mL and 3.2 mg/mL, a concentration around that of commercial formulations (U100), to yield clear gels (Figures 5.28a and 5.28d). Addition of 1 equivalent of calcium to the insulin gels was found to not yield stable materials, likely due to slightly different network formation for the **CD-005** gels in presence of insulin. Indeed, a 10-fold increase in stiffness was observed in the gels containing insulin compared to the **CD-005** gels in absence of calcium (Figures 5.28b and 5.28e), highlighting an effect of the encapsulation of insulin on material stiffness.

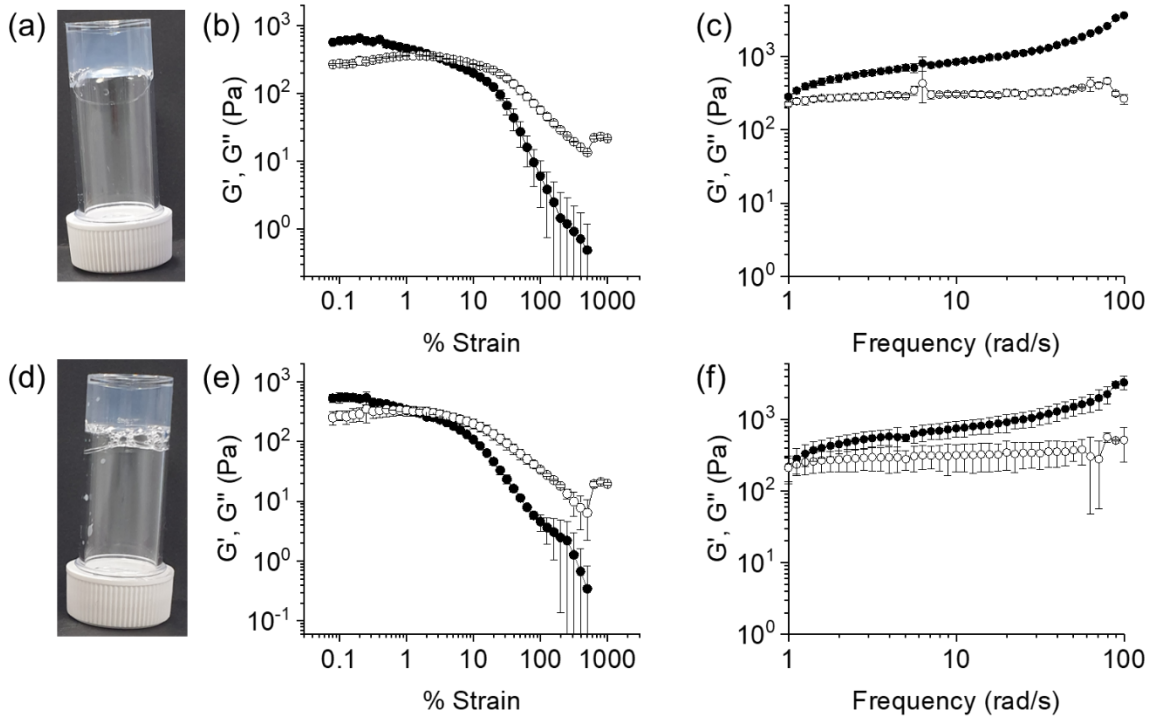

Figure 5.28. Photographs of gels obtained using **CD-005** in presence of 0.2 mg/mL insulin (a) and 3.2 mg/mL insulin (d). (b) Strain sweep and (c) frequency sweep for the **CD-005** gel with 0.2 mg/mL insulin. (e) Strain sweep and (f) frequency sweep for the **CD-005** gel with 3.2 mg/mL insulin. In all cases, full circles represent G′ and open circles represent G″.

To investigate whether this stiffening was induced by insulin interaction with the fibres, saturation transfer difference (STD) NMR spectroscopy was performed by Dr Matthew Wallace (UEA) (Figure 5.29). The size of the peaks is similar between the fresh insulin in buffer and the insulin trapped in the gel, strongly implying that the insulin is not adsorbed onto the fibres. Therefore, we assume that the effect is simply a slight re-adaptation of the gel network in presence of insulin.

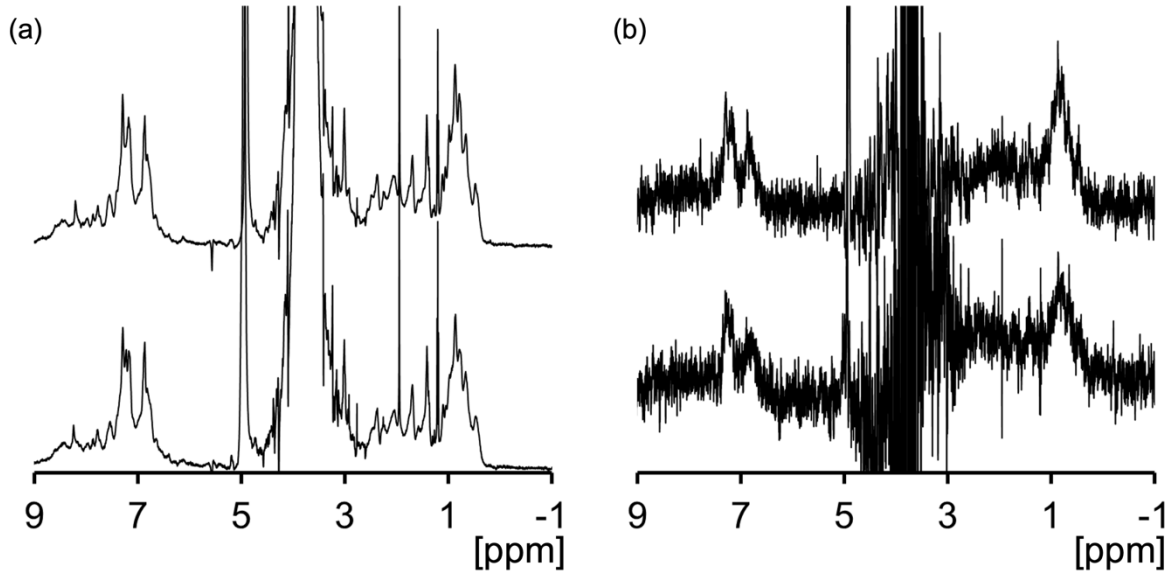

Figure 5.29. (a) ^{1}H NMR spectrum with perfect echo solvent suppression for (bottom) insulin in buffer and (top) insulin in a **CD-005** gel. In both cases, the insulin concentration was 3.2 mg/mL. The signals in both cases are very similar in terms of strength and width, strongly implying that the insulin is not absorbed on to the fibres in the gel. (b) STD-NMR with perfect echo solvent suppression for (bottom) insulin in buffer and (top) insulin in a **CD-005** gel. In both cases, insulin concentration was 3.2 mg/mL. Presaturation is applied at ≈3.8 ppm.[29] the size of the STD difference peaks are very similar with and without gel, again implying that the insulin is not sticking to the gel fibres. Data collected by Dr. Matthew Wallace (UEA).

We thus hypothesised that the increase in stiffness in these materials would allow release of the insulin without passing of the gelator compared to the unloaded **CD-005** gels. ^{1}H NMR was used to investigate the presence of insulin in the extrudate solutions. The data was compared to **CD-005** (Figure 5.30, black data) and insulin (Figure 5.30, green data). Significant overlapping peaks were observed in the data, so the solutions were further compared to an ^{1}H NMR spectra of insulin and **CD-005** at the expected concentrations in the gel (Figure 5.30, brown data). The extruded samples for both 0.2 mg/mL (Figure 5.30, orange data) and 3.2 mg/mL (Figure 5.30, red data) exhibit characteristic peaks of insulin, while no gelator was observed in the data. Although overlapping of peaks here make the analysis more difficult compared to dextran, the lack of peaks at around 4.0 ppm and 8.0 ppm strongly suggests the absence of gelator in the extrudates.

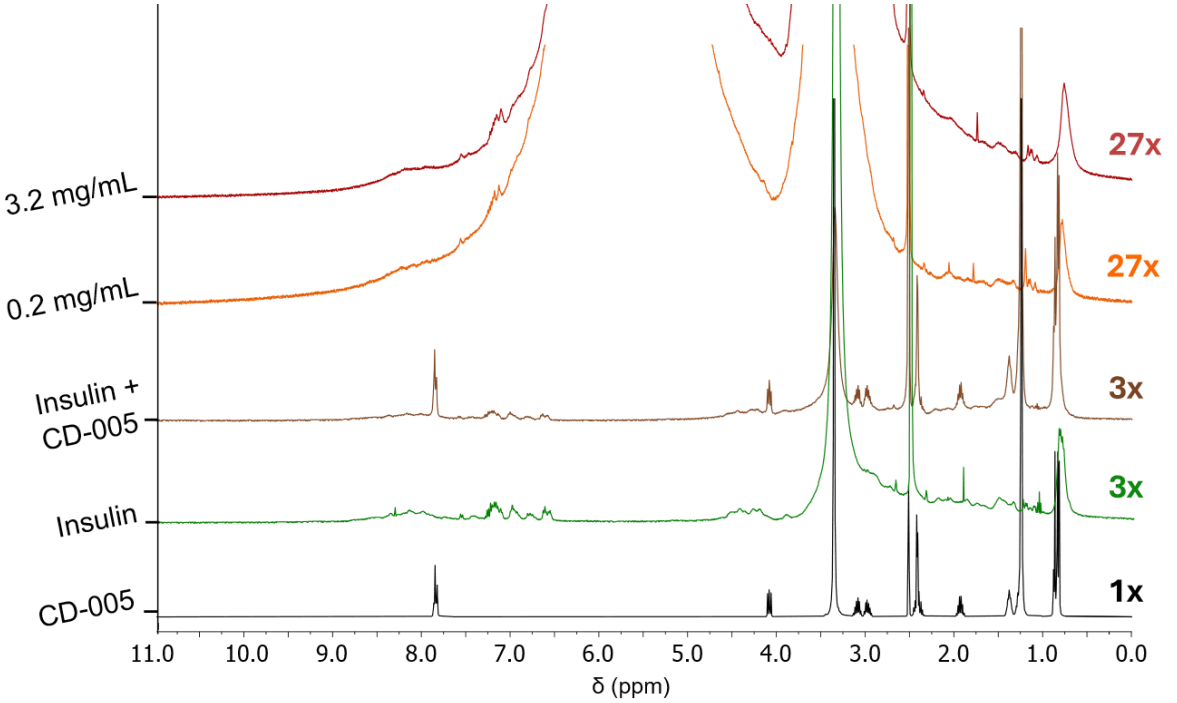

Figure 5.30. Full NMR spectra in d6-DMSO for **CD-005** (black data) compared to liquid released through the syringe filter for **CD-005** gels formed in presence of 0.2 mg/mL (orange) and 3.2 mg/mL (red) insulin. The spectrum of dextran is also shown for comparison (green) and the spectra obtained from mixing **CD-005** and insulin in the ratios used in the gel (brown) to elucidate presence of gelator in the extruded solutions. Scaling of the data with respect to each other has been added for clarity.

To quantify the released insulin from the gel, a calibration curve was first obtained in 1.5 M Tris-HCl buffer by preparing the insulin at different dilutions using UV-Vis (Figures 5.31a and 5.31b). As the UV-Vis absorbance could be influenced by aggregation of the insulin, all samples for the calibration curve were prepared by syringing through a syringe fitted with a 2.7 μm filter. The absorbance at 277 nm was then plotted and fitted using a linear fitting to obtain the following equation:

$$y = -(0.0094 \pm 0.0017) + (0.11 \pm 6.38E-4)x \qquad Equation\ 5.3$$

Then, UV-Vis was performed on buffer solutions obtained from syringing the gel through the filter and compared to the calibration curve data (Figure 5.31c) . The absorption at 277 was recorded and plugged in the solution. We note here that a complete overlap was observed with the data obtained after syringing and the fresh buffer solution at 3.3 mg/mL, although the sample is expected to be at a concentration of 3.2 mg/mL. However, as the gel preparation in syringe involves transferring of the solution using other syringes, this increase in concentration can be ascribed to a lower final volume in the gel. The increased UV-Vis absorption could also be ascribed to a slight increase in aggregation after applying more

force on the stiff gel. Nevertheless, the UV-Vis data suggests that 100% of the insulin expected is collected after syringing, highlighting the strength of our approach.

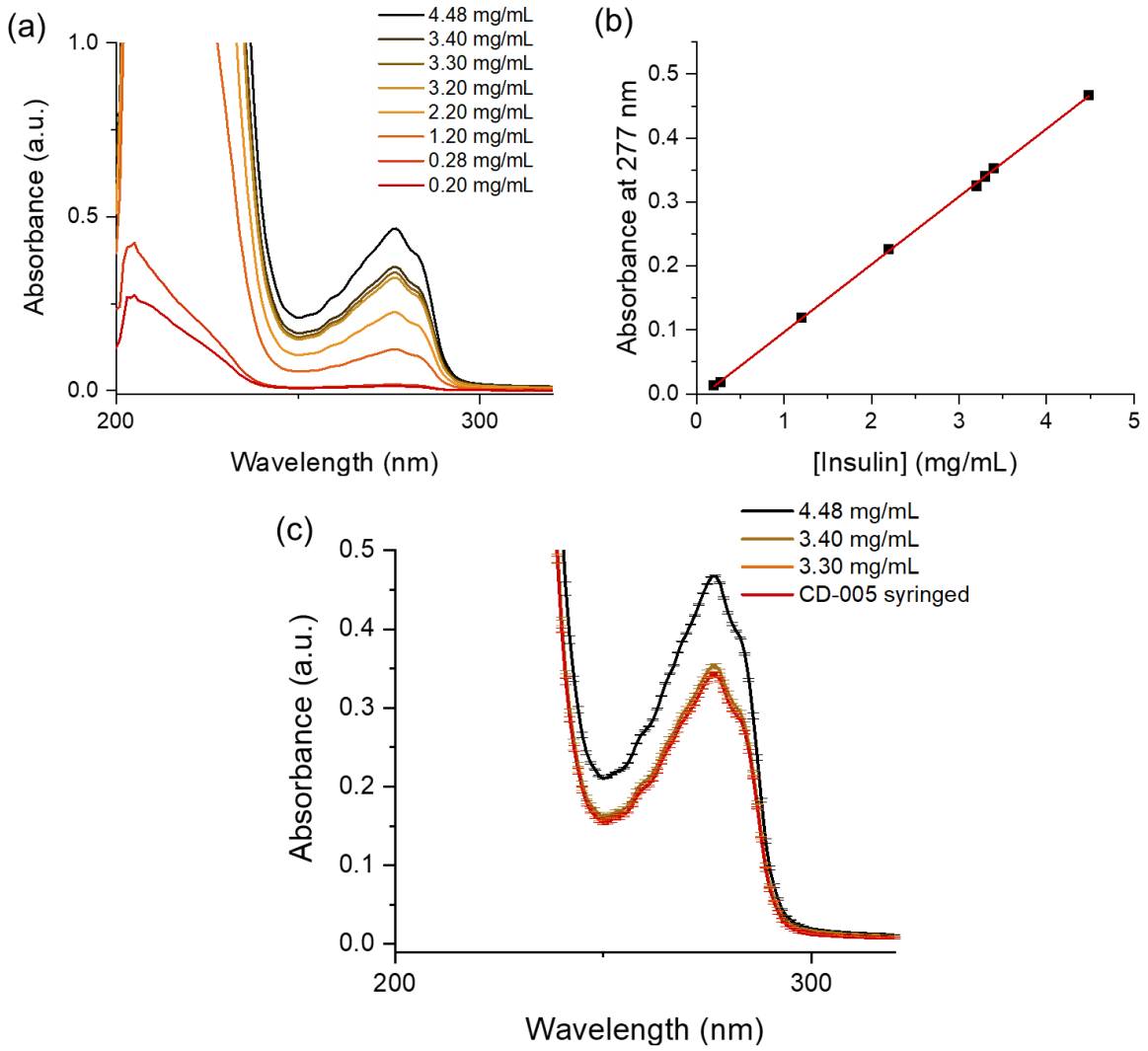

Figure 5.31. (a) Spectra of insulin at different concentrations in buffer. (b) Calibration curve obtained from (a). The data was fit using the Linear fitting function on Origin v2020b. (c) Data for solutions of insulin at various concentrations: 4.48 mg/mL (black), 3.4 mg/mL (brown), 3.3 mg/mL (orange) and the data from the solution extruded from the gel (red) at the expected concentration of 3.2 mg/mL. Small volume loss during sample preparation likely resulted in a lower dilution and an increase in insulin final concentration.

To investigate the effect of syringing on the aggregation of insulin, SAXS was performed on fresh insulin solutions and compared to solutions obtained after syringing the **CD-005** gels (Figure 5.32). The SAXS data shows no significant scattering from the 0.2 mg/mL insulin solutions (Figure 5.32a), due to the low concentration of insulin in the sample. Nevertheless, no changes in the scattering pattern were observed after releasing the solution from the gel (Figure 5.32a, red data). At higher insulin concentration, 3.2 mg/mL, the SAXS

data obtained showed appreciable scattering for all samples (Figure 5.32b), with no significant changes to the scattering pattern after syringing from the gel (Figure 5.32b, red data).

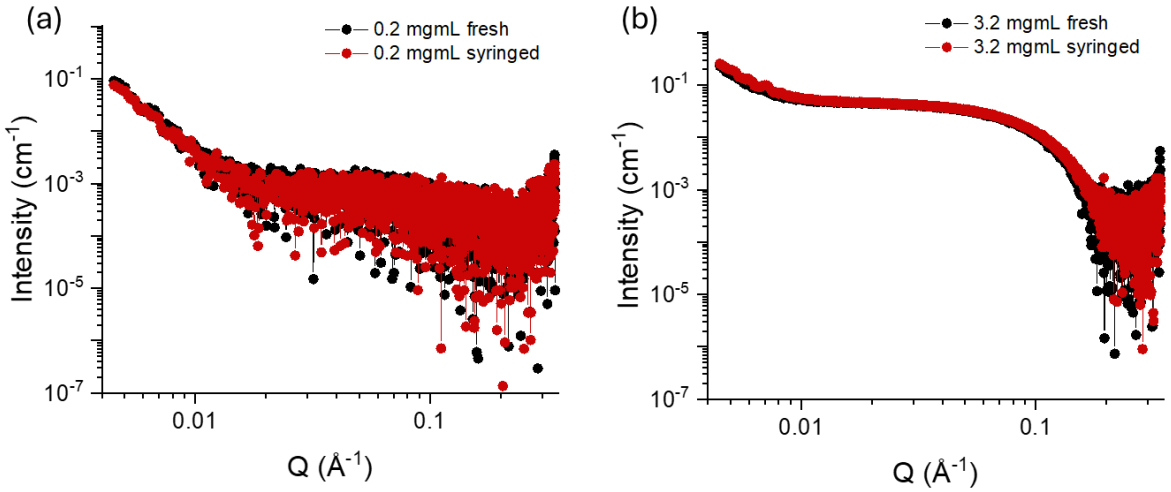

Figure 5.32. Small angle X-ray scattering patterns for fresh solutions of insulin (black data) and solutions obtained after extruding through the gel (red data) at concentrations of 0.2 mg/mL (a) and 3.2 mg/mL (b).

Overall, the data obtained for gelator **CD-005** highlights the potential for this supramolecular system to store biologically relevant macromolecules and prevent aggregation. To further confirm this, a cell-based assay was performed for CD220 recognition by Muhammad Hasan (University of Warwick) on released insulin after being stored in harsh conditions (shaken at 600 rpm). The data showed that the released insulin retained CD220 binding equal to fresh, indicating that the molecule is folded correctly and retained biological activity.[30]

5.2.5 Gel stability tests

5.2.5.1 Aging

For long-term storage applications, it is further important to test the stability of the gels in real world conditions. For instance, aging of the gels can have a significant impact on gel properties, as discussed in Chapter 1. Therefore, gels of **CD-005** (1 eq. $CaCl_2$) and **2NapIF** were also prepared in presence of 0 wt%, 0.1 wt%, 1 wt% and 10 wt% dextran in both vials and in syringes. The samples were allowed to age over a period of 4 months for **CD-005** and 5 months for **2NapIF**, while testing their mechanical properties and releasability using rheology and ^{1}H NMR.

For **CD-005** gels formed in the presence of a calcium salt, slight fluctuations in the G′ and G″ were observed over the 4-month period (Figure 5.33) but overall showing similar

properties in all the gels. For the gels formed in the presence of dextran (Figures 5.33b, 5.33c and 5.33d), an increase in stiffness was observed after 2 months. This is likely due to both drying of the gel as well as the hygroscopic nature of dextran, resulting in a smaller gel volume. The ^{1}H NMR data for the extruded solutions after 4 months (Figure 5.34) shows characteristic peaks for dextran, indicating that our release approach still works after long periods of time and therefore the gels are suitable for storing applications. We note that very small peaks were observed around 1.2 ppm, but no other peaks related to the **CD-005** gelator could be seen at around 4.0 or 2.0 ppm, suggesting that these peaks can be ascribed to grease in the NMR tubes rather than gelator passing through.

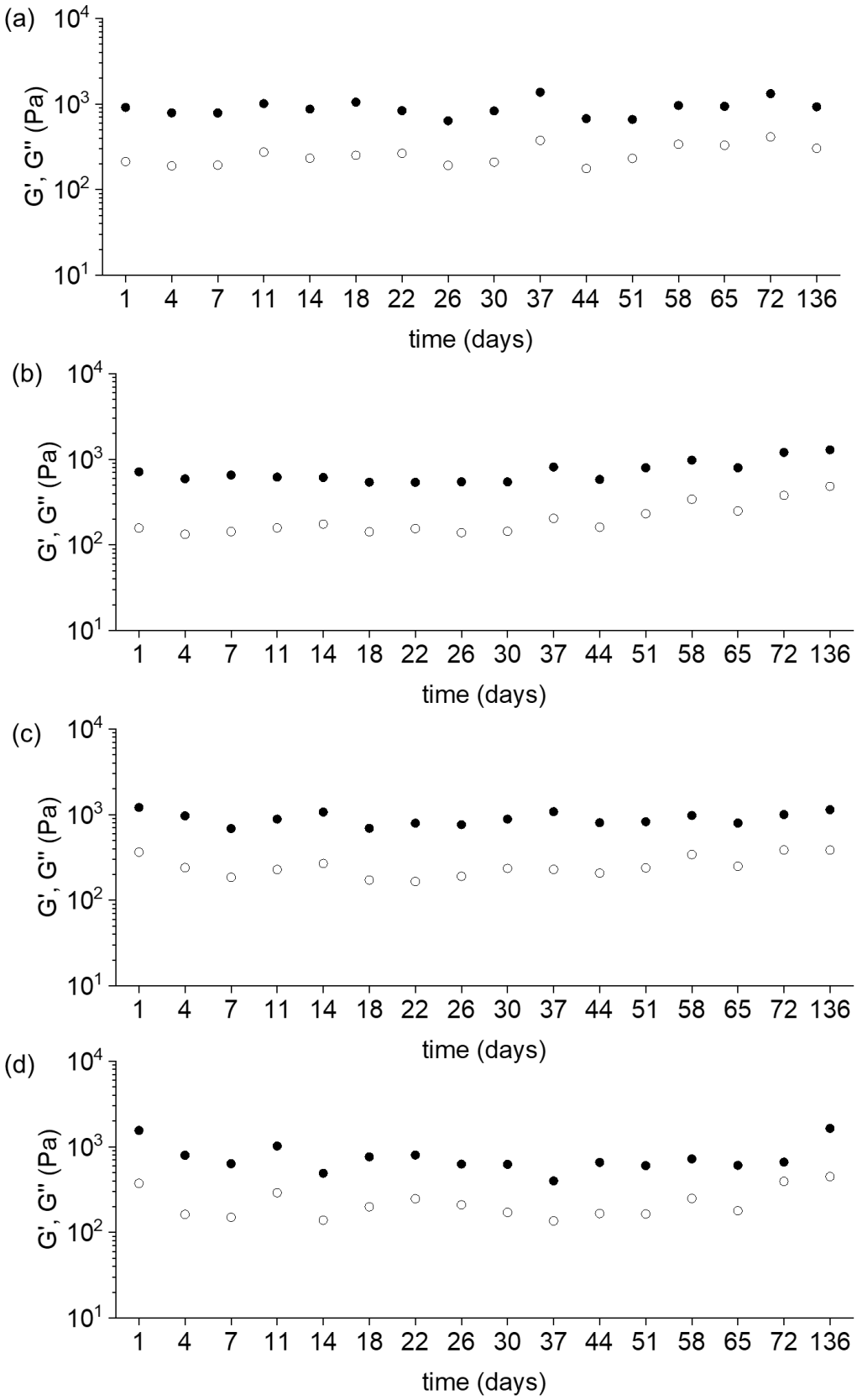

Figure 5.33. Rheological data over time for **CD-005** gels formed in presence of a calcium salt loaded with (a) 0 wt%, (b) 0.1 wt%, (c) 1 wt% and (d) 10 wt% dextran. In all cases, full circles represent G′ and open circles represent G″. Data was collected on a fresh gel at each time point.

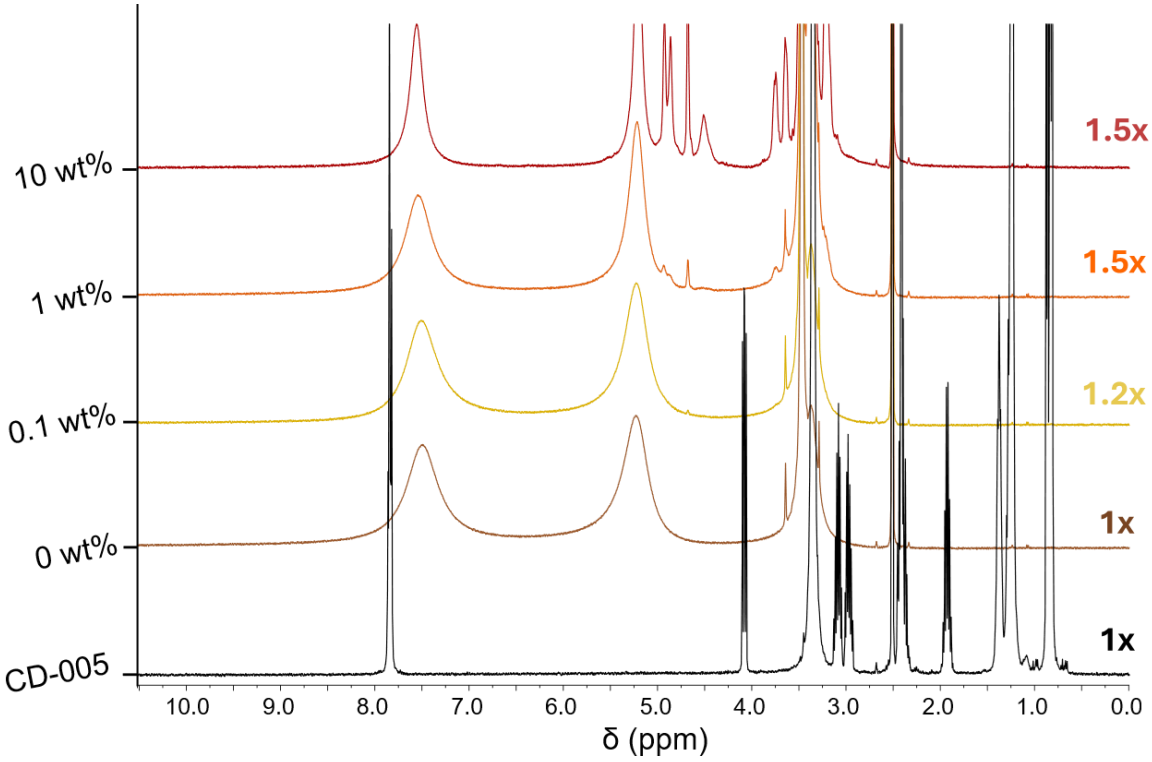

Figure 5.34. Full NMR spectra in d6-DMSO of **CD-005** (black data) compared to liquid released through the syringe filter for **CD-005** gels formed in presence of 0 wt% (brown), 0.1 wt% (yellow), 1 wt% (orange) and 10 wt% (red) dextran after 4 months of aging. We note a small peak in all the data around 1.2 ppm likely arising from grease in NMR tubes. Broad peaks at around 5.0 and 7.5 ppm are ascribed to the buffer (Figure 5.23, green data). Scaling of the data with respect to each other has been added for clarity.

For the **2NapIF** gels, the rheological data showed very similar values over 5 months, with a similar slight increase in stiffness of the gels in presence of dextran (Figure 5.35). This again can be ascribed to drying of the gels over time and the hygroscopic nature of dextran, leading to stiffer materials. ^{1}H NMR data for the liquid extruded from the **2NapIF** gels (Figure 5.36) further shows no peaks arising from the gelator in the aromatic region, also indicating that the pH triggered gels are stable to store and release the macromolecule over time.

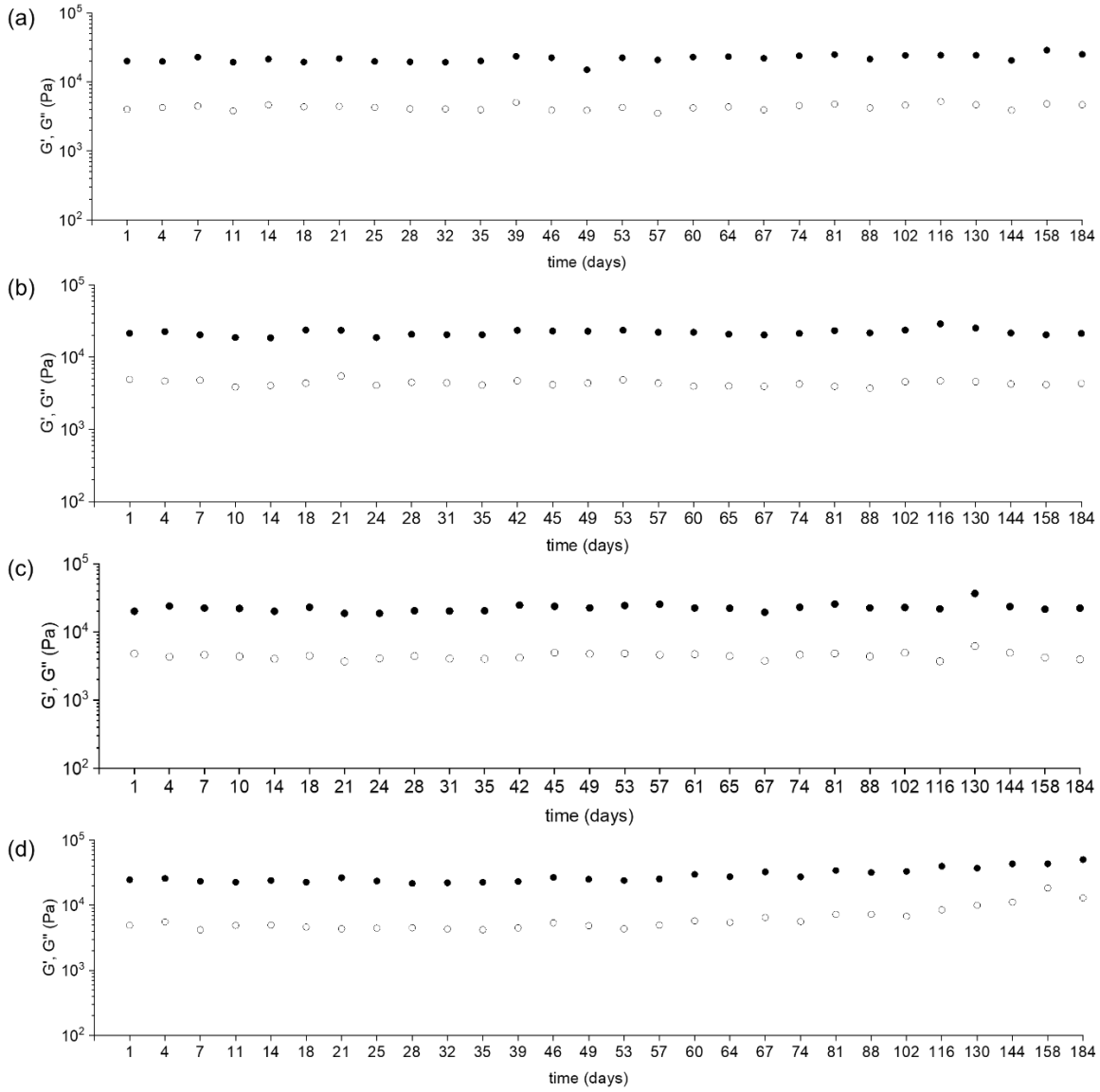

Figure 5.35. Rheological data over time for **2NapIF** gels formed in presence of (a) 0 wt%, (b) 0.1 wt%, (c) 1 wt% and (d) 10 wt% dextran. In all cases, full circles represent G′ and open circles represent G″. Data was collected on a fresh gel at each time point.

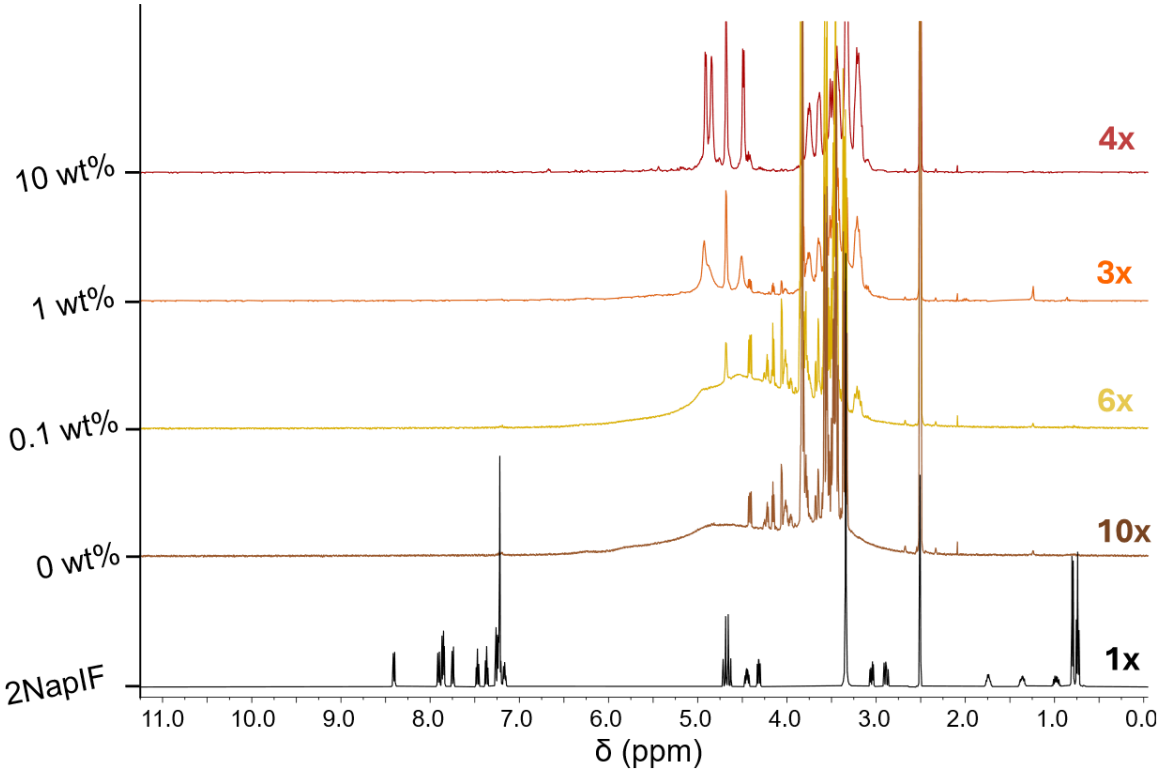

Figure 5.36. Full NMR spectra in d6-DMSO of **2NapIF** (black data) compared to liquid released through the syringe filter for **2NapIF** gels formed in presence of 0 wt% (brown), 0.1 wt% (yellow), 1 wt% (orange) and 10 wt% (red) dextran after 5 months of aging. A peak around 1.2 ppm is observed in the 1 wt% data, likely due to grease in the NMR tubes. Scaling of the data with respect to each other has been added for clarity.

5.2.5.2 Temperature

Temperature is another essential variable to consider when designing systems for applications in drug storage, as the samples might need to be transported to warmer countries, where higher storage temperatures can be reached. To test the stability of the **CD-005** 1 eq. $CaCl_2$ gels at higher temperatures, a frequency sweep was collected at a temperature of 60 °C, which is higher than the temperatures likely reached during transport. The rheological data shows that the sample retains its gel character even at 60 °C, with a cross-over at higher frequency between G′ and G″, likely due to inertial effects in the rheometer (Figure 5.37). This is an encouraging result, as it suggests that **CD-005** can still encapsulate the sample even at high temperatures and maintain its network.

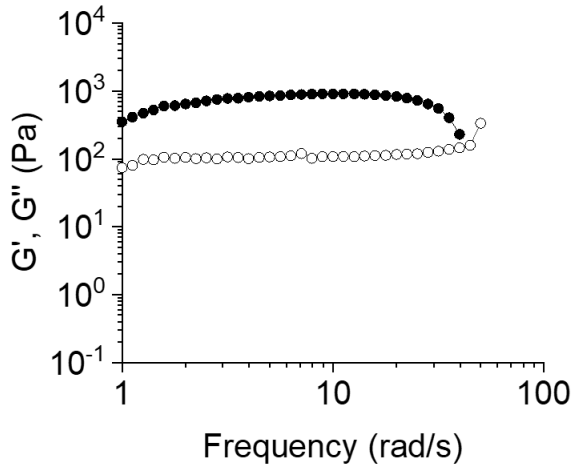

Figure 5.37. Frequency sweep for a gel formed from **CD-005** with the addition of $CaCl_2$ after heating up to 60°C. The gel was pre-formed in an aluminium cup and then heated on the rheometer in the cup, prior to measuring the frequency sweep. In all cases, the full circles represent G′ and the open circles represent G″.

To further understand the stability of the gels at such temperatures, **CD-005** gels were prepared in the presence of a calcium salt at room temperature and then allowed to age over time in an oven at 60°C. The rheological data of the gels shows that, upon keeping the samples in the oven, an increase in stiffness is observed (Figure 5.38). This then stabilizes, with the samples showing the same rheological behavior after 7 days in the oven. The samples possess the same yield point, suggesting that there are no significant changes in the way the bulk network responds to mechanical stimulus.

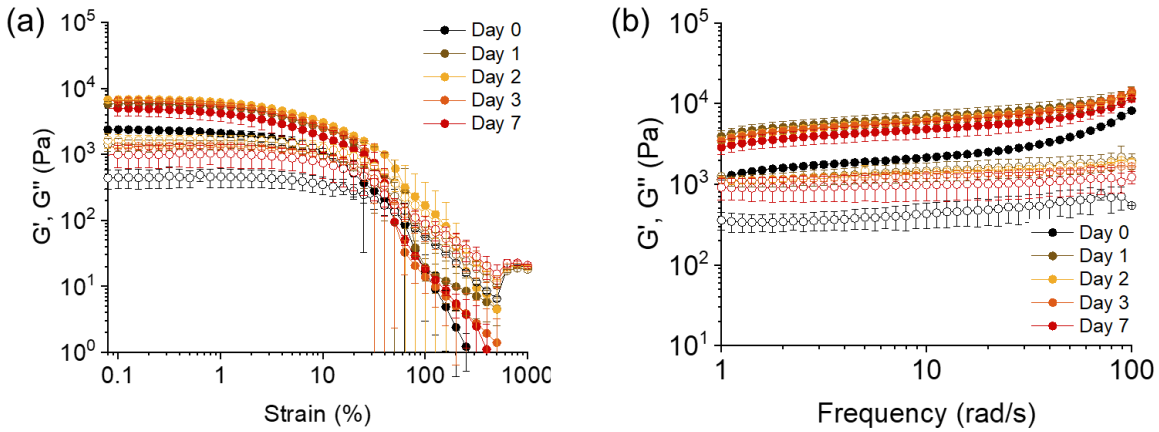

Figure 5.38. Strain sweeps (a) and frequency sweeps (b) obtained for **CD-005** gels formed in presence of a calcium salt and heated at 60°C for 7 days. The data was compared to a sample prepared overnight at room temperature (black data). In all cases, full circles represent G′ and open circles represent G″.

CD was performed on the solutions after 7 days of heating at 60 °C (Figure 5.39a, red data) and compared to the CD of **CD-005** (1 eq. $CaCl_2$) (Figure 5.39a, black data). The data shows here a similar shape in the data, with a slight blueshift observed in the region between 200 and 230 nm. This can be either due to minor changes in the packing of the molecules on the secondary structure level, but it can also arise from sample preparation errors in the small 0.01 mm cuvette.

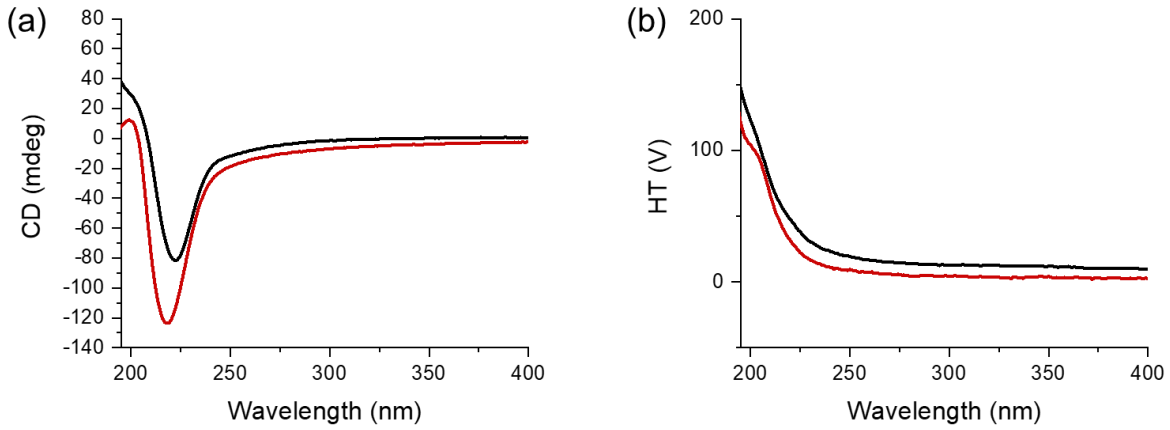

Figure 5.39. (a) Circular dichroism and (b) HT from gels of **CD-005** prepared in presence of a calcium salt at 22 °C (black data) and after heating at 60 °C (red data).

SAXS was performed on the sample after heating at 60 °C overnight and then allowing the sample to reach room temperature. The data shows a change on the nanoscale level in these materials compared to the sample at 22 °C (Figure 5.40). The data was fitted to a similar elliptical cylinder model with the presence of a Lorentzian peak. Here, compared to the gel prior to heating, the radius decreases significantly from 15.6 nm to 5.7 nm, with an increase in axis ratio from 2.2 to 5.6 (Table 5.9). Furthermore, the Bragg peak observed at 0.154 Å was observed to shift to 0.18 Å and broaden (10x increase in half width at half maximum). This data suggests that after heating, the self-assembled structures pack more tightly in space (d = 34.9 Å) in a less ordered manner. This results in either increased lateral association or the formation of more tape-like fibres. Thus, as the sample shows gel-like characteristics at 60 °C, this system shows a unique temperature induced gel-to-gel transition. Only one other example of such thermally induced structural change has been reported for a supramolecular polymer based on a glycosylated amino acid.[31]

Despite the change in structure, the ability of these gels to store and release biologics is unaffected. As a test, β-galactosidase was encapsulated, and gels were placed in an incubator at 50 °C for 7 days and 4 weeks by Muhammad Hasan (University of Warwick). Here, it was shown that gel-stored protein recovered on average 97.1% of its function after 7 days

and up to 20% after 4 weeks after being kept at such temperatures.[30] Additionally, ^{1}H NMR for the extruded solutions after encapsulation at 60 °C (Figure 5.41) shows no peaks from the gelator, suggesting the robustness of our release approach even at high temperatures. We note that a very small peak was observed around 1.2 ppm, but no other peaks related to the **CD-005** gelator could be seen at around 4.0 or 2.0 ppm, which may indicate that these peaks arise from grease in the NMR tubes rather than gelator passing through.

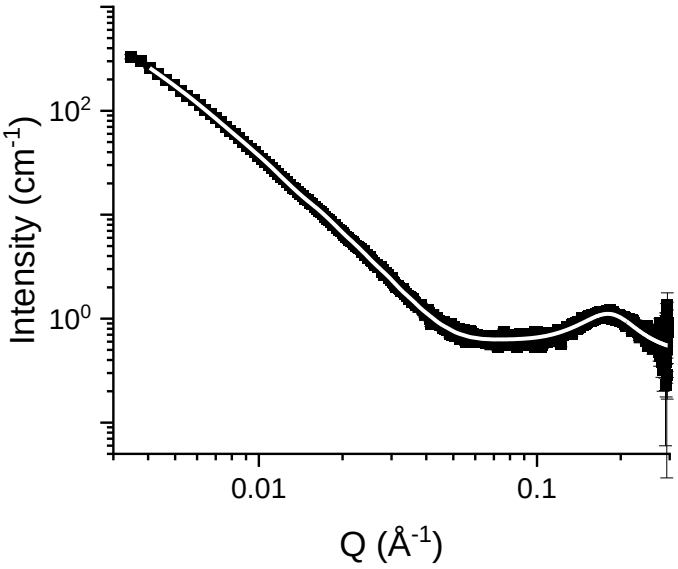

Figure 5.40. Small angle X-ray scattering pattern for **CD-005** gel prepared in presence of 1 eq. $CaCl_2$ after heating to 60 °C and cooling to room temperature. The white line indicates model fit.

Table 5.9. Fitting parameters for SAXS data in Figure 5.40. The data was fitted to an elliptical cylinder (EC) combined with a Lorentzian peak (Peak) and power law (PL) model. Values that were manually added and fixed have been labelled with *.

CD-005, 1 eq. CaCl2		
Sample	**Sample after heat cooling at 60 °C**	
Model	**EC+Peak+PL**	
	Value	**Error**
Scale	1	
Background (cm^{-1})	0.438	0.012
A_scale	0.002	6.38×10^{-5}
A_radius (Å)	56.8	0.62
A_axis_ratio	5.6	0.06
A_length (Å)	1000*	/
B_scale	0.66	0.011
B_peak_pos	0.18*	/
B_peak_HWHM	0.05	0.0012
C_scale	3.75×10^{-5}	8.89×10^{-6}
C_power	2.7	0.04
χ^2	1.23	

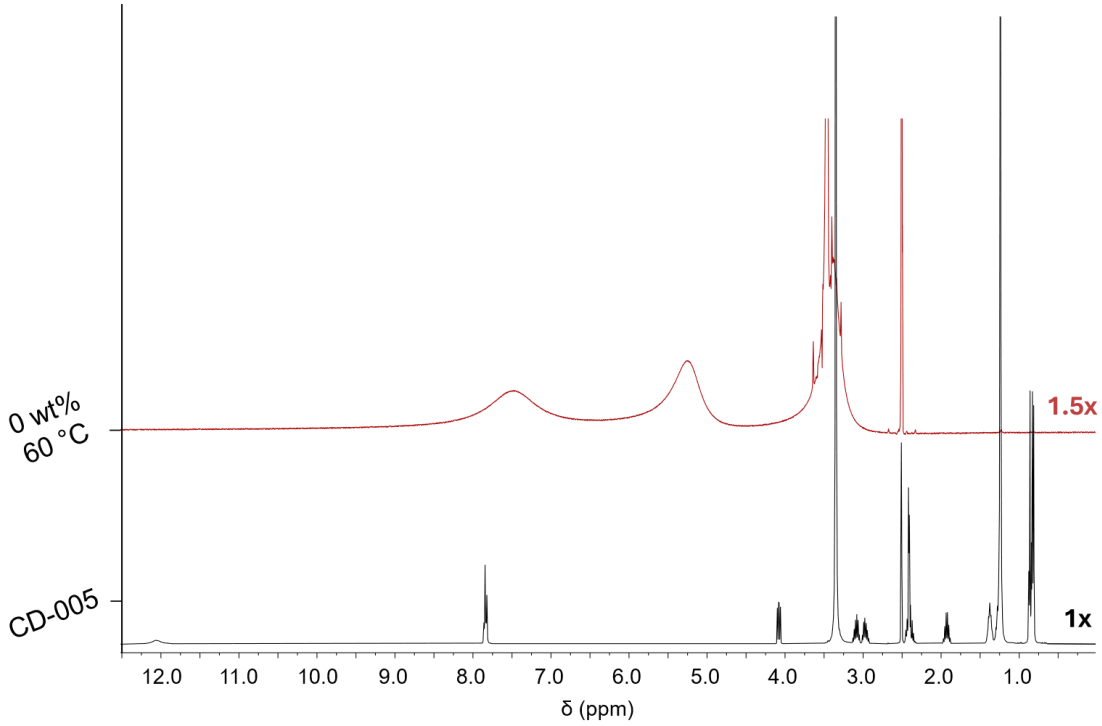

Figure 5.41. Full NMR spectra in d6-DMSO of **CD-005** (black data) compared to liquid released through the syringe filter for **CD-005** gels (1 eq. $CaCl_2$) after storing at 60 °C (red data). A peak around 1.2 ppm is observed in the 1 wt% data, likely due to grease in the NMR tubes. Broad peaks at around 5.0 and 7.5 ppm are ascribed to the buffer (Figure 5.23, green data). Scaling of the data with respect to each other has been added for clarity.

5.2.6 Discussion on gelator design

The data presented so far suggests that supramolecular gels formed by LMWGs can be used as effective materials for the storing and release of biologically relevant macromolecules using a simple approach. By analysing samples prepared in a variety of ways and possessing initial different morphologies, we are also able to then outline design rules to prepare materials that predictably respond to mechanical stimulus to release gel-free solutions.

Firstly, for the gel to be trapped in the filter, it is necessary for the gel to possess a persistent extended supramolecular network. As such, all systems that showed cylinder-like scattering patterns in the SAXS were successful in storing and releasing molecules. Further, stiffer materials are crucial for these applications, with stiffness values higher than 10^3 Pa. Indeed, the data obtained for the **CD-005** in presence of insulin compared to the **CD-005** with no salt suggest that the increased stiffness in the network allowed this gelator system to work. High stiffness is also key to ensure that the sample can retain its gel network during any transportation conditions.

Moreover, comparison of all the rheological data suggests that gels that show a single yielding process in the breaking (G′ deviating from linearity) can successfully be used through our approach, whilst gels showing two-step yielding, like the **CD-005** gels in absence of salt, are not as suitable. We ascribe this to the fact that the formation of disconnected clusters during breaking allows the gel to go through the filter, as it does not retain its extended supramolecular network upon breaking.

5.3 Conclusions

In this Chapter, we investigate the ability of various LMWGs to physically entrap proteins and release them through a simple new approach. There are currently examples of gels that can store and release un-aggregated proteins, but often these approaches result in the release of protein mixed with unknown gel components. This is a key issue to solve when designing materials for storing release applications.

We show that we can form supramolecular gels *via* a pH trigger and a buffer trigger with encapsulated additive molecules, such as dextran and insulin. We used rheology to investigate the effect of the encapsulated molecules on the system, combined with SAXS to elucidate the material properties on the nanoscale and on the bulk level. Using these, we were able to show that the samples are not affected by the presence of the additives, confirming that the molecules are physically encapsulated within the supramolecular gel network.

By forming the gels in syringes and releasing through an in-line filter, we have shown *via* ^{1}H NMR and fluorescence that minimal or no gelator passes through the filter. This is due to the unique mechanical properties of the LMWGs, as they break with no need for any chemical triggers. The key to this approach is the extended supramolecular network formed by the gelators, which results in all the gel components (e.g., excipients) to be retained in the filter. This means only pure protein in buffer is delivered, unlike all competing technologies.

Further, we have demonstrated that these supramolecular gels can work even at temperatures as high as 50°C for up to 4 weeks and show sample stability for months at room temperature, removing temperature requirements that are often needed for current formulations. As the work in this Chapter shows the versatility of this approach to a variety of gel types, future work would look to examine further the method of release. For instance, testing different sizes of syringes or syringe filters would be necessary to expand the range of macromolecules that can be added to the gels. Moreover, quantifying and optimizing the

necessary force to apply to improve biologic release would be crucial for real-world applications.

In summary, the approach shown in this work has provided a new means of storing, transporting and safely using biologically relevant molecules without the need for frozen formulations and ease of release, opening up a novel strategy to deliver therapeutics.

5.4 Experimental

5.4.1 Materials

All chemicals were purchased from Sigma-Aldrich and used as received. Deionized water was used throughout. The gelator **CD-005** was synthesised by Dr. Bart Dietrich (University of Glasgow) following the protocols of Angulo-Pachón and Miravet.[32] The other gelators (**2NapIF**, **2NapFV** and **BrNapLFF**) were prepared as described elsewhere by Prof. Dave J. Adams (University of Glasgow).[33,34]

5.4.2 Methodology

5.4.2.1 Formation of gels for CD-005 gelator

CD-005 gels were prepared either with or without the addition of $CaCl_2$. For both, 50 mg of **CD-005** were added to 20 mg of K_2CO_3 and dissolved in 5 mL de-ionised water under overnight stirring. For the samples without $CaCl_2$, 0.4 mL of the gelator solution were transferred to a vial, to which 1 mL of 1.5M Tris HCl (pH 6.8) was added. For the samples formed with the calcium trigger, 5.5 µL of a 200 mg/mL $CaCl_2$ solution were first added to 1 mL of 1.5M Tris HCl (pH 6.8) in a separate vial. This was then added in one aliquot to 0.4 mL of gelator buffer. For rheological measurements, the gels were prepared in vials and left undisturbed overnight on the bench. To prepare the samples in syringes, the gels were prepared as above and immediately transferred (< 1 minute) to a syringe through a 21G needle. It is relevant to note that all the samples needed to be prepared at 19 °C to ensure optimal gelation.

5.4.2.2 Pre-gel solution preparation for other tested gels formed using GdL

5.4.2.3 Formation of gels using GdL

Micellar solutions were prepared as previously described at concentrations of 5 mg/mL.[33] Gel samples were prepared in 7 mL Sterilin vials by addition of 2 mL of stock solution (adjusted to pH 10.5) to 16 mg of solid GdL for 5 mg/mL solutions. The vials were swirled

briefly by hand to ensure complete dissolution of GdL then left to stand overnight undisturbed.

5.4.2.4 Encapsulation of dextran and insulin

For the **CD-005** gels, dextran was encapsulated in the gel by dissolution of dextran powder in 1.5M Tris HCl, pH 6.8 at a range of concentrations (0.14 wt% to 14 wt%). 1 mL of this solution was transferred to 0.4 mL of the gelator solution described above to achieve the desired final concentrations of dextran (0.1 wt% to 10 wt%). For **CD-005** gels loaded with insulin, insulin was first dissolved in 1.5M Tris HCl, pH 6.8 at 0.28 mg/mL and 4.48 mg/mL. To avoid aggregation, the samples were left overnight on a roller at 76 rpm to ensure dissolution. 1 mL of this solution was transferred to 0.4 mL of the gelator solution described above to achieve the desired final concentrations of insulin (0.2 mg/mL and 3.2 mg/mL). For the gels obtained by reduction in pH, the dextran was dissolved at the various required concentrations in deionized H_2O under stirring. These solutions were then used to prepare the micellar solutions of the gelators at 5 mg/mL.

5.4.2.5 Release protocols through syringe filter

To release the gel with dextran inclusion, the gel prepared in the syringe was passed through a 2.7 μm filter. Figure 5.1 exemplifies the methodology of release through the filter: the sample is firstly allowed to gel overnight in a syringe, then the gel is gently passed through the 2.7 μm syringe filter releasing a clear solution. Generally, ca. 80% of the liquid is recovered from the procedure.

5.4.2.6 Release protocols for UV-Vis and fluorescence

For the quantification of released insulin and dextran, samples were prepared as follows. Insulin was dissolved in 1.5M Tris HCl (pH 6.8) at concentrations of 0.28 mg/mL and 4.48 mg/mL. To avoid aggregation, the samples were left overnight on a roller at 76 rpm to ensure complete dissolution. To form gels in the syringes, 0.4 mL of the **CD-005** gelator solution prepared as described above was transferred to a 12 mL syringe. Then, 1 mL of the insulin solution in Tris was transferred using a 5 mL syringe and a 21G needle directly in the 12 mL syringe. This resulted in quick formation of the gels at final concentrations of 0.2 mg/mL and 3.2 mg/mL. The gels were left overnight to stabilise and then gently passed through a 2.7 μm filter, releasing a clear solution. UV-Vis was measured directly on the obtained solution. To quantify the amount of insulin released, insulin solutions were prepared at a range of concentrations (0.2 mg/mL to 4.48 mg/mL) in a similar way in 1.5M Tris HCl.

For the quantification of released dextran, 1.4 wt% (14 mg/mL) solution of fluorescein isothiocyanate-dextran was prepared in 1.5M Tris HCl buffer by dissolving 14 mg of the dextran in 1 mL of buffer. 5.5 μL of 200 mg/mL $CaCl_2$ solution was then added to 1 mL of this solution and swirled briefly. To form gels in syringes, a similar method was used as described above, achieving a final concentration of 1 wt% (10 mg/mL). The gels were left overnight to stabilise and then gently passed through a 2.7 μm filter. The resulting dextran solution was too concentrated to study *via* UV-Vis and fluorescence. For UV-Vis a dilution of a factor of 10 was carried out using buffer, reaching a final concentration of 1 mg/mL. For fluorescence a factor of 100 was needed (0.1 mg/mL) to avoid self-quenching at higher concentrations. To quantify the amount of released dextran, fluorescein isothiocyanate-dextran was dissolved in 1.5M Tris-HCl buffer at desired concentrations (1 mg/mL to 0.05 mg/mL), ensuring the same pH throughout.

5.4.3 Characterisation

5.4.3.1 Rheology

Rheological measurements were carried out using Anton Paar Physica MCR301 and M101 Rheometers. A cup and vane (ST10-4V-8.8/97.5-SN42404) system was used for all frequency and strain sweeps, with a measuring gap of 1.35 mm. Gels were prepared directly in 7 mL Sterilin vials, which were loaded on to the rheometer and measured in situ to ensure that no damage was carried out to the gels by transfer from vials. Strain sweeps were performed from 0.08 % to 1000 % at a frequency of 10 rad/s. Frequency sweeps were performed from 1 rad/s to 100 rad/s at a constant strain of 0.1 % (within the linear viscoelastic region for all gels). To test the behaviour of the materials at low frequency, frequency sweeps were further collected from 0.01 rad/s to 100 rad/s at a constant strain of 0.1 % (within the linear viscoelastic region for all gels). To measure the yield stress of the gels, strain sweeps were performed at a frequency of 1 rad/s from 0.1% and 1000%. The yield stress value was obtained by plotting the elastic stress ($G' \times \gamma_0$) against the strain amplitude, according to previously published methods.[23-27]

To obtain frequency sweeps of the samples at higher temperatures, gels were prepared directly in 7 mL aluminium cups and loaded on to the rheometer. The temperature was raised linearly from 25 °C to 60 °C with a heating rate of 2 °C/min. Then, frequency sweeps were collected from 1 rad/s to 100 rad/s, while keeping a constant strain of 0.1% and temperature of 60 °C.

5.4.3.2 pH measurements

The pH of solutions and gels was measured using a FC200 pH probe (Hanna instruments) calibrated using pH 4.01, 7.01 and 10.01 buffer solutions. The probe was rinsed with deionized water between measurements.

5.4.3.3 Small angle X-ray scattering

Small angle X-ray scattering experiments were performed at Diamond Light Source, Didcot at the I22 beamline.[35] The beamline operates at an energy of 12.4 keV and the camera length was set to 4.275 m to give a Q range of 0.002 - 0.30 $Å^{-1}$. The gels were prepared as described in the next section and immediately loaded in glass capillaries using a 1 mL syringe with a 21G needle. The raw data were processed using the DAWN Science software (version 2.27),[36] according to a standard I22 pipeline.[37] As part of the processing, the backgrounds were subtracted from the raw 2D SAXS data and a full azimuthal integration was performed to reduce the data to a *I* vs *q* plot. The plots were then fitted to structural models using the SasView software (version 5.0.4).

BioSAXS experiments were performed at the B21 beamline at Diamond Light Source using the BioSAXS EMBL Arinax sample-handling robot. These experiments were performed on the samples in buffer prior to gel storage and after release in Figures 5.26 and 5.32. The beamline operates at a fixed energy of 13 keV and a camera length of 3.600 meters to obtain a q-range of 0.0031 to 0.38 $Å^{-1}$. 50 µL of each sample was loaded into a 96-well plate and measured. For each sample, 30 x 1 s frames were collected at 20°C. The 2D raw data was processed in the DAWN Science software (version 2.27[37]) to yield the *I* vs *q* plots. The data was then averaged, and the buffer background was manually subtracted using the *ScÅtter* software (https://www.bioisis.net/, R. P. Rambo).

Small angle X-ray scattering experiments on the gel after storage at 60°C and cooling to room temperature (Figure 5.40) were performed at the CoSAXS beamline at the diffraction limited 3 GeV storage ring at the MAX IV Laboratory in Sweden. An X-ray beam of 15 keV was used, with the camera length set at 3.5 m to achieve a q-range of 0.003 – 0.3 $Å^{-1}$ (where $q= 4\pi/\lambda \sin(\theta)$, λ=0.8267 Å and 2θ the scattering angle). The data was collected using an EIGER2 4M hybrid photon-counting pixel detector (Dectris AG).

To calculate the X-ray scattering length densities (SLDs) for all samples, the NIST neutron activation and scattering calculator was used (https://www.ncnr.nist.gov/resources/activation/), assuming a density of 1.58 g/cm^3 for the low molecular weight gelators and a density of 1.54 g/cm^3 for dextran. The SLDs used

are summarised in the table below (Table 5.10). For samples comprising of dextran and LMWGs, the SLD of each component was added in the respective model used (sphere for dextran and cylindrical model for the LMWG).

Table 5.10. SLDs values used in this Chapter for SAXS model fitting on Sasview.

Sample	SLD ($x10^{-6}$) ($Å^2$)
2NapIF	14.309
2NapFV	14.277
BrNapLFF	13.956
CD-005	14.828
Dextran	13.922

5.4.3.4 Circular Dichroism

Circular dichroism data was acquired on a Chirascan VX spectrometer (Applied Photophysics) using a quartz cuvette with a 0.01 mm path length. The spectra were collected in the range 180-400 nm with a scanning step size of 1.0 nm and scanning rate of 0.25 s at room temperature. The samples were prepared in Sterilin vials as described keeping the same volumes of the components. Small amounts of the gels were then transferred to the cuvette prior to measurement.

5.4.3.5 UV-Vis

Absorption spectra were recorded on an Agilent Cary 60 UV-Vis spectrophotometer using a quartz cuvette with 0.1 mm path length. Samples were prepared as above and 300 μL of the solution was transferred to the cuvette using a 200 μL pipette.

5.4.3.6 Fluorescence

Fluorescence data were collected using an Agilent Technologies Cary Eclipse fluorescence spectrometer. Samples were prepared as described above at a 2 mL volume and transferred to a quartz cuvette with a 1 cm path length. For the fluorescein isothiocyanate-dextran, the excitation wavelength was 470 nm. For the **2NapIF** release studies, the excitation length was 320 nm. In all cases, the excitation and emission slit widths were 5 nm and 5 nm. To quantify the amount of **2NapIF** in the extrudate, a known volume of the extruded sample was freeze-dried (1 mL) and then fully re-dissolved in DMSO.

5.4.3.7 FTIR spectroscopy

Data were recorded using an Agilent Cary 630 FTIR spectrometer (with ATR attachment). The filter paper from the 2.7 μm filter was removed by carefully opening the syringe filters. Then, the background of the empty ATR crystal was taken. Small amounts of a clean filter and one after extrusion were deposited on the ATR crystal to record the spectra.

5.4.3.8 ^{1}H NMR

Water suppression and STD experiments were performed by Dr. Matthew Wallace, University of East Anglia. The measurements were recorded on a Bruker spectrometer operating at 499.31 MHz and equipped with a Neo console and Bruker 5 mm SmartProbe™. ^{1}H experiments were recorded using the perfect echo WATERGATE sequence of Adams *et al*.[38] incorporating the double echo W5 sequence of Liu *et al*.[39] The delay between successive pulses in the selective pulse train was set at 333 μs, corresponding to 3000 Hz between the null points. ^{1}H spectra were acquired in 4 dummy scans and 128 scans with a relaxation delay of 1 s and signal acquisition time of 4.2 s. STD spectra were obtained using the same sequence but with an overall relaxation delay of 5 s. Presaturation was applied during the final 4 seconds of the relaxation delay using a train of 100 Gaussian pulses (40 ms) with peak powers of 243 Hz at 100 ppm (off resonance) and -3.8 ppm (on resonance) in separate experiments, which were recorded with 16 dummy scans and 16 scans. Spectra were processed with an exponential line broadening factor of 1 Hz and referenced to the CH_3 triplet of ethanol (1.2 ppm) present as an impurity in our commercial insulin sample.[40]

The 3.2 mg/mL insulin solution and the **CD-005** gel were prepared and aged in 5 mm NMR tubes (Wilmad 528-PP) for 20 hours at 22 °C.

5.5 References

1 P. Terech and R. G. Weiss, Low Molecular Mass Gelators of Organic Liquids and the Properties of Their Gels, *Chem. Rev.*, 1997, **97**, 3133–3160.

2 E. R. Draper and D. J. Adams, Low-Molecular-Weight Gels: The State of the Art, *Chem*, 2017, **3**, 390–410.

3 C. C. Piras, P. G. Genever and D. K. Smith, Combining gellan gum with a functional low-molecular-weight gelator to assemble stiff shaped hybrid hydrogels for stem cell growth, *Mater. Adv.*, 2022, **3**, 7966–7975.

4 J. Wang, Z. Wang, J. Gao, L. Wang, Z. Yang, D. Kong and Z. Yang, Incorporation of supramolecular hydrogels into agarose hydrogels—a potential drug delivery carrier, *J. Mater. Chem.*, 2009, **19**, 7892–7896.

5 A. Altunbas, S. J. Lee, S. A. Rajasekaran, J. P. Schneider and D. J. Pochan, Encapsulation of curcumin in self-assembling peptide hydrogels as injectable drug delivery vehicles, *Biomaterials*, 2011, **32**, 5906–5914.

6 L. Chen, S. Revel, K. Morris, D. G. Spiller, L. C. Serpell and D. J. Adams, Low molecular weight gelator–dextran composites, *Chem. Commun.*, 2010, **46**, 6738–6740.

7 D. M. Raymond, B. L. Abraham, T. Fujita, M. J. Watrous, E. S. Toriki, T. Takano and B. L. Nilsson, Low-Molecular-Weight Supramolecular Hydrogels for Sustained and Localized in Vivo Drug Delivery, *ACS Appl. Bio Mater.*, 2019, **2**, 2116–2124.

8 M. G. Faidra Angelerou, R. Markus, V. Paraskevopoulou, R. Foralosso, P. Clarke, C. V. Alvarez, M. Chenlo, L. Johnson, C. Rutland, S. Allen, C. Brasnett, A. Seddon, M. Zelzer and M. Marlow, Mechanistic investigations into the encapsulation and release of small molecules and proteins from a supramolecular nucleoside gel in vitro and in vivo, *J. Control. Release*, 2020, **317**, 118–129.

9 S. Sutton, N. L. Campbell, A. I. Cooper, M. Kirkland, W. J. Frith and D. J. Adams, Controlled Release from Modified Amino Acid Hydrogels Governed by Molecular Size or Network Dynamics, *Langmuir*, 2009, **25**, 10285–10291.

10 M. L. Jagrosse, P. Agredo, B. L. Abraham, E. S. Toriki and B. L. Nilsson, Supramolecular Phenylalanine-Derived Hydrogels for the Sustained Release of Functional Proteins, *ACS Biomater. Sci. Eng.*, 2023, **9**, 784–796.

11 J. Lee, E.-W. Lin, U. Y. Lau, J. L. Hedrick, E. Bat and H. D. Maynard, Trehalose Glycopolymers as Excipients for Protein Stabilization, *Biomacromolecules*, 2013, **14**, 2561–2569.

12 B. Marco-Dufort, J. R. Janczy, T. Hu, M. Lütolf, F. Gatti, M. Wolf, A. Woods, S. Tetter, B. V. Sridhar and M. W. Tibbitt, Thermal stabilization of diverse biologics using reversible hydrogels, *Sci. Adv.*, 2022, **8**, eabo0502.

13 B. V. Sridhar, J. R. Janczy, Ø. Hatlevik, G. Wolfson, K. S. Anseth and M. W. Tibbitt, Thermal Stabilization of Biologics with Photoresponsive Hydrogels, *Biomacromolecules*, 2018, **19**, 740–747.

14 A. vander Straeten, M. Sarmadi, J. L. Daristotle, M. Kanelli, L. H. Tostanoski, J. Collins, A. Pardeshi, J. Han, D. Varshney, B. Eshaghi, J. Garcia, T. A. Forster, G. Li, N. Menon, S. L. Pyon, L. Zhang, C. Jacob-Dolan, O. C. Powers, K. Hall, S. K. Alsaiari, M. Wolf, M. W. Tibbitt, R. Farra, D. H. Barouch, R. Langer and A. Jaklenec, A microneedle vaccine printer for thermostable COVID-19 mRNA vaccines, *Nat. Biotechnol.*, 2024, **42**, 510–517.

15 P. G. Georgiou, I. Kontopoulou, T. R. Congdon and M. I. Gibson, Ice recrystallisation inhibiting polymer nano-objects via saline-tolerant polymerisation-induced self-assembly, *Mater. Horiz.*, 2020, **7**, 1883–1887.

16 B.-M. Chen, T.-L. Cheng and S. R. Roffler, Polyethylene Glycol Immunogenicity: Theoretical, Clinical, and Practical Aspects of Anti-Polyethylene Glycol Antibodies, *ACS Nano*, 2021, **15**, 14022–14048.

17 M. Wallace, D. J. Adams and J. A. Iggo, Analysis of the mesh size in a supramolecular hydrogel by PFG-NMR spectroscopy, *Soft Matter*, 2013, **9**, 5483–5491.

18 M. I. Smith, V. Foderà, J. S. Sharp, C. J. Roberts and A. M. Donald, Factors affecting the formation of insulin amyloid spherulites, *Colloids Surf. B: Biointerfaces*, 2012, **89**, 216–222.

19 D. J. Adams, M. F. Butler, W. J. Frith, M. Kirkland, L. Mullen and P. Sanderson, A new method for maintaining homogeneity during liquid–hydrogel transitions using low molecular weight hydrogelators, *Soft Matter*, 2009, **5**, 1856–1862.

20 J. D. Simpson, L. Thomson, C. M. Woodley, C. M. Wallace, B. Dietrich, A. S. Loch, D. J. Adams and N. G. Berry, Predicting the Mechanical Properties of Supramolecular Gels, *Adv. Mater.*, 2025, **37**, 2415031.

21 S. Panja, B. Dietrich and D. J. Adams, Controlling Syneresis of Hydrogels Using Organic Salts, *Angew. Chem.*, 2022, **134**, e202115021.

22 E. R. Draper, B. Dietrich, K. McAulay, C. Brasnett, H. Abdizadeh, I. Patmanidis, S. J. Marrink, H. Su, H. Cui, R. Schweins, A. Seddon and D. J. Adams, Using Small-

Angle Scattering and Contrast Matching to Understand Molecular Packing in Low Molecular Weight Gels, *Matter*, 2020, **2**, 764–778.

23 M. C. Yang, L. E. Scriven and C. W. Macosko, Some Rheological Measurements on Magnetic Iron Oxide Suspensions in Silicone Oil, *J. Rheol.*, 1986, **30**, 1015–1029.

24 H. J. Walls, S. B. Caines, A. M. Sanchez and S. A. Khan, Yield stress and wall slip phenomena in colloidal silica gels, *J. Rheol.*, 2003, **47**, 847–868.

25 M. Laurati, S. U. Egelhaaf and G. Petekidis, Nonlinear rheology of colloidal gels with intermediate volume fraction, *J. Rheol.*, 2011, **55**, 673–706.

26 M. Castro, D. W. Giles, C. W. Macosko and T. Moaddel, Comparison of methods to measure yield stress of soft solids, *J. Rheol.*, 2010, **54**, 81–94.

27 M. Das and G. Petekidis, Shear induced tuning and memory effects in colloidal gels of rods and spheres, *J. Chem. Phys.*, 2022, **157**, 234902.

28 M. Qafary, F. Rashno, K. Khajeh, M. Khaledi and A. A. Moosavi-Movahedi, Insulin fibrillation: Strategies for inhibition, *Prog. Biophys. Mol. Bio.*, 2022, **175**, 49–62.

29 M. Wallace, J. A. Iggo and D. J. Adams, Probing the surface chemistry of self-assembled peptide hydrogels using solution-state NMR spectroscopy, *Soft Matter*, 2017, **13**, 1716–1727.

30 S. Bianco, M. Hasan, A. Ahmad, S.-J. Richards, B. Dietrich, M. Wallace, Q. Tang, A. J. Smith, M. I. Gibson and D. J. Adams, Mechanical release of homogenous proteins from supramolecular gels, *Nature*, 2024, **631**, 544–548.

31 S. Kiyonaka, K. Sugiyasu, S. Shinkai and I. Hamachi, First Thermally Responsive Supramolecular Polymer Based on Glycosylated Amino Acid, *J. Am. Chem. Soc.*, 2002, **124**, 10954–10955.

32 C. A. Angulo-Pachón and J. F. Miravet, Sucrose-fueled, energy dissipative, transient formation of molecular hydrogels mediated by yeast activity, *Chem. Commun.*, 2016, **52**, 5398–5401.

33 J. K. Gupta, D. J. Adams and N. G. Berry, Will it gel? Successful computational prediction of peptide gelators using physicochemical properties and molecular fingerprints, *Chem. Sci.*, 2016, **7**, 4713–4719.

34 C. Colquhoun, E. R. Draper, E. G. B. Eden, B. N. Cattoz, K. L. Morris, L. Chen, T. O. McDonald, A. E. Terry, P. C. Griffiths, L. C. Serpell and D. J. Adams, The effect of self-sorting and co-assembly on the mechanical properties of low molecular weight hydrogels, *Nanoscale*, 2014, **6**, 13719–13725.

35 A. J. Smith, S. G. Alcock, L. S. Davidson, J. H. Emmins, J. C. Hiller Bardsley, P. Holloway, M. Malfois, A. R. Marshall, C. L. Pizzey, S. E. Rogers, O. Shebanova, T. Snow, J. P. Sutter, E. P. Williams and N. J. Terrill, SAXS/WAXS beamline at Diamond Light Source - an overview of 10 years operation, *J. Synchrotron Radiat.*, 2021, **28**, 939–947.

36 J. Filik, A. W. Ashton, P. C. Y. Chang, P. A. Chater, S. J. Day, M. Drakopoulos, M. W. Gerring, M. L. Hart, O. V. Magdysyuk, S. Michalik, A. Smith, C. C. Tang, N. J. Terrill, M. T. Wharmby and H. Wilhelm, Processing two-dimensional X-ray diffraction and small-angle scattering data in DAWN 2, *J. Appl. Crystallogr.*, 2017, **50**, 959–966.

37 B. R. Pauw, A. J. Smith, T. Snow, N. J. Terrill and A. F. Thunemann, The modular small-angle X-ray scattering data correction sequence, *J. Appl. Crystallogr.*, 2017, **50**, 1800–1811.

38 R. W. Adams, C. M. Holroyd, J. A. Aguilar, M. Nilsson and G. A. Morris, A. "Perfecting" WATERGATE: clean proton NMR spectra from aqueous solution, *Chem. Commun.*, 2013, **49**, 358–360.

39 M. Liu, X.-a. Mao, C. Ye, H. Huang, J. K. Nicholson and J. C. Lindon, Improved WATERGATE Pulse Sequences for Solvent Suppression in NMR Spectroscopy, *J Magn. Reson.*, 1998, **132**, 125–129.

40 N. R. Babij, E. O. McCusker, G. T. Whiteker, B. Canturk, N. Choy, L. C. Creemer, C. V. D. Amicis, N. M. Hewlett, P. L. Johnson, J. A. Knobelsdorf, F. Li, B. A. Lorsbach, B. M. Nugent, S. J. Ryan, M. R. Smith and Q. Yang, NMR Chemical Shifts of Trace Impurities: Industrially Preferred Solvents Used in Process and Green Chemistry, *Org. Process Res. Dev.*, 2016, **20**, 661–667.

Chapter 6. Conclusions and Future work

6. Conclusions and Future work

Supramolecular gels made from the self-assembly of peptide-based molecules are advantageous materials both due to their ease of synthesis and to the non-covalent nature of the interactions that hold their networks. Despite several efforts, the process of self-assembly is still difficult to predict and often molecules able to form gels are found serendipitously. Further, the link between molecular structure, structures formed in the gel phase and final gel properties is currently poorly understood. One potential way to overcome this issue is to design materials that exhibit predictable changes, leading to controllable final material properties. In this Thesis, we have investigated several ways to design stimuli-responsive materials that exhibit tuneable properties. To do this, we utilise a variety of external stimuli and focus on understanding material changes on different length scales.

Although rheology is a useful technique to measure the mechanical properties of gels, the mechanical stimulus applied by rheometers can be further used to tune material properties. In Chapter 2, we focused on the rheological analysis of a pH-responsive LMWG system undergoing gel-to-sol-to-gel transitions. We established that the values of strain and frequency used during the rheological measurement affect the properties of the final gels and therefore suggest that care needs to be taken when choosing parameters to measure these evolving systems. Furthermore, we showed that this approach can be used to form a wide variety of gels with different mechanical properties from a single starting gel. As such, future work would focus on examining this for other LMWG systems and fully elucidating the link between strain applied and final mechanical properties.

Building on this, in Chapter 3, we have shown how mechanical stimuli in the solution phase can be harnessed to induce fibre alignment in gels. We designed a new system exhibiting gel-to-sol-to-gel transitions based on a different LMWG. By applying monodirectional shear in the solution phase, we demonstrated how we can align fibrillar structures in a rheometer. We showed that this anisotropy is “locked in” the final gel by optimising the duration of shear in the solution phase. Furthermore, we have used a novel custom technique to simultaneously test the properties of this system on different length scales using SAXS, rheology and polarised light imaging. We used these results to confirm that alignment was only kept on the mesoscale, while anisotropy was lost on the nanoscale level once the gel reformed. This was ascribed to the formation of the gel network and highlights how crucial it is to test material properties on different length scales. Future work would involve using

this approach using conductive LMWGs to form conductive aligned films or test this approach in multi-component systems where, for instance, only one LMWG can align.

Light is an attractive external stimulus to design responsive materials, as it is non-invasive and can be applied in localised areas. In Chapter 4, we explored the design of a light-responsive system based on a dipeptide LMWG and a photoacid molecule capable of switching pH under irradiation. We showed that we can achieve reversible and fast changes in viscosity by irradiating with visible light. By using in situ irradiation techniques in rheology, SAXS and NMR, we further characterised and gained insight on the properties of this system on different length scales. We demonstrated that potential interactions between the dipeptide molecule and the photoacid aided this viscosifying behaviour by minimising gelator-gelator interactions in the dark, which were instead promoted upon irradiation. We finally illustrated how this system can be used to stop flow at specific locations by building a custom set-up. Future work would therefore involve testing this system in microfluidic environments to potentially generate photoresponsive microvalves.

Finally, in Chapter 5, we showed how the unique stimuli-response of gels to mechanical strain can be harnessed to design systems capable of storing and releasing encapsulated molecules. To do this, gels were prepared in syringes fitted with syringe filters. We investigated potential relationships between gel morphology, bulk properties and release ability by using rheology, SAXS and NMR. We showed that the ability to release cargo molecules is independent on type of gel morphology and yield point but related to the way materials break after application of strain. Based on this, we therefore extrapolated and suggested key gel properties for these applications. We demonstrated how this novel approach can be used to form gels that can successfully store and release insulin at room temperature, avoiding aggregation and need for cold storage requirements. Future work would involve tailoring gel properties for different biologics or exploring different filter sizes and syringe sizes for optimal release.

In conclusion, the work presented in this Thesis highlights the potential of supramolecular peptide-based systems for the design of smart responsive materials. This work provides further understanding and knowledge on how to tailor the behaviour of self-assembled structures using external stimuli, allowing to achieve predictable final properties in materials with high spatio-temporal control.